

Integrated Aeroservoelastic Design and Optimization of Large Offshore Wind Turbines

Turaj Ashuri

*Beyond Classical Upscaling:
Integrated Aeroservoelastic Design
and Optimization of
Large Offshore Wind Turbines*

Turaj Ashuri



Beyond Classical Upscaling:

Integrated Aeroservoelastic Design and
Optimization of Large Offshore Wind Turbines

Beyond Classical Upscaling:

Integrated Aeroservoelastic Design and Optimization of Large Offshore Wind Turbines

PROEFSCHRIFT

ter verkrijging van de graad van doctor
aan de Technische Universiteit Delft,
op gezag van de Rector Magnificus Prof. ir. K.C.A.M. Luyben,
voorzitter van het College voor Promoties,
in het openbaar te verdedigen
op woensdag 14 november 2012 om 15.00 uur
door

Turaj ASHURI

Master of science in Aerospace Engineering
Sharif University of Technology, Iran
geboren te Iran.

Dit proefschrift is goedgekeurd door de promotoren:

Prof. dr. G.J.W van Bussel
Prof. dr. ir. G.A.M. van Kuik

Samenstelling promotiecommissie:

Rector Magnificus	voorzitter
Prof. dr. ir. G.A.M. van Kuik	Technische Universiteit Delft, promotor
Prof. dr. G.J.W van Bussel	Technische Universiteit Delft, promotor
Prof. dr. Z. Gürdal	Technische Universiteit Delft
Prof. J.D. Sørensen	Aalborg Universiteit, Denemarken
Prof. dr. ir. R. Benedictus	Technische Universiteit Delft
P Jamieson MSc.	University of Strathclyde, UK
Ir. B.H. Bulder	Energieonderzoek Centrum Nederland
Prof. dr. R. Curran	Technische Universiteit Delft, reservelid

Printed by Wöhrmann Print Service, Zutphen, The Netherlands

Copyright © 2012 by Turaj Ashuri

ISBN: 978-94-6203-210-1

All rights reserved. No part of the material protected by this copyright notice may be reproduced or utilized in any form or by any means, electronic or mechanical, including photocopying, recording or by any information storage and retrieval system, without the prior permission of the author.

Typeset by the author with the \LaTeX Documentation System.

Author email: T.Ashuri@tudelft.nl

*Dedicated to the memory of my loving mother, Monir Parsazad (1947-2011) and my father
Iraj Ashuri; taghdim be shoma va mamnon az in hame lotf
and my wife Mali Afshar for her love and support*

Acknowledgement

This thesis is submitted as partial fulfillment of the requirements for obtaining the PhD degree at Delft University of Technology. The work has been carried out at the Aerodynamics and Wind Energy department at the faculty of Aerospace Engineering. The PhD research was supported by INNWIND (Innovation in Wind Energy) project, funded by Agentschap NL. I am thankful to the contract monitor, Jaap 't Hooft, and the INNWIND Upscaling leader, Bernard Bulder, with this project.

From the beginning of my studies, I already knew that I wanted to do a PhD, therefore I wish to particularly acknowledge three people who trusted me and gave me the opportunity to do so. Without whom I certainly would not be writing this today:

1. My first promotor Professor Dr. Gerard van Bussel has contributed with a magnificent academic support and made my research at Delft very enjoyable. I would like to acknowledge with appreciation the help, support, numerous and valuable comments, suggestions and criticism of my work. I never forget how gentle he and his wife, drs. Anny Beckers, welcomed and treated me and my wife upon first weeks of arrival in Delft, and this has been repeated at many different occasions where I needed help and support during these years.
2. I am very grateful for the qualified guidance of my second promotor Professor Dr. Ir. Gijs van Kuik. I had many inspiring discussions during the progress meetings with him. He has played a key role in my academic development through his advice on many topics. Through working with him I have become more mature as a researcher and learned how to be a well balanced scientist.
3. Michiel Zaaijer, my daily supervisor, for all of his assistance and help. He spent much time in his office with me confronting interesting aspects of the work that often appeared in the content of this research. He is truly a remarkable person and his extraordinary efforts in my success are greatly appreciated.

I owe a special debt of gratitude to my past educational supervisors. Dr. Eng. Sasan Mohamadi, my BSc supervisor, for his collaboration and friendship over years. His deep knowledge in many fields has been inspiring and eye opening. Also, Professor Dr. Eng. Saied Adibnazari, my MSc supervisor, who has done much to further my academic and professional growth. Dr. Alireza Novinzade, my advanced mathematics professor, for his unique perspective on life and his great effort to strengthen my scientific background in

applied mathematics. I am honored to have developed a friendship with him.

I wish to thank my parents who instilled within me a constant desire for knowledge and mankind. It is difficult to express the profound sense of gratitude that I feel towards my family who have been unfailingly supportive throughout my educational career.

Also contributing in no small way to my success are the many friends I have made at Delft over the past several years. I wish to express my deepest thanks to Herdis Heine-mann and Carlos Ferreira with whom I have shared so many enjoyable moments. My many other friends have also been a great help, especially Eeke Mast who helped me many times with problems I was facing as a foreigner in Delft. She has been always patient and supportive and I could always rely on her on whatever problem I had. I must also thank my other friends, Jessica Holierhoek, Mostafa Abdalla, Ameya Sathe, Claudia Hofemann, Thanasis Barlas, Busra Akay, Jaume Bartan, Ali Khani, Ben Geurts, Fanzhong Meng, Wybren de Vries and Ghanshyam Shrestha for the great moments we had together.

To the staff of the department, Sylvia Willems, Eric van der Pol, Nando Timmer, Wim Bierbooms and Ruud van Rooij for their support and help. You will be sorely missed but not forgotten. Also many thanks to my colleagues at Siemens Wind Power, especially Dr. Ir. David Molenaar for pushing and encouraging me to finish the last two chapters of this work, while I joined Siemens and giving me the support to finalize it. Also thank you to Paul van der Valk and Sven Voormeeren for reviewing some chapters of the thesis and translating the summary to Dutch.

I would like to thank my sons, Ryan and Dorian for putting up with Papa being a student and saying sorry for many moments that I should have shared and played with you but I could not. Finally, I wish to express my deepest gratitude to my lovely wife who has been an extremely valuable support during my MSc and PhD study. Without her, I would never have finished this thesis. I know the God has blessed me by the gift of having you as wife and a truly friend, mamnonam azizam.

This thesis is the result of many years of continuous research and during those years, I experienced many changes. I became a father and have lost my mother, have had the joy of being a lecturer at university and have learned how to be flexible and strong to deal with many problems that could potentially prevent finishing a PhD research while being abroad, but I did manage to finish it and I do praise God for finishing it. As a proverb says: *'A good PhD is a finished PhD'*.

Turaj Ashuri

June 2012

Summary

Issues related to environmental concern and fossil fuel exhaustion has made wind energy the most widely accepted renewable energy resource. However, there are still several challenges to be solved such as the integrated design of wind turbines, aeroelastic response and stability prediction, grid integration, offshore resource assessment and scaling related problems.

While analyzing the market of wind turbines to find the direction of the future developments, one can see a continuous upscaling of wind turbines. Upscaling is performed to harness a larger resource and benefit from economy of scale. This will pose several fundamental implications that have to be identified and tackled in advance.

This research focuses on investigating the technical and economical feasibility and limits of large scale offshore wind turbines using the current dominant concept, i.e. a three-bladed, upwind, variable speed, pitch regulated wind turbine installed on a monopile in an offshore wind farm.

Thus, the objective of this research is to investigate how upscaling influences the offshore wind turbines. Specifically, following questions are of interest:

1. How do the technical characteristics of the larger scales change with size and can these technical characteristics appear as a barrier?
2. How does the economy of the future offshore wind turbines change with size?
3. What are the considerations and required changes for future offshore wind turbines?

To address these questions, a more sophisticated method than the classical upscaling method should be employed. This method should provide the detailed technical and economical data at larger scales and address all the design drivers of such big machines to identify the associated problems.

However, interdisciplinary interactions among structure, aerodynamics and control subject to constraints on fatigue, stresses, deflections and frequencies as well as considerations on aeroelastic instability make the development of such a method a cumbersome and complex task.

Among many different methods, integrated aeroservoelastic design optimization is found to be the best approach. Therefore, the scaling study of this research is formulated as an multidisciplinary design optimization problem. This method enables the design

of the future offshore wind turbines at the required level of details that is needed to investigate the effect of size on technical and economical characteristics at larger scales.

Using this method, 5, 10 and 20 MW wind turbines are designed and optimized, including the most relevant design constraints and levelized cost of energy as the objective function. In addition to the design of these wind turbines, the method itself shows a clear way forward for the future offshore wind turbine design methodology development.

Based on these optimized wind turbines, scaling trends are constructed to investigate the behavior of a wind turbine as it scales with size. These trends are formulated as a function of rotor diameter to properly reflect the scale. Loading, mass, cost and some other useful trends are extracted to investigate the scaling phenomenon. Blades and tower as the most flexible load carrying components are examined with more attention.

Using these results, the challenges of very large scale offshore wind turbines up to 20 MW range are explored and identified. These results demonstrate that a 20 MW design is technically feasible though economically not attractive. Therefore, upscaling of the current wind turbine configurations seems to be an inappropriate approach for larger offshore wind turbines.

Samenvatting

Zorgen over milieu en klimaat en het uitputten van fossiele brandstoffen hebben wind energie de breedst geaccepteerde bron van hernieuwbare energie gemaakt. Echter, er zijn nog altijd meerdere uitdagingen die om oplossingen vragen, zoals het geïntegreerd ontwerpen van windturbines, het voorspellen van aero-elastische respons en stabiliteit, inpassing in het elektriciteitsnetwerk, inschatting van offshore windbronnen en problemen gerelateerd aan opschaling.

Bij het analyseren van de markt voor windturbines, op zoek naar richtingen voor toekomstige ontwikkelingen, ziet men een continue opschaling van windturbines. Door dit opschalen kan een grotere hoeveelheid wind energie worden gevangen en kunnen schaalvoordelen worden behaald. Dit zorgt voor een aantal fundamentele implicaties die vooraf dienen te worden geïdentificeerd en opgelost.

Dit onderzoek focust op het bepalen van de technische en economische haalbaarheid en limieten van grootschalige offshore windturbines die gebaseerd zijn op het huidige dominante concept, i.e. een windturbine met variabele snelheid, drie bladen, tegen de wind in georiënteerde rotor met pitch-regulering en geïnstalleerd op een monopaal in een offshore wind park.

Het doel van dit onderzoek is dus om na te gaan welke invloed het opschalen heeft op offshore windturbines. Daarbij zijn de volgende specifieke vragen van belang:

1. Hoe veranderen de technische karakteristieken met grootte en manifesteren deze karakteristieken zich als barrière?
2. Hoe veranderen de economische aspecten van toekomstige offshore windturbines met grootte?
3. Wat zijn de aandachtspunten en vereiste veranderingen voor toekomstige offshore windturbines?

Om deze vragen te beantwoorden dient een meer vooruitstrevende methode te worden gebruikt dan de klassieke opschalingmethoden. Deze methode dient gedetailleerde technische en economische data te leveren en de belangrijkste ontwerpinvloeden, evenals de samenhangende problemen, voor zulke grote machines te kunnen identificeren.

Echter, de interdisciplinaire interacties tussen de structuur, aerodynamica en het regelsysteem die bovendien zijn onderworpen aan beperkingen op het gebied van vermoeiing, spanningen, vervormingen en frequenties alsmede de beschouwing van aero-elastische instabiliteit, maken de ontwikkeling van een dergelijke methode een zeer complexe taak.

Uit de vele verschillende methoden is een geïntegreerde aero-servo-elastische ontwerpoptimalisatie gekozen als beste aanpak. De studie naar opschaling in dit onderzoek is om die reden geformuleerd als een probleem van multidisciplinaire ontwerpoptimalisatie. Deze methode maakt het mogelijk toekomstige offshore windturbines te ontwerpen op het gewenste niveau van detail, om zo het effect van opschaling op de technische en economische eigenschappen te kunnen onderzoeken.

Met deze methode zijn windturbines van 5, 10 en 20 Megawatt ontworpen en geoptimaliseerd, met inachtneming van de meest relevante ontwerpbeperkingen en de genormaliseerde energiekosten als doelfunctie. Naast het ontwerp van deze windturbines laat de methode zelf een duidelijk ontwikkelingspad zien voor toekomstige offshore windturbine ontwerpmethodologieën.

Op basis van deze geoptimaliseerde windturbines zijn schaal-trends gemaakt om het gedrag van een windturbine te onderzoeken als deze opschalen. Deze trends zijn geformuleerd als een functie van rotordiameter om de schaal adequaat weer te geven. Nuttige trends zoals de belasting versus diameter, massa versus diameter en kosten versus diameter zijn bepaald om de fenomenen die optreden bij opschaling te onderzoeken. De bladen en toren hebben hierbij extra aandacht gekregen omdat dit de meest flexibele lastdragende componenten zijn.

Uit deze resultaten zijn de uitdagingen verkend en geïdentificeerd voor zeer grote offshore windturbines in de orde van 20 Megawatt. Deze resultaten laten zien dat een 20 Megawatt ontwerp technisch haalbaar is maar economisch niet aantrekkelijk. Hierdoor lijkt het opschalen van huidige windturbine configuraties een ongeschikte aanpak voor grotere offshore windturbines.

Contents

Acknowledgement	i
Summary	iii
Samenvatting	v
Nomenclature	xiii
1 Introduction	1
1.1 Motivation and goal	1
1.2 The main and key research questions	3
1.3 Research methodology	3
1.4 Structure of the thesis	4
2 Classical upscaling methods	9
2.1 Introduction	9
2.2 Historical development of large scale wind turbines	9
2.2.1 Earlier developments	10
2.2.2 Recent developments	10
2.3 Linear scaling laws	12
2.3.1 Blade	13
2.3.2 Low speed shaft	14
2.3.3 Gearbox	15
2.3.4 Generator	15
2.3.5 Tower	15
2.4 Upscaling using existing data	16
2.4.1 Loading-diameter trends	16
2.4.2 Mass-diameter trends	18

2.4.3	Cost-diameter trends	21
2.5	Comparison of linear scaling law and existing data	22
2.6	Why a new approach for upscaling?	24
3	Integrated aeroservoelastic design and optimization	27
3.1	Introduction	27
3.2	Classification of design problems	27
3.2.1	Routine design problems	28
3.2.2	Nonroutine design problems	28
3.3	Difficulties of design problems	28
3.3.1	Size of the design space	28
3.3.2	Psychological inertia	29
3.3.3	Uncertainties in the design process	29
3.4	Methods of solving design problems	29
3.4.1	Trial-and-error methods	30
3.4.2	Inventive based methods	30
3.4.3	Knowledge-based engineering methods	31
3.4.4	Design search and optimization methods	32
3.5	Selection of the design methodology and its overview applicable to upscaling	33
3.6	Architecture of the MDO	33
3.7	Optimization problem formulation	35
3.7.1	Design variables	35
3.7.2	Design Constraints	38
3.7.3	Partial safety factors	39
3.7.4	Objective function	42
3.7.5	Wind turbine simulation tools	44
3.8	Design integration	44
3.9	Controller design automation	46
3.9.1	Wind turbine models for designing the controller	48
3.9.2	Control model of the generator torque controller	50
3.9.3	Control model of the blade pitch controller	51
3.9.4	Tower top motion feedback loop	54
3.9.5	Controller design and implementation	54
3.10	Automation of extracting structural properties	57
3.10.1	The methodology to extract structural properties	58
3.11	Wind turbine's model specification	62
3.11.1	Aerodynamic design definition	62
3.11.2	Structural design definition	63
3.11.3	Definition of the design load cases	64
3.12	Some practical issues about the optimization procedure	66
3.12.1	Reducing the number of design variables	66
3.12.2	The starting point of design variables	66
3.12.3	Decomposition of design variables	67
3.12.4	Multilevel optimization approach	67

3.13	Concluding remarks	69
4	Verification of the integrated aeroservoelastic optimization method	71
4.1	Introduction	71
4.2	Purpose of the design optimization of the NREL wind turbine	71
4.3	MDO of the 5 MW wind turbine	72
4.3.1	The 5MW NREL wind turbine	72
4.3.2	Design variables of the optimized 5 MW wind turbine	73
4.3.3	Design constraints of the optimized 5 MW wind turbine	73
4.3.4	Objective function of the optimized 5 MW wind turbine	74
4.3.5	Computational Expense	75
4.4	Comparison of the results	75
4.5	Concluding remarks	79
4.5.1	Validating the integrated aeroservoelastic optimization method	79
4.5.2	Improved understanding of the 5 MW wind turbine design	80
4.5.3	Providing consistent data points to make scaling trends	80
5	Integrated aeroservoelastic design and optimization of large wind turbines	81
5.1	Introduction	81
5.2	MDO of the 10 and 20 MW wind turbines	81
5.2.1	Design variables of the 10 and 20 MW wind turbines	81
5.2.2	Design constraints of the 10 and 20 MW wind turbines	83
5.2.3	Objective function of the 10 and 20 MW wind turbines	85
5.3	Properties of the 10 and 20 MW wind turbines	85
5.3.1	Gross properties	85
5.3.2	Blade properties	85
5.3.3	Aerodynamic properties	85
5.3.4	Drive train properties	87
5.3.5	Hub and nacelle properties	89
5.3.6	Support structure properties	90
5.3.7	Controller properties	91
6	Aeroelastic stability analysis using eigenvalue method	93
6.1	Introduction	93
6.2	Aeroelastic instability in wind turbines	93
6.3	Modeling approach	95
6.4	Structural model of the wind turbine	97
6.4.1	Displacement, velocity, acceleration and forces in the inertial frame	97
6.4.2	Mass, stiffness and damping in the inertial frame	99
6.5	Aerodynamic model of the rotor	100
6.5.1	Modification of the wind velocities	101
6.5.2	Modification of the airfoil data	102
6.5.3	The inclusion of the drag force	102
6.5.4	Discretization of the 3D blade to 2D sections	103
6.5.5	Derivation of the aerodynamic matrices in a FE form	104

6.6	Coupling structural and aerodynamic FE matrices	104
6.7	Eigenvalue analysis of the coupled aeroelastic model	105
6.7.1	Static instability	106
6.7.2	Dynamic instability	106
6.8	Implementation of the method	108
7	Verification and aeroelastic stability analysis of the 20 MW wind turbine	111
7.1	Introduction	111
7.2	The finite element model of the wind turbine	111
7.3	Verification of the stability analysis method	112
7.3.1	2D analytical stability analysis	113
7.3.2	Undeformed state eigenvalue analysis of the structural model . . .	116
7.3.3	Full aeroelastic stability analysis	116
7.4	Stability analysis of the 20 MW wind turbine	118
7.5	Concluding remarks	120
8	Scaling trends for future offshore wind turbines	121
8.1	Introduction	121
8.2	Development of scaling trends	121
8.2.1	Loading-diameter trends	122
8.2.2	Mass-diameter trends	128
8.2.3	Cost-diameter trends	138
8.2.4	Other useful trends	144
9	Conclusion and recommendation for future work	147
9.1	Introduction	147
9.2	Discussion on the methodology	147
9.2.1	Upscaling context	147
9.2.2	Design context	149
9.3	Conclusions	150
9.3.1	Overall conclusions	150
9.3.2	Conclusions based on research questions	150
9.4	Contribution to the state of the art	153
9.5	Recommendations for future work	154
9.5.1	Upscaling context	154
9.5.2	Design context	155
A	Mass and cost models	157
A.1	Introduction	157
A.2	Mass and cost modeling description	158
A.2.1	Blades	158
A.2.2	Hub	159
A.2.3	Blade pitch system and its bearing	159
A.2.4	Nose cone of the hub	160

A.2.5	Low speed shaft	160
A.2.6	Main bearing and its housing	161
A.2.7	Gearbox	161
A.2.8	Mechanical brake and coupling	162
A.2.9	Generator	162
A.2.10	Power electronic	163
A.2.11	Bed plate	163
A.2.12	Platform and railing	163
A.2.13	Hydraulic and cooling system	164
A.2.14	Nacelle cover	164
A.2.15	Electrical connections	165
A.2.16	Yaw system	165
A.2.17	Control system	166
A.2.18	Tower	166
A.2.19	Marinization	166
A.2.20	Foundation system	167
A.2.21	Offshore transportation	167
A.2.22	Port and staging equipment	168
A.2.23	Offshore turbine installation	168
A.2.24	Offshore electrical interface and connection	168
A.2.25	Offshore permits, engineering, and site assessment	169
A.2.26	Personnel access equipment	169
A.2.27	Scour protection	169
A.2.28	Offshore warranty premium	170
A.2.29	Decommissioning	170
A.2.30	Offshore levelized replacement	170
A.2.31	Operation and maintenance	171
B	A theoretical background of the used simulation tools	173
B.1	Introduction	173
B.2	TurbSim	173
B.3	AeroDyn	174
B.4	AirfoilPrep	175
B.5	FAST	175
B.6	BModes	176
B.7	Crunch	176
B.8	Fatigue	176
C	Verification of the controller design automation	177
C.1	Introduction	177
C.2	Applying the controller design task	177
C.3	Analysis and results	178

- D Verification of extracting structural properties 181**
 - D.1 Introduction 181
 - D.2 Verification of the method 181

- E Theoretical aspects of optimization algorithms 185**
 - E.1 Introduction 185
 - E.2 CONLIN 185
 - E.3 Lagrange Multiplier (LM) 187

- F Scaling laws for initial design variable generation 191**
 - F.1 Introduction 191
 - F.2 Derivation of scaling laws for design studies 191
 - F.3 Application of scaling laws 192

- G Properties of the optimized 5 MW wind turbine 195**
 - G.1 Properties of the optimum 5 MW wind turbine 195
 - G.1.1 Blade properties 195
 - G.1.2 Aerodynamic properties 196
 - G.1.3 Drive train properties 198
 - G.1.4 Hub and nacelle properties 198
 - G.1.5 Support structure properties 199

- H Derivation of the aerodynamic forces in a finite element form 201**
 - H.1 Introduction 201
 - H.2 Defining the aerodynamic coordinate system 201
 - H.3 Coupling aerodynamic loads with nodal deformations 207
 - H.4 Defining aerodynamic loads in terms of functionals 208
 - H.5 Transforming the functionals domain of integration to coordinate system 1 209
 - H.6 Symbolic integral replacement of the deformations 210
 - H.7 Integrating functionals using Gauss-Legendre technique 212
 - H.8 Minimizing the functionals 213
 - H.9 Element matrices for the aerodynamic model 214
 - H.10 Assembling the global aerodynamic matrices 215

- Bibliography 224**

- Curriculum vitae 225**

Nomenclature

Latin symbols

\dot{Z}	Tower top speed	$(\frac{m}{s})$
a	Axial induction factor	(-)
$A_{bld}(x)$	Blade sectional area distribution	(m^2)
A_{lss}	Low speed shaft area	(m^2)
b	Semi-chord	(m)
c	Chord	(m)
c	Scale factor	(-)
C_d	Drag coefficient	(-)
C_l	Lift coefficient	(-)
C_m	Moment coefficient	(-)
C_p	Aerodynamic power coefficient	(-)
C_{2a}	Influence of aging safety factor	(-)
C_{3a}	Temperature effect safety factor	(-)
C_{4a}	Hand layup laminate safety factor	(-)
C_{5a}	Post-cured laminate safety factor	(-)
$c_{bld}(x)$	Blade chord distribution	(m)
D_a	Aerodynamic damping matrix	$(\frac{kg}{s})$
D_s	Structural damping matrix	$(\frac{kg}{s})$
E_x	Module of elasticity in fiber direction	(Pa)
E_y	Module of elasticity perpendicular to fiber direction	(Pa)
F_a	Aerodynamic force	(N)
F_t	External force	(N)
G_β	Gain scheduled correction factor	(-)
G_{xy}	Shear modulus of elasticity in x-y plane	(Pa)

G_{yz}	Shear modulus of elasticity in y-z plane	(Pa)
I_{α}	Mass moment of inertia around elastic axis	(kg.m ²)
$I_{are-lss}$	Low speed shaft area moment of inertia	(m ⁴)
$I_{are}(x)$	Area moment of inertia distribution	(m ⁴)
I_{dr}	Drive train mass moment of inertia	(kg.m ²)
$I_{mas}(x)$	Mass moment of inertia distribution	(kg.m ²)
k	Reduced frequency	(Hz)
k	Shape factor	(-)
K_a	Aerodynamic stiffness matrix	($\frac{kg}{s^2}$)
K_s	Structural stiffness matrix	($\frac{kg}{s^2}$)
K_{α}	Torsional stiffness	($\frac{N.m}{deg}$)
K_D	Derivative gain	($\frac{RPM}{\frac{deg}{s}}$)
K_g	Generator torque proportionality factor	($\frac{N.m}{rpm^2}$)
K_I	Integral gain	($\frac{\frac{deg}{s}}{RPM}$)
K_P	Proportional gain	($\frac{deg}{RPM}$)
K_t	Tower stiffness	(N.m ²)
L	Blade length	(m)
L	Lift force	(N)
L_{lss}	Low speed shaft length	(m)
L_{tow}	Tower length	(m)
m	Mass per unit length	($\frac{kg}{m}$)
M_a	Aerodynamic mass matrix	(kg)
M_s	Structural mass matrix	(kg)
M_{bld}	Blade mass	(kg)
$M_{bnd-wgt}$	Low speed shaft bending moment due to weight	(N.m)
$M_{bnd-yaw}$	Low speed shaft bending moment due to tilt and yaw	(N.m)
M_{edg}	Edgewise moment	(N.m)
M_{flp}	Flapwise moment	(N.m)
$M_{for-aft}$	Tower fore-aft bending moment	(N.m)
M_{gb}	Gear box mass	(kg)
M_{gen}	Generator mass	(kg)
$M_{sid-sid}$	Tower side-to-side bending moment	(N.m)
$M_{trs-lss}$	Low speed shaft torsional moment	(N.m)
M_{trs}	Tower torsional moment	(N.m)
P_{gen}	Generator power	(W)
P_{rot}	Rotor power	(W)
R	Rotor radius	(m)

S_{α}	Static moment related to elastic axis	$(kg.m^2)$
$t_{bld}(x)$	Blade thickness distribution	(m)
T_{gb}	Gear box torque	$(N.m)$
T_{gen}	Generator torque	$(N.m)$
t_{lss}	Low speed shaft thickness	(m)
T_{rot}	Rotor torque	$(N.m)$
$t_{tow}(x)$	Tower thickness distribution	(m)
U	Wind velocity	$(\frac{m}{s})$
u	Nodal displacement	(m)
V	Wind velocity	$(\frac{m}{s})$
V_{eff}	Effective wind velocity	$(\frac{m}{s})$
V_f	Volumetric fraction	$(-)$
W	Work	$(Watt)$
w	Shape function	$(-)$
x	Distributed property	$(-)$
Z	Tower top displacement	(m)
Z_{gb}	Gear box ratio	$(-)$

Greek symbols

α	Angle of attack	(deg)
α	Wind shear	$(-)$
β	Blade pitch angle	(deg)
β_r	Resultant wind velocity angle	(deg)
β_t	Aerodynamic twist	(deg)
$\ddot{\omega}$	Rotational acceleration	$(\frac{rev}{min^2})$
γ_M	General material safety factor	$(-)$
ν_{xy}	Poisson ratio in x-y plane	$(-)$
Ω	Angular velocity	(RPM)
$\omega_{\varphi n}$	Resonance frequency	$(\frac{1}{s})$
ω_{gen}	Generator rotational speed	(RPM)
ω_i	Weighting factor	$(-)$
ω_{rat}	Rated rotational speed	(RPM)
ω_{rot}	Rotor rotational speed	(RPM)
ρ	Material density	$(\frac{kg}{m^3})$
$\theta_{bld}(x)$	Blade twist distribution	(deg)
ξ_{φ}	Damping ratio	$(-)$

Subscripts

are area

bld	blade
dr	drive train
edg	edge
flp	flap
for	fore
gb	gear box
gen	generator
lss	low speed shaft
mas	mass
rat	rated
ref	reference
rot	rotor
sid	side
tow	tower
trs	torsion
wgt	weight

Abbreviations

AEP	Annual Energy Production
BEM	Blade Element Method
BOS	Balance Of Station
CFRP	Carbon Fiber Reinforced Plastic
CONLIN	CONvex LINearization
CPU	Central Processing Unit
DLL	Dynamic Link Library
DOP	Design Optimization Process
EA	Elastic Axis
EWM	Extreme Wind Model
FAST	Fatigue Aerodynamic Structure Turbulence
FCR	Fixed Charge Rate
FEA	Finite Element Analysis
FEM	Finite Element Method
FIO	Fully Integrated Optimization
GFRP	Glass Fiber Reinforced Plastic
GII	General Inflation Index
ICC	Initial Capital Cost
LCOE	Levelized Cost Of Energy
LM	Lagrange Multiplier
LRC	Levelized Replacement Cost

MDO	Multidisciplinary Design Optimization
NAICS	North American Industry Classification System
NREL	National Renewable Energy Laboratory
NTM	Normal Turbulence Model
O&M	Operations and Maintenance
OWT	Offshore Wind Turbine
PDE	Partial Differential Equation
PPI	Producer Price Index
RPM	Revolution Per Minute
SR	Scaling Factor
SR	Scaling Ratio
TCC	Turbine Capital Cost
USD	United States Dollar

1.1 Motivation and goal

The available onshore area for wind energy development in and around Europe is restricted. This is because of the high population density and natural areas that do not allow any further wind turbine installation for bulk generation of electricity. Going offshore and large scale wind turbines are the two promising solutions that probably enable further reduction in costs as well.

Offshore winds are typically stronger and more stable than onshore, resulting in significantly higher production per installed turbine. In addition, in many European waters the water depth increases slowly with the distance from shore which is an important advantage for the utilization of bottom-mounted offshore wind turbines (OWTs). There are several large research projects which have been set up to study harvesting the offshore wind energy resources such as: OPTI-OWECS, [Kühn et al. \(1998\)](#), POWER, [Online-Reader \(2007\)](#) and COD, [Roth et al. \(2005\)](#).

The development of large offshore wind turbines is supported by four facts:

1. The energy capture per area land use is higher for larger machines.
2. Many cost elements such as operation and maintenance and infrastructure may decrease per rated MW capacity with fewer larger machines for the same installed capacity.
3. The wish to minimize the number of wind turbines required for the bulk generation of electricity. This means that the wind energy industry thinks on manufacturing larger machines instead of several smaller machines for the same installed capacity.
4. Size is often considered as a merit index for technology progress and development.

DOWEC, [Hendriks and Zaaijer \(2004\)](#), UPWIND, [Online-Reader \(2012\)](#), ICORASS, [Bulder et al. \(2007\)](#) and WindPact, [Fingersh et al. \(2006\)](#) are also among the most rel-

evant projects related to doing research on large scale wind turbines, and each of these projects focuses on one aspect of upscaling.

The DOWEC project focused on the research and development needs for the design of large-scale offshore wind farms. Although, the project ends up with preliminary design of a 6 MW OWT and addresses some issues related to larger scale turbines, upscaling has not been the direct interest of the project. Both the NREL 5 MW model, [Jonkman et al. \(2009\)](#), and the UPWIND project utilized data from the DOWEC consortium.

In the ICORASS project, by reducing the number of components and integrate functions as far as possible into single components a 10 MW wind turbine was designed. The aim of the project was to see how much cost reduction could be achieved by a large scale wind turbine and less attention is paid to the technical aspects of such a machine.

The WindPact project studied the impact of increased turbine size and configuration on levelized cost of energy, by developing cost and mass models of wind turbine components. However, the project does not address any of the design constraints and limitations that a large scale OWT may encounter.

The main objective of the UPWIND project was to identify major technological and economical barriers of large scale OWTs, with the wind turbine as the essential of a wind farm. However, to identify the technical and economical characteristics of the large scale OWTs, linear scaling laws and engineering judgment of the involved experts and participants were used rather than making realistic wind turbine configurations through simulation and optimization.

Though significant improvements in upscaling have been made in the past (see chapter 2 for upscaling literature review), there is still much research needed before many of the technical and economical characteristics associated with upscaling are fully understood and solved.

In line with the UPWIND project, this research deals with the upscaling of large scale OWTs. Hence, the goal of this research is to study the challenges which will be faced during increasing the size of OWTs. The focus is towards a better understanding of the aeroservoelastic behavior of large OWTs. This understanding is needed because of following reasons:

1. It leads to accurate load prediction (fatigue and ultimate loads), which is an important factor to determine technical feasibility.
2. It is governing the dynamic behavior of a wind turbine that is primarily responsible for stability. Especially when the focus is on larger scales, considering the fact that they are more flexible and therefore their design may suffer from aeroelastic instabilities.
3. It is the basis for control design which can lead to significant increase in efficiency and load reduction, and thus influencing the economical characteristics.

Considering all the facts, conceptual and preliminary design activities may reveal fundamental issues that need to be handled before further progress in upscaling can be achieved. Therefore, the outcome of the research is the stepping stone toward larger multi megawatt OWTs up to 20 MW range.

1.2 The main and key research questions

For a critical evaluation that larger wind turbines are feasible to manufacture and may eventually be more cost effective, it is needed to analyze how size influences the wind turbine itself. Therefore, based on the motivation and objective of this research, the main research question to deal with can be formulated as:

How does upscaling influence the design of current offshore wind turbines?

To plan the construction and utilization of the future OWTs one should know the probable changes and modifications to the existing wind turbines. In other words, the specifications and characteristics of the future OWT need to be known well in advance before taking any action to rely on these giant machines of the future. This is also an important subject for the society to know how much they can rely on wind as a renewable source for the future energy planning.

Answering this question is the encompassing subject of this thesis. However, to answer it, three key questions need to be answered first. These are:

How do the technical characteristics of the larger scales change with size and can these technical characteristics appear as a barrier?

One of the most frequently asked questions that is still open to the wind energy community is the size limitation. Several attempts have been made to address this issue, but none of them provides a concrete answer. A reason for that is the huge amount of time needed to do this investigation for a wind turbine, while facing lots of details and complexities to fully cover all the aspects.

This research will deal with this question by upscaling a 5 MW wind turbine to larger sizes up to 20 MW, and investigating the effect of size on the technical characteristics of these enlarged machines. Based on these machines, scaling trends will be constructed to identify the size associated problems and find the probable limiting factors.

How does the economy of the future OWTs change with size?

One of the most important factors that can act as a good motivation to utilize large scale wind turbines is the wish to have a lower cost of energy. Therefore, this research explores this aspect carefully. It could be the case that there is not a technical barrier but the economy of larger scales is not in favor of any size increment.

What are the considerations and required changes for future OWTs?

The results of this research should help to identify probable changes and modifications to the existing wind turbines. Upscaling can present many challenges and the early identification of these challenges helps to make better research planning and come up with better design solutions and modifications.

1.3 Research methodology

To study the effect of size on characteristics of a wind turbine two different methods are frequently used. First, the analytical relation between a number of important parameters that govern the turbine characteristics can be formulated as a function of rotor diameter,

under the assumption that all geometrical parameters scale linearly. This approach is called linear scaling law (also similarity or scaling rule).

Linear scaling law does not quantify the technical and economical characteristics at any scale, and the usage of this method is limited to give an overall impression in conceptual design phase. This makes the method less attractive for studying detailed technical and economical characteristics, and tradeoff studies in which the quantified end results play an important role.

Second, the relation between rotor diameter and other parameters that govern the turbine characteristics can be formulated by studying the trends in the existing wind turbines. In this approach, real data are viewed collectively and by interpolating these data scaling trends can be extracted. However, to study wind turbines that are larger than existing ones, an extrapolation must be used. The further the extrapolation goes outside the data range, the more the uncertainty will be.

To overcome the drawbacks of the first two methods, this research uses a novel method. In this method, for several given scales of interest a wind turbine will be designed and optimized. Based on these optimized wind turbines the relation between different parameters and rotor diameter can be extracted and used to develop trends. Since for every given scale an optimum wind turbine is designed, studying the technical and economical characteristics of larger OWTs can be made more precisely.

For the upscaling study of this research, the 5 MW NREL wind turbine is used as the baseline design, [Jonkman et al. \(2009\)](#). This guarantees the use of earlier works and experiences in the field of wind energy which is gained and evaluated in real situations for decades and considered in the design of this machine. Also all the data of this machine are publicly available and has been based on some of the most recent commercial wind turbine designs in the same class (Multibrid M5000 and the REpower 5M).

To do the upscaling, the 5MW NREL wind turbine is scaled up to 10 and 20 MW wind turbines without any conceptual change. That is, a 5 MW machine is redesigned for larger sizes and physical phenomena of these enlarged machines will be analyzed and evaluated. The analysis and evaluation is based on the results such as: stresses, natural frequencies, displacements, fatigue, aeroelastic stability and cost of energy. Also based on these results judgments about feasibility and problems associated to upscaling will be made, as well as generating trends.

The results of this method are used to identify major technical and economical barriers of larger scale wind turbines. They also help to improve designs with respect to performance, weight or any other objectives which makes it possible to study the advantage and disadvantage of the given concept for larger scales.

This research ends up with an optimized outline design of 5, 10 and 20 MW wind turbines, which can be used as a reference baseline design for many other research studies.

1.4 Structure of the thesis

This thesis is built up of 9 chapters as follow:

Chapter 1: Introduction

This chapter discusses the research motivation, research questions and scope of the thesis. At the end of the chapter the thesis outline is presented.

Chapter 2: Classical upscaling methods

This chapter explains the classical upscaling methods in detail. It also compares them in terms of advantage and disadvantage. Shortcoming of these methods motivated this research to develop a more powerful alternative.

Chapter 3: Integrated aeroservoelastic design and optimization

A review of existing design methodologies applicable to wind turbines is made first in this chapter to find the best approach that is suited for upscaling. This review showed the integrated multidisciplinary design optimization (MDO) as the best alternative for scaling study. Then, the formulation of scaling study as a MDO problem is explained together with the architecture of this method. Based on this setup an integrated design code is developed that enables the design and optimization of any conventional wind turbine at any other size of interest.

Chapter 4: Verification of the integrated aeroservoelastic optimization method

Using the developed design code of the previous chapter, the MDO of the 5MW NREL concept is carried out in this chapter. This is to show the usefulness of this approach and verify its correct implementation as a computational code by comparing the 5 MW NREL wind turbine with the optimized 5 MW wind turbine utilized by this research.

Chapter 5: Integrated aeroservoelastic design and optimization of large wind turbines

The same approach that was used to optimize the 5 MW NREL wind turbine in the previous chapter is followed in this chapter to design large scale OWTs. This provides the necessary data that needs to be analyzed in a systematic way to extract technical and economical trends for large scale OWTs as presented in chapter 8.

Chapter 6: Aeroelastic stability analysis using eigenvalue method

Development of a simulation code for performing aeroelastic stability analysis of wind turbines is presented in this chapter. The rationale behind this code is described in a general form, as independent of the particular aeroelastic modeling as possible. This simulation code enables aeroelastic stability analysis of any wind turbine configuration and at any size since it is made parametric.

Chapter 7: Verification and aeroelastic stability analysis of the 20 MW wind turbine

The developed code in the previous chapter is verified with the available instability prediction results in the literature followed by some other test cases. The verified simulation code is used to check the aeroelastic stability boundary of the optimized 20 MW wind turbine and make sure that its design does not suffer from any unwanted instability during operation.

Chapter 8: Scaling trends for future offshore wind turbines

Based on the optimized wind turbine designs of the previous chapters, this chapter constructs scaling trends. All the trends are a function of rotor diameter to reflect size

dependency and they cover both the technical and economical characteristics. These scaling trends help to identify the design challenges of the future OWTs as they scale in size.

Chapter 9: Conclusion and future work

This chapter concludes the approach and results of this research in a comprehensive way. This discussion is followed by highlighting the contribution of the research to the state of the art knowledge. Based on the results of the research the future work to design large OWTs is formulated.

The outline of this thesis is visualized in figure [1.1](#).

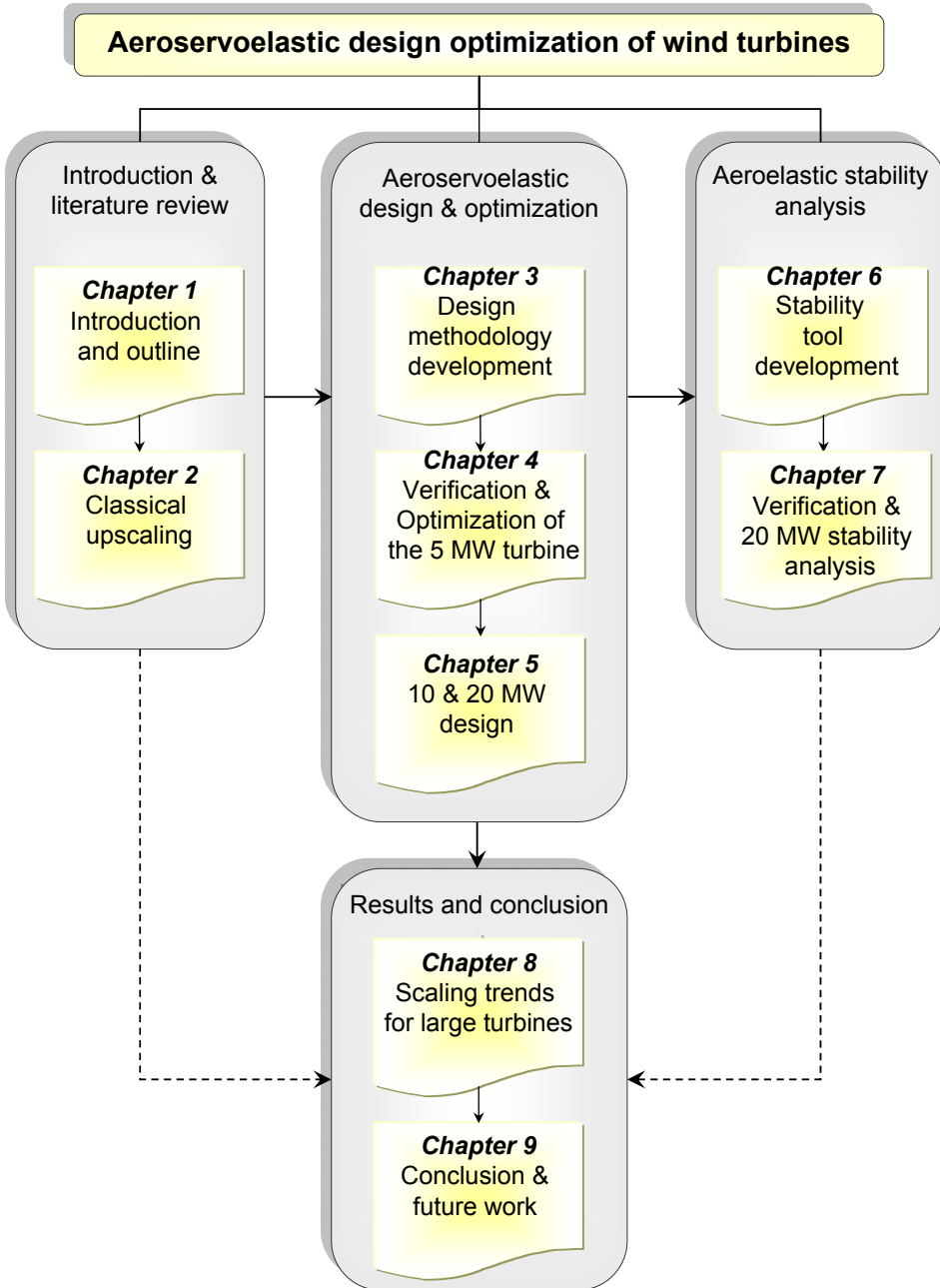


Figure 1.1: Thesis outline

2.1 Introduction

To study the effect of size on characteristics of a wind turbine two classical scaling methods are used, i.e. the linear scaling law and existing data trends. These two methods are presented and compared in this chapter together with a review of the historical development of wind turbines in the context of upscaling.

The deficiencies of these two methods motivated this work to search for an alternative to comply fully with the objective of this research. The new methodology should enable designing larger scale OWTs and providing detailed insight to their technical and economical characteristics in order to identify size related challenges.

A brief review of existing design methods is made to select the best technique that is well suited for scaling study. It is found that multidisciplinary design optimization is the best method to design large scale OWTs. This chapter presents the first two classical methods, and chapter 3 discusses the multidisciplinary design optimization formulation for the upscaling problem.

2.2 Historical development of large scale wind turbines

The question regarding the optimal size of a wind turbine is as old as the idea of inventing such a machine. From a historical point of view, there are contradictory claims about the origin of wind turbines, but the earliest documented design is a vertical-axis windmill built in Persia, [Spera \(1994\)](#). However, wind turbines only evolved rapidly in technology and size, after realizing that they can also be used to generate electricity by James Blyth in 1887, Charles Brush 1888 and Poul La Cour in 1891, [Warne and Calnan \(1977\)](#).

The development efforts to explore larger scale wind turbines will be presented in this section. These efforts can be classified in the earlier studies mainly done by individuals,

and the more recent national or international plans driven by the oil crisis of 1970s and more awareness about the negative environmental impact of other conventional energy resources.

2.2.1 Earlier developments

In 1922, Joseph and Marcellus Jacobs started to develop a 4 meter, three-bladed rotor directly connected to a low-speed DC generator, [Online-Reader \(2010\)](#). They also established a company in 1925, which is the oldest manufacturer of wind electric systems in USA. In 1931 a large wind turbine was built in Russia named Wime D-30 with a three-bladed rotor of 30 m diameter and a power output of 100 kW, [Sektorov \(1933\)](#). A second similar wind turbine with the name of Zwei D-30 was installed some years later on the coast of the Arctic Ocean.

In 1930s the German engineer Hermann Honneff proposed a wind turbine concept with a tower height of 250 m, a rotor diameter of 160 m and the number of blades between 3 to 5, [Honneff \(1932\)](#). However, his idea about "the larger the more economical" was far ahead of its time and the concept was never build.

In October 1941, the world's first really large wind turbine that was based on the idea of the American engineer Palmer Cosslett Putnam was installed on Grandpa's Knob, a hill in the state of Vermont, USA . It had a rotor diameter of 53.3 m, a power output of 1250 kW and a tower height of 35.6 m. This two-bladed downwind turbine was made of a lattice tower and the speed and power output of the turbine were controlled by a hydraulic blade-pitching mechanism. This was most probably the first wind turbine interconnected to conventional power plants within the public utility grid.

In addition, he also tackled the question of the wind turbine size optimality and concluded that a rotor diameter of 53.3 to 68.5 m, a tower height of 45.7 to 53.3 m and a power output of 1500 to 2500 kW is the range for an optimum configuration, [Putnam \(1947\)](#). Also Ulrich Hütter published the similar results carried out by Putnam about size optimality, [Hütter \(1942\)](#).

In 1942, the German engineer Franz Kleinhenz presented a design of a very large wind turbine that was improved and refined in many details over 5 years of effort. This turbine had a rotor diameter of 130 m, a power output of 10 MW and a hub height of 250 m. Unlike Honneff, Kleinhenz knew how to cooperate with famous scientists and industrial firms of the time. Therefore, his design was confirmed by Albert Betz and the Maschinenfabrik Augsburg Nürnberg (MAN), but unfortunately the second world war prevented the actual construction of such a giant machine, [Kleinhenz \(1942\)](#).

2.2.2 Recent developments

After World War II, the prices of fossil fuels dropped again and electricity generation was relying on conventional power plants. In addition, the subject of environmental protection and air pollution had not yet been considered and as the result there were not considerable activities to generate electrical power using wind turbines or other renewables.

1970s oil crisis prompted investigation of alternative energies, among them wind energy as the most promising. However, the high energy cost of wind turbines (compared

to fossil fuels) delayed the utility scale realization of electricity generation from wind. This high demand to wind energy provided more financial support to do research and development on wind turbines aiming to better solutions, hence technology development and size increment.

In 1975, the Danish "Tvind Turbine" was erected in Ulfborg. The turbine was designed with a high level of idealism with a rotor diameter of 52 m and a power output of 2 MW. After the successful operation of the Tvind turbine in MW scale, the Danish utilities built the smaller Nibe A and Nibe B wind turbines, each having a rotor diameter of 40 m and a power output of 630 kW.

In Germany, the Growian project became the largest research program in the late 1970s. The project aimed at a 3 MW wind turbine with a rotor diameter of 113 m and a hub height of 72 m. However, after the construction, it never completed the test programme due to numerous severe design faults. The total operation time was 420 hours and the turbine was demolished in 1987.

In 1982, the Swedish research program intended for the first experimental turbine named WTS-75 (later named Aeolus I). This turbine had a rotor diameter of 75 m and a power output of 2 MW and it was erected in the island of Gotland. A similar project was followed few months later by another large turbine with a rotor diameter of 78 m and a power output of 3 MW and the wind turbine was installed in the South of Sweden in Marglarp.

In these years, the governmental research institutions in Canada had a special focus on vertical axis wind turbines. In 1985 one of these large research projects named Eole was designed with a Darrieus rotor of an equatorial diameter of 64 m, a height of 100 m and a power output of 4 MW.

The development of large scale wind turbines in the United States started from 1975 to 1987 with a series of large experimental turbines named MOD-0 to MOD-5. However, the final and largest project, the MOD-5A, never reached completion. The turbine was intended to have a rotor diameter of 122 m and a rated power of 7.3 MW. In 1993, the MOD-5A project was canceled in favor of the MOD-5B since it had a better design with a smaller size. The MOD-5B wind turbine had a rated capacity of 3.2 MW, a rotor diameter of 100 m and a two-bladed rotor on a 60 m steel tower.

Considering the lessons learned during all these years, at the end of the 1980s, there were less developed ambitious projects with regard to size. Further, in contrast to the first attempts initiated by pioneers which had a bottom-up approach and mainly in the national level, most of the projects were launched from a top-down approach and by contributing institutions from several countries.

In Europe, the first phase of this action, named WEGA has led to the development of three experimental large wind turbines with a power output from 1 to 2 MW and rotor diameters from 55 to 60 m. The first wind turbine, the Tjaereborg 2 MW machine, was installed at Tjaereborg in Denmark. A few months later, the Spanish-German industrial consortium AWEC-60 completed the erection of the second turbine at Cabo Villano in Spain. Finally, third wind turbine, the 1 MW machine at Richborough developed by the Scottish firm James Howden was installed.

At the same time some more projects that were supported in the frame work of the THERMIE program have been realized: LS-1 (3 MW) in Britain, GAMMA-60 (1.5 MW) in Italy, NEWECS-45 (1 MW) in the Netherlands and WKA-60 (1.2 MW) in Germany.

Apart from theoretical approaches relating to the relationship between size and economic feasibility, the WEGA project also contained proposals for the further development of wind turbines in the MW power range. Therefore, it was followed by the WEGA II project some years later. In the second program the market's needs were becoming the research interest, therefore also many industrial partners were asked to participate. Five completely new prototypes of large horizontal-axis turbines were developed and built from 1993 to 1995.

In the mid to late 1990s, the three-bladed upwind rotor with variable-speed-pitch-regulated design became the dominant utility-scale configuration. Around the same period the University of Sunderland made a set of scaling rules for the machines of the period, [Harrison and Jenkins \(1993\)](#). This report had valuable models to predict the impact of machine size on turbine components. However, after just some few years of this report the machine size had increased drastically which made the report less accurate for larger scales.

Beginning in 1999 in the US, the Department of Energy began the WindPACT project. The focus of this project was on the determination of potential technology pathways that would lead to more cost-effective wind turbine design. The main goal of this project was to study the impact of increased turbine size and configuration on the cost of energy.

This was done by setting up several major studies. In each study, the preliminary design of many concepts at the range of sizes from 750 kW to 5 MW was carried out. These studies resulted in scaling relations of wind turbine subsystems and components across the range of sizes. The project ended officially at 2006 and by far this is the most complete source of scaling relations, [Fingersh et al. \(2006\)](#).

Due to the success of these joint projects, many other research projects were also launched. These projects can be divided into different categories such as: offshore wind turbine design, blades and rotors, wind resources forecasting and mapping, wind farm development and management and integration of wind power to the grid.

UPWIND was the largest wind energy research project funded under the EU's Sixth Framework Program (FP6), consisting of 15 scientific and industrial work packages. The project looked towards the wind power of tomorrow. More precisely, it looked at the design of very large wind turbines (over 10 MW), both for onshore and offshore application.

UPWIND had 11 different work packages, with upscaling work package dedicated to identify major technological and economic barriers associated with the development of future wind turbine technology. Development of scaling trends was supported by experienced engineering judgment of the partners.

2.3 Linear scaling laws

As explained before, upscaling in the literature is done using linear scaling laws and existing data. Linear scaling laws provide the fundamental physical and geometrical relation between a number of important parameters that govern the wind turbine design and the rotor diameter.

Linear upscaling is realized based on three distinct assumptions:

1. The number of blades, airfoils type, turbine materials, drive train and support struc-

ture concepts are the same

2. The tip speed remains constant
3. All other geometrical parameters vary linearly with rotor diameter (except gearbox, generator and power electronics)

The first documented representation of such a relation goes back to the late 1980s, and it was presented by [Molly \(1989\)](#) in the form that we see and recognize today.

In 2001 linear scaling laws were further extended and as a case study they were implemented in the upscaling process of a wind turbine by [Nijssen et al. \(2001\)](#). In the framework of the UPWIND project, [Chaviaropoulos \(2007\)](#) applied the linear scaling law on most of the components of the wind turbine to see the effect of wind turbine upscaling on its loading and operational behavior.

This work can be further improved by including the effect of wind shear, Reynolds number modification on aerodynamic properties and some other modifications to make it a more powerful tool for scaling studies. While the inclusion of the wind shear is straightforward, it is not so easy to make a closed form relation when other modifications are considered.

To identify the design drivers and critical issues for very large scale wind turbine blades, [Ashuri and Zaayer \(2008\)](#) used the linear scaling laws and a finite element model for the analysis. Stresses and displacements due to aerodynamic, gravity and inertial loadings are analyzed for 5, 10, 15 and 20 MW blades, and based on these data scaling trends are constructed to examine how upscaling influences the design.

In 2010, [Capponi and Ashuri \(2010\)](#) presented a nonlinear upscaling approach for the blade based on stresses. In this work, the resultant stress level due to aerodynamic, weight and centrifugal loads are seen as a design constraint to be fixed as the size increases from a 5 MW reference wind turbine to an upscaled 20 MW wind turbine. To reach the constant stress level, the geometry of the blade is upscaled nonlinearly (in the linear scaling law the geometry varies linearly with size).

In the book of [Jamieson \(2011\)](#) a chapter is dedicated to upscaling of wind turbines. This chapter gives a good overview of upscaling in general with a detailed analysis of linear scaling laws.

Based on scaling laws assumptions (either linear or nonlinear) and using physical relations between rotor diameter and other parameters of interest, scaling a wind turbine to a different size becomes possible. To have a better overview, these physical relations are studied for the main components of the wind turbine and presented in the following subsections using linear scaling laws.

2.3.1 Blade

For the blade, a linear scaling relation is used for all the geometrical parameters and based on that the results are presented in table 2.1. Upscaling the blade increases the load levels that can be considered as a negative effect. At the same time an increase in the captured energy can be seen as the result of upscaling.

Making a tradeoff between the increase in the load levels and power production using this crude model is not possible. Therefore, the overall impact of scaling is not clear using

the linear scaling law and a sophisticated model is needed to precisely address this issue. This can be considered as a main drawback of using linear scaling laws for upscaling.

Table 2.1: Geometric linear scaling laws for blade, *Chaviaropoulos (2007)*

Symbol	Description	Size dependency
L	Blade length	R
ω_{rot}	Rotor rotational speed	R^{-1}
$\omega_{rot} \cdot L$	Tip speed	I
$c_{bld}(x)$	Blade chord distribution	R
$t_{bld}(x)$	Blade thickness distribution	R
$\theta_{bld}(x)$	Blade twist distribution	I
M_{flp}	Flapwise moment	R^3
M_{edg}	Edgewise moment	R^3
P_{rot}	Rotor power	R^2
T_{rot}	Rotor torque	R^3
$A_{bld}(x)$	Blade sectional area	R^2
$I_{are}(x)$	Area moment of inertia	R^4
$I_{mas}(x)$	Mass moment of inertia	R^5
M_{bld}	Blade mass	R^3

R: Linear dependency, I: Size independency

2.3.2 Low speed shaft

The linear scaling law for the low speed shaft is presented in table 2.2. Due to the simple geometry of the low speed shaft, it is assumed that all the dimensions linearly vary with size. This geometrical assumption dictates the mass of the low speed shaft to increase with R^3 .

Table 2.2: Linear scaling laws for low speed shaft, *Chaviaropoulos (2007)*

Symbol	Description	Size dependency
L_{lss}	Shaft length	R
t_{lss}	Shaft thickness	R
A_{lss}	Shaft sectional area	R^2
$I_{are-lss}$	Shaft area moment of inertia	R^4
$M_{bnd-wgt}$	Shaft bending moment due to weight	R^3
$M_{bnd-yaw}$	Shaft bending moment due to tilt and yaw	R^2
$M_{trs-lss}$	Shaft torsional moment	R^3

2.3.3 Gearbox

For the gearbox a multistage configuration is assumed. Table 2.3 shows the linear scaling laws for the gearbox. Because of the complex geometry of the gearbox, its mass can not be formulated as a function of size directly. To overcome that, it is assumed that the mass of the gearbox changes proportional to the torque that it experiences. Although, this is a hard assumption, it provides enough insight to see how the gearbox mass changes with size as it is shown in table 2.3.

Table 2.3: *Linear scaling laws for gearbox, Chaviaropoulos (2007)*

Symbol	Description	Size dependency
ω_{rot}	Rotor rotational speed	R^{-1}
ω_{gen}	Generator rotational speed	I
Z_{gb}	Gearbox ratio	R
T_{gb}	Gearbox torque	R^3
M_{gb}	Gearbox mass	R^3

2.3.4 Generator

For this scaling study, a conventional generator is used and the rotational speed of it is assumed to be independent of scale and therefore remains constant. Similar to the gearbox, the generator mass is formulated as a function of the generator torque. The linear scaling laws are presented in table 2.4.

Table 2.4: *Linear scaling laws for generator, Chaviaropoulos (2007)*

Symbol	Description	Size dependency
T_{gen}	Generator torque	R^2
M_{gen}	Generator mass	R^2

2.3.5 Tower

A tubular tower configuration is used for scaling study and based on that the linear scaling laws are presented in table 2.5. For the tower, upscaling has less negative consequences in an offshore environment than onshore. This is due to a steeper wind shear profile that offshore wind turbines experience.

This is not the case, however, in onshore environment with a higher value of wind shear, therefore, it is expected that offshore wind turbines will suffer less from wind shear induced loads when compared to an onshore wind turbine. This is a benefit when one considers upscaling in offshore environment.

Table 2.5: Linear scaling laws for tower, *Chaviaropoulos (2007)*

Symbol	Description	Size dependency
L_{tow}	Tower length	R
$t_{tow}(x)$	Tower thickness distribution	R
$A_{tow}(x)$	Tower sectional area	R^2
$I_{are}(x)$	Area moment of inertia	R^4
$I_{mas}(x)$	Mass moment of inertia	R^5
$M_{for-aft}$	Fore-aft bending moment	R^3
$M_{sid-sid}$	Side-to-side bending moment	R^3
M_{trs}	Torsional moment	R^3

2.4 Upscaling using existing data

The most comprehensive work on extracting wind turbines mass and load trends using certification calculations is carried out by [Jamieson \(2007\)](#) in the framework of the UP-WIND project. These data are presented in two parts. In the first part load data are presented as a function of rotor diameter and in the second part mass of different components. These data are systematically presented again by Jamieson in his recent book, innovation in wind turbine design, [Jamieson \(2011\)](#).

2.4.1 Loading-diameter trends

To construct loading-diameter trends, Jamieson used a set of 42 pitch regulated, variable or two-speed controlled wind turbines. However, differences in design configurations and the wind class result in scattering the data, therefore they should be viewed collectively to see what may be suggested in terms of scaling trends. Because of the commercial confidentiality of the data points only a trend line is shown in most of the graphs.

Among the main components of the wind turbine, those that are carrying most of the loads are of the interest of this research, since they are more relevant from upscaling point of view. These are the blade, tower and low speed shaft. Unfortunately, in the work of Jamieson, the low speed shaft is not included. Therefore, the loading-diameter trend is only presented for the blade and tower :

1. Blade

For the blade the extreme loads at the blade root are presented in figure [2.1](#) and [2.2](#). Based on linear scaling law formulation, the flapwise and edgewise loads should scale with R^3 .

However, as it can be seen from these two figures, the edgewise bending moment scales more rapidly with size than the flapwise moment. This issue will be discussed in the next subsection.

2. Tower

All the studied towers are of a tubular type and are made of steel. In the original report, the results are only given for the extreme bending moments at the tower base and shown for fore-aft and side-to-side bending moments in figure [2.3](#) and [2.4](#) respectively.

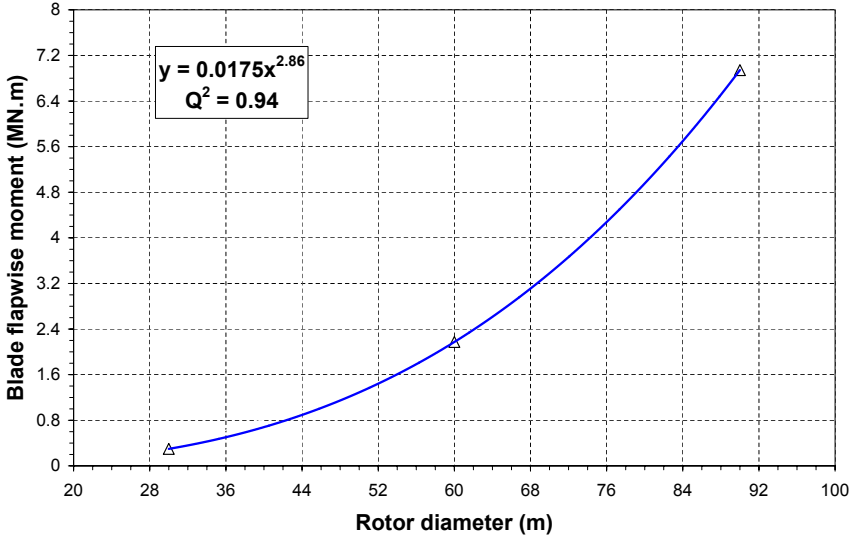


Figure 2.1: Extreme flapwise bending moment at blade root, *Jamieson (2007)*

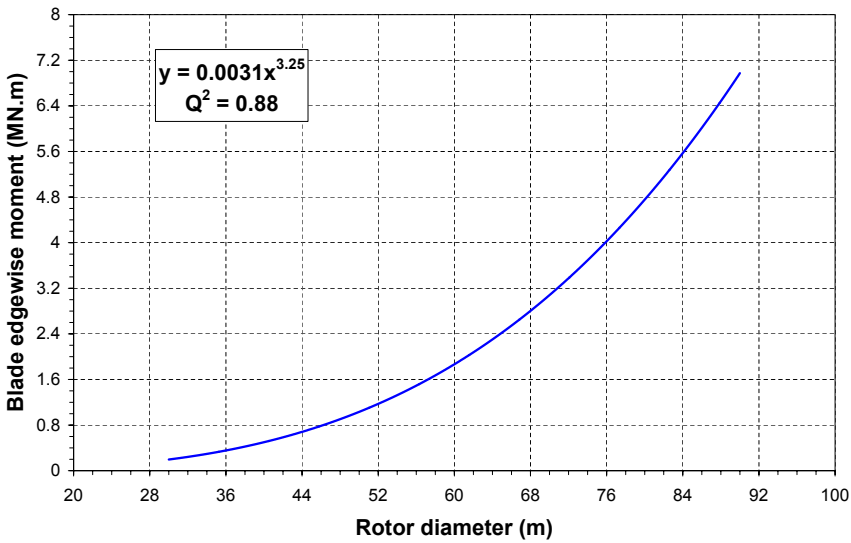


Figure 2.2: Extreme edgewise bending moment at blade root, *Jamieson (2007)*

As shown by the graphs, the fore-aft bending moment has the lowest trends exponent, followed by the side-to-side and torsional moments. This is a deviation from what linear scaling law predicts and the reason will be analyzed and explained in chapter 8 of this thesis.

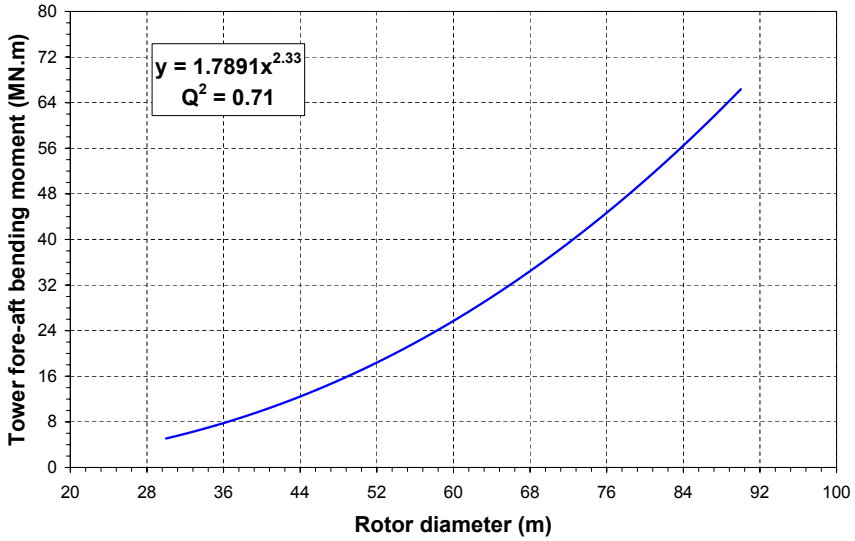


Figure 2.3: Extreme fore-aft bending moment at tower base, *Jamieson (2007)*

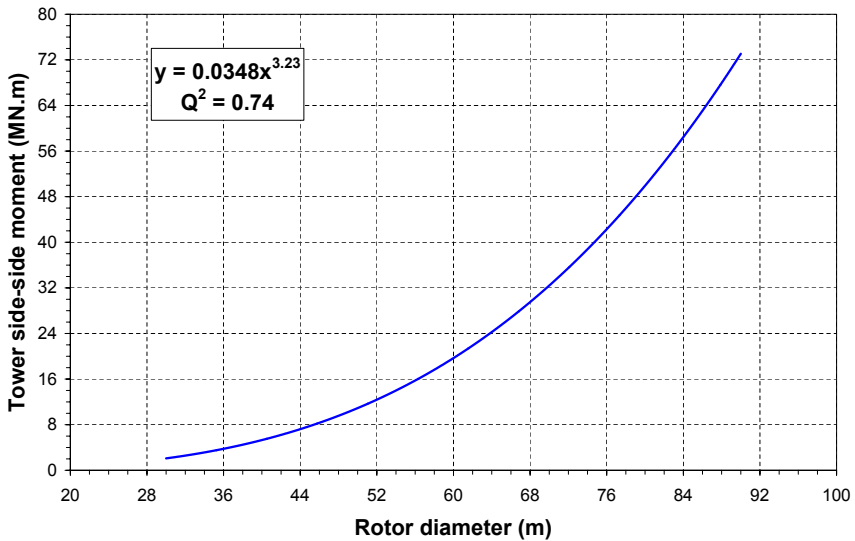


Figure 2.4: Extreme side-to-side bending moment at tower base, *Jamieson (2007)*

2.4.2 Mass-diameter trends

The mass-diameter trends are presented in this subsection. Here, the focus will be on the scaling trends of the blade, the tower top mass and the tower. The tower top mass refers to all the components atop the tower including the rotor. Studying the mass trend not only gives useful information on how the mass itself scales, but also provides insight

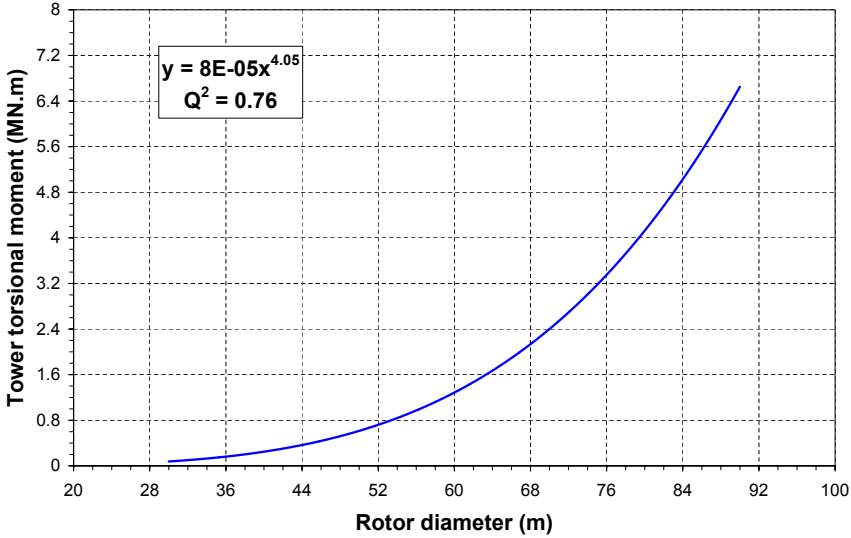


Figure 2.5: Extreme torsional moment at tower base, *Jamieson (2007)*

on the scaling of gravity driven loads such as the tower side-to-side and blade edgewise moments.

1. Blade

The blade mass and its scaling behavior is one of the most important parameters for the dynamic load analysis of the blade and wind turbine. To construct the blade-diameter trend, 52 data points from 7 manufacturers are used. A power law fit to the data of figure 2.6 yields an exponent of 2.09 that is less than the predicted value by the linear scaling law.

This is mainly because of the ongoing development efforts to reduce mass and associated costs in the recent decade and better manufacturing techniques, as well as better airfoils and aerodynamic designs.

2. Tower top mass

Generally, there is a big difference in the tower top mass associated with each manufacturer. This is due to the accumulated effect of adding all the masses atop the tower, which introduces a big scatter in the data. Furthermore, the addition of some non-standard components that are only introduced by some manufacturer (like an internal crane) adds to the scatter.

Figure 2.7 shows the tower top mass of 37 wind turbines in the range of 20 to 120 *m* rotor diameter. The data trend shows a lower value than the linear scaling law with an exponent of 2.39. Here, the effect of rotor diameter range is not taken into account.

As a matter of fact, smaller rotor diameters have a lower trend exponent than the bigger ones. That is, the more recent wind turbines have a higher tower top mass trend exponent than the smaller wind turbines when classified in separated

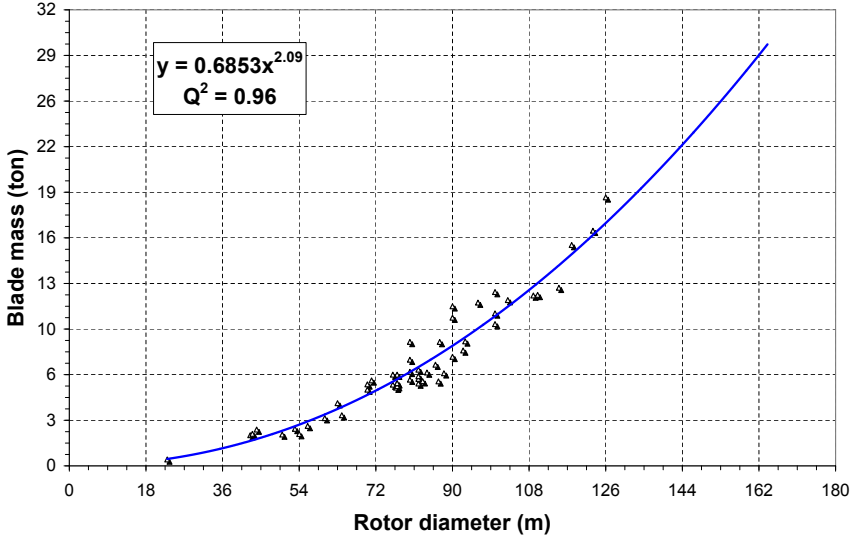


Figure 2.6: Blade mass trend based on blade manufacturers data, data is taken from magazines, product brochures and company web sites

categories.

This issue represents the stage of the technical development of a wind turbine, which for larger scales means that they have not yet reached the maturity that the smaller wind turbines have reached.

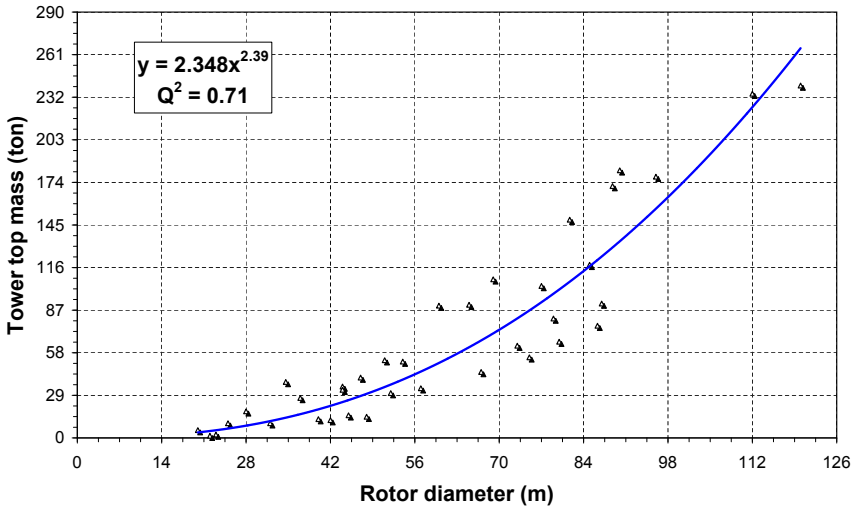


Figure 2.7: Tower top mass trends of different manufacturers, data is taken from magazines, product brochures and company web sites

3. Tower

Figure 2.8 shows the tower mass versus the rotor diameter for 37 wind turbines. The scatter in the data is mainly because of the variation of the tower heights for a given wind turbine, since many manufacturers offer a range of tower heights that best matches the site condition.

As it can be seen from the figure, the tower mass trend exponent has a value that is close to what linear scaling law predicts. However, the scatter in the data that is represented by the Q-squared value shows a relatively poor curve fit, and perhaps it would be better to not make such a judgment based on this figure. Therefore, it would be always difficult to make comparisons like that when a high scatter is present in the data.

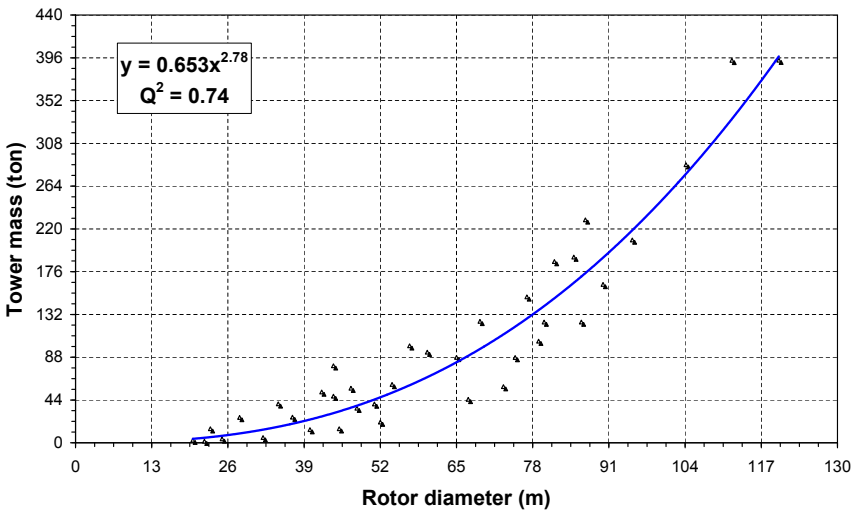


Figure 2.8: Tower mass scaling trend, data is taken from magazines, product brochures and company web sites

2.4.3 Cost-diameter trends

The cost-diameter trend of the wind turbine per kW installed capacity is presented in figure 2.9. The cost data includes the turbine units alone i.e., excluding transportation and installation costs. As it can be seen, there is a region where the specific cost is minimal. This region shows that the applied technological improvements have reached maturity after an initial startup and helped the reduction of costs.

This is a typical behavior of a learning curve in many engineering applications, where the positive sign of improvement becomes apparent only after being implemented and revised over a period of time. This also explains the slight rise in the right hand side of the curve where more recent wind turbines are located.

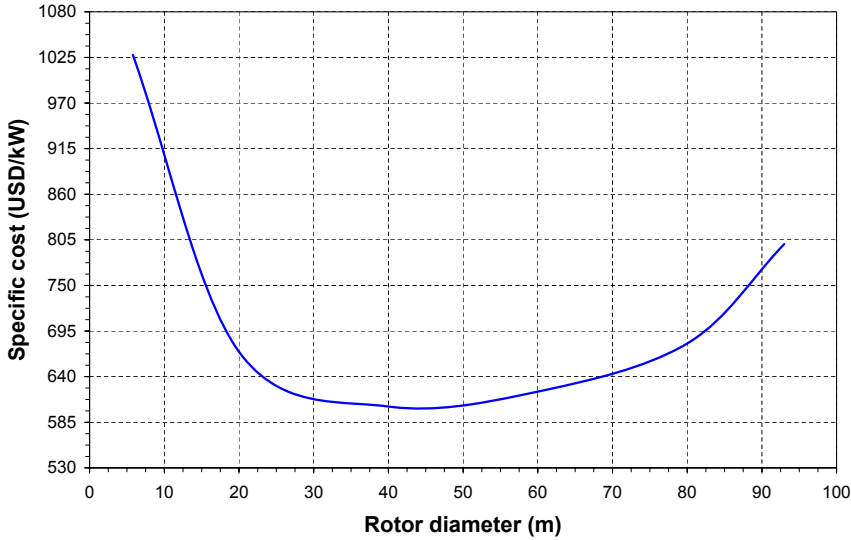


Figure 2.9: *Specific cost trend, Jamieson (2007)*

2.5 Comparison of linear scaling law and existing data

Linear scaling laws describe in a simple way how to scale a wind turbine to another size, and they are often considered as not accurate when compared with existing data. This is partly true due to the complexity of a wind turbine, which can not be captured accurately using some simple assumptions on the geometry as the linear scaling laws formulate. Therefore, these assumptions and simplifications to derive closed form relations of the problem seem to push the method away from reality.

However, when comparing the linear scaling laws with the current engineering practices, a good match between part of the predicted "square-cube" law with reality exists. In fact, the "square" part of the prediction has a valid predictive value. This means that the energy production of the real wind turbines follows well the prediction of the linear scaling laws.

Figure 2.10 shows the rated power output of 27 wind turbines versus diameter in the range of 15 to 130 m. As it is shown, the curve fit to the data points shows almost a "square" relation with size. This is due to the fact that most of the aerodynamic designs of the wind turbines have reached a level that can be considered as the achievable ideal efficiency.

As it is known from Betz limit, the energy capture is at its maximum at an axial induction factor of $\frac{1}{3}$ and this is often the strategy that most of the variable speed wind turbines follow up to the rated power point. Therefore, the rotor area in the same wind regime is a good measure to predict the captured energy by the wind turbine as it scales.

Similarly, by looking to figure 2.1 and 2.2 for the flapwise and edgewise bending moments, a fair match between the trends in existing data and linear scaling law can be seen. Linear scaling law predicts the increase as R^3 for both the flapwise and edgewise bending moments, and these are $R^{2.86}$ and $R^{3.25}$ using the existing data. However, one

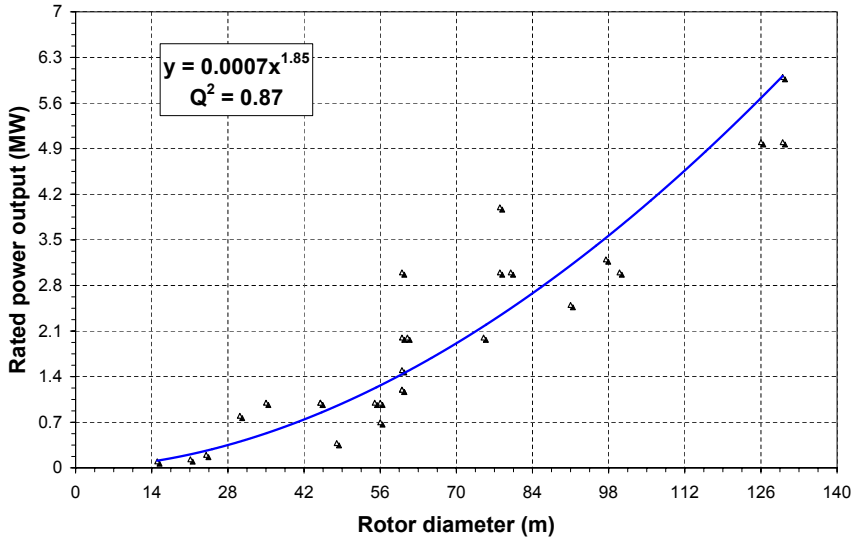


Figure 2.10: Rated power output as a function of rotor diameter; data is taken from magazines, product brochures and company web sites

should be aware that linear scaling law only predicts the stationary bending moments and the values in the existing data correspond to the non-stationary loads.

For mass predictions, linear scaling laws sometimes fail at first glance to describe the behavior of the existing data. This is the second part of the "square-cube" term, which states that mass scales with R^3 as the size increases. Figure 2.6 shows that the mass scaling of the blade using existing data has an $R^{2.29}$ relation with size that is far below R^3 as predicted by linear scaling law.

This is the influence of the ongoing efforts in airfoil developments as well as having better manufacturing techniques specially for composite blades in which all the data points of the figure are based on. If the blade would be made totally from metal then probably R^3 relation could be still a valid prediction. Therefore, the composite blade should be seen as an exception representing development in technology.

The mass trend of existing towers also does not match with linear scaling laws as shown in figure 2.8. Here, the trend exponent shows a lower value than what linear scaling law predicts. This discrepancy has two main reasons. First, by looking to the tower geometrical dimensions, it can clearly be seen that they do not scale linearly in practice. This is mainly due to the simple geometry of the tower that allows the use of design optimization techniques to search systematically the design space, which results in design solutions that do not follow anymore a linear scaling relation.

Second, the specific tower top mass decreases on average as the size increases. Table 2.6 compares some recent multi-MW wind turbines with the prototypes of the 1970s and 1980s. This effect clearly is the result of technology development that somehow counteracts the principles of linear scaling laws.

In spite of often being violated and therefore of limited use in engineering design, linear scaling laws provide a firm physical basis to understand the scaling phenomenon

Table 2.6: Specific tower head mass of some early and recent multi-MW wind turbines, *Martin and Roux (2011)*

Earlier turbines	Value ($\frac{kg}{m^2}$)	Recent turbines	Value ($\frac{kg}{m^2}$)
WTS-75 (Aelous)	46	Siemens SWT-3.6	26
WTS-3	41	Vestas V90	17
Aeolus-II	31	Nordex N90	23
MOD-2	24	WinWind WWD-3	25
MOD-5B	35	GE 2.5xl	16
Growian	51	Multibrid M5000	30
Average	38		23

in the early stages of design studies. This is of quite importance, since no other design study aiming at scales should be justified without an underlying physical understanding that accounts for the general scaling behavior as appears in the trends.

2.6 Why a new approach for upscaling?

To address the research questions of this work a more sophisticated method than the classical upscaling methods should be employed. Classical upscaling methods are not capable of making accurate realizations of large scale offshore wind turbines. This is needed to investigate the technical feasibility, economical characteristic and to construct reliable scaling trends based on size specific optimized wind turbines.

Linear scaling law is only of a limited direct use. This is due to the formulation (the inherent assumptions and simplifications) of the linear scaling law that is mainly suitable in the conceptual design phase and realizing representative wind turbines at larger scales using this method is not possible. Therefore, the technical feasibility and economical characteristics of a linearly upscaled wind turbine may not be accurate enough to make realistic judgment about its design.

Also technical data from manufacturers are obviously not available at larger scales and extrapolating existing data trends introduces large uncertainties in the design. Additionally, distributed model properties can not be extracted from existing data trends taking into account the wide range of design solutions from every different manufacturer present in the trends.

Considering these facts, the goals of this research are beyond the reach of classical upscaling methods, and this necessitates the search for alternatives. Such an alternative method should have the following specifications:

- The method should provide the detailed technical data at larger scales and enable the evaluation of all the design constraints of such big machines to identify the associated design problems. Only, based on these technical data and their associated design constraints a judgment on the technical feasibility of large scale wind turbines can be made.
- The method should provide the detailed economical data of larger scales and enable the evaluation of cost of energy to investigate the economical benefit of scale

as size increases.

- The method should enable the realization of optimized wind turbines at any specific size to construct reliable scaling trends.

To meet these specifications, all the involved disciplines and their dynamic interactions, important components relevant to upscaling, design constraints, cost elements and several other details need to be considered. Based on these considerations, a proper design methodology needs to be formulated and by having that in place, size specific optimized wind turbines can be realized to construct reliable scaling trends and investigate the influence of size on the design of large wind turbines.

This will be the subject of next chapter to study different design methods. Integrated aeroservoelastic design methodology will be selected as the best approach to deal with the research questions of this work.

Integrated aeroservoelastic design and optimization

3.1 Introduction

In the previous chapter, the two classical upscaling methods (linear scaling law and up-scaling using existing data) were discussed. Because of the restrictions associated with the classical upscaling methods, it was concluded that they cannot be used for addressing the research questions of this work. This resulted in looking for an alternative method and the main features of such an alternative method were formulated.

This chapter reviews first the existing design methodologies applicable to engineering design. Having the formulated specifications in mind the best alternative design methodology will be selected and developed. The developed methodology of this chapter will be applied on the turbine sizes from 5 to 20 MW in the following chapters to extract upscaling trends and identify technical barriers and address the economy.

3.2 Classification of design problems

This section explains the features of a good design problem solving technique and lies the foundation of a good design methodology that is needed for the successful implementation of this research.

A good design methodology is needed to make sound design wind turbines and allow the identification of their design barriers that may require further attention for. Therefore, one should know different classes of design problems and methods, as well as the advantages and disadvantages of each to be able to make the best selection.

3.2.1 Routine design problems

A design problem is called routine (or engineering) if all the steps to find the solution are known, and the designer knows in advance that there is at least one feasible solution (see VanGundy (1992), Pahl et al. (1996), Savransky (2000) and Bayazit (2004)).

There are many methods to solve a routine design problem in different fields such as aerodynamics or structure, and they can be solved by standardized or automated procedures. Normally, computer codes are employed to simulate the behavior of the system under study and based on this behavior a solution can be proposed that satisfies all the requirements.

The loop of proposing a solution, simulating the behavior of the system and checking the satisfaction of all the requirements is repeated many times until all the designers are satisfied. Typically, all the solutions of a routine design problem (also the nonroutine ones) must satisfy the three following requirements:

1. Physically possible (corresponding to the laws of nature)
2. Technically possible (corresponding to available materials and manufacturing techniques)
3. Economically profitable (the lowest possible cost)

3.2.2 Nonroutine design problems

A design problem is called nonroutine (or inventive) if at least one critical step to a solution or the solution itself is unknown, Semyon (2000). Inventive problems are often mistakenly considered as engineering problems. Actually, any inventive problem becomes at some moment a routine problem, since the recognition of the important steps increases with time. In short, an inventive problem is usually novel, elusive, ambiguous and poorly understood.

Based on this classification, this research deals with a nonroutine design problem, since the solution itself is not known in advance. It could be the case that the design process of a large scale wind turbine using the existing concept ends up with no feasible design solution, which then requires a different concept to be studied.

3.3 Difficulties of design problems

Since the design problem of this research is a nonroutine design problem, only the difficulties of this type of design problem are considered and presented below:

3.3.1 Size of the design space

For a design problem, the difficulty can be correlated to the number of variables involved. While simple design problems involve only a few variables, complicated design problems involve many variables and are usually solved by a team of designers. The design space in which a solution exists is defined in terms of the allowable ranges of the involved variables.

The design space is closed if there is a finite number of correct solutions that satisfy all the requirements. Rarely, only one acceptable solution exists for a design and usually there are several possible solutions that make the design space open.

3.3.2 Psychological inertia

The problem-solving process itself depends strongly on the ability of the designer to enable a search in the entire design space, specially when it deals with an open design problem. Psychological inertia is the tendency of the designer to preserve the current stable state or to resist dramatic changes in that state.

It often keeps the designer away from the best solution and complicates decision making. To overcome this problem, in reality many design processes rely on an optimization algorithm instead of the designer experience to search the entire design space.

3.3.3 Uncertainties in the design process

Uncertainties can be classified based on their origin into two groups: aleatory and epistemic. Aleatory uncertainty is the inherent variation of the physical system under consideration or its operating environment. Epistemic uncertainty arises because of the lack of knowledge or information in any phase or activity of the design process, and could be removed if sufficient data is provided, [Oberkampf et al. \(2004\)](#).

Design in the presence of uncertainty consists of three steps, [Roy et al. \(2009\)](#):

1. Identification, modeling and representation of uncertainties into mathematical models based on probability theory or nonprobabilistic approaches
2. Propagating uncertainties (in computer codes) to quantify their impact on the design problem
3. Selection of an appropriate optimization algorithm to ensure that the optimum solution obtained is robust against uncertainties

3.4 Methods of solving design problems

In the context of design, a problem is any situation where the designer has the opportunity to make things better using a problem solving method. The effectiveness of such a method depends on many factors such as: the quality of the solution, time spent on the problem resolution, and acceptance of a solution. However, any problem solving method should have at least the following characteristics:

1. It should have a mechanism for directing the solver (or designer) to the most appropriate and strong solutions. This is the heart of the method: it must reduce quickly the design space and eliminate the nonfeasible solutions.
2. A good problem solver must obtain very high quality solutions with a high level of recognition in a short time. This is specially very important when one deals with large scale problems with many variables and different disciplines involved.

3. A good problem solver has to know practically all relevant human knowledge. However in practice it is almost impossible for a human to meet this requirement, but a good design methodology needs to have the necessary knowledge for even difficult and complex nonroutine problems.
4. A good design methodology should "turn off" his psychological inertia. This requirement is a big challenge, therefore many methods to remove psychological inertia have been proposed for.

Next subsection presents some of the most important solving methods.

3.4.1 Trial-and-error methods

Trial-and-error methods are the oldest solving methods that regardless of the class of the problem can be applied both on the routine and nonroutine problems. However, they are more efficient for simple, well-defined, routine and closed problems and only be used for the open problems, if the possible direction of search is known.

Due to the disadvantages of the trial-and-error method it is not widely used in modern engineering designs. Some of the disadvantages of this method are:

1. The number of ideas (trials) that succeed per unit of time is small. As a result the design process lasts a long period of time, which means the method is not time effective.
2. There is no mechanism for directing the solver's thinking towards the solution. Thus the solver is unable to define the direction in which the solution might be found. This is the crucial disadvantage of the trial-and-error method.
3. There is no mechanism to systematically find the best solutions. As a result, solving the same design problem might lead to different solutions.

These disadvantages were recognized in the middle of the twentieth century and since then many attempts have been made to perfect that. These include methods such as:

1. Brainstorming, synectics, lateral thinking, neurolinguistic programming and mind mapping to overcome the psychological inertia.
2. Morphological analysis, focal objects and forced analogy to expand the search method.
3. Decision aids such as T-charts and probabilistic decision analysis to make the method more systematic.

3.4.2 Inventive based methods

Inventive based methods need creativity to solve a design problem that is usually believed to be beyond comprehension and, thus, methodology. However, they have proven their benefits for finding original and useful ideas by systematically examining alterations in existing components within a system, their attributes, functions or internal relationships.

Inventive design enables the designer to change old paradigms, and institute new feasible design solutions without getting rid of the old ones and create out of the box solutions. There are three premises on which these methods are based:

1. To make an ideal design with no harmful function.
2. Identifying contradictory behaviors of the system and wholly or partially eliminating them.
3. Giving structure to the design process such that it can be universally applied to any design problem.

Among many inventive based methods like Quality Function Deployment (QFD), Theory of Constraints (TOC), Taguchi approach and Six Sigma, TRIZ (the theory of inventive problem solving according to the acronym for the same phrase in Russian) is the most systematic method for engineering design problems. It is an algorithmic approach, based on a set of patterns of evolution, which can be used to generate ideas for developing the next generation of a technological system.

3.4.3 Knowledge-based engineering methods

Knowledge is a key component of engineering design that can be collected from specialists and stored in a knowledge base system. They capture process and product information to make models of engineering design problems and then use the model to automate all or part of the design process, or make analogies with other engineering design problems to solve a problem. Some of the advantages of knowledge-based methods is as follow :

1. **Simplification of the design process**

The design process is simplified for the designer as his/her intervention is required less in decisions making situations.

2. **Expertise base elimination**

Eliminates the need for the designer to develop expertise and skills in areas not necessarily in his/her own field.

3. **Innovation encouragement**

The simplification of the design process enables the designer to put more time and efforts for looking to more innovative design solutions.

4. **Error-proofing**

Complex calculations and tedious database/catalog lookups can be performed in a quick and error-free manner.

5. **Speed**

Enables automation of repetitive tasks, which otherwise occupies the designer's productive time.

There are many development methodologies for the knowledge-based engineering domain such as: MOKA (Stokes (2001)), CommonKADS (Schreiber et al. (2000)) and 47-Step Procedure (Milton (2007)). However, each method has its own advantages and disadvantages for a given field and application.

3.4.4 Design search and optimization methods

The use of optimization methods is steadily increasing in design. At its simplest form, optimization can be defined as the search for a set of inputs x , design variables, that optimizes the objective function $f(x)$, subject to inequality $g_j(x) \geq 0$, and equality $h_k(x) = 0$ constraints, Haftka and Gürdal (1992).

Design optimization problems can be characterized in different ways as follows:

1. The mathematical form of equation involved

Both the objective function and constraints can be classified as linear or nonlinear equations resulting in a linear or a nonlinear optimization problem.

2. The number of objective functions

If the problem under study has only one objective function to optimize, then we are dealing with a single optimization problem, otherwise we have a multi-objective function problem.

3. The deterministic nature of design variables

If the design variables have a stochastic distribution rather than a deterministic value, then we are dealing with a stochastic design optimization problem. Deterministic optimization problems always yield the same optimum if started from the same point in the design space, stochastic methods make no such guarantees.

4. The presence of constraints

In an unconstrained optimization problem the design space is infinity and the objective function can take any value, whereas in a constrained optimization problem, either the design variables are bounded by a lower and upper limit or the design space is bounded by some functional constraints.

5. Type of optimization algorithm

An optimization algorithm is a numerical method that explores the design space to find a set of design variables, which optimizes (minimize or maximize) the objective function. In this process, if the algorithm uses the derivative of the objective function or constraints, it is called a gradient based method (sometimes also called first order), otherwise it is called direct (sometimes also zero order or evolutionary) method.

6. The permissible value of design variables

The design variables can be continuous or discrete. If they are continuous then both the zero and first order optimization algorithm can be used to solve them. However, for discrete values the most common method is integer programming, although constraint logic programmes are also applicable.

7. The number of involved disciplines

When proper modeling of the system requires a number of disciplines that interact with each other, then the design optimization problem is called a multidisciplinary design optimization (MDO).

3.5 Selection of the design methodology and its overview applicable to upscaling

The common practice in designing a wind turbine is the isolated approach. In this approach, the structural, aerodynamic and control designs do not occur at once. To cope with more complex future wind turbines, the isolated approach does not seem to be appropriate. An integrated design approach is essential to guarantee the minimum design time and to cover all the interdisciplinary aspects of design.

Considering all different choices explained before, it is the MDO that offers such an integrated capability. Additionally, to address both the technical and economical characteristics at the same time and realize size specific optimized wind turbines (as it was formulated in section 2.6) none of the other methods can be of direct use. Therefore, the scaling study of this research will be formulated as an MDO. The MDO formulation enables in a clear way to address the technical feasibility and economical characteristic of a wind turbine as follows:

- Through the definition of the design variables and optimizing them an accurate realization of the technical characteristics of the future wind turbines can be made. These optimized wind turbines are needed to construct reliable scaling trends.
- Through the inclusion of the design constraints all the problems that may result the design to become nonfeasible or challenging can be covered and by referring to these design constraints an assessment of the technical feasibility can be made.
- Through the definition of the objective function all the important elements that can influence the cost of energy such as the cost of all the components, operational and maintenance cost, installation and the energy yield can be included. This enables the assessment of the economical characteristic of large scale wind turbines.

For this purpose, all the disciplines influencing the design should be involved. For a wind turbine, aerodynamic, control and structure are the dominating disciplines and to preserve their dynamic interactions the wind turbine should be seen as an aeroservoelastic system. This requires the methodology to be an integration of different computational models each representing one discipline. Also, the data exchange among all computational models should be consistent and automated. It also should enable the exchanged data to be processed at any stage before or after passing that among models.

Unfortunately, most of the wind turbine computational models currently in use rely on an architecture that is not suitable for multidisciplinary design studies (for a review of existing simulation codes of the wind turbines see [Ashuri and Zaaijer \(2007\)](#)). Therefore, in this research a large effort has been made to integrate the best candidate out of many existing simulation tools and automate the data flow among them and finally parameterize the entire design process. Next section discusses the architecture of the MDO used in this research.

3.6 Architecture of the MDO

A common practice in wind turbine design optimization is to employ a sequential approach to solve multidisciplinary design problems, each focusing on one discipline, for

example, structure, aerodynamic and control. Here, the simplest approach is to first do an aerodynamic shape optimization of the blade and structural considerations are not directly entered into the aerodynamic design formulation. However, some bound constraints that comes from structural consideration can be applied in the aerodynamic optimization such as the airfoil thickness at several stations along the blade.

Subsequently, knowing the aerodynamic loading and external shape of the blade, the structural team can do an optimization to find the optimal internal blade geometry. Unfortunately, this sequential approach neglects the coupling between aerodynamic and structure known as aeroelasticity, which leads to convergence to a suboptimal solution.

There are however several other different optimization architectures that can be used at different situations, [Martins and Lambe \(2011\)](#). This study uses a Fully Integrated Optimization (FIO) architecture. The idea is to directly couple an optimizer to a multidisciplinary computational model, see figure 3.1. This preserves the interaction of different disciplines. Here, the design variables are passed to the simulation tools and objective function and constraints are send back by them to be assessed by the optimizer. This iterative approach continues until the convergence is achieved.

During this process, a chain of computational activities is needed that are classified as aerodynamic, structure and control evaluation as well as a proper assessment of the associated costs and design constraints. This classification, while clearly very general, provides a standard for simulating the behavior of machines that is needed for design studies (also usable in different fields of machine design, [Ashuri et al. \(2012\)](#)).

Furthermore, in this process many configurations, many alternative shapes and struc-

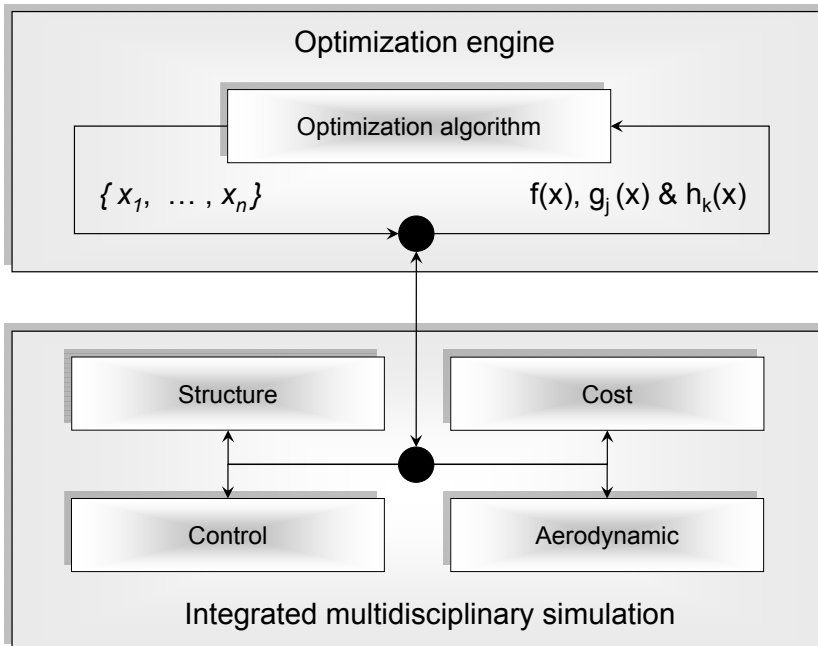


Figure 3.1: Fully integrated optimization architecture

tural arrangements including many design variables, design constraints and the objective function need to be simulated and evaluated iteratively. In order to be able to easily and effectively develop such a methodology the design optimization formulation should be defined in advance. This will be explained in the next section.

3.7 Optimization problem formulation

In order to construct an optimization model the design variables, the design constraints and their relevant safety factors, and the objective function should be defined. In addition, to evaluate the design constraints and the objective function, a set of simulation tools is required. Then the optimization model can be expressed in the following form:

$$\text{Find } x = \{x_1, \dots, x_n\} \text{ that minimizes } f(x) \quad (3.1)$$

subject to side constraints as:

$$x_{lower} \leq x \leq x_{upper} \quad (3.2)$$

and functional constraints as:

$$g_j \{x\} > 0 \quad (3.3)$$

$$h_k(x) = 0 \quad (3.4)$$

where x is an n -dimensional vector of design variables to be found with a lower and upper bound as side constraints, $g_j(x)$ as the inequality and $h_k(x) = 0$ as equality constraints to be satisfied, and $f(x)$ as the objective function to be optimized.

3.7.1 Design variables

A design variable is a changeable parameter by the optimizer, whose influence on the constraints and objective function needs to be evaluated during the design process. Among many components of a wind turbine, blade and tower are the most important components to optimize. Major reasons for such a conclusion are:

- They are the most flexible components of a wind turbine, thus they require many design considerations. This is of great importance in larger wind turbines and upscaling studies, since the larger the wind turbines become the more flexible it gets.
- Their failure is more critical to the safe state of the entire wind turbine.
- Blade and tower (also the controller) have the highest influence on the energy yield of the wind turbine. Therefore, to make a cost effective design, which is the target of any design they need special attention.
- Blades and tower (also the gearbox) have the highest cost share of a wind turbine. Typically, blade and tower make up 25% to 30% of the capital cost of an offshore wind turbine.

- To represent the dynamics and economy of the components of a wind turbine other than the blade and tower, a mass and cost model is used (this will be explained later in this chapter). In many components, these cost and mass models are a function of the blade length. Thus, optimizing the blade length provides the mass and cost of these items in such a way that at the end they result in the lowest LCOE (Levelized Cost of Energy).

Figure 3.2 shows different stations along the blade and tower in which the wind turbine parametrization is taking place. Also table 3.1 presents the 23 design variables and their relevant stations.

Table 3.1: *Wind turbine design variables to be optimized*

No.	Description of the variable
1	Blade length
2	Tower height
3	Rated rotational speed
4-5	Blade structural twist at stations 9 and 15
6-9	Blade structural chord at stations 3, 7, 15 and 18
10-13	Blade skin thickness at stations 1, 3, 6 and 16
14-16	Blade shear web thickness at stations 3, 6 and 16
17-19	Blade spar cap thickness at stations 3, 6 and 16
20-21	Tower diameter at stations 1 and 22
22-23	Tower thickness at stations 1 and 22

In this research, optimization of the blade is carried out with 17 design variables. For the external geometry of the blade that is needed for aerodynamic design optimization, chord at 4 stations along the blade, twist 2 stations along the blade, and the blade length itself are introduced as design variables.

For the internal thickness distribution of composite lay-ups needed for structural design optimization of the blade, spar thickness at 3 stations along the blade, shell thickness at 3 stations along the blade, and web thickness at 3 stations along the blade are introduced as design variables.

Also the rotational speed of the rotor is a design variable, since together with the blade length they control the tip speed of the blade, which is an important design parameter. In addition, the rotational speed has a big influence in the drive train loads and thus the costs.

All these design variables are continuous and defined at some stations along the blade and tower. An interpolation scheme is used to define the values at different stations.

To make a smooth interpolation of the design variables, some other design parameters are fixed for all different scales from 5 to 20 MW as it is shown in table 3.2. The location of the shear caps from station 6 to the blade tip are the same as station 6. From station 1 to 6 an interpolation is used to find the location of the shear cap.

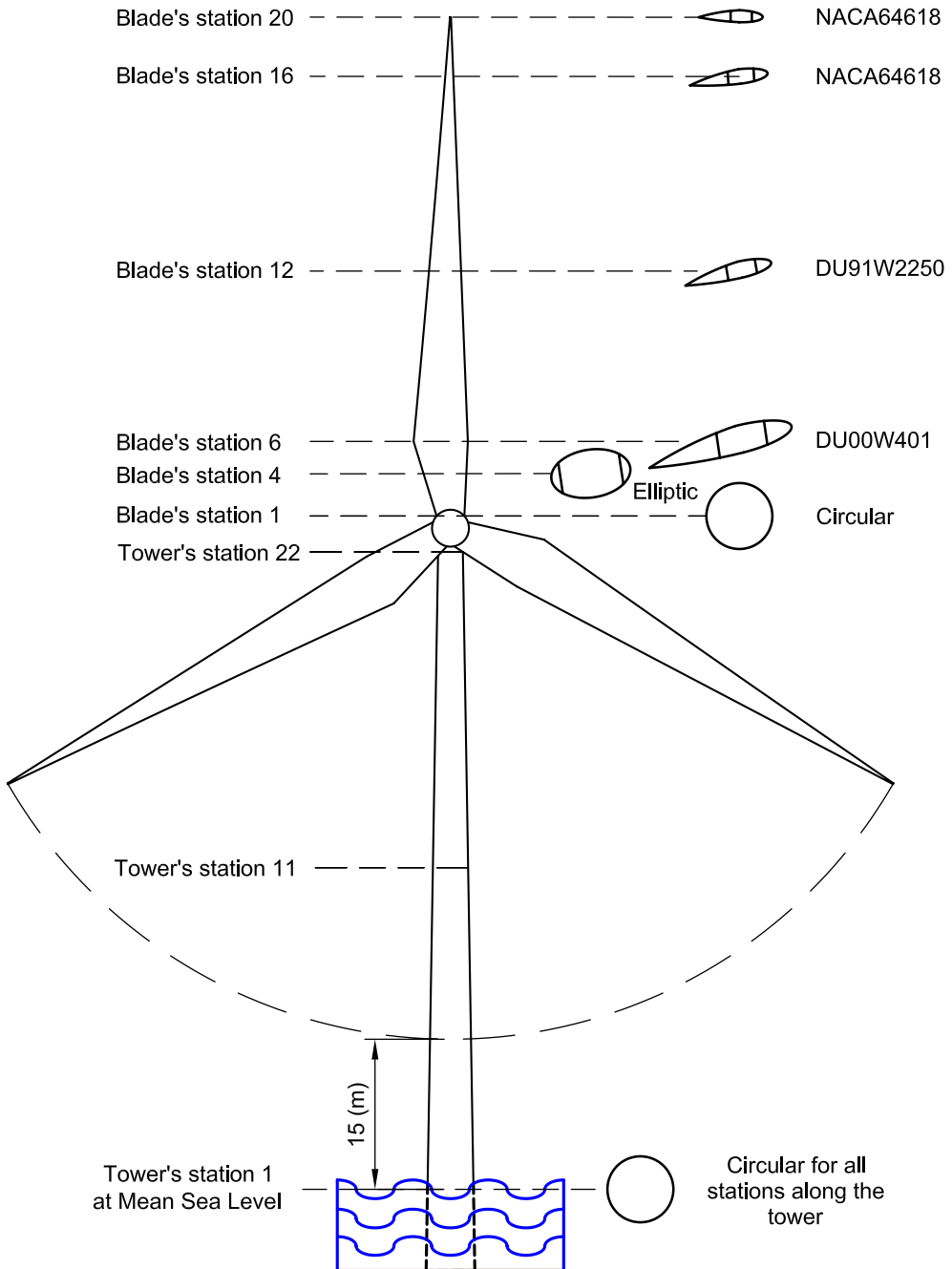


Figure 3.2: Parametrization of the wind turbine configuration

Table 3.2: Fixed design parameters of the blade

Description of the parameter	Value (unit)
Shear web thickness at station 1	0.00 (m)
Spar cap thickness at station 1	0.00 (m)
Structural twist at station 20	0.00 (deg)
Structural chord at station 20	0.12 (m)
Nondimensionalized location of the 1 st shear cap at station 1	0.00 (-)
Nondimensionalized location of the 2 nd shear cap at station 1	1.00 (-)
Nondimensionalized location of the 1 st shear cap at station 6	0.25 (-)
Nondimensionalized location of the 1 nd shear cap at station 6	0.50 (-)

3.7.2 Design Constraints

A constraint is a condition that needs to be satisfied to have a feasible design. There are two types of constraints considered in this research; side and functional constraints. The side constraints are the upper and lower limits of a design variable that bound its value to be in a range that the designer defines in advance.

Functional constraints are mathematical equations which must be satisfied in an optimization problem. They represent some physical principles which govern the relationship among the design variables. For the functional constraints, in total, 51 inequality constraints are used to obtain feasible design solution of the blade and tower as shown in table 3.3 and 3.4.

Table 3.3: Wind turbine blade design constraints

No.	Description of the design constraint	Value (unit)
1-9	Max flapwise tip deflection from 9 to 25 $\frac{m}{s}$	Scale dependent
10-15	Max flapwise fatigue at stations 1, 3, 7, 10, 12 and 14	≤ 0.7 (-)
16-21	Max edgewise fatigue at stations 1, 3, 7, 10, 12 and 14	≤ 0.7 (-)
22-27	Max flapwise stress at stations 1, 3, 7, 10, 12 and 14	≤ 200 (MPa)
28-33	Max edgewise stress at stations 1, 3, 7, 10, 12 and 14	≤ 200 (MPa)
34-36	First, second and third natural frequency	Scale dependent
37	Tip speed	≤ 120 ($\frac{m}{s}$)

In these functional constraints, the partial safety factors are also included. However, the selection of the appropriate partial safety factors that is applied on the design constraints of table 3.3 and 3.4 is treated separately in the next subsections.

For the blade, stresses and cumulative fatigue damage (fatigue damage calculation is done using rain flow cycle counting of the stress signals and applying Miner's rule on these signals) at 5 stations along the blade, tip deflections for different wind speeds during operation, and the first 3 natural frequencies are the design constraints. While all the side constraints are scale dependent, only some of the functional constraints are scale dependent. Therefore, those scale dependent constraints are defined in the subsequent

chapters for each scale individually.

For the tower, stresses and fatigue damage at 6 stations along the tower and the first two natural frequencies are the design constraints. In addition to the inequality constraints mentioned above, some side constraints are used to bound each design variable that are scale dependent and their values will be presented in the following chapters.

Table 3.4: *Wind turbine tower design constraints*

No.	Description of the design constraint	Value (unit)
1-6	Fore-aft stress at stations 1, 5, 9, 13, 17 and 21	≤ 150 (MPa)
7-12	Fore-aft fatigue at stations 1, 5, 9, 13, 17 and 21	≤ 0.7 (-)
13	First natural frequency of the tower	$0.3 \leq \omega_{1n} \leq$ Scale dependent
14	Second natural frequency of the tower	$0.3 \leq \omega_{2n} \leq$ Scale dependent

3.7.3 Partial safety factors

It is a common practise to use partial safety factors in wind turbine design for achieving sound designs, as prescribed by many standards. The technique comes from an analogy with ISO2394 (General principles on reliability for structures) standard on limit-state design theory, which describes loads (actions) and strengths (resistances) in a structure.

The ISO2394 standard defines limit-state design procedures that use partial safety factors to cover uncertainties in the design process. These partial safety factors are dependent on the uncertainties in the analysis methods, the uncertainties in materials, loads, and the consequences of failure for component classes. To account for all the uncertainties in the design process, partial safety factors are applied to loads, materials and the failure consequence of different components.

There are many standards that specify the various aspects of the design process, however little agreement exists among them, therefore it is always useful to check at least two different standards (the approach used in this research).

The well known standard and certification bodies in the wind turbine industry, based on their popularity are: International Electrotechnical Commission (IEC), Germanischer Lloyd (GL) and Det Norske Veritas (DNV). Each certification body has its own rules and requirements by which a specific turbine type is certified, tested, manufactured and documented. One of the major differences among these standards is the treatment of partial safety factors.

Most design codes address partial safety factors for loads, strength and failure separately. According to IEC 61400-1 standard, a series of partial safety factors for each type must be used to cover these uncertainties. However, IEC did not always provide sufficient guideline in the selection of these factors. The GL standard provides an explicit list of partial safety factors and prescribes all of the individual factors to be applied and non of the adjustments are left to the designer.

The partial safety factors for materials from the GL standard are shown in table 3.5. Applying the GL factors as specified implies a combined material factor of 2.94 for composites, which seems to be conservative, and 1.35 for non-composites. In this case the IEC standard only provides a general material factor of 1.1.

Table 3.5: *GL partial safety factors for material*

Type of safety factor	Symbol	Value (-)
General material factor	γ_{M0}	1.35
Influence of aging	C_{2a}	1.5*
Temperature effect	C_{3a}	1.1*
Hand layup laminate	C_{4a}	1.2*
Post-cured laminate	C_{5a}	1.1*
Total (Π)		2.94

* Only applicable to composites

In both the IEC and GL standard, the load safety factors are classified in an ultimate and fatigue category. Table 3.6 summarizes the IEC and GL partial safety factors for ultimate loads, and table 3.7 shows that for fatigue loads. The consequence of failure is also shown in the same table, since it is classified based on the load type in both standards.

Table 3.6: *Partial safety factors for ultimate load analysis*

Type of safety factor	IEC	GL
Loads	1.35	1.35
Blade consequence of failure	1.0	1.0
Tower consequence of failure	1.0	1.0
Materials	1.1	2.45-2.940
Total (Π)	1.485	3.307-3.969

The total partial safety factors for ultimate loads is maximum 1.485 and 3.969 for the IEC and GL, respectively. A detailed comparison between these two standards is given by [Musial and Butterfield \(1997\)](#). No adjustment is required under both standards to cover the consequences of failure for ultimate load analysis for the rotor blade and tower.

Table 3.7: *Partial safety factors for fatigue load analysis*

Type of safety factor	IEC	GL
Loads	1.0	1.0
Blade consequence of failure	1.15	1.0
Tower consequence of failure	1.15	1.0
Materials	1.1	1.485-1.960
Total (Π)	1.265	1.485-1.960

The IEC fatigue load analysis is 1.265 that excludes the designer-specified material property adjustments mentioned before. In the GL code, the total partial safety factors is between 1.485 and 1.96, In both tables the safety factor to cover the consequences of failure is component dependent and these values are given for rotor blades and tower as non-fail-safe components.

These standard partial safety factors are the minimum requirements that a design should meet, and can be used as a guideline to select representative values. However, the values used in this work are selected as such as to give consistent values with the 5 MW NREL design, while satisfying the minimum standard requirements. Table 3.8 shows the selected values of partial safety factor throughout this work.

Table 3.8: *Definition of partial safety factors used in this work*

Type of safety factor	Value (–)
Material safety factor	1.10
Consequence of failure	Blade 1.0
	Tower 1.0
Ultimate load factors	1.48
Fatigue load factor	1.43

Referring to table 3.3 that shows the design constraints of the blade, the followings partial safety factors for each design constraint is considered:

Maximum flapwise tip deflection of the blade

For item 1 to 9 of table 3.3, the load and the material partial safety should be considered. This combination of safety factor results in a total safety factor of 1.628 (1.1×1.48). That is, if the distance between the unloaded blade at the tip and the tower is for example 5 m, then the maximum flapwise deflection of the blade when it is loaded should not be larger than 3.07 m. However, this distance varies at different scales, therefore this design constraint is scale dependent.

Maximum flapwise and edgewise fatigue of the blade

As it was mentioned before cumulative fatigue damage calculation is done using Palmgren-Miner rule. Using this rule and usually for design purposes, fatigue failure does not happen if the total cumulative damage is less than 1. As table 3.8 shows, for item 10 to 21 of table 3.3, a partial safety factor of 1.43 safety for fatigue load is considered. This means that the total cumulative damage should not be larger than 0.7.

Maximum flapwise and edgewise stress of the blade

In this work, it is assumed that the yield stress of the composite blade is 325 MPa. However, application of a material safety factor for composite materials is not as straight and applicable as it is for isotropic and homogeneous materials.

Composite materials have many failure modes, and their yield stress depends strongly on the layup and the volumetric mixture of the elements that the composite sample is made of. Exceeding this yield stress in some elements of a composite material does not necessarily mean the entire structure will fail, since the experienced load of that element will be distributed among other elements. Considering these facts, the defined value in this work is just a representative value suitable for the design applications.

For stress calculation, the combination of the material safety factor and ultimate load safety factor has to be considered. Thus, the total safety factor becomes 1.628 ($1.1 \times$

1.48). Using this definition, the maximum allowable flapwise and edgewise stresses at the selected stations along the blade (item 22 to 33 of table 3.3) are 200 MPa.

Allowable natural frequencies of the blade

As it is shown in table 3.3 for item 34 to 36, the natural frequencies are scale dependent. Therefore, after finding the optimum rated rotational speed of the rotor in each scale (5, 10 and 20 MW) a safety margin of $\pm 10\%$ for the 1P and 3P excitations is considered.

Similarly, the design constraints of the tower presented in table 3.4 are obtained as follow:

Maximum fore-aft stress of the tower

In this work, it is assumed that the tower is made of structural steel. Typically, the yield stress of the structural steel is around 270 MPa. By applying the combination of the ultimate and material safety factor of 1.628 (1.1×1.48) to the defined yield stress, a maximum allowable fore-aft stress of 150 MPa for the tower is obtained. This maximum allowable stress is shown at different stations along the tower height (item 1 to 6) in table 3.4.

Maximum fore-aft fatigue of the tower

Similar to the fatigue damage calculation of the blade, the fatigue damage calculation of the tower is carried out. As table 3.4 shows, for item 6 to 12 the total cumulative damage should not be larger than 0.7.

Allowable natural frequencies of the tower

Unlike the blade, the tower has an extra natural frequency constraint. In fact, the tower is in touch with water and its natural frequency should not coincide with the wave frequency. The typical wave frequency for the shallow to medium level waters is from 0.1 to 0.3 Hz.

This forces the natural frequencies of the tower to be larger than 0.3 Hz. As it is shown in table 3.4 for item 13 and 14, the lower bound of the natural frequency is 0.3 Hz and the upper bound is scale dependent. Similar to the blade, a safety margin of $\pm 10\%$ for the 1P and 3P excitations is considered.

3.7.4 Objective function

When applying any changes to a given design, it is important to know the influence of this change in the system level. As an example, an increase in blade length to increase annual energy production (AEP) increases loads and installation costs. If one change does not balance out the other change, then the proposed improvements end up with a negative overall impact.

The LCOE is a good indication to see the influence of all these cross couplings in an MDO, and results in a true assessment of all technical changes. Therefore, it is selected in this work to be the objective function of the MDO to minimize. For an offshore wind turbine operating in a wind farm, LCOE is made up of all the system cost elements, which is explained by [Fingersh et al. \(2006\)](#). This covers the following items:

- Turbine Capital Cost (TCC): TCC is the cost of all the components of a wind turbine. These are: blades, hub, pitch mechanism and bearings, nose cone, low speed shaft and bearings, gearbox, mechanical brake, high speed shaft and coupling, generator, power electronics, yaw drive and bearing, main frame, electrical connections, hydraulic system, cooling system, nacelle cover, control equipments, safety system, condition monitoring, tower, marinization (extra cost to protect against marine environment like salty water).
- Balance of Station (BOS): BOS is the cost of following items: monopile, port and staging equipment, turbine installation, electrical interface and connections, permits, engineering, site assessment, personnel access equipment, scour protection, offshore warranty premium and decommissioning. Transportation over land is not considered as an element in the BOS, since it is assumed that all the manufacturing facilities will be located near the shore for larger scale offshore wind turbines.
- Initial Capital Cost (ICC): ICC is the summation of the TCC and BOS costs.
- Levelized Replacement Cost (LRC): LRC is the cost of major replacements and overhauls, distributed over the life time of the wind turbine.
- Operations and Maintenance (O&M): O&M is the cost associated to fix failures of mechanical or electrical components and all the regular and irregular inspection of the wind turbine. Table 3.9 gives an overview of all the cost elements that are calculated using these definitions for the 5 MW NREL wind turbine.

LCOE can be calculated using the following equation:

$$LCOE = \left(\frac{(ICC \times FCR) + LRC + O\&M}{AEP} \right) \quad (3.5)$$

here: FCR is the fix charge rate and includes construction financing, financing fees, return on debt and equity, depreciation, income tax, and property tax and insurance.

AEP is the amount of generated electricity in a year for a given wind speed distribution, $f(V)$. It also includes the mechanical and electrical conversion losses, and machine availability. Wind speed distribution is modelled as:

$$f(V) = \left(\frac{k}{c}\right) \cdot \left(\frac{V}{c}\right)^{k-1} \cdot \exp \left[-\left(\frac{V}{c}\right)^k \right] \quad (3.6)$$

where V is the wind velocity, k the shape factor, and c the scale factor. In this research, k is 2 corresponding to the Rayleigh distribution and c is defined to be 9.47. These values typically represent the condition of the Dutch part of the North Sea, Brand (2008). Then the AEP production can be expressed as:

$$AEP \approx 8760 \times \sum_{i=cut-in}^{cut-out} P(V_i) \cdot f(V_i) \quad (3.7)$$

in which 8760 is the number of hours per year, and $P(V)$ is the power curve of the wind turbine.

However, these cost models were calculated based on the cost of materials and products in 2002 and should be updated based on the cost of materials and products in the present time to account for the inflation of materials, products and labors.

To compensate for this difference a component cost escalation model that is based on the Producer Price Index (PPI) is used. The PPI is an index that is updated on a monthly basis by the US Department of Labor, Bureau of Labor Statistics, to track the changes of costs of products and materials over a wide range of industries and industrial products.

The PPI provides a more accurate update than a general inflation index (GII). As an example, the increase in the cost of structural steel and copper in 2004 and 2005, were considerably higher than the GII in the same year. This means that cost of products made of structural steel and copper increased also rapidly and the GII is unable to track such changes and using that instead of PPI results in a considerable error.

Table 3.9 is an example of a cost estimate and LCOE calculation from a run of the cost model (the cost is escalated to 2009 USD) for the offshore (shallow water), 5 MW NREL wind turbine. The detailed cost models used in this table are presented in appendix A.

3.7.5 Wind turbine simulation tools

Wind turbines are complex systems and to simulate the physical behavior of such a system computer-based simulations are required. In this work, the NREL series of simulation tools are used, since they are all open source and free, suitable for research purposes.

The theoretical background of the analysis methods employed in each code is presented in appendix B. Table 3.10 briefly presents each code, and its usage for this research.

Unfortunately, all these simulation tools are in principle independent and do not communicate effectively with other simulation tools, and the data transfer between these tools has to be done manually by the designer. However, in an MDO problem the manual intervention of the designer is impossible, since the process needs to run iteratively many times to find the optimum design solution. To overcome this problem, these tools need to be integrated. This issue is explained in the next section.

3.8 Design integration

With the available fast computers (especially when used as a cluster), it is possible to analyze a large scale nonlinear unsteady multidisciplinary design problem. However the design framework within which the system simulation and analysis should evolve is itself not a single entity, but a combination of different simulation tools that need to be integrated in advance and in such a way that it promotes an efficient working environment.

To develop a responsive and effective design a successful integration of all the simulation tools is needed. This integration should also enable the evaluation of requirements as the design constraints, and targets as the objective function to be achieved.

Figure 3.3 shows the integration of several simulation tools that are needed to capture the aeroservoelastic behavior of the wind turbine and evaluate the design constraints and objective function.

Table 3.9: Cost estimate of the 5 MW NREL wind turbine (2009 USD)

Components	Cost (1000 USD)	Mass (kg)
Blades	1062.3	17480
Hub	130.2	60540
Pitch mechanism and bearing	242.0	28878
Nose cone	13.6	1810
Low speed shaft	166.8	16526
Main bearings	64.4	5400
Gearbox	877.2	39688
Mechanical brake and coupling	11.0	1053
Generator	398.0	17623
Power electronics	393.2	-
Yaw drive and bearing	146.3	13152
Main frame	162.7	31773
Electrical connections	308.8	-
Hydraulic and cooling system	77.2	423.7
Control,safety and condition monitoring	65.3	-
Tower	1491.3	596520
Marinization	939.1	-
Turbine capital costs (TCC)	4722.2	-
Foundation system	2174.7	-
Transportation	1568.3	-
Port and staging equipment	144.9	-
Turbine installation	732.8	-
Electrical interface and connection	2063.5	-
Permits, engineering and site assessment	215.5	-
Personnel access equipment	70.2	-
Scour protection	403.0	-
Decommissioning	362.8	-
Balance of station costs (BOS)	7373.2	-
Offshore warranty premium	624.1	-
Initial capital cost (ICC)	13083.0	-
Levelized replacement costs	99.0	-
Operation and maintenance	561.4	-
Fixed charge rate	0.1185	-
AEP (kWhr)	23911817.1	-
LCOE ($\frac{USD}{kWhr}$)	0.0658	-

This integration is carried out by writing a shell program that manages the data flow between all the codes. The program is used to manage the design optimization process with the following tasks and features:

- The combination of different simulation tools works effectively and correctly

Table 3.10: *Selection of the simulation tools*

Tool	Usage
TurbSim	Simulating the 3D turbulent wind flow
AeroDyn	Simulating the steady and unsteady aerodynamic loads
AirfoilPrep	Modifying 2D airfoil data for 3D effects
FAST	Simulating the aeroelastic behavior of the wind turbine
BModes	Calculating mode shapes and frequencies
Crunch	Postprocessing the output data of FAST
Fatigue	Rainflow cycle count of the load histories

- The data exchange among this integrated framework can be done automatically
- All the design changes are reflected in the relevant locations in the framework
- The iterative simulation of the system that is needed for the MDO process is possible
- Parameterize the integrated framework in such a way that simulating different wind turbine concepts and scales can be done easily
- Giving access to intermediate data at any stage of the design process
- Interfacing with any other optimizer than the one currently in use
- Keeping the architecture of the program modular
- Enabling the integrated framework to run on a cluster of computers

However, the integrated frame work of this research still lacks two important features that are needed for an MDO of a wind turbine. First, automating the controller design and updating its parameters in every iteration, second automating the extraction of blade and tower structural properties. These issues are treated separately in the following sections.

3.9 Controller design automation

One of the main complexities of designing a wind turbine is due to the dynamic interactions of aerodynamic forces, structural flexibility and control actions, known as aeroservoelasticity. A good design optimization process (DOP) should consider these interactions from the first iterations of the system design.

Although the integration of the tools explained in the previous section can simulate the combined effects of control, structure and aerodynamics, the DOP cannot be done with all disciplines at a time involved.

Until now, the experience to optimize aerodynamics, structure and control, subject to many design constraints does not exist in the field of wind energy and there has been no reported development of a truly aeroservoelastic design optimization capability within the wind energy industry.

In fact, up to now, the role of the control engineer in wind turbine design activities has been mainly focused on designing the controller for a given configuration. However, the shift towards more flexible structures equipped with active control devices operating

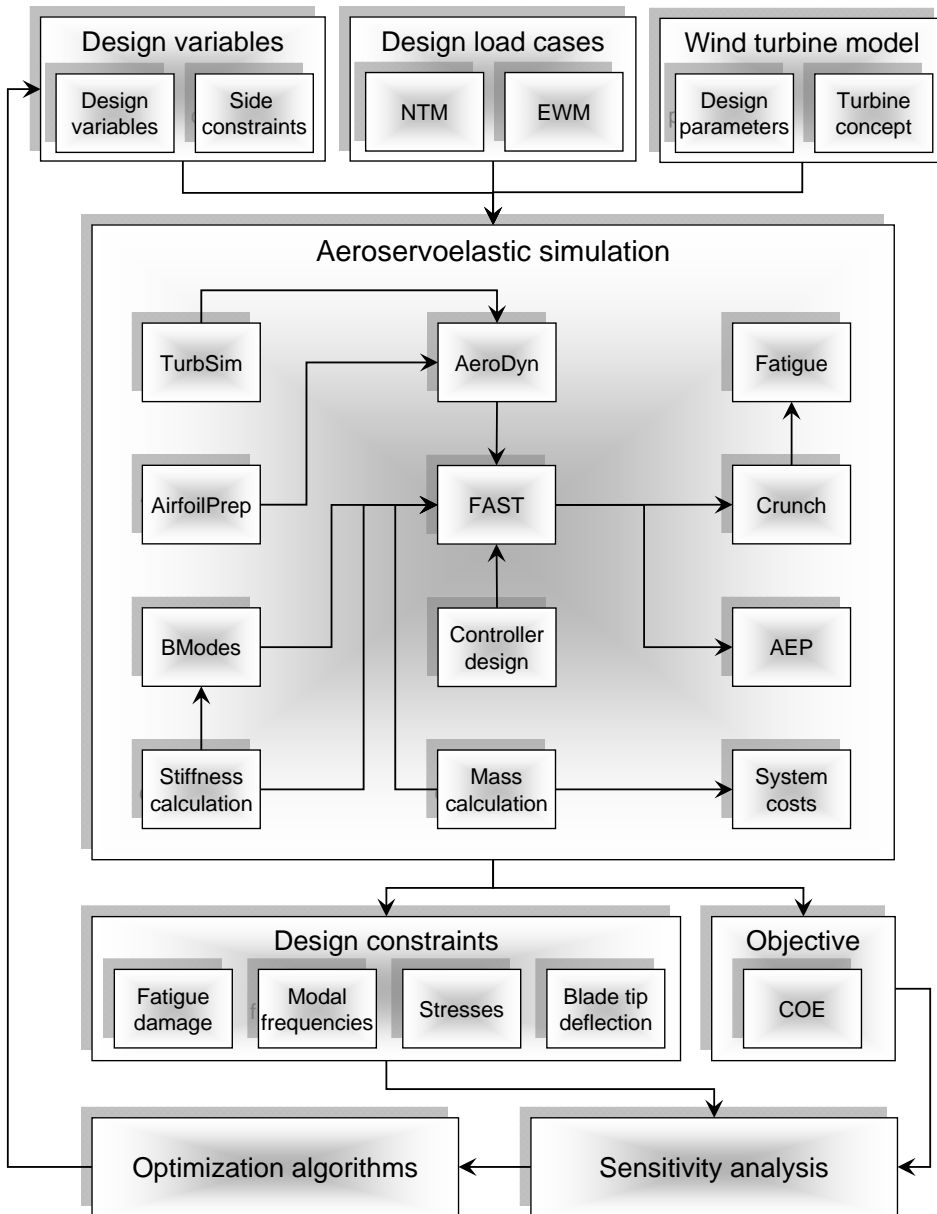


Figure 3.3: Integrated Design Optimization Engine

in the entire working domain of the wind turbine is changing this role.

As the design becomes more integrated with multidisciplinary design optimization, the design problem is changing from how do regulate the power or decrease the loads to how can aerodynamics, structure and active control be optimally combined to build a wind turbine that has the lowest LCOE, while satisfying all the constraints.

In the context of design and design optimization, most of the DOPs do not take the controller design as part of the study from the beginning, and those rare cases that include the controller in the DOP are based on a fixed controller setting that is developed for the initial design, (see for instance [Fuglsang et al. \(2002\)](#), [Hansen et al. \(2005\)](#) and [Xudong et al. \(2009\)](#)). In both cases, the influence of the controller on the objective function and design constraints cannot be evaluated properly. This leads to a system that is not a real optimum.

To properly evaluate the objective function and design constrains, controller design should be part of the DOP and redesigned within every iterations, with its parameters introduced either as design variables in the loop, or as fixed variables being updated in every iteration, [Ashuri et al. \(2010b\)](#). However, this is a challenging problem in an automated DOPs, in which the manual intervention of a designer is not possible in every iteration.

This new methodology enables the shifting of the wind turbine design problems from a single discipline design optimization to a highest level that is aeroservoelastic design optimization. In this way, control design is also becoming a part of the optimization process and updated in every iteration.

The implemented controller design contains three control algorithms, a torque controller for below rated region and the transition part, a pitch controller for the above rated region, and a tower top motion feedback loop to correct the relative wind velocity that the rotor experiences due to the flexibility of the tower.

For below rated region, the generator torque is assumed to be proportional to the square of the filtered generator speed. For above rated region, the periodic steady state operating points are found and the system is linearized around these steady state operating points. Based on this linearized model, the above rated pitch controller can be designed. Then the controller parameters are updated and provided as a DLL (Dynamic Link Library) file for every iteration of the DOP

To find out the usefulness of this methodology and its positive influence in a MDO, it is applied on the 5 MW NREL wind turbine DOP. To do that, as a case study two different optimization scenarios are defined. However, to ease the readability and avoid presenting unnecessary information, these two case studies are explained in detail in appendix C and not presented here.

In the following subsections, different aspects and features of controller design automation are presented.

3.9.1 Wind turbine models for designing the controller

The model of the entire wind turbine is structured as several interconnected subsystem models, and represented by a block diagram shown in figure 3.4. The block diagram consists of a wind model, an aerodynamic model, a mechanical model of the drive train and a control block model for the generator torque controller, tower top motion controller,

and the blade pitch controller. These models are explained as follow:

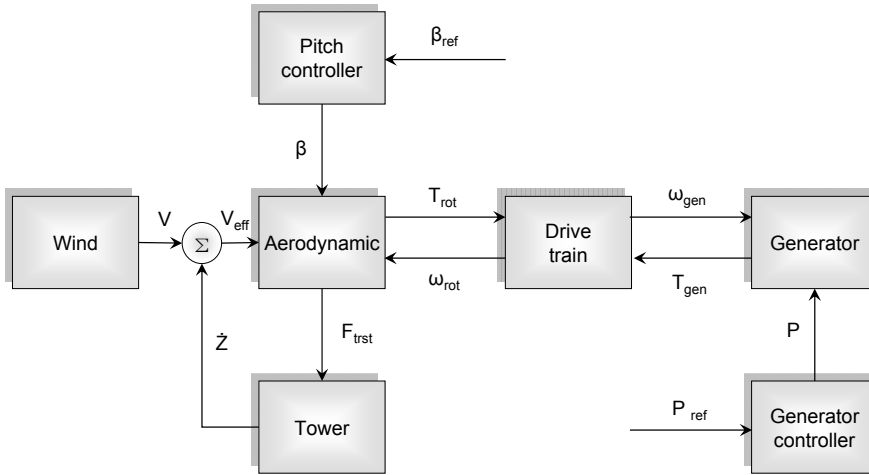


Figure 3.4: Subsystem block diagram of the wind turbine

Wind model

The simulation tool to model the physics of the wind is TurbSim and it is described in detail in appendix B. The main advantage of this model is its flexibility to model a wide range of problems; from a simple stationary hub wind model to more complex situations. Because of the changes of wind turbine design variables that influence the rated wind speed during the optimization process, the simple hub wind model is used to find the rated wind speed. For the rest of the control design task a wind model on the rotor plane with a turbulence wind is implemented.

Aerodynamic model

The aerodynamic model transfers the three-dimensional wind speed field into forces on the blades. The aerodynamic model that is used for the control design task is AeroDyn and it is explained in appendix B. For the controller design task, it was observed that a frozen-wake assumption, in which the induced wake velocities are held constant during the perturbation of the blade-pitch angle, gives a more accurate linearization for heavily loaded rotors at wind speeds close to rated.

Mechanical model of the drive train

The mechanical model transfers the aerodynamic torque on the blades to the generator shaft. It consists of the rotor, the gearbox and the mechanical parts of the generator. Only for the purpose of calculating the gains of the blade pitch controller, a one-mass model with an equivalent mass moment of inertia, stiffness and damping properties of the drive train is used (as it will be explained later in this section, the linearization of the wind turbine at different operating points is carried out in FAST that is a wind turbine aeroelastic code).

The mass moment of inertia of the high and low speed shafts and the gearbox wheels are neglected, since they are very small compared with the huge mass moment of inertia of the rotor and generator. Using this model, the shaft rotation is the only degree of freedom of drive train. Thus, for such a model the equation of motion can be described by:

$$T_{rot} - Z_{gb} \cdot T_{gen} = I_{dr} \cdot \ddot{\omega} \quad (3.8)$$

Where:

T_{rot} Rotor torque, ($N \cdot m$)

Z_{gb} Gear box ratio, (-)

T_{gen} Generator torque, ($N \cdot m$)

I_{dr} Drive train mass moment of inertia ($I_{dr} = I_{rot} + Z_{gb}^2 \cdot I_{gen}$) in ($kg \cdot m^2$)
with: I_{rot} as the rotor mass moment of inertia and I_{gen} as the generator mass moment of inertia

$\ddot{\omega}$ Rotational acceleration of the drive train, ($\frac{rev}{min^2}$)

3.9.2 Control model of the generator torque controller

As figure 3.5 shows, the generator torque controller consists of five different regions. In region 1, which is below the cut-in wind speed, the generator torque is zero and the kinetic energy in the wind is used to accelerate the rotor for the startup.

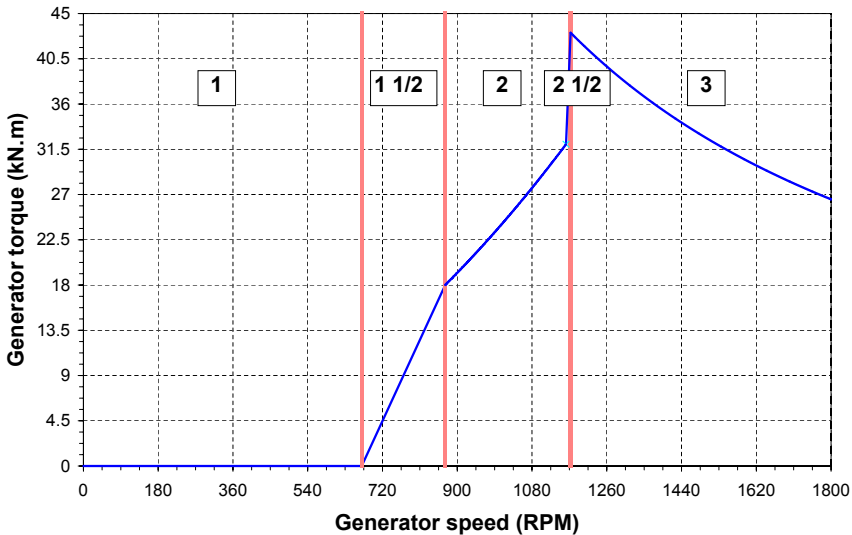


Figure 3.5: Generator-torque controller of the 5 MW wind turbine in different regions

Region 2 is the power production region, in which the generator torque is assumed

to be proportional to the square of the filtered generator speed to keep a constant (theoretically optimal) tip-speed ratio. That is:

$$T_{gen} = K_g \cdot \omega_{gen}^2 \quad (3.9)$$

with K_g as the generator torque proportionality factor.

In region 3, the generator torque changes inversely with generator speed to keep a constant power output. Region $1\frac{1}{2}$ is a linear transition between region 1 and 2. Also in region $2\frac{1}{2}$ a linear transition between region 2 and 3 occurs, in which its slope is equal to the slip of an induction generator.

3.9.3 Control model of the blade pitch controller

In full load region, the control objective is to maintain the power production constant. As the result, the generator torque becomes inversely proportional to the generator speed:

$$T_{gen}(Z_{gb}, \omega) = \frac{P}{Z_{gb} \cdot \omega} \quad (3.10)$$

Also for the rotor in full load region we have:

$$T_{rot}(\omega) = \frac{P}{\omega} \quad (3.11)$$

Using Taylor series and expanding equation 3.10 around the rotational DOF of the drive train ω , where $\omega = \omega_{rat} + \Delta\omega$ (note that $\Delta\omega$ is the rotational speed difference between the actual, ω , and rated value, ω_{rat}), and neglecting the second and higher order terms result in:

$$T_{gen} \simeq \frac{P_{rat}}{Z_{gb} \omega_{rat}} - \frac{P_{rat}}{Z_{gb} \omega_{rat}^2} \cdot \Delta\omega \quad (3.12)$$

Similarly, expanding equation 3.11 around blade pitch angle β and neglecting the second and higher order terms, we have:

$$T_{rot} \simeq \frac{P_{rat}}{\omega_{rat}} + \left(\frac{1}{\omega_{rat}} \right) \cdot \left(\frac{\partial P}{\partial \beta} \right) \cdot \Delta\beta \quad (3.13)$$

The small perturbation in rotor speed ($\Delta\omega$), and blade pitch angle ($\Delta\beta$) can be correlated with a *PID* controller as follow:

$$\Delta\beta = K_P \cdot Z_{gb} \cdot \Delta\omega + K_I \cdot Z_{gb} \cdot \int_0^t \Delta\omega \cdot dt + K_D \cdot Z_{gb} \cdot \dot{\Delta\omega} \quad (3.14)$$

Where:

K_P Proportional gain, $\left(\frac{deg}{rpm} \right)$

K_I Integral gain, $\left(\frac{s}{rpm} \right)$

K_D Derivative gain, $\left(\frac{rpm}{deg} \right)$

Replacing $\Delta\beta$ from equation 3.14 into equation 3.13, and substituting the resultant equation together with equation 3.12 into equation 3.8, and setting $\Delta\omega = \phi$ and rearranging all the terms results in:

$$\begin{aligned} & \underbrace{\left[I_{dr} + \left(\frac{Z_{gb}}{\omega_{rat}} \right) \cdot \left(-\frac{\partial P}{\partial \beta} \right) \cdot K_D \right]}_I \ddot{\phi} + \\ & \underbrace{\left[\left(\frac{Z_{gb}}{\omega_{rat}} \right) \cdot \left(-\frac{\partial P}{\partial \beta} \right) \cdot K_p - \frac{P_{rat}}{\omega_{rat}^2} \right]}_D \dot{\phi} + \\ & \underbrace{\left[\left(\frac{Z_{gb}}{\omega_{rat}} \right) \cdot \left(-\frac{\partial P}{\partial \beta} \right) \cdot K_I \right]}_K \phi = 0 \end{aligned} \quad (3.15)$$

However, experience shows that a satisfactory response can be obtained by choosing a *PI* controller instead of a *PID*. Therefore, the *D* controller is ignored in this research. The *PI* controller also has been used with success in many research wind turbines such as the Nibe B and Tjareborg wind turbines.

In equation 3.15, the *I*, *D* and *K* denote the system's inertia, damping and stiffness, respectively. Making the assumption that the dynamic characteristic of equation 3.15 behaves as a second order system as it is shown in equation 3.16:

$$\frac{K_{dr}}{I_{dr} \cdot S^2 + D_{dr} \cdot S + K_{dr}} = \frac{\omega_{\phi n}^2}{S^2 + 2 \cdot \xi_{\phi} \cdot S + \omega_{\phi n}^2} \quad (3.16)$$

Then, the natural frequency ($\omega_{\phi n}$), and the damping ratio (ξ_{ϕ}) of such a system can be found by:

$$\omega_{\phi n} = \sqrt{\frac{K_{dr}}{I_{dr}}} \quad (3.17)$$

and:

$$\xi_{\phi} = \frac{D_{dr}}{2 \cdot I_{dr} \cdot \omega_{\phi n}} \quad (3.18)$$

It is known from the literature that for the transient response analysis of equation 3.15, the proportional gain K_p , is proportional to the damping D_{dr} , of the system. Also the integral gain K_I , is proportional to the stiffness K_{dr} of the system, and similarly the derivative term K_D , is proportional to the inertia I_{dr} of the system. Using this definition the *PI* terms used for this work can be expressed as:

$$K_p(\beta) = \frac{2 \cdot I_{dr} \cdot \omega_{rat} \cdot \xi_{\phi} \cdot \omega_{\phi n}}{Z_{gb} \cdot \left(-\frac{\partial P}{\partial \beta} \right)} \quad (3.19)$$

and:

$$K_I(\beta) = \frac{I_{dr} \cdot \omega_{rat} \cdot \omega_{\phi n}^2}{Z_{gb} \cdot \left(-\frac{\partial P}{\partial \beta}\right)} \quad (3.20)$$

Where $\frac{\partial P}{\partial \beta}$ is the aerodynamic power sensitivity to the blade pitch angle.

Notice that when this parametrization is used, the *PI* control parameters show a dependency to the variation of $\left(-\frac{\partial P}{\partial \beta}\right)$ at different operating points in the full load region.

This derivative, $\left(-\frac{\partial P}{\partial \beta}\right)$, can be obtained by doing a sensitivity analysis of the aerodynamic power of the rotor to the blade pitch angle at different wind speeds above the rated. It is calculated by doing a central finite difference method with a small perturbation of the pitch angle to each side, and using a frozen wake assumption for the induced velocities as mentioned before.

The calculated power sensitivity to the blade pitch angle shows a large variation with wind speed (proportionally increasing with higher winds with a negative sign), so constant values of gains do not yield the desired results. However, this large variation of the power sensitivity to the wind speed shows nearly a linear relation with blade-pitch angle (see figure C.1), and the equation of this line is as follow:

$$\frac{\partial P}{\partial \beta} = \left[\frac{\frac{\partial P}{\partial \beta_{\beta=rat}}}{\beta_k} \right] \beta + \frac{\partial P}{\partial \beta_{\beta=rat}} \quad (3.21)$$

Where β_{rat} is the blade pitch angle at rated, and β_k is the blade pitch angle at which the aerodynamic power sensitivity is doubled from its value at the rated. That is:

$$\frac{\partial P}{\partial \beta_k} = 2 * \frac{\partial P}{\partial \beta_{rat}} \quad (3.22)$$

Replacing equation 3.22 into equation 3.21, and substituting that into equation 3.19 and 3.20 results in a closed form solution of the gains as follow:

$$K_P(\beta) = \frac{2 \cdot I_{dr} \cdot \omega_{rat} \cdot \xi_{\phi} \cdot \omega_{\phi n}}{Z_{gb} \cdot \left(-\frac{\partial P}{\partial \beta_{rat}}\right)} \cdot (G_{\beta}) \quad (3.23)$$

and:

$$K_I(\beta) = \frac{I_{dr} \cdot \omega_{rat} \cdot \omega_{\phi n}^2}{Z_{gb} \cdot \left(-\frac{\partial P}{\partial \beta_{rat}}\right)} \cdot (G_{\beta}) \quad (3.24)$$

where G_{β} is the dimensionless gain-correction factor that is dependent on the blade pitch angle:

$$G_{\beta} = \left(\frac{1}{1 + \frac{\beta}{\beta_k}} \right) \quad (3.25)$$

3.9.4 Tower top motion feedback loop

To find the optimum value of the design variables, the optimizer needs to search the design space. As a result, in many iterations the tower natural frequency gets close to the $1P$ rotation of the rotor, and the wind turbine experiences substantial tower motion parallel to the wind direction resulting in fatigue damage. A tower top feedback controller is used to minimize this phenomenon during the optimization iterations, with the tower top acceleration as an input to the pitch demand controller.

While such a controller can minimize the tower top motion, beyond a certain limit it acts as a cyclic wind speed input to the rotor and results in rotor speed oscillation. This rotor speed oscillation in turn causes a pitch oscillation. Finding the best trade off between tower fatigue damage reduction and pitch oscillation reduction is a matter of trial and error with many simulations and tuning involved prior to optimization iterations.

To design the tower feedback loop, the tower dynamic is represented as a second order system with a transfer function from rotor thrust to tower top velocity as presented in equation 3.26. This is to simplify the tower dynamic by representing its behavior as a transfer function that only contains the first mode properties (damping and natural frequency). Such a representation works for the first mode properly and for higher modes it becomes less effective.

$$T(S) = \frac{\left(\frac{1}{K_t}\right) \cdot S}{\frac{S^2}{\omega_{tn}^2} + \frac{2 \cdot \xi_t \cdot S}{\omega_{tn}} + \omega_{tn}^2} \quad (3.26)$$

Where K_t is the tower stiffness, ξ_t is the tower structural damping with a fixed value of 4% and ω_{tn} is the tower natural frequency.

Figure 3.6 shows the control flow diagram for the speed controller, including the tower acceleration as an input to the pitch demand controller. In this figure Q is the rotor thrust, T the rotor torque, \dot{Z} tower top velocity and \ddot{Z} tower top acceleration.

3.9.5 Controller design and implementation

In this research a conventional variable-speed, variable blade-pitch-to-feather controller is selected. In such a configuration the strategy to control the power-production operation and load reduction is based on the design of three separable control systems:

- A generator torque controller for partial and transition load region
- A full-span rotor-collective blade-pitch controller for the full load region
- A tower top motion feedback controller to account the flexibility of the tower in both above mentioned controllers.

Generator-torque controller

Maximization of power production in partial load region is the most logical strategy for the generator torque controller. As discussed in many research papers (see Johnson et al. (2004)), variable speed operation results in a higher energy capture than constant

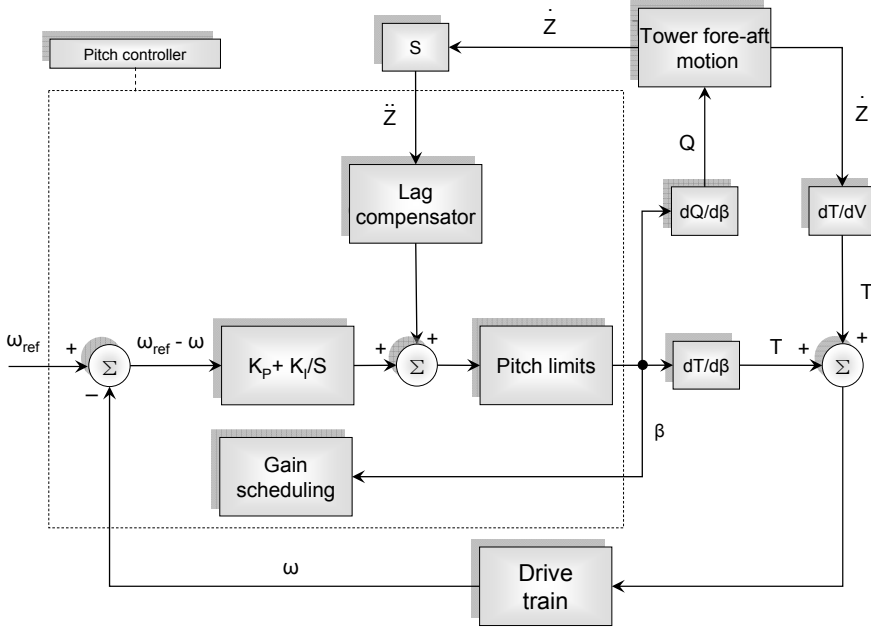


Figure 3.6: Controller flow diagram with tower acceleration feedback

speed. Therefore, a variable speed controller is also used here. The aim of the controller is to find a value of K_g such that it maximizes the energy capture.

As discussed before, the generator torque is proportional to the square of generator speed below rated, then constant (or very slowly changing) above the rated generator speed. This enables operation at a constant tip speed ratio below rated as long as the blade pitch remains constant. Thus, the generator torque characteristics must be matched to the rotor torque in order to actually achieve this constant tip speed ratio operation.

At above rated region, the system power output changes only in proportion to rotor speed, since the torque should remain almost constant, and power regulation is mainly dependent on speed regulation.

Blade-pitch controller

The goal of the blade-pitch controller is to regulate the generator speed above the rated operating point. The blade-pitch controller is designed using a gain scheduled *PI* controller. The error between the filtered generator speed and the rated generator speed is used as the input for the *PI* controller. The output of this *PI* controller is the reference pitch angle for the pitch actuator system.

The pitch demand is also limited to a minimum of 0° and a maximum of 90° . The minimum is the pitch angle at which the optimum rotor aerodynamic performance is achieved when operating at constant tip speed ratio in below rated region. When the rotor speed is less than the desired setpoint, the pitch remains fixed at its minimum value.

The single DOF model of subsection 3.9.2 is used to obtain the proportional, K_p , and integral, K_I gains. However, due to the nonlinear characteristics of the aerodynamic forces that change during different operating conditions, the K_p and K_I gains are scheduled as functions of the aerodynamic power sensitivity to the pitch angle.

In addition, because of the changes of blade design variables in the DOP, the value of the rated wind speed needs to be recalculated in each iteration. This is done using a time domain simulation with a steady wind at the hub height (the wind hub model).

After finding the rated wind speed, the system is linearized at different wind speeds above the rated wind speed to find the steady state operating points. This process is mainly named as periodic steady state linearization, since it is performed at different blade azimuth angles and then the azimuth averaged values are used to design the pitch-controller (see [Jonkman and Buhl \(2004\)](#), [van Engelen \(2007\)](#)). Using this process, the ω_{rot} - β - V space (with ω_{rot} as rotor rotational speed, β as blade pitch angle and V as the wind velocity), in which the system is in dynamic equilibrium can be mapped, [Bianchi et al. \(2006\)](#).

Based on the mapped values, another linearization is carried out that is mainly named as initial steady state linearization, with previous obtained points as the inputs. In this stage the aerodynamic power sensitivity is calculated using the linearized model with the drive train DOF as the only state variable, blade pitch angle as the system input and the rotor power as the system output.

Since the system has only one state variable, the derivative of the system output to the system input is the aerodynamic power sensitivity to the blade pitch angle, which is equal to the transmission matrix of the linearized system. Based on this strategy and using equation 3.19 and 3.20 the proportional and integral gains are calculated.

Tower top motion feedback controller

To implement the tower controller, the aerodynamic sensitivity of rotor thrust to blade pitch angle $\left(\frac{\partial Q_{rot}}{\partial \beta}\right)$, and the aerodynamic sensitivity of rotor torque to wind speed $\left(\frac{\partial T_{rot}}{\partial V}\right)$ should be calculated. These two sensitivities are obtained using the same technique used to calculate the aerodynamic power sensitivity to blade pitch angle. However, it also should be mentioned that both sensitives have a linear behavior at different operating points.

In addition, a lag compensator is applied for the tower top acceleration to determine a change in pitch in response to the motion. A lag compensator adds gain at the low frequencies. This means larger low frequency gain to reduce the steady-state error. In the context of this research, the lag compensator increases the pitch sensitivity (by adding gain) to reduce the speed oscillation (steady-state error). This compensator is of the form:

$$T_{LC}(S) = \frac{S + \frac{1}{T}}{S + \frac{1}{\kappa T}} \quad (3.27)$$

where $\kappa > 1$ is a parameter, and T is the time scale of tower motion.

During many simulations, it was found that this feedback reduces tower loads slightly, improves speed regulation and prevents the simulations from crashing when the tower natural frequency gets close to 1P. It is obvious that this simplification does not work

perfectly in combination with unsteady aerodynamic effects. Therefore, the tower top motion controller is verified and fine-tuned before level 2 optimization (level 1 and 2 optimization will be discussed later).

However, the selection of the controller concept and all the controller parameters is a matter of experience that tightly depends on how these parameters lower LCOE and influence design constraints. This goal can be achieved by introducing all the controller parameters as design variable in the DOP, however, the computational time becomes more expensive and unpredicted numerical instabilities may occur. Therefore this is not considered as an option (despite having the potential of the developed methodology) in this research due to time restriction.

In addition to the controller design automation, modeling the structural properties of the blade and tower need to be automated. However, the emphasis will be on the blade, since the derivation of its properties is more challenging. This issue is explained in next section.

3.10 Automation of extracting structural properties

The blades of a wind turbine are complex structural components to design. Orthotropic material properties, nonuniform distribution of different materials and the complex shape of the blade are the most important reasons for this complexity.

To model this complexity, usually FE models are employed (see [Malcolm and Laird \(2007\)](#)). These models are of value in investigating the distribution of strains and stresses within the blade, thus suitable for the final design stage. They are very detailed for an aeroelastic or aeroservoelastic design optimization, which in general only requires mass and stiffness distribution along the blade.

To avoid FE models, many design optimization methods use either a linear elastic I -beam model for the blade like [Fuglsang and Madsen \(1999\)](#), or a prescribed mathematical distribution of design variables along the blade like [Benini and Toffolo \(2002\)](#). These models can easily represent the stiffness and mass distribution of the blade, but to ensure their dependability they should be tuned with measurements. Despite their simplicity, model tuning is a challenge, particularly for upscaling studies where there is no data available to do any proper tuning.

This work offers a different methodology that enables the extraction of structural properties of a composite wind turbine blade, while avoiding model tuning. This new methodology is based on an analytical model of the composite blade, [Ashuri et al. \(2010a\)](#).

The method starts with calculating the second area moment of inertia of different structural elements (shear webs, spar caps and shell) of a blade section to cope with the geometrical complexity. Generally, each structural element has a directional property. That is, the elastic constants depend on the orientation. Since each element consists of different materials with different thicknesses, the weighting method is used to find the equivalent directional properties of each section.

Clearly, the complicated nonuniform distribution of materials can be represented by the bulk representation that has equivalent properties as the original. The actual thickness of each element is maintained, since it is used to extract weights. Combining the contribution of different elements, the bending centroid of each section is calculated.

Parallel-axis theorem is used to move each second moment of inertia to the section centroid. Stiffnesses are found by multiplying each element equivalent modulus to its second moment of inertia and integrated over all elements. Mass per unit length of each section is found by the same strategy. That is, the weighting method is applied on the density of each material, and using equivalent density of each element multiplied by its area, the mass per unit length is calculated. Other properties are also calculated in the same manner.

This method is verified with the sectional structural properties of a commercial 660 kW wind turbine blade over 20 stations along the blade. However, to ease the readability and avoid presenting unnecessary information, the verification of this method is presented in appendix D.

3.10.1 The methodology to extract structural properties

In any wind turbine blade design study, structural properties such as area and mass moment of inertia, stiffness, strength, radius of gyration and mass per unit length are needed. These properties are used to calculate the mass of the blade, natural frequencies, deflections, buckling, stresses, fatigue and so on.

This subsection explains how to extract these properties for any arbitrary cross section of the blade. It starts with explaining different sectional definitions and assumptions made for the rest of the work. Then, based on these assumptions different sectional properties relative to the principal axis are calculated. Finally, using a coordinate rotation matrix, these properties can be transformed to any arbitrary plane.

Sectional description and assumptions

Usually a wind turbine blade cross section consists of two parallel shear webs located on any point along the chord, two spar cups atop and under the shear webs and a shell that surrounds the section form leading-edge to the trailing-edge, passing over the spars.

To extract the structural properties for such a section, certain assumptions based on Euler-Bernoulli theory are made, (see [Bauchau and Craig \(2009\)](#) for more background information). These assumptions are as follow:

- The strain is proportional to the distance from the neutral surface
- Deflections remain small
- Plane sections of the beam remain plane an perpendicular to the neutral axis

Sectional properties calculation

Since the cross section of a wind turbine blade consists of several elements like shell and shear webs that have different material properties, the weighting method is used to extract the equivalent properties of each section.

This helps to represent the complicated nonuniform distribution of materials with a gross representation that has equivalent properties as the original (see [Beer et al. \(2006\)](#) for more background information). The actual thickness of each element is maintained, since it is used to extract weights, see figure 3.7.

For instance the equivalent module of elasticity of the shell, $E_{equivalent}^{shell}$, consisting of some $\pm 45^\circ$ layers of composite in top, t_{top}^{shell} , and bottom, t_{bottom}^{shell} , which is filled with a

foam having a modulus of elasticity of E_{foam}^{shell} and thickness of t_{bottom}^{shell} in between (see figure 3.7) can be calculated as:

$$E_{equivalent}^{shell} = \frac{\sum_1^n E_i^{shell} \cdot t_i^{shell}}{\sum_1^n t_{equivalent}^{shell}} \quad (3.28)$$

and the numerator is defined as:

$$\sum_1^n E_i^{shell} \cdot t_i^{shell} = E_{top}^{shell} \cdot t_{top}^{shell} + E_{bottom}^{shell} \cdot t_{bottom}^{shell} + E_{foam}^{shell} \cdot t_{foam}^{shell} \quad (3.29)$$

As it can be seen, the denominator of equation 3.28, which is the total thickness of the shell remains unchanged:

$$\sum_1^n t_{equivalent}^{shell} = t_{top}^{shell} + t_{bottom}^{shell} + t_{foam}^{shell} \quad (3.30)$$

However, the same approach can be used to extract equivalent densities for each element of the cross section, by simply replacing the modulus of elasticity with the density. Section centroids in edgewise, $\bar{X}_c^{section}$, direction is calculated as follow:

$$\bar{X}_c^{section} = \frac{\sum_1^n E_{equivalent}^i \cdot A_{equivalent}^i \cdot \bar{X}_{ci}^i}{\sum_1^n E_{equivalent}^i \cdot A_{equivalent}^i} \quad (3.31)$$

In which the numerator and denominator are defined respectively as:

$$\begin{aligned} \sum_1^n E_{equivalent}^i \cdot A_{equivalent}^i \cdot \bar{X}_{ci}^i &= E_{equivalent}^{shell} \cdot A_{equivalent}^{shell} \cdot \bar{X}_c^{shell} \\ &+ E_{equivalent}^{spar} \cdot A_{equivalent}^{spar} \cdot \bar{X}_c^{spar} \\ &+ E_{equivalent}^{web} \cdot A_{equivalent}^{web} \cdot \bar{X}_c^{web} \end{aligned} \quad (3.32)$$

and:

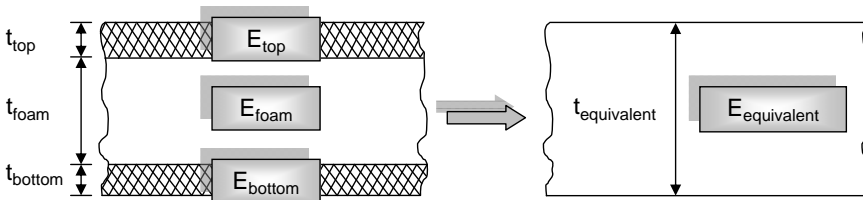


Figure 3.7: Equivalent representation of properties

$$\begin{aligned}
\sum_1^n E_{equivalent}^i \cdot A_{equivalent}^i &= E_{equivalent}^{shell} \cdot A_{equivalent}^{shell} \\
&+ E_{equivalent}^{spar} \cdot A_{equivalent}^{spar} \\
&+ E_{equivalent}^{web} \cdot A_{equivalent}^{web}
\end{aligned} \tag{3.33}$$

and similarly for $\bar{Y}_c^{section}$ we have:

$$\bar{Y}_c^{section} = \frac{\sum_1^n E_{equivalent}^i \cdot A_{equivalent}^i \cdot \bar{Y}_{ci}^i}{\sum_1^n E_{equivalent}^i \cdot A_{equivalent}^i} \tag{3.34}$$

In which the denominator is the same as equation 3.33, and numerator is defined as:

$$\begin{aligned}
\sum_1^n E_{equivalent}^i \cdot A_{equivalent}^i \cdot \bar{Y}_{ci}^i &= E_{equivalent}^{shell} \cdot A_{equivalent}^{shell} \cdot \bar{Y}_c^{shell} \\
&+ E_{equivalent}^{spar} \cdot A_{equivalent}^{spar} \cdot \bar{Y}_c^{spar} \\
&+ E_{equivalent}^{web} \cdot A_{equivalent}^{web} \cdot \bar{Y}_c^{web}
\end{aligned} \tag{3.35}$$

These section centroids are used to transfer the area moments of inertia that are calculated relevant to each element centroids to the section centroids using parallel-axis theorem, which will be explained later in this subsection.

Area moments of inertia can simply be calculated using an integration scheme. In this scheme, the cross section (X, Y) coordinates of the shell, spars and webs are separately used to find the area moment of inertia relevant to their local axis. However, with the same integration scheme, these integrals also need to be calculated for other elements like spar and web. These integrals for the shell are as follow:

$$I_{xx}^{shell} = \int y_{shell}^2 dx dy \tag{3.36}$$

$$I_{yy}^{shell} = \int x_{shell}^2 dx dy \tag{3.37}$$

$$I_{xy}^{shell} = \int x_{shell} y_{shell} dx dy \tag{3.38}$$

Now the calculated area moments of inertia that are calculated relative to their local centroids need to be transferred to the section centroids using the parallel-axis theory, (see [Beer et al. \(2006\)](#)). For the shell, it is as follow (note the difference between shell and SHELL in the equation where shell refers to local centroids and SHELL refers to section centroid):

$$I_{xx}^{SHELL} = I_{xx}^{shell} + A_{shell} \cdot (\bar{X}_c^{shell} - \bar{X}_c^{section})^2 \quad (3.39)$$

$$I_{yy}^{SHELL} = I_{yy}^{shell} + A_{shell} \cdot (\bar{Y}_c^{shell} - \bar{Y}_c^{section})^2 \quad (3.40)$$

$$I_{xy}^{SHELL} = I_{xy}^{shell} + A_{shell} \cdot (\bar{X}_c^{shell} - \bar{X}_c^{section}) \cdot (\bar{Y}_c^{shell} - \bar{Y}_c^{section}) \quad (3.41)$$

These area moments of inertia can be rotated around any arbitrary axis. This is a necessary step to take when one wants to use the in-plane and out-of-plane values instead of flapwise and edgewise and can be done using the following transformation:

$$I_{x'x'}^{SHELL} = \frac{I_{xx}^{SHELL} + I_{yy}^{SHELL}}{2} + \frac{I_{xx}^{SHELL} - I_{yy}^{SHELL}}{2} \cdot \cos 2\theta - I_{xy}^{SHELL} \cdot \sin 2\theta \quad (3.42)$$

$$I_{y'y'}^{SHELL} = \frac{I_{xx}^{SHELL} + I_{yy}^{SHELL}}{2} - \frac{I_{xx}^{SHELL} - I_{yy}^{SHELL}}{2} \cdot \cos 2\theta - I_{xy}^{SHELL} \cdot \sin 2\theta \quad (3.43)$$

$$I_{x'y'}^{SHELL} = \frac{I_{xx}^{SHELL} - I_{yy}^{SHELL}}{2} \cdot \sin 2\theta + I_{xy}^{SHELL} \cdot \cos 2\theta \quad (3.44)$$

Based on the calculated flapwise area moment of inertia around the section centroid and the calculated section equivalent modulus of elasticity in flapwise direction for all different elements, section flapwise stiffness can be calculated using the following equation (using the same strategy, the stiffness in the edgewise direction can also be calculated):

$$\begin{aligned} E_{total}^{section} \cdot I_{xx}^{section} &= E_{equivalent}^{shell} \cdot I_{xx}^{SHELL} \\ &+ E_{equivalent}^{spar} \cdot I_{xx}^{SPAR} \\ &+ E_{equivalent}^{WEB} \cdot I_{xx}^{WEB} \end{aligned} \quad (3.45)$$

To calculate torsional stiffness following replacement in the above equations needs to be done:

- Modulus of elasticity with modulus of rigidity
- Flapwise or edgewise second moment of inertia with polar moment of inertia

Mass distribution calculation along the blade can be simply done as follow:

$$\begin{aligned} \left(\frac{M}{L}\right)_{station} &= \rho_{equivalent}^{shell} \cdot A_{equivalent}^{shell} \\ &+ \rho_{equivalent}^{spar} \cdot A_{equivalent}^{spar} \\ &+ \rho_{equivalent}^{web} \cdot A_{equivalent}^{web} \end{aligned} \quad (3.46)$$

Where ρ is the density of each cross section, and L is the length of each station along the blade. The mass of the blade is calculated by using this equation and knowing the length of each station of the blade in advance as:

$$M_{blade} = \sum_{i=1}^n M_i \cdot L_i \quad (3.47)$$

The same method that is used for the blade can also be used for the tower. However, with the isotropic material property of the tower and its simple geometry, all the above equations can be considerably reduced to some simple equations.

3.11 Wind turbine's model specification

A set of design parameters (airfoil shapes, structural arrangement and materials properties) is selected to be consistent with current commercial wind turbine designs. Using this baseline configuration, the aerodynamics, structural and control designs are carried out. The NREL wind turbine is used as the baseline turbine configuration in this research with the following specifications and assumptions:

- A three bladed, upwind rotor with rigid hub and full-span pitch control
- A maximum tip speed bound of $120 \frac{m}{s}$
- Air density of $1.225 \frac{kg}{m^3}$
- A Rayleigh distribution of wind speed
- A vertical wind shear power exponent of 0.14
- Annual mean wind speed at 90 m height of $8.4 \frac{m}{s}$
- A cut-in wind speed of $4 \frac{m}{s}$
- A cut-out wind speed of $25 \frac{m}{s}$
- A variable speed operation with maximum power coefficient of 0.5

The following subsections describe the design definitions used in this work.

3.11.1 Aerodynamic design definition

Figure 3.2 shows the planform of the blade, with a nonlinear taper from the maximum chord location at station 6 to the blade tip. The circular blade root (station 1) is located at $0.0 \frac{r}{R}$ with R as the blade length. The blade shape is transitioning from a circular cross section in station 1 to a pure airfoil shape at station 6.

Eight different airfoil types are incorporated for the blade. The three innermost airfoil types have a circular cross section with a drag coefficients of 0.50, the next two airfoils have an elliptic cross section with a drag coefficient of 0.35, and no lift. The remaining six airfoils are a combination of Delft University and NACA types.

As it was explained before, AirfoilPrep is used to modify the airfoil properties. First, using the Selig and Eggars methods, the lift and drag coefficients from 0 to 90 degree

angle of attack are corrected for rotational stall delay. Then the drag coefficient is corrected using the Viterna method for 0 to 90 degree angles of attack with an aspect ratio which is varying automatically for every optimization iteration. Finally, the Beddoes-Leishman dynamic-stall hysteresis parameters are estimated.

Table 3.13 shows a summary of the airfoil type and location along the blade.

Table 3.11: *Airfoil shapes and their location along the blade*

Airfoil Type	Spanwise location	Pitch axis
Circular	0.0000	0.500
Circular	0.0195	0.500
Circular	0.0520	0.500
Elliptic	0.0845	0.460
Elliptic	0.1170	0.420
DU00W401	0.1495	0.390
DU00W401	0.1821	0.375
DU00W401	0.2146	0.375
DU00W350	0.2471	0.375
DU00W350	0.2959	0.375
DU97W300	0.3935	0.375
DU91W2250	0.4910	0.375
DU93W210	0.5886	0.375
NACA64618	0.6861	0.375
NACA64618	0.7837	0.375
NACA64618	0.8813	0.375
NACA64618	0.9300	0.375
NACA64618	0.9544	0.375
NACA64618	0.9788	0.375
NACA64618	1.0000	0.375

3.11.2 Structural design definition

The structural elements of the blade consist of two shear webs, two spar caps between the shear webs, and a skin that externally has surrounded the shear webs and the spar caps. This arrangement is depicted in figure 3.8, where the thickest airfoil section (station 6) is shown.

Table 3.12 lists the material type of each element. The CDB340 is a triaxial fabric and has a 25%, 25%, and 50% distribution of $+45^\circ$, -45° , and 0° fibers, respectively. The spar cap is made of triaxial and uniaxial (A260) fabric. This layout results in spar cap laminate with 70% uniaxial and 30% off-axis fibers by weight.

Since the tower is made of steel with isotropic material properties, only a modulus of elasticity of 210 (GPa), a density of 7800 ($\frac{kg}{m^3}$) and a Poisson ratio of 0.3 are needed to define its properties.

Table 3.12: Material type definition of each blade element

Element	Layer No.	Material	Thickness
Skin (Shell)	Layer 1	Gel coat	0.5 (mm)
	Layer 2	Random mat	0.4 (mm)
	Layer 3	CBD340	20% Shell thickness
	Layer 4:		
	From 0% – 15% <i>c</i>	Balsa	60% Shell thickness
	From 15% – 50% <i>c</i>	Spar cap mixture	2 (mm)
	From 50% – 100% <i>c</i>	Balsa	60% Shell thickness
	Layer 5	CBD340	20% Shell thickness
Shear webs	Layer 1	Gel coat	0.2 (mm)
	Layer 2	Random mat	0.4 (mm)
	Layer 3	CBD340	20% Shell thickness
	Layer 4	Balsa	60% Shell thickness
	Layer 5	CBD340	20% Shell thickness
	Layer 6	Random mat	0.4 (mm)
	Layer 7	Gel coat	0.2 (mm)
Spar cap	Layer 1	Fill epoxy	4 (mm)
	Layer 2	A260	100% Spar cap thickness
	Layer 3	Random mat	0.4 (mm)
	Layer 4	Gel coat	0.2 (mm)

For the flexible components of the wind turbine (blade and tower in FAST) these definitions of the material properties are used to calculate the stiffnesses. In addition, a mass model based on [Fingersh et al. \(2006\)](#) is used for all the other components. These mass models are needed for a proper modeling of the aeroservoelastic behavior of the wind turbine and are presented in appendix A.

3.11.3 Definition of the design load cases

As part of the design process and to evaluate the design constraints, a variety of loading conditions that a wind turbine is experiencing in its lifetime must be analyzed. This

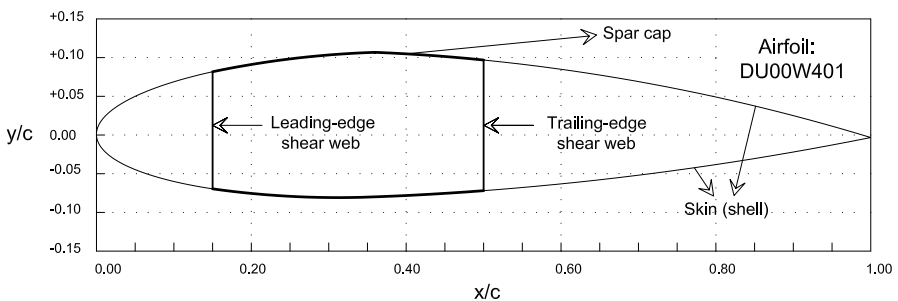
**Figure 3.8:** Layout of the Blade structural model

Table 3.13: Summary of material properties of elements

Material property	CDB340	A260	Spar cap mix.	Balsa	Gel coat	Random mat	Fill epoxy
$E_x(GPa)$	24.2	31.0	27.1	2.07	3.44	9.65	2.76
$E_y(GPa)$	8.97	7.59	8.35	2.07	3.44	9.65	2.76
$G_{xy}(GPa)$	4.97	3.52	4.7	0.14	1.38	3.86	1.10
$\nu_{xy}(-)$	0.39	0.31	0.37	0.22	0.3	0.3	0.3
$\rho(\frac{kg}{m^3})$	1670	1700	1700	130	130	1670	120

forces the designer to verify that the turbine will be able to withstand these loads with a sufficient safety margin. This activity in the design process is standardized by analyzing the wind turbine for a number of relevant load cases prescribed by standard bodies.

In the IEC standard, the external conditions are site dependent and wind turbine classes are defined in terms of wind speed and turbulence parameters at the hub-height with a reference period of 10 min. Three classes of turbulence intensity are defined according to the Normal Turbulence Model (NTM), A (high), B (medium) and C (low).

The GL and DNV rules also use the same classification as IEC uses, however they specify the largest number of loading conditions and are the most complete in defining the design documentation and process, which must be followed to obtain certification of the turbine.

However, all these standards are common in defining a set of three limit state load cases covering operational conditions: normal wind and machine states, normal wind conditions with machine fault states, and extreme wind conditions with normal machine states, [Bossanyi et al. \(2001\)](#).

According to IEC, wind turbines must be designed to resist for a minimum of 20 years against two types of loads, the fatigue and ultimate. The fatigue loading has two components, a periodic deterministic and a stochastic. The periodic deterministic loading is caused either by the rotational associated loads like tower shadow and gravity or the wind associated loads like yaw errors and wind shear. Wind turbulence is the only source of the stochastic loading applied on the wind turbine that causes fatigue. For simple terrains Gaussian statistics of turbulence is used, whereas for more complex terrains non-Gaussian statistics is preferred.

In civilian structures the ultimate load due to the wind occurs at the extreme wind speed. However, for wind turbines the ultimate load is more difficult to predict, but most of the designs assume that the extreme load occurs when the turbine is in parked mode with an Extreme Wind Model (EWM) of a 50-year recurrence.

It is a common practice in the field of wind energy to apply these loads as a design load case (DLC) prescribed by the IEC standard. Therefore, this work also follows the IEC prescription. After checking different DLCs to find those which would likely govern the design, two primary load cases were selected, each representing either fatigue or extreme loading.

For fatigue loads, a normal turbulence model (NTM) during the power production mode is used. This model is applied from the cut-in to cut-out wind speed. For extreme loads, an extreme wind model (EWM) with a 50-year recurrence period with the turbine

in parking condition is used.

This research uses the edition 3 of IEC 61400-1 standard for defining the design load cases (DLC), and based on section 7.4 of this standard, the design load cases used for simulations are defined in table 3.14.

Table 3.14: *Definition of DLCs based on IEC standard*

Design situation	DLC	Wind condition	Type of analysis
Power production	1.2-00	NTM	Fatigue
Parked	6.1	EWM 50-year	Ultimate

EWM: Extreme Wind Model, NTM: Normal Turbulence Model

3.12 Some practical issues about the optimization procedure

There are some issues related to the multidisciplinary design optimization approach in this research that are unique, therefore an explanation for each of them is given in the following subsections:

3.12.1 Reducing the number of design variables

The blade and the tower of a wind turbine are long slender bodies, which require the definition of their properties along their longitudinal axis at several stations. Since this research is unique in the sense of doing a simultaneous design optimization of the blade, tower and rated rotational speed, the number of design variables and constraints are high. This forces another reduction technique to be implemented to further reduce the size of the problem.

Unlike some other design optimization practices that use a prescribed curve fitting technique like Bezier (see [Benini and Toffolo \(2002\)](#) and [Fuglsang and Madsen \(1999\)](#)), to define the design variables at some stations, this research defines the design variables of the blade and tower at some stations along their longitudinal axes and uses an interpolation scheme to find the design variables at all other stations.

The same technique is also used to define the design variables of the tower. Such a setup clearly reduces the definition of design variables, and significantly reduces the computational time. Table 3.1 shows the selected stations for design variables of the blade. For the tower, the design variables are defined at the tower base and top.

3.12.2 The starting point of design variables

"The closer the starting point to the optimum, the faster the optimization convergence". This is a general rule in most of the gradient based optimization algorithms. A starting point that lies outside the feasible design space, not only requires the usage of a different algorithm suitable to work with unfeasible designs, but also will slow the convergence

speed. Therefore, a good estimation of the initial design variables reduces the number of optimization iterations and results in less optimization time.

The developed shell program explained in subsection 3.7.5 uses the 5 MW NREL design as the starting point, and by implementing the linear scaling law described in chapter 2, provides an initial set of design variables for any different size asked by the user. The fundamental relations of this technique are explained in detail in appendix F. Using this technique, all the initial design variables and parameters of the 10 and 20 MW wind turbines are calculated.

3.12.3 Decomposition of design variables

Since this research deals with the simultaneous design optimization of the blade and tower, the number of design variables hence the size of the problem is large. To overcome this problem a size reduction technique should be used. System decomposition is a powerful technique that primarily is involved with dividing the system under study into subsystems. In many multidisciplinary design optimization problems, it is preferable to decompose the system based on the disciplines involved. However by doing so the interaction between the disciplines is lost, which is not desired in this research.

However, system decomposition is a very general technique and can be implemented in different ways. Here, it is used to decompose design variables instead of disciplines. This decomposition results in a multilevel optimization problem. Tower height, blade length and rated rotational speed are the first set of design variables that can change in the first level of system optimization, while keeping all other design variables fixed.

It is also a common practice in the field of wind energy to define and fix them in the conceptual design and then do the preliminary design with other design variables involved. Here, the optimization process runs very fast since there are no design constraints present, and the number of design variables is not too much.

This results in finding a global optimum rather than a local one. This is because of the reduced degree of feedback among all design variables that results in a monotonic change of the selected design variables, which in turn helps the optimizer to not trap in a local optimum.

In the second level, the optimum values of tower height, blade length and rated rotational speed are fixed and all other design variables can change. Again, LCOE is minimized but with all the design constraints involved. This process continues until the point where the specified convergence is satisfied.

Contrary to level one, there is no need to generate a 3D turbulence wind field in level two in every iteration, which saves a considerable amount of time. This is because of a fixed blade length and tower height in level two that does not need a different wind grid size and height in each iteration and once it is generated it can be used until the end of process. This is one of the main advantages of the multilevel approach implemented in this work, which saves a huge amount of computational time in the optimization process.

The multilevel approach is explained in the next subsection.

3.12.4 Multilevel optimization approach

As figure 3.9 shows, the design optimization process is done in a multilevel approach. In the first level, the blade length, tower height and rated rotational speed are optimized,

while all other design variables are fixed. From the list of functional constraints of table 3.3, only item 37 that is the blade tip speed is involved. Form the side constraints, a lower and upper limit is applied on the design variables mentioned before, however, since they are size dependent they will be explained in the subsequent chapters. This setup results in an optimization problem with one objective function (LCOE), one functional constraint, three side constraints, and three design variables.

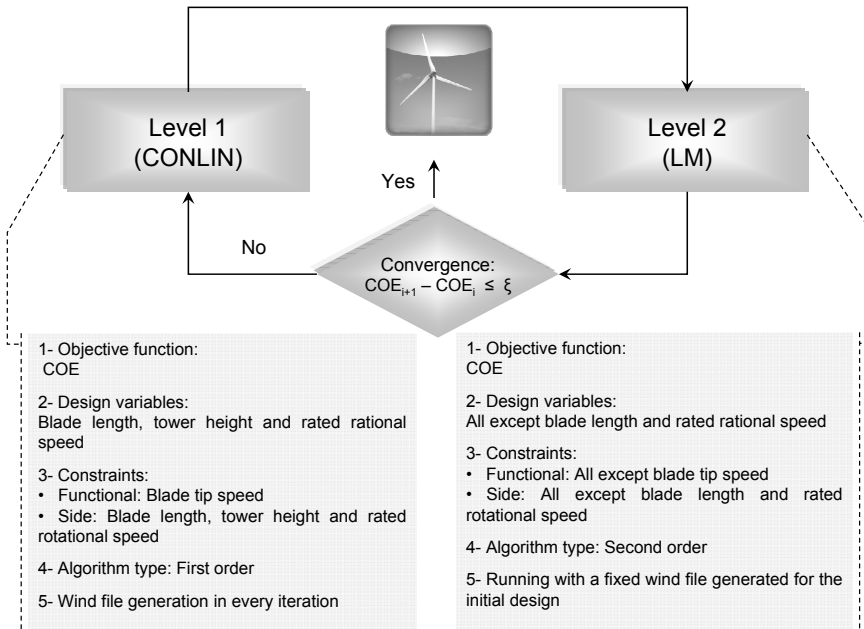


Figure 3.9: Multilevel optimization of the wind turbine

After finding the optimum values of the blade length, tower height and rated rotational speed, the second level of optimization takes place. In the second level, the blade length, tower height and rated rotational speed are fixed and all other design variables are varying. Here, all the functional and side constraints (except item 37 of table 3.3) are involved and the optimization problem has one objective function, 20 design variables and 50 design constraints.

Because of an expensive objective function and design constraints evaluation time, gradient based algorithms are the best options. However, the nature of the problem in level one is totally different from level two.

In the first level, since each radial position along the blade where the chord and twist are defined changes with blade length, the information between each iteration is not consistent and the gradient based algorithm must be first order (the same thing holds true for the tower). A first order algorithm does not use the information from a previous iteration, which is a useful feature for shape optimization problems.

For the first level Convex linearization (CONLIN) is used, which is a first order al-

gorithm, [Fleury \(1989\)](#). For the second level of the optimization process, the blade length and tower height are fixed and the topology of the blade does not change from one iteration to another. Therefore, Lagrange Multiplier (LM) is used, which is a second order algorithm, [Birgin and Martinez \(2008\)](#). A brief explanation of each algorithm and the settings used for this research are given in appendix [E](#).

The level one and two optimization process is carried out sequentially in a loop, until an acceptable convergence on the objective function is achieved. However it was found that for all different scales only after 3 iterations of a multilevel optimization the convergence on objective function is achieved and no further optimization is needed.

3.13 Concluding remarks

The approach of this research justifies the purpose of upscaling in the following ways:

- Assessing the technical feasibility of large wind turbines

To examine the technical feasibility of a wind turbine, the design constraints that can appear as a barrier to the design need to be considered. This will be achieved by evaluating fatigue, stresses, blade-tower clearance, natural frequencies and aeroelastic instability (as will be explained in the following chapters) as the main driving constraints on the blade and tower.

Blades and tower are the most dynamic and flexible components of a wind turbine. Their design is more challenging as the size increases and thereby considered for upscaling study of this research.

- Characterizing the economy of large wind turbines

To show how the design can benefit from upscaling and characterize it, a trade off between what can be gained (AEP), and what should be paid (cost elements) is essential. This is achievable by introducing the LCOE as the objective function of the design to be optimized. This enables the evaluation of the cost elements and the AEP at the same time, and the trade off between them defines the overall economy of large wind turbines.

It should be mentioned that an accurate estimation of the AEP requires all the influencing variables to be introduced in the design. This includes tower height, blade chord and twist, rotor diameter and rated rotational speed. Therefore, the focus on optimizing the blade and tower (as well as the rated rotational speed) has another strong supportive argument; making an accurate calculation of the AEP needed to address the economical feature.

- Developing size specific optimized wind turbines to construct scaling trends

The main drawback of the classical upscaling methods is the limitation in realizing size specific optimized wind turbines. Using the methodology of this research, size specific optimized wind turbines can be developed. This is achievable by formulating the upscaling research of this work as an MDO. Through the use of the mass models fed with the optimized design variables and the optimized design variables themselves, large future offshore wind turbines can be realized.

These optimized wind turbines will be used to construct reliable scaling trends us-

ing a consistent design concept and design assumptions. Therefore, the constructed trends based on these designs have the least data spread and can identify truly the design changes as size increases.

Verification of the integrated aeroservoelastic optimization method

4.1 Introduction

Using the developed design methodology of the previous chapter, the design optimization of the 5 MW NREL wind turbine is carried out in this chapter. This is to validate the implementation of the developed design methodology, and illustrate the power of the MDO for wind turbine design applications.

The objective of the MDO is to minimize the LCOE, which is calculated from the AEP and the system costs. The design variables of the blade are: chord, twist, thicknesses at different stations along the blade, and rated rotational speed. For the tower, diameter and thickness at different stations along the tower, and the tower height are the design variables. Design constraints are fatigue, stresses and natural frequencies of the blade and tower, as well as the tower clearance.

Using this design optimization model, the 5 MW NREL wind turbine is optimized and the results of the original and the optimized wind turbine are compared. The optimized 5 MW design of this chapter also serves as the starting point to make trends for larger scales. The same methodology of this chapter is used in the next chapter to design 10 and 20 MW wind turbines.

4.2 Purpose of the design optimization of the NREL wind turbine

There are three main purposes to optimize the 5 MW NREL wind turbine as follow:

1. **Validating the integrated aeroservoelastic optimization method** Making an optimized 5 MW wind turbine can validate the integrated aeroservoelastic design

approach by offering a better design solution than the NREL wind turbine that is based on a conventional design approach relying mainly on a team of experts and engineering judgments.

2. **Improved understanding of the 5 MW wind turbine design** By making use of the integrated design methodology, an improved understanding of the underlying principles and assumptions of designing the NREL wind turbine can be achieved. This will be done by evaluating the design constraints and the objective function of this machine and exploring the boundaries of its design space.
3. **Providing consistent data points to make scaling trends** The optimized 5 MW wind turbine provides the first point of the trends toward larger scales. This design will be in consistency with the 10 and 20 MW wind turbines that will be developed later, since the same design criteria and assumptions are used to develop all these wind turbines.

With these particular intentions in mind, the novel integrated aeroservoelastic design optimization approach is followed, and the results are presented in the following sections.

4.3 MDO of the 5 MW wind turbine

In this section, the concept of integrated aeroservoelastic design optimization is used to optimize the 5 MW NREL wind turbine. For conciseness, only important results are presented. Some of these results are used at the end of this chapter to validate the methodology.

4.3.1 The 5MW NREL wind turbine

As mentioned in the previous chapter, the NREL wind turbine is a wind turbine most widely used nowadays both in onshore and offshore wind energy research studies. For the purposes of the present work, this concept is then regarded as the base case, and the optimized version of this turbine is employed for the upscaling studies.

The optimized 5 MW, and the 10 and 20 MW wind turbines have the same conceptual design as the original 5 MW NREL wind turbine, proposed by [Jonkman et al. \(2009\)](#). The NREL 5 MW wind turbine is a 3 bladed, upwind, variable-speed, pitch-controlled machine with a Doubly Fed Induction Generator (DFIG) and a gearbox. Its main characteristics are shown in table 4.1.

It should be noted that blades of the 5 MW NREL wind turbine are made from Carbon Fibre Reinforced Plastics (CFRP). However, in this research Glass Fibre Reinforced Plastics (GFRP) is used as the material of the blade. The main reason for not using CFRP in this research is the uncertainties in defining representative carbon fibre structural properties (especially the S-N curve), while these properties are well known for GFRP that are used for many years in the wind turbine industry.

Thus, this machine is used in the MDO of this work and the design variable, design constraints and objective function are presented in the next subsection. The properties of

Table 4.1: *Baseline 5 MW NREL offshore gross properties*

Design specification	Value (Unit)
Rated power	5 (MW)
Rotor, hub diameter	126, 3 (m)
Rotor orientation, configuration	Upwind, 3 bladed (-)
Hub height, overhang	90, 5 (m)
Cut-in, rated and cut-out wind speed	3, 11.4, 25 ($\frac{m}{s}$)
Cut-in and rated rotor speed	6.9 and 12.1 (RPM)
Rated tip-speed	80 ($\frac{m}{s}$)
Shaft tilt, precone	5, 2.5 (deg)
Rotor, nacelle, tower mass	110, 240, 347.46 (ton)
Control strategy	Variable-speed, collective pitch (-)
Peak power coefficient	0.482 (-)
Blade-pitch angle at peak power	0.0 (deg)
Rated mechanical power	5.297 (MW)
Rated generator torque	43.093 (kN.m)
Generator slip in transition region	10 (%)
Maximum blade pitch rate	8 ($\frac{deg}{s}$)

the optimized 5 MW wind turbine are presented in appendix G.

4.3.2 Design variables of the optimized 5 MW wind turbine

As mentioned in subsection 3.7.2, two types of design constraints are considered in this work; side and functional constraints. While all the side constraints that are applied on the design variables are scale dependent, only some of the functional constraints are so.

Table 4.2 shows all the design variables used for the MDO of the 5 MW wind turbine, with their related lower and upper limits appearing as side constraints in level 1 or 2 of the optimization process, as well as the final achieved optimum.

4.3.3 Design constraints of the optimized 5 MW wind turbine

The design space in which the optimizer searches for the optimum design variables is highly constrained with 51 functional constraints as presented in subsection 3.7.2 of chapter 3. Therefore, only those that have the highest active value are presented in this work. For the blade, these active design constraints are the tip deflection and natural frequency. For the tower, fatigue is the highest design constraint. Table 4.3 shows these constraints for both the blade and tower at the optimized values of the design variables.

As the table shows, the flapwise deflection of the blade reaches a maximum at values close to the rated wind speed. This peak is due to the high loads that a variable-speed, pitch-regulated wind turbine experiences at the rated wind speed and as the blade pitches above the rated operational point the loads on the blade decrease.

Also what is not shown in this table is the blade mass. As explained before the 5 MW NREL blade has CFRP in its construction. CFRP has a higher stiffness to density ratio, which means for the same stiffness as a Glass Fiber Reinforced Plastics (GFRP), it weighs

Table 4.2: *optimized 5 MW wind turbine design variables and side constraints*

Description	Opt. level	Min	Optimum	Max
Blade length (m)	1	56.0	63.5	65.0
Tower height (m)	1	78.5	80.0	95.0
Rated rotational speed (rpm)	1	10.5	12.9	13.4
Twist at station 9 (deg)	2	9.0	10.4	14.0
Twist at station 15 (deg)	2	1.0	3.0	4.0
Chord at station 3 (m)	2	3.0	3.1	4.0
Chord at station 7 (m)	2	4.0	5.3	5.5
Chord at station 15 (m)	2	2.1	3.0	3.0
Chord at station 18 (m)	2	1.3	1.5	2.3
Skin thickness at station 1 (cm)	2	8.0	10.0	14.0
Skin thickness at station 3 (cm)	2	5.0	6.0	10.0
Skin thickness at station 6 (cm)	2	2.0	2.3	5.0
Skin thickness at station 16 (cm)	2	1.0	1.5	4.0
Web thickness at station 3 (cm)	2	1.0	1.0	5.0
Web thickness at station 6 (cm)	2	2.0	2.0	4.0
Web thickness at station 16 (cm)	2	1.0	1.3	3.0
Spar thickness at station 3 (cm)	2	1.0	1.0	4.0
Spar thickness at station 6 (cm)	2	1.0	2.5	4.0
Spar thickness at station 16 (cm)	2	1.0	2.4	4.0
Tower diameter at station 1 (m)	2	4.0	6.0	7.0
Tower diameter at station 22 (m)	2	3.0	4.1	5.0
Tower thickness at station 1 (cm)	2	4.0	4.0	6.0
Tower thickness at station 22 (cm)	2	2.0	2.4	5.0

less. This explains why a blade of the 5 MW NREL wind turbine weighs only 17740 kg, compared to 22851 kg for the optimized design made from GFRP.

4.3.4 Objective function of the optimized 5 MW wind turbine

LCOE is the objective function of the design process and the derivation of that was explained in detail in chapter 3. The calculated LCOE of the 5 MW NREL wind turbine using the cost functions of this research is $0.0658 \frac{USD}{kW \cdot hr}$, while this value for the optimized wind turbine is $0.0630 \frac{USD}{kW \cdot hr}$, which shows 4.2% reduction.

Table 4.4 shows the cost comparison of the NREL and the optimized 5 MW wind turbines. All the cost elements in this table are in 1000 USD.

As the table shows, the blades of the 5 MW NREL wind turbine are more expensive, since they are made from Carbon Fiber Reinforced Plastics (CFRP). Also, there are several cost elements with same cost for both wind turbines. These cost elements are a function of rated power output, and since both wind turbines have the same rated power, the associated costs are the same.

Table 4.3: *Optimized 5 MW wind turbine functional constraints*

Description	Opt. level	bound	Optimum
Max blade deflection at $9 \frac{m}{s}$	2	$\leq 5.6(m)$	4.5 (m)
Max blade deflection at $11 \frac{m}{s}$	2	$\leq 5.6(m)$	4.6 (m)
Max blade deflection at $13 \frac{m}{s}$	2	$\leq 5.6(m)$	4.4 (m)
Max blade deflection at $15 \frac{m}{s}$	2	$\leq 5.6(m)$	4.3 (m)
Max blade deflection at $17 \frac{m}{s}$	2	$\leq 5.6(m)$	3.7 (m)
Max blade deflection at $19 \frac{m}{s}$	2	$\leq 5.6(m)$	3.2 (m)
Max blade deflection at $21 \frac{m}{s}$	2	$\leq 5.6(m)$	2.9 (m)
Max blade deflection at $23 \frac{m}{s}$	2	$\leq 5.6(m)$	2.9 (m)
Max blade deflection at $25 \frac{m}{s}$	2	$\leq 5.6(m)$	2.8 (m)
1 st blade's nat. freq. (Hz)	2	≤ 0.7	0.70
2 nd blade's nat. freq. (Hz)	2	≤ 0.7	0.90
3 rd blade's nat. freq. (Hz)	2	≤ 0.7	2.2
Fatigue at station 1 of the tower	2	≤ 0.7	0.66
Fatigue at station 5 of the tower	2	≤ 0.7	0.52
Fatigue at station 9 of the tower	2	≤ 0.7	0.33
Fatigue at station 13 of the tower	2	≤ 0.7	0.18
Fatigue at station 17 of the tower	2	≤ 0.7	0.10
Fatigue at station 21 of the tower	2	≤ 0.7	0.40

4.3.5 Computational Expense

The computational expense of performing optimization in level 1 and 2 is different. This is due to different number of design variables and constraints as well as differences in function evaluation. Level 1 optimization takes approximately 50 CPU hours using a standard HP400 workstation and generally requires 10 to 14 iteration to meet the design requirements (please refer to appendix E for the list of design requirements). In this level, about 65% of the iteration time is spent on function evaluation and the rest to perform optimization.

Level 2 optimization takes approximately 1500 CPU hours. Around 25 iterations are performed to meet the design requirements. Every function evaluation uses about 40% of the iteration time and the rest 60% is used by the algorithm to do sensitivity analysis and providing a new set of design variables to be evaluated in the next iteration.

For optimizing the 5 MW wind turbine, level 1 optimization was performed at first followed by level 2. However, after doing level 1 again, the differences between the two level 1 results were found to be negligible and therefore no further optimization was performed. This means that results of level 2 optimization were considered as the final optimum results.

4.4 Comparison of the results

As discussed before, the cost models used in this work contain all the relevant components of a wind turbine, as well as the costs of procedures such as decommissioning and

Table 4.4: Cost comparison of the NREL and optimized 5 MW wind turbines

Components	NREL	optimized
Blades	1062.3	1057.5
Hub	130.2	158.3
Pitch mechanism and bearing	242.0	263.0
Nose cone	13.6	14.2
Low speed shaft	166.8	182.6
Main bearings	64.4	71.9
Gearbox	877.2	877.2
Mechanical brake and coupling	11.0	11.0
Generator	398.0	398.0
Power electronics	393.2	393.2
Yaw drive and bearing	146.3	160.5
Main frame	162.7	172.9
Platform and railing	89.5	95.1
Nacelle cover	73.3	73.3
Electrical connections	308.8	308.8
Hydraulic and cooling system	77.2	77.2
Control,safety and condition monitoring	65.3	65.3
Tower	939.1	968.9
Marinization	561.6	722.2
Turbine capital costs (TCC)	4722.4	6072.3
Foundation system	2174.7	2174.7
Transportation	1568.3	1568.3
Port and staging equipment	144.9	144.9
Turbine installation	732.8	732.8
Electrical interface and connection	2063.5	2063.5
Permits, engineering and site assessment	215.5	215.5
Personnel access equipment	70.2	70.2
Scour protection	403.0	403.0
Decommissioning	362.8	403.3
Balance of station costs (BOS)	7373.2	7373.2
Offshore warranty premium	624.1	802.5
Initial capital cost (ICC)	13083.0	14651
Levelized replacement costs	99.0	99.0
Operation and maintenance	561.4	664.5
Fixed charge rate	0.1185	0.1185
AEP (kWhr)	23911817.1	28396817.4
LCOE ($\frac{USD}{kWhr}$)	0.0658	0.0630

O&M. Most of the cost models are a function of the design variables, as used in the optimization process. As an example, an increase in the blade length to capture more energy, not only increases the blade cost but also increases the loads on the hub and raises its

cost.

However, the optimizer decides what would be the lowest LCOE among many different design solutions. To show the power and the reliability of the optimization method proposed in this work a comparison between the 5 MW NREL and the optimized wind turbine is performed in this section.

Chord, twist angle, blade length, rated rotational speed and the internal thicknesses are the design variables of the blade to optimize, while, the airfoil shapes remain unchanged in the optimization process.

Figures 4.1 and 4.2 show the chord and twist angle distributions of the NREL and the optimized blades, respectively.

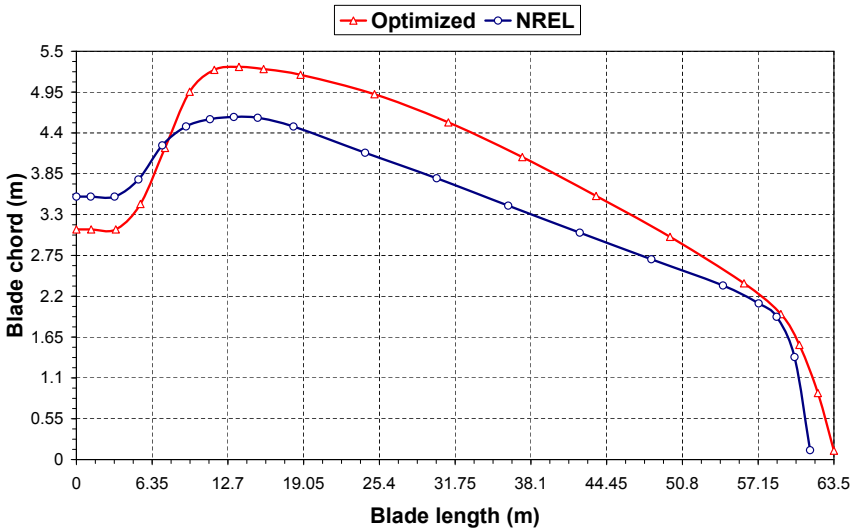


Figure 4.1: Chord distributions of the NREL and the optimized 5 MW wind turbine

As figure 4.1 shows, in the region between 0 and 8.5 m, the optimized rotor has a smaller chord than the NREL rotor. The chord reduction reaches a maximum value of 17.5% at the rotor radius of 3.3 m. This chord reduction is mainly due to the structural reason. In fact, because of having a better controller design, the loads on the blade root of the optimized wind turbine are decreased. Lower loads in the blade root demand less strength and this results in a smaller chord. From 8.5 m to the tip, the optimized blade has a larger chord than the NREL, with a maximum value of 16.2% at the rotor radius of 25.0 m. For the optimum twist angle, figure 4.2 shows a reduction in the region between 12 and 28 m, and an increase for the rest compared to the NREL design.

Considering the fact that both rotors have a different chord, twist angle, blade length and rated rotational speed, a one by one comparison is difficult to make. It is the combination of these properties that makes one design better than another, with respect to the objective function and the design constraints.

The power curve of both the NREL and the optimized wind turbines is presented in figure 4.3. As the figure shows, the optimized rotor has a rated wind speed of $11.0 \frac{m}{s}$,

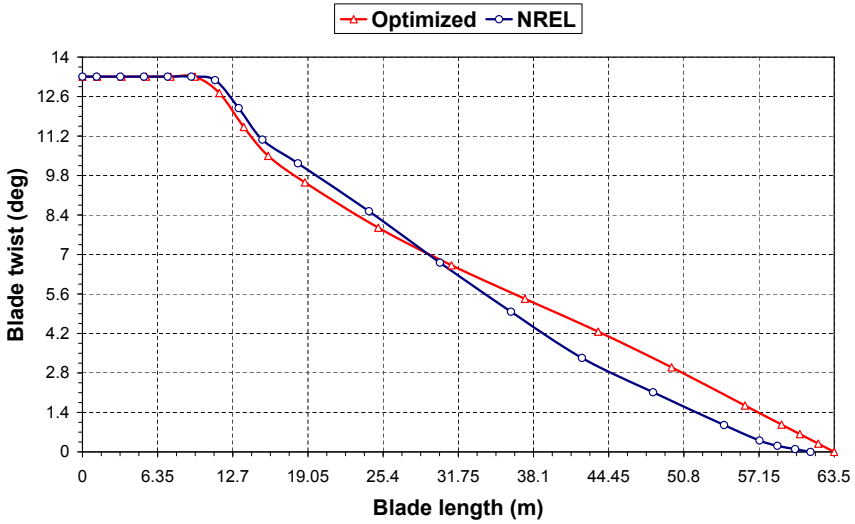


Figure 4.2: Twist distributions of the NREL and the optimized 5 MW wind turbine

compared to $11.4 \frac{m}{s}$ of the NREL. This is mainly because of having a larger rotor radius for the optimized rotor that results in capturing more energy in the below rated region.

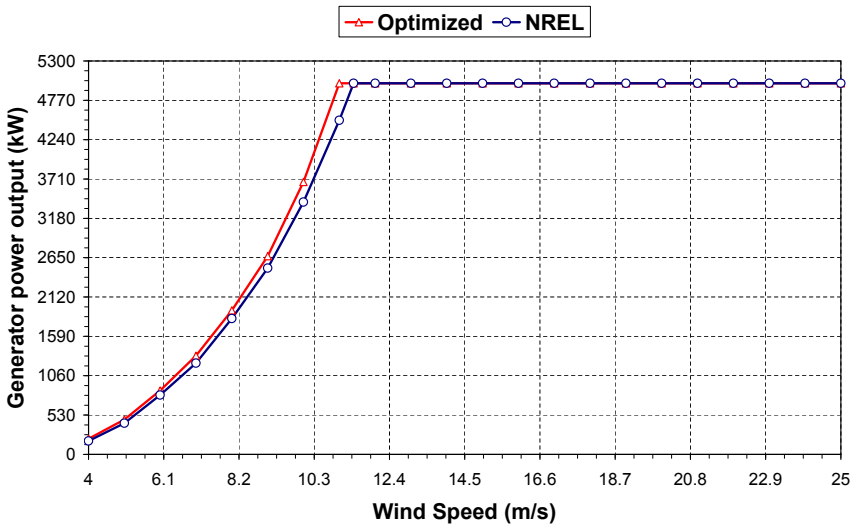


Figure 4.3: Power curve of the NREL and the optimized 5 MW wind turbine

In addition, the optimized wind turbine has a higher hub height of about 2.4 m, compared with the 80 m hub height of the NREL wind turbine. This is an increase of 2.5% in the tower height that consequently results in a higher AEP

Considering all the facts, the results show an increase of 15.7% for the AEP, and 22.2%

for the TCC. However, the higher AEP pays off the higher costs related to having a larger rotor and tower, and at the end results in a decrease of 4.2% in the LCOE.

The same comparison can also be made for the design constraints. However, the most significant change with respect to the design of the 5 MW NREL wind turbine is the system's natural frequencies. The optimized 5 MW wind turbine is a soft-stiff design, compared to a soft-soft design of the NREL wind turbine (see [Petersen et al. \(2010\)](#) for a description of soft-soft and soft-stiff designs). This is mainly related to the difference in the rated rotational speed of both wind turbines.

The optimized wind turbine has higher rated rotational speed of about 4.2% (12.9 RPM for the optimized and 12.1 for the NREL design). This increase has an influence on the allowable natural frequencies, and makes the wind turbine from being a soft-soft (NREL wind turbine) to a soft-stiff (optimized wind turbine) design.

Another influence of this increased rated rotational speed together with a larger rotor diameter is the tip speed. While the NREL design has a maximum designed tip speed of $80 \frac{m}{s}$, the optimized design has a tip speed of $87.8 \frac{m}{s}$. This shows 8.9% increase in the tip speed of the optimized design.

It is well known in the literature that for the OWTs, there is a clear potential benefit in higher tip speeds, since there is less constraint on noise emission levels compared to the $80 \frac{m}{s}$ limit for onshore wind turbines, [Malcolm and Hansen \(2002\)](#). Therefore, it is not surprising to see a higher tip speed for the optimized wind turbine design of this work that proves the idea of having a better design with an increase in the tip speed.

However, with increasing tip speed, the blade solidity usually decreases and this may result in a more flexible blade. Although, this can be beneficial for system loads, it is problematic for maintaining the preferred tower clearance in extreme loading conditions. Therefore, there is an optimum for the tip speed that is governed by several design considerations. In the design of the optimized 5 MW, this is the first natural frequency of the blade that prevents a further decrease in the blade's solidity (in this case also blade's flexibility) by having a higher rotational speed.

4.5 Concluding remarks

The purpose of optimizing the 5 MW wind turbine was stated in section 4.2. Referring to these goals, the knowledge gained in the MDO of the 5 MW wind turbine can be characterized as follows:

4.5.1 Validating the integrated aeroservoelastic optimization method

Aeroservoelastic design optimization of a wind turbine, if used effectively and correctly, can result in an improved and economical design, and save a huge amount of engineering

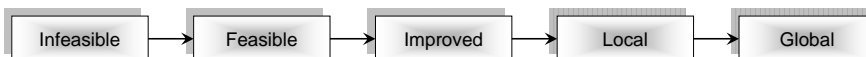


Figure 4.4: Different stages of optimization

design time. However, it is important to understand the limitation of this technique, and use it as only one of the many tools at our disposal.

Having this in mind, it can be seen that the aeroservoelastic design optimization can be applied at different stages of a design process. As figure 4.4 shows, one can use this tool to make an infeasible design a feasible design. This is exactly the technique that was used in level 2 of the optimization process to make the results of level 1 feasible. Improving the quality of a feasible design is another application of this method. This step was used in the design optimization process by iterating between level 1 and 2 until the designer or the design criteria are satisfied.

It is already known that the NREL wind turbine is a properly designed wind turbine and using the integrated aeroservoelastic design optimization comparable results can be achieved. However, it should be noted that in this research a limited number of design load cases are used and in practice several other load cases are required to get a wind turbine certified.

All in all, it can be concluded that the integrated aeroservoelastic design optimization has the capability to provide feasible design solutions for larger scale OWTs, in which the scaling trends are going to be based on. Therefore, this tool will be used in the next chapter to design and optimize 10 and 20 MW wind turbines.

4.5.2 Improved understanding of the 5 MW wind turbine design

In the context of design optimization, defining the design space of a wind turbine is not an easy task. However, by simulating the physical behavior of the NREL wind turbine, a good understanding of its design constraints was achieved. This helped to narrow down the design space and properly fix the lower and upper bounds of the design variables. It also helped to get an idea about the applied safety factors used to developed this wind turbine.

This improved understanding can also be helpful for larger scales, since some of these design constraints can also be scaled using the scaling laws. As an example, the system natural frequencies are fairly well predictable, and if one knows these values for a 5 MW, then the initial guess for a 10 to 20 MW wind turbines can be made more accurately.

4.5.3 Providing consistent data points to make scaling trends

To make representative scaling trends of the future wind turbines a consistent set of data points are beneficial. Therefore, it is needed to use the same design assumptions at all sizes. In that respect, the same design criteria that are used to optimize the 5 MW wind turbine will be used for the 10 and 20 MW wind turbines and developing scaling trends using these three data points has the least inconsistency.

Integrated aeroservoelastic design and optimization of large wind turbines

5.1 Introduction

The previous chapter has presented the design optimization of the 5 MW wind turbine. This chapter uses the same design methodology to design the 10 and 20 MW wind turbines. The characteristics of these wind turbines presented in this chapter include the important properties, as well as all the design variables, design constraints and the objective function.

These wind turbines together with the optimized 5 MW wind turbine act as data points to make scaling trends and investigate the influence of size on technical and economical characteristics of larger scales wind turbines. These include loading-diameter, mass-diameter and cost-diameter trends that help to study the influence of scale on design and identify future design challenges.

5.2 MDO of the 10 and 20 MW wind turbines

This section presents the results of the optimized 10 and 20 MW wind turbines. As it was proofed before, the concept of aeroservoelastic design optimization serves as a useful method to find the optimum design solution for such giant wind turbines. However, for conciseness, only important results are presented.

5.2.1 Design variables of the 10 and 20 MW wind turbines

To start the MDO of the 10 and 20 MW wind turbines, an initial set of design variables and parameters are needed. Ideally, the initial design variables should be the closest possible to their optimums to reduce computational time and provide a sound design.

In this work, linear scaling laws are used to find such an initial set of design variables and parameters. That is, the linear scaling laws are applied to the optimized 5 MW wind turbine to find the initial value of the design variables and parameters of the 10 and 20 MW wind turbines with no conceptual change in their design with respect to the optimized 5 MW wind turbine.

The initial values of the linearly upscaled design variables also help to make an engineering judgment on the upper and lower bounds of the side constraints. Based on these initial design variables, several test runs were performed to adjust the upper and lower bounds of the side constraints, while evaluating the functional design constraints and their sensitivity with respect to the design variables. This results in a trial and error process to find reasonable side constraints to form a design space which is neither computationally expensive nor narrow bounded.

After setting these initial design variables and their bounds, the MDO of the 10 and 20 MW is carried out. The same process as the MDO of the 5 MW wind turbine is followed here.

Table 5.1 and 5.2 show the list of design variables for the 10 and 20 MW wind turbines, respectively. These tables also contain the lower and upper limits appearing as side

Table 5.1: 10 MW wind turbine design variables and side constraints

Description	Opt. level	Min	Initial	Optimum	Max
Blade length (m)	1	85.0	89.8	90.0	92.0
Tower height (m)	1	107.0	113.1	107.0	115.0
Rated rotational speed (rpm)	1	8.0	9.1	8.5	10.0
Twist at station 9 (deg)	2	9.0	10.4	10.0	12.0
Twist at station 15 (deg)	2	2.0	3	2.6	4.0
Chord at station 3 (m)	2	3.0	4.4	4.4	5.0
Chord at station 7 (m)	2	4.0	7.5	6.0	7.7
Chord at station 15 (m)	2	3.0	4.2	5.2	5.5
Chord at station 18 (m)	2	0.25	2.1	0.3	2.5
Skin thickness at station 1 (cm)	2	8.0	14.1	12.0	15.0
Skin thickness at station 3 (cm)	2	6.0	8.5	7.0	10.0
Skin thickness at station 6 (cm)	2	3.0	3.3	5.5	7.0
Skin thickness at station 16 (cm)	2	1.6	2.1	2.0	3.0
Web thickness at station 3 (cm)	2	1.0	1.4	3.0	6.0
Web thickness at station 6 (cm)	2	2.0	2.8	3.5	5.0
Web thickness at station 16 (cm)	2	1.0	1.8	3.0	4.0
Spar thickness at station 3 (cm)	2	1.0	1.4	2.5	4.0
Spar thickness at station 6 (cm)	2	1.0	3.5	3.5	4.0
Spar thickness at station 16 (cm)	2	1.0	3.4	2.0	4.0
Tower diameter at station 1 (m)	2	7.0	8.5	9.4	10.0
Tower diameter at station 22 (m)	2	4.0	5.8	5.4	7.0
Tower thickness at station 1 (cm)	2	5.0	5.7	8.5	10.0
Tower thickness at station 22 (cm)	2	3.0	3.4	4.0	5.0

constraints for level 1 and 2 optimization, as well as their initial and optimum values. By looking to the initial and optimized design variables, it can be argued that generally the linear scaling law provides reasonable initial design variables, though such a set of design variables do not respect the design constraints.

Table 5.2: 20 MW wind turbine design variables and side constraints

Description	Opt. level	Min	Initial	Optimum	Max
Blade length (m)	1	125.0	127.0	140.1	143.0
Tower height (m)	1	146.0	150.0	157.1	170
Rated rotational speed (rpm)	1	6.0	6.45	6.5	8.0
Twist at station 9 (deg)	2	6.5	10.4	7.5	12.0
Twist at station 15 (deg)	2	2.7	3.0	5.5	6.0
Chord at station 3 (m)	2	6.0	6.2	7.9	8.0
Chord at station 7 (m)	2	7.0	10.6	10.0	11.0
Chord at station 15 (m)	2	5.0	6.0	7.0	8.0
Chord at station 18 (m)	2	1.0	3.0	1.2	3.2
Skin thickness at station 1 (cm)	2	15.0	20.0	19.3	21.0
Skin thickness at station 3 (cm)	2	7.0	12.0	10.0	13.0
Skin thickness at station 6 (cm)	2	4.0	4.6	7.7	10.0
Skin thickness at station 16 (cm)	2	2.0	3.0	2.0	7.0
Web thickness at station 3 (cm)	2	1.5	2.0	2.7	5.0
Web thickness at station 6 (cm)	2	2.0	4.0	2.9	4.0
Web thickness at station 16 (cm)	2	2.0	2.6	3.3	4.0
Spar thickness at station 3 (cm)	2	1.5	2.0	1.8	4.0
Spar thickness at station 6 (cm)	2	1.5	5.0	2.3	6.0
Spar thickness at station 16 (cm)	2	1.0	4.8	3.2	5.5
Tower diameter at station 1 (m)	2	14.0	12.0	16.1	18.0
Tower diameter at station 22 (m)	2	7.0	8.2	9.1	10.0
Tower thickness at station 1 (cm)	2	7.0	8.0	10.7	11.0
Tower thickness at station 22 (cm)	2	4.0	4.8	6.0	7.0

5.2.2 Design constraints of the 10 and 20 MW wind turbines

In total there are 52 design constraints to fully bound the design space. However, only the highest active constraints are presented here. For the optimum 10 MW blade, the highest active constraint is the tip deflection. For the optimum 10 MW tower, fatigue is the highest active constraint.

For the optimum 20 MW blade, the highest active constraints are the tip deflection and fatigue at the root. For the optimum 20 MW tower, fatigue is the highest active constraint.

Table 5.3 and 5.4 show these constraints for both the blade and tower at the optimum values of design variables of the 10 and 20 MW wind turbines, respectively.

Table 5.3: 10 MW wind turbine functional constraints

Description	Opt. level	bound	Optimum
Max blade deflection at $9 \frac{m}{s}$	2	$\leq 7.9(m)$	6.6 (m)
Max blade deflection at $11 \frac{m}{s}$	2	$\leq 7.9(m)$	7.9 (m)
Max blade deflection at $13 \frac{m}{s}$	2	$\leq 7.9(m)$	7.7 (m)
Max blade deflection at $15 \frac{m}{s}$	2	$\leq 7.9(m)$	6.3 (m)
Max blade deflection at $17 \frac{m}{s}$	2	$\leq 7.9(m)$	5.1 (m)
Max blade deflection at $19 \frac{m}{s}$	2	$\leq 7.9(m)$	4.9 (m)
Max blade deflection at $21 \frac{m}{s}$	2	$\leq 7.9(m)$	4.9 (m)
Max blade deflection at $23 \frac{m}{s}$	2	$\leq 7.9(m)$	4.5 (m)
Max blade deflection at $25 \frac{m}{s}$	2	$\leq 7.9(m)$	3.6 (m)
Fore-aft fatigue at station 1 of the tower	2	≤ 0.7	0.49
Fore-aft fatigue at station 5 of the tower	2	≤ 0.7	0.61
Fore-aft fatigue at station 9 of the tower	2	≤ 0.7	0.70
Fore-aft fatigue at station 13 of the tower	2	≤ 0.7	0.67
Fore-aft fatigue at station 17 of the tower	2	≤ 0.7	0.52
Fore-aft fatigue at station 21 of the tower	2	≤ 0.7	0.23

Table 5.4: 20 MW wind turbine functional constraints

Description	Opt. level	bound	Optimum
Max blade deflection at $9 \frac{m}{s}$	2	$\leq 11.8(m)$	11.4 (m)
Max blade deflection at $11 \frac{m}{s}$	2	$\leq 11.8(m)$	11.8 (m)
Max blade deflection at $13 \frac{m}{s}$	2	$\leq 11.8(m)$	10.4 (m)
Max blade deflection at $15 \frac{m}{s}$	2	$\leq 11.8(m)$	9.2 (m)
Max blade deflection at $17 \frac{m}{s}$	2	$\leq 11.8(m)$	8.5 (m)
Max blade deflection at $19 \frac{m}{s}$	2	$\leq 11.8(m)$	6.8 (m)
Max blade deflection at $21 \frac{m}{s}$	2	$\leq 11.8(m)$	6.1 (m)
Max blade deflection at $23 \frac{m}{s}$	2	$\leq 11.8(m)$	6.2 (m)
Max blade deflection at $25 \frac{m}{s}$	2	$\leq 11.8(m)$	5.5 (m)
Flapwise fatigue at the root of the blade	2	≤ 0.7	0.68
Fore-aft fatigue at station 1 of the tower	2	≤ 0.7	0.58
Fore-aft fatigue at station 5 of the tower	2	≤ 0.7	0.66
Fore-aft fatigue at station 9 of the tower	2	≤ 0.7	0.65
Fore-aft fatigue at station 13 of the tower	2	≤ 0.7	0.54
Fore-aft fatigue at station 17 of the tower	2	≤ 0.7	0.30
Fore-aft fatigue at station 21 of the tower	2	≤ 0.7	0.14

Similar to the optimum 5 MW wind turbine design, the flapwise deflection of the blade reaches a maximum at values close to the rated operating point for a NTM. This peak is due to the transition of the controller at rated between the generator-torque and the blade-pitch control.

5.2.3 Objective function of the 10 and 20 MW wind turbines

The derivation of LCOE and introduction of that as the objective function is explained in detail in chapter 3. Table 5.5 shows the cost of the optimum 10 and 20 MW wind turbines. The cost elements in this table are in 1000 USD.

5.3 Properties of the 10 and 20 MW wind turbines

Most of the data presented in this section are summarized for conciseness and clarity. However, the design methodology used in this research contains a huge amount of data for the optimized 10 and 20 MW wind turbines, which can not be presented all. Key data about these optimized wind turbines are selected and presented in the following subsections.

5.3.1 Gross properties

Table 5.6 shows the gross properties of the optimized 10 and 20 MW wind turbines. To enable comparison, the optimized 5 MW wind turbine data is presented as well.

5.3.2 Blade properties

The rotor of both the 10 and 20 MW optimum wind turbines is equipped with three blades of 90 and 140 m length, respectively. In the structural computations of the blade, 20 nonuniformly distributed elements are used. The properties between these elements are found by a cubic interpolation. Also for both the 10 and 20 MW blades, a structural damping ratio of 0.48% (critical in all modes of the isolated blade) that is equal to a 3.0% logarithmic decrement (similar to the 5 MW NREL and the 6 MW DOWEC turbines) is assumed as a fixed input.

Table 5.7 and 5.8 list the resulting structural properties of the 10 and 20 MW wind turbines. The first column of both tables labeled *Rad* is the spanwise locations along the blade-pitch axis measured from blade root. The second column labeled *BldFrac* is the nondimensional distance along the blade-pitch axis from the root to the tip varying from 0 to 1, respectively.

The distributed blade section mass per unit length values labeled as *BMsDen* are given in the third column. With this mass distribution, a mass of 53.0 ton and 182.7 ton is calculated for the optimum 10 and 20 MW wind turbine blade.

The flapwise, *BFlpStf*, and edgewise, *BEdgStf*, section stiffnesses are presented in the 4th and 5th column respectively. These values are calculated about the principal structural axes of each cross section.

5.3.3 Aerodynamic properties

The aerodynamic properties of the optimum 10 and 20 MW wind turbines are obtained by running a series of simulations from the cut-in to cut-out wind speeds. The first 60

Table 5.5: Cost estimation of the optimized 10 and 20 MW wind turbines

Components	10 MW	20 MW
Blades	2474.9	8570.7
Hub	324.2	1037.5
Pitch mechanism and bearing	664.5	2143.0
Nose cone	21.8	36.1
Low speed shaft	499.9	1783.4
Main bearings	245.2	1151.5
Gearbox	2085.0	4955.0
Mechanical brake and coupling	22.2	44.4
Generator	796.1	1592.2
Power electronics	786.4	1572.8
Yaw drive and bearing	451.2	1665.5
Main frame	341.8	808.1
Platform and railing	188.1	444.7
Nacelle cover	142.1	279.6
Electrical connections	617.7	1235.5
Hydraulic and cooling system	154.5	309.0
Control,safety and condition monitoring	65.3	65.3
Tower	3765.6	12497.0
Marinization	1842.3	5042.5
Turbine capital costs (TCC)	15489.0	45618.0
Foundation system	4349.5	8699.0
Port and staging equipment	289.9	579.9
Turbine installation	1465.8	2931.5
Electrical interface and connection	4127.0	8253.9
Permits, engineering and site assessment	431.0	862.1
Personnel access equipment	70.2	70.2
Scour protection	806.2	1612.3
Decommissioning	810.8	2058.9
Balance of station costs (BOS)	11539.6	23009.0
Offshore warranty premium	2047.0	6028.8
Initial capital cost (ICC)	29886.4	76714.4
Levelized replacement costs	198.0	396.1
Operation and maintenance	1316.8	2873.7
Fixed charge rate	0.1185	0.1185
AEP (kWhr)	56273009.4	122806072.9
LCOE ($\frac{USD}{kWhr}$)	0.0641	0.0704

seconds of the simulation lengths were ignored to ensure that all transient behavior were damped out.

The results are obtained by running a steady wind, and the steady BEM model. Using this steady model, a rated wind speed of $11.5 \frac{m}{s}$ for the 10 and $10.7 \frac{m}{s}$ for the 20 MW

Table 5.6: Gross properties of the optimized 5, 10 and 20 MW wind turbines

Design specification	5 MW	10 MW	20 MW
Rotor diameter (m)	130	182	286
Rated tip speed (m/s)	88	82	98
Rated rotational speed (RPM)	12.9	8.5	6.5
Hub height (m)	82.4	110.4	162

Table 5.7: Optimized 10 MW wind turbine blade structural properties

Rad. (m)	BldFrac (-)	BMsDen ($\frac{kg}{m^3}$)	BF1pStf ($N \cdot m^2$)	BEdgStf ($N \cdot m^2$)
0.0	0.000	1067.1	4.16×10^{10}	4.16×10^{10}
13.5	0.149	935.0	1.63×10^{10}	3.35×10^{10}
26.6	0.295	805.9	1.13×10^{10}	2.95×10^{10}
44.2	0.491	530.0	2.33×10^9	1.60×10^{10}
61.7	0.686	374.6	8.34×10^8	9.85×10^9
79.3	0.881	113.5	4.25×10^7	5.41×10^8
90.0	1.000	4.2	4.26×10^3	6.00×10^4

wind turbines is obtained. Figures 5.1 and 5.2 show the generator power output curve and the blade pitch angle of the 10 and 20 MW wind turbines.

5.3.4 Drive train properties

The 10 MW wind turbine has an optimized rated rotor speed of 8.4 rpm that is found in level 1 optimization. By assuming a rotational speed of 1173.7 rpm similar to the 5 MW

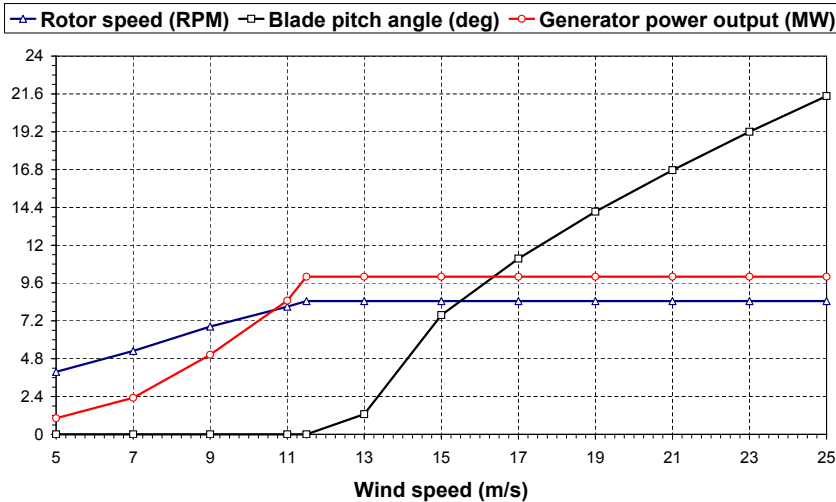


Figure 5.1: Aerodynamic properties of the optimized 10 MW wind turbine

Table 5.8: Optimized 20 MW wind turbine blade structural properties

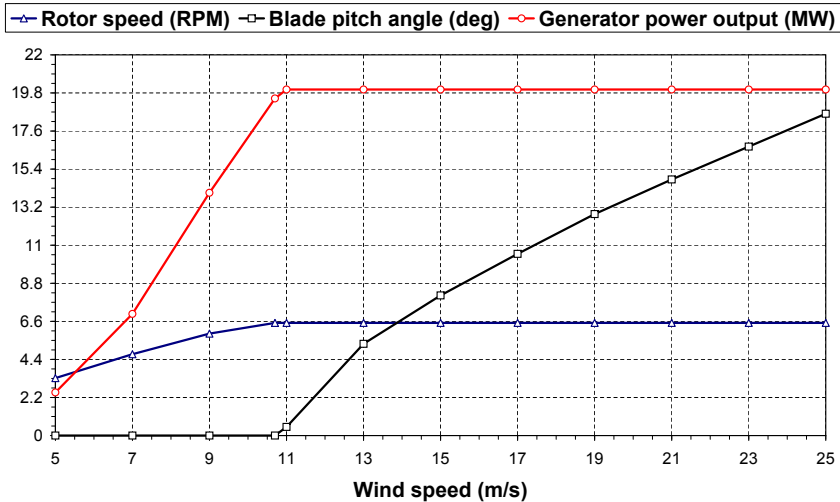
Rad. (m)	BldFrac (-)	BMsDen ($\frac{kg}{m^3}$)	BFlpStf ($N \cdot m^2$)	BEdgStf ($N \cdot m^2$)
0.0	0.000	3104.7	3.96×10^{11}	3.96×10^{11}
16.4	0.117	2133.8	3.20×10^{11}	2.77×10^{11}
34.7	0.247	1695.8	7.20×10^{10}	2.09×10^{11}
55.1	0.393	1284.9	1.99×10^{10}	1.40×10^{11}
82.5	0.588	1076.5	7.72×10^9	9.86×10^{10}
123.5	0.881	401.8	4.44×10^8	7.17×10^9
140.1	1.000	4.2	4.26×10^3	6.00×10^4

wind turbine in the generator side, a gearbox ratio of 139:1 can be obtained for the 10 MW wind turbine that is used during simulation. The total mechanical-to-electrical conversion loss is assumed to be 5.6%, which is the same as both the NREL and DOWEC turbines at the rated power.

Using the properties of the 5 MW wind turbine and applying linear scaling law, an equivalent drive shaft linear-spring constant of $2.45 \times 10^9 \frac{N \cdot m}{rad}$, and an equivalent linear-damping constant of $1.75 \times 10^7 \frac{N \cdot m}{rad \cdot s}$ can be calculated and used for the design of the 10 MW wind turbine.

For the 20 MW wind turbine an optimum rated rotor speed of 6.5 rpm is found. With a fixed rated generator speed of 1173.7 rpm, a gearbox ratio of 180:1 is obtained. Similar to the 10 MW wind turbine, the total mechanical-to-electrical conversion loss is assumed to be 5.6%.

Using a the similar approach as the 10 MW wind turbine, for the 20 MW wind turbine an equivalent drive shaft linear-spring constant of $6.94 \times 10^9 \frac{N \cdot m}{rad}$, and an equivalent

**Figure 5.2:** Aerodynamic properties of the optimized 20 MW wind turbine

linear-damping constant of $4.97 \times 10^7 \frac{N \cdot m}{rad \cdot s}$ can be calculated and used in simulation.

The drive train gross properties of the optimum 10 and 20 MW wind turbine are presented in table 5.9.

Table 5.9: Drive train gross properties of the 10 and 20 MW wind turbines

Property (Unit)	10 MW	20 MW
Rated rotor speed (RPM)	8.5	6.5
Gearbox ratio	139	180
Low speed shaft mass (ton)	49.5	176.7
Gearbox mass (ton)	84.1	173.7
High speed shaft, coupling and brake mass (ton)	1.98	3.96
Generator mass (ton)	31.5	59.7
Hydraulic and cooling system mass (ton)	0.79	1.59

5.3.5 Hub and nacelle properties

From the mass models developed for the hub, a mass of 56.2 ton for the 10 MW, and a mass of 180.0 ton for the 20 MW wind turbines are calculated. It is assumed that the hub is made from ductile iron castings and has a spherical shape. The diameter of this sphere is obtained using the scaling laws to be 3 m for the 10 and 6 for the 20 MW wind turbines.

Since the mass and geometry of the hub are known, with a simple algebraic equation, the thickness of the hub is found. Based on this thickness, a hub mass moment of inertia of $2.29 \times 10^5 \text{ kg} \cdot \text{m}^2$ for the 10 MW, and $1.47 \times 10^6 \text{ kg} \cdot \text{m}^2$ for the 20 MW wind turbine are calculated.

The nacelle mass (mass of all tower top components except the rotor and hub) of the 10 MW wind turbine is 379.9 ton. For the 20 MW wind turbine this value is 1026.2 ton. For both wind turbines, the yaw actuator has a natural frequency of 3 Hz, which is the same as the NREL wind turbine.

The gross properties of the hub and nacelle for both wind turbines are presented in table 5.10.

Table 5.10: Hub and nacelle gross properties of the 10 and 20 MW wind turbines

Property (Unit)	10 MW	20 MW
Hub mass (ton)	56.2	180.0
Hub mass moment of inertia ($\text{kg} \cdot \text{m}^2$)	2.29×10^5	1.47×10^6
Nacelle mass (ton)	379.9	1026.2
Nacelle mass moment of inertia ($\text{kg} \cdot \text{m}^2$)	1.35×10^7	8.82×10^7
Elevation of yaw bearing from tower base (m)	107.0	157.1
Yaw bearing to shaft vertical distance (m)	2.77	3.92
Hub center to yaw axis distance (m)	7.1	10.0

5.3.6 Support structure properties

The support structure of the wind turbines consists of the foundation system (monopile and transition piece) and tower. In this work, the soil mechanics of the monopile is not modeled and thus it is assumed that all the DOFs of the monopile at the seabed are constrained, and tower is the only element of the support structure assembly that is optimized.

However the dynamic and cost of the foundation system is present in the design process by using engineering models developed in WindPACT project for mass and cost of these two components (see appendix A. These engineering models provide a basis with which the integrity of the design is preserved without losing too much of accuracy in representing the dynamic and cost.

Table 5.11 and 5.12 give the resulting distributed tower properties of the 10 and 20 MW wind turbines. In both tables, the first column, *Height* is the vertical locations along the tower centerline relative to the tower base. It is also assumed that the tower base is located at the mean sea level.

Table 5.11: *Optimized 10 MW wind turbine tower properties*

Height (m)	TowFrac (-)	TowDia (m)	TowTick (cm)	TowStif ($N \cdot m^2$)
0.0	0.000	9.4	8.5	5.6×10^{12}
29.4	0.275	8.5	7.3	3.3×10^{12}
77.6	0.725	6.7	5.2	1.2×10^{12}
107.0	1.000	5.4	4.0	5.1×10^{11}

The second column, *TowFrac*, of the tables is the fractional height along the tower centerline from the tower base to the tower top that ranges from 0 to 1, respectively. The third, fourth and fifth columns also represent the diameter, thickness and stiffness of different tower heights.

As discussed before in chapter 3, only the diameter and thickness at the base and top of the tower are introduced as design variables, and a linear interpolation is used at other heights.

The resulting overall tower mass is 1393.1 *ton* for the 10 and 4623.4 *ton* for the 20 MW wind turbines.

Table 5.12: *Optimized 20 MW wind turbine tower properties*

Height (m)	TowFrac (-)	TowDia (m)	TowTick (cm)	TowStif ($N \cdot m^2$)
0.0	0.000	16.1	10.7	3.6×10^{13}
43.2	0.275	14.2	9.4	2.2×10^{13}
113.9	0.725	11.0	7.3	7.9×10^{12}
157.1	1.000	9.1	6.0	3.6×10^{12}

5.3.7 Controller properties

The controller design development is explained in detail in chapter 3. The 10 and 20 MW wind turbines gross controller properties are given in table 5.13.

Table 5.13: Controller gross properties of the 10 and 20 MW wind turbines

Property (Unit)	10 MW	20 MW
Cut-in, rated and cut-out wind speed ($\frac{m}{s}$)	3, 11.7, 25	7, 10.7, 25
Rated tip-speed ($\frac{m}{s}$)	82	98
Peak power coefficient	0.47	0.47
Blade-pitch angle at peak power (deg)	0.0	0.0
Rated rotational speed (rpm)	8.5	6.5
Rated mechanical power (MW)	10.6	21.2
Rated generator torque (kN.m)	119.1	202.3
Generator slip in transition region(%)	10	10
Maximum blade pitch rate ($\frac{deg}{s}$)	5.6	4.8

Figure 5.3 shows the final aerodynamic power sensitivity to the blade pitch angle at different steady state operating points for the above rated pitch controller of both wind turbines. Since the proportional and integral gains are a function of the aerodynamic power sensitivity, the data presented in this figure are used to design the KP and KI gains.

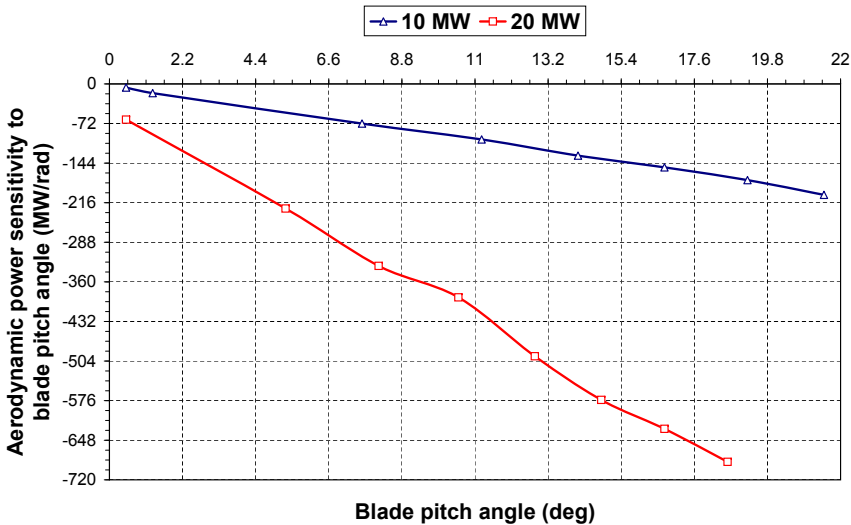


Figure 5.3: Aerodynamic power sensitivity to the blade pitch of the 10 and 20 MW wind turbines

The variation of the proportional and integral gains to balance out the changes of the aerodynamic power is shown in figure 5.4 and 5.5 for the 10 and 20 MW wind turbines.

The calculated proportional and integral gains are obtained using equation 3.19 and 3.20 of chapter 3.

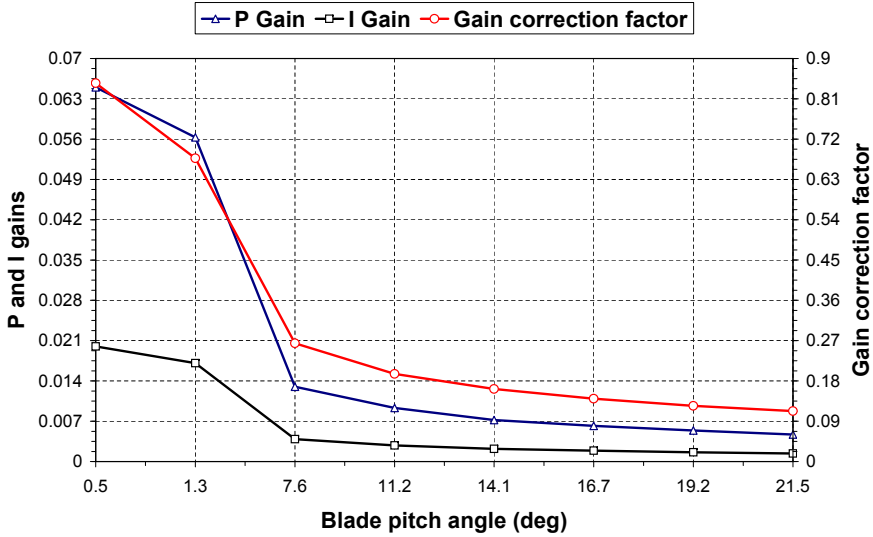


Figure 5.4: PI gains and gain scheduled correction factor of the 10 MW wind turbine

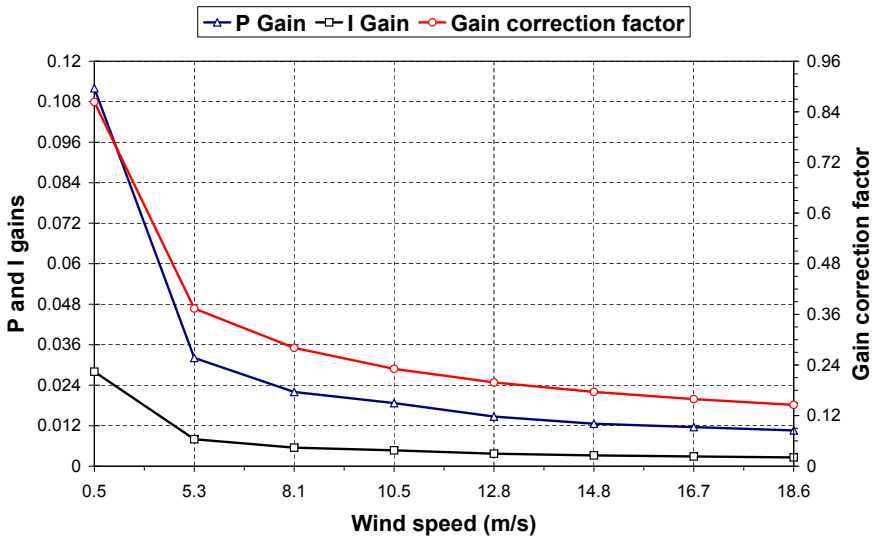


Figure 5.5: PI gains and gain scheduled correction factor of the 20 MW wind turbine

Aeroelastic stability analysis using eigenvalue method

6.1 Introduction

Historically, aeroelastic instabilities have not been a driving issue in wind turbine design. Therefore, the aeroelastic instability is rarely addressed in the past while designing a wind turbine. However, with more lighter and flexible blades the aeroelastic instability may become a design driver and therefore necessary to consider as a constraint in the design process.

The previous chapter presented the MDO of the 10 and 20 MW wind turbines. However, these wind turbines should be checked against aeroelastic instabilities to have a safe design. This chapter presents a method to find the unstable operational points for these wind turbines using an eigenvalue method and serves as a rough check during the preliminary wind turbine design process.

For this purpose, the structure and aerodynamics of the wind turbine are modeled independently and coupled together to account for aeroelasticity. Eigenvalue analysis of this coupled aeroelastic model provides the unstable operational mode of the wind turbine.

Since, larger wind turbines are fitted with relatively soft blades and tower, classical flutter may become a more important instability mode to check. Therefore, the focus of this chapter is to develop an analysis tool that is well suited for this type of instabilities.

6.2 Aeroelastic instability in wind turbines

Theodorsen (1935) was the first who investigated the aeroelastic instability phenomenon of a 2D airplane wing section. In Theodorsen's investigation, an aerodynamic model with an unsteady lift and moment term was coupled with a simple structural model with plunging and torsion as the only degrees of freedom. The model used the potential flow

assumption with an oscillatory motion and no damping was included. He found out that under certain conditions aerodynamic forces can be coupled with structural deformation that results in an increase in the amplitude of motion in every cycle called aeroelastic instability.

Since then, aeroelastic instability has been studied extensively for aircrafts, helicopters and bridges at many different conditions and configurations, [Goland \(1957\)](#), [Dowell \(1970\)](#), [Hong and Chopra \(1985\)](#), [Agar \(1989\)](#), [Patil et al. \(2001\)](#), [Dessi and Mastroddi \(2008\)](#) and [Su and Cesnik \(2010\)](#).

However, the literature on the aeroelastic design of wind turbines is relatively new, with a considerable amount of it being reproduced and adapted from rotary-wing aeroelasticity of helicopters and other rotor blades. Among the early studies in this area, [Ormiston \(1973\)](#) investigated the effect of size, hub configuration, type of control system and number of blades on the wind turbine dynamic characteristic and stability. Some years later he studied the aeroelastic stability of a wind turbine blade using a simple analytical technique. He modeled the blade as a centrally hinged and spring restrained element to study the dynamic response of the flapping motion in time domain, [Ormiston \(1975\)](#).

[Friedmann \(1976\)](#) studied the aeroelastic stability and response of large wind turbine blades using a set of coupled flap-lag-torsional equations of motion. He derived a general nonlinear, partial differential equation for determining the aeroelastic envelop. He also made an excellent survey of helicopter rotor aeroelastic studies of value in wind turbine design. Also [Kaza and Hammond \(1976\)](#) used a similar approach to study the flap-lag stability of the blade in the presence of velocity gradients. They used a single centrally-hinged model of the blade without any rotor-tower interaction.

In 1983, [Janetzke and Kaza \(1983\)](#) investigated the possibility of whirl flutter and formulated the effect of flap-torsion flutter on teetering motion of a 2 bladed wind turbine. The wind turbine had a 3.5 m diameter and they found an unstable point at 77.1 $\frac{m}{s}$ wind speed, and 320 RPM angular velocity.

[Kirchgässner \(1983\)](#) presented a linear aeroelastic stability analysis method for analyzing the stability of rotorcrafts. However, he also showed how the method could be used to analyze the stability of a two-bladed wind turbine. In his model, a quasi-steady aerodynamic model was coupled with a simple structural model to analyze the stability.

At the late 1980's and early 1990's when the stall regulated wind turbines were dominating the market, it was observed that the blades of these machines that operate in a separated flow experience stall-induced vibration, [Stiesdal \(1994\)](#). This resulted in high loads and instabilities during the operational condition, challenging the designers. Therefore, it became the concern of many researcher who were attempting to address and predict it, [Björck et al. \(1997\)](#) and [Petersen et al. \(1998\)](#).

[Chaviaropoulos \(1999\)](#) and [Chaviaropoulos et al. \(2003\)](#) studied the stall-induced flap and edgewise oscillation in a stall-regulated rotor. Nonlinear aerodynamic loads in the dynamic stall regime were calculated using a quasi-steady Onera model and Navier-Stokes solvers respectively. However, the effect of structural nonlinearity was not included in these studies.

In 2003, [Lindenburg and Snel](#) showed the importance of finding the aeroelastic boundaries in the next generation of wind turbines, [Lindenburg and Snel \(2003\)](#). This work also presents the ECN research projects on the aeroelastic stability of the rotor

blade vibration. They also showed three different research projects aiming to develop new tools; STABTOOL-3, DAMPBLADE and STABCON.

Hansen (2004) presented a design tool for performing aeroelastic stability analysis of wind turbines. In his work, the aerodynamic loads are modelled using the BEM theory with an extension of Beddoes-Leishman dynamic stall model in a state-space formulation. A finite beam element method is used to model the structure. The multi-blade transformation was employed to eliminate the periodic coefficients.

Lobitz (2005) studied the sensitivity of two parameters on the flutter speed of a 35 m wind turbine blade. These parameters were the chordwise location of the center of mass and the ratio of the flapwise to torsional frequency. This study showed how these parameters can highly influence the flutter speed.

To have a view of the stability characteristics of the wind turbine, the aeroelastic damping of the operational turbine modes can be used as a good indicator. Therefore, **Hansen et al. (2006)** presented two experimental methods for estimating the modal damping of a wind turbine during operation. In the first method, the turbine modal mode is excited with a harmonic force at its natural frequency, and damping is obtained by a decaying response. The second method uses a stochastic subspace identification. Here, the linear model of the turbine is estimated from the response of measured signals.

For stall-induced flutter, structural damping, blade airfoil characteristics and the effective direction of blade vibrations govern the instability phenomenon, whereas for the classical flutter the frequency ratio of the two unstable modes, the location of the elastic axis and the center of gravity and the torsional blade stiffness are the main parameters. These instability characteristics are exemplified by **Hansen (2007)** in an aeroelastic stability analysis for different wind turbines.

The main research objective on the next years were to develop new structural and aerodynamic models to find instabilities for large wind turbines, since it was observed that they are more susceptible to aeroelastic instabilities. These models should have the capability of simulating large deformations (non-linear models) with high accuracy.

Currently, many different approaches are used to address the aeroelastic instability of wind turbines at different conditions; nonlinear structural modeling using superelements coupled with BEM model to setup equations of motion and find instabilities, **Holierhoek (2008)**, search for aeroelastic instabilities using reduced order system identification based on flexible multibody method, **Meng et al. (2008)**, nonlinear aeroelastic models for stall-induced vibration, **Sarkar and Bijl (2008)**, stability analysis for high angle of attack on parked wind turbine blades, **Politis et al. (2009)**, and study the effect of steady deflections on the aeroelastic stability of a turbine blade, **Kallesoe (2011)**.

6.3 Modeling approach

The structure of the wind turbine is modeled by articulated nonlinear elements using Finite Element Method (FEM). For this purpose the commercial FE package, NASTRAN, is used. This model expresses the structural mass, damping and stiffness matrices in a noninertial (rotary) reference frame. To account for the rotational effects of the rotor, these matrices are modified and transformed to an inertial (stationary) reference frame.

The primary application for an inertial (rather than noninertial) frame of reference is in the field of rotor dynamics where a rotating structure (rotor) is modeled along with

a stationary support structure. Examples of such an application include a gas turbine engine rotor-stator assembly or wind turbine rotor-tower, where the rotor spins with respect to a fixed supporting structure.

For classical flutter prediction an unsteady aerodynamic model is needed. The Blade Element Momentum (BEM) model is used as the basis to calculate the axial induction factors over the rotor plane and find the real wind velocity that each element of the blade experiences. Then, the unsteady aerodynamic forces are calculated by Theodorsen function in frequency domain, using the wind velocities obtained from the BEM model.

In the next step, the aeroelastic equations of motion are constructed by coupling the structural model with the unsteady aerodynamic model. This enables the treatment of the aeroelastic instability problem of the wind turbine as an eigenvalue analysis problem. Here, the nonlinear aeroelastic model of the wind turbine is linearized about a steady state equilibrium to set up an eigenvalue problem. This is similar to an eigenvalue analysis that is performed in structural analysis, except that here all degrees of freedom of the turbine and all terms of the unsteady aerodynamics are included.

Using this approach, it is possible to evaluate a limited number of eigenvalues of the coupled aeroelastic matrix using Arnoldi's iterative algorithm, [Jia \(1998\)](#). Based on this eigenvalue analysis, the unstable operational points of the wind turbine will be obtained. Figure 6.1 shows the steps of developing this methodology.

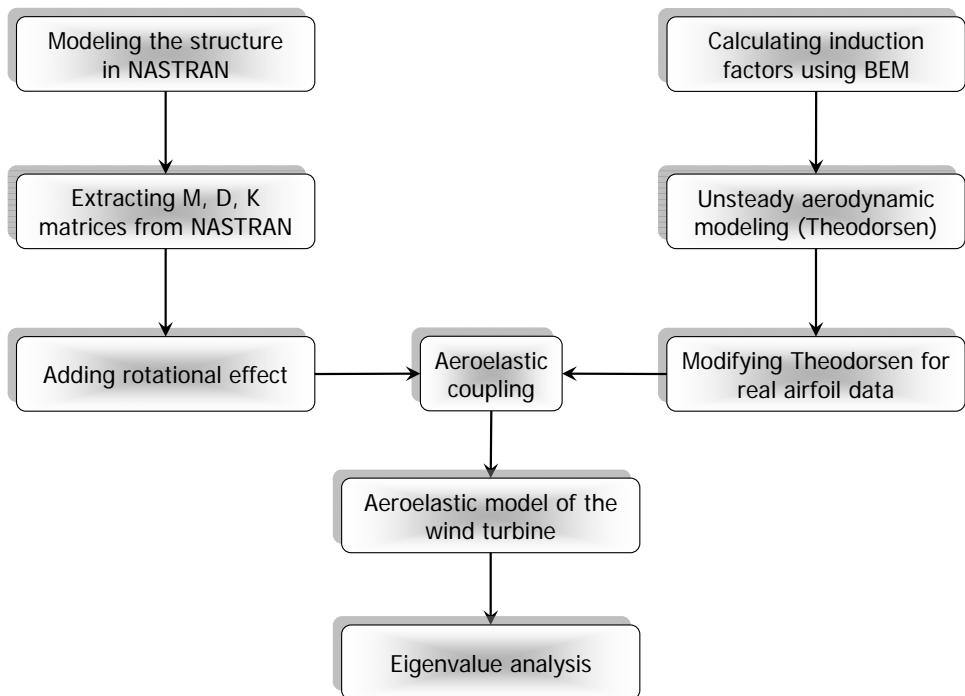


Figure 6.1: *The flowchart of the aeroelastic instability tool*

6.4 Structural model of the wind turbine

The dynamic behavior of a structural body can be represented by the elastodynamic equations. The elastodynamic equations are a set of Partial Differential Equations (PDE) and their boundary conditions. However, these equations are only solvable for simple geometries and for complex engineering problems a closed form solution does not exist.

The Finite Element Analysis (FEA) is a numerical technique for finding approximate solutions of these PDEs by means of discretization. Two different approaches can be used to find the solution of a PDE. In the first method the problem can be treated as a steady state problem by eliminating the differential equation completely. The second method renders the PDE into an approximating system of ordinary differential equations, which are then numerically integrated using standard techniques such as Euler's method, Runge-Kutta, Newmark, etc.

By using the second method, the continuous equations of an elastodynamic system can be represented by a set of Ordinary Differential Equations (ODE) as:

$$[\mathbf{M}_s] \frac{d^2 \mathbf{u}(t)}{dt^2} + [\mathbf{D}_s] \frac{d\mathbf{u}(t)}{dt} + [\mathbf{K}_s] \mathbf{u}(t) = \mathbf{F}(t) \quad (6.1)$$

Where:

\mathbf{M}_s : structural mass matrix

\mathbf{D}_s : structural damping matrix

\mathbf{K}_s : structural stiffness matrix

\mathbf{u} : vector which contains all the nodes displacement in time

$\mathbf{F}(t)$: external forces applied on the structural system

To find the structural matrices, (\mathbf{M}_s , \mathbf{D}_s and \mathbf{K}_s), NASTRAN finite element software is used. These matrices contain the structural information of the wind turbine that are needed to find the instabilities. However, these system of equations (matrices and DOFs) are in a noninertial reference frame and they need to be modified for the rotational effect. Next subsections explain the required modifications.

6.4.1 Displacement, velocity, acceleration and forces in the inertial frame

As explained before, all DOF's obtained from NASTRAN are in the noninertial reference frame (labeled as coordinate system 2 in figure 6.2). To express these DOF's in an inertial reference frame, the relation between the inertial and noninertial reference frames should be formulated. As figure 6.2 shows, the position of an arbitrary differential mass can be described by:

$$\mathbf{u}_1 = \mathbf{R}_1 + \mathbf{R}_2 \quad (6.2)$$

Here:

\mathbf{u}_1 : the position vector of the differential mass in the inertial reference frame

\mathbf{R}_1 : the position vector that relates the origin of the inertial and the noninertial reference

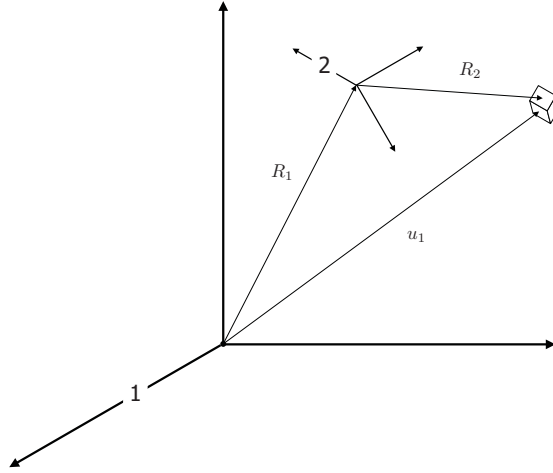


Figure 6.2: Inertia and noninertia reference frames

frames

\mathbf{R}_2 : the position vector of the differential mass in the noninertial reference frame

This general expression of the differential mass is used as the basis to derive the velocity and acceleration terms in the inertial reference frame. Using this formulation, the velocity of the differential mass can be obtained by taking the time derivatives of equation 6.2 as follow:

$$\left(\frac{d\mathbf{u}_1}{dt}\right)_1 = \left(\frac{d\mathbf{R}_1}{dt}\right)_1 + \boldsymbol{\Omega} \times \mathbf{R}_2 + \left(\frac{d\mathbf{R}_2}{dt}\right)_2 \quad (6.3)$$

Here, $\boldsymbol{\Omega} = (\Omega_x, \Omega_y, \Omega_z)$ is the angular velocity of the noninertial reference frame with respect to the inertial reference frame. Similarly, the acceleration of the differential mass is obtained by taking the time derivative of the velocity terms given in equation 6.3 as:

$$\begin{aligned} \left(\frac{d^2\mathbf{u}_1}{dt^2}\right)_1 = & \left(\frac{d^2\mathbf{R}_1}{dt^2}\right)_1 + \left(\frac{d^2\mathbf{R}_2}{dt^2}\right)_2 + \frac{d\boldsymbol{\Omega}}{dt} \times \mathbf{R}_2 + \\ & 2\boldsymbol{\Omega} \times \left(\frac{d\mathbf{R}_2}{dt}\right)_2 + \boldsymbol{\Omega} \times (\boldsymbol{\Omega} \times \mathbf{R}_2) \end{aligned} \quad (6.4)$$

The equivalent force in the inertial reference frame acting on the differential mass m , due to the acceleration in the noninertial reference frame is obtained by applying the Newton's second law (knowing the acceleration term from equation 6.4) as:

$$\mathbf{F} = m \cdot \frac{d^2\mathbf{u}_1}{dt^2} \quad (6.5)$$

Substituting equation 6.4 in equation 6.5 and integrating over the domain of the differential mass, the forces on the internal reference frame can be obtained. This is presented in equation 6.6 as:

$$\mathbf{F} = \int_V \left(\left(\frac{d^2 \mathbf{R}_1}{dt^2} \right)_1 + \left(\frac{d^2 \mathbf{R}_2}{dt^2} \right)_2 + \frac{d\boldsymbol{\Omega}}{dt} \times \mathbf{R}_2 + 2\boldsymbol{\Omega} \times \left(\frac{d\mathbf{R}_2}{dt} \right)_2 + \boldsymbol{\Omega} \times (\boldsymbol{\Omega} \times \mathbf{R}_2) \right) dm \quad (6.6)$$

Where V is the volume domain of the differential mass. The fourth and fifth terms of equation 6.6 are called the Coriolis and centrifugal forces. They change the apparent damping and stiffness of the structure as experienced in an inertial reference frame. This is explained in the next subsection.

6.4.2 Mass, stiffness and damping in the inertial frame

In the previous subsection, the modification of the displacement, velocity, acceleration and forces of a finite element mass to account for the changes from a noninertial to an inertial reference frame was formulated. This subsection explains how these forces influence the structural matrices.

To have the structural matrices, the wind turbine is modeled in NASTRAN. Hence, these matrices should be extracted from NASTRAN and modified to account for the rotational effect. Equation 6.1 shows the relation between the mass, stiffness and damping matrices with the displacement, velocity, acceleration and the external forces applied on a finite mass element in the noninertial reference frame.

To modify the structural matrices of equation 6.1, additional terms should be added to this initial FE model that is extracted from NASTRAN as described by Guo et al. (2001). Thus, the new FE model that includes the equivalent rotational effect should read as:

$$[\mathbf{M}_s] \frac{d^2 \mathbf{u}}{dt^2} + [\mathbf{D}_s + \mathbf{D}_r] \frac{d\mathbf{u}}{dt} + [\mathbf{K}_s - \mathbf{K}_r] \mathbf{u} = \mathbf{F}(t) \quad (6.7)$$

The added terms that represent the equivalent rotational effect in this new formulation are:

\mathbf{D}_r as the damping matrix due to the rotation of the element. It is usually called Coriolis matrix in a noninertial reference frame, and gyroscopic matrix in an inertial reference frame given by the following equation:

$$[\mathbf{D}_r]_e = \begin{bmatrix} 0 & \int_V -2 \cdot \Omega_z dm & \int_V 2 \cdot \Omega_y dm \\ \int_V 2 \cdot \Omega_z dm & 0 & \int_V -2 \cdot \Omega_x dm \\ \int_V -2 \cdot \Omega_y dm & \int_V 2 \cdot \Omega_x dm & 0 \end{bmatrix}_e \quad (6.8)$$

\mathbf{K}_r as the stiffness matrix due to the rotation of the element given by the following equation (spin softening matrix due to the rotation of the structure). It changes the apparent stiffness of the structure in a rotating reference frame.

$$[\mathbf{K}_r]_e = \begin{bmatrix} -\int_V (\Omega_y^2 + \Omega_z^2) dm & \int_V \Omega_y \Omega_x dm & \int_V \Omega_z \Omega_x dm \\ \int_V \Omega_x \Omega_y dm & -\int_V (\Omega_z^2 + \Omega_x^2) dm & \int_V \Omega_z \Omega_y dm \\ \int_V \Omega_x \Omega_z dm & \int_V \Omega_y \Omega_z dm & -\int_V (\Omega_x^2 + \Omega_y^2) dm \end{bmatrix}_e \quad (6.9)$$

6.5 Aerodynamic model of the rotor

As discussed before, for classical aeroelastic flutter prediction an unsteady aerodynamic model is required. Figure 6.3 shows a sketch of the developed method by Theodorsen, which addresses the unsteady aerodynamic forces of a 2D flat plate that experiences oscillatory pitching and plunging motion.

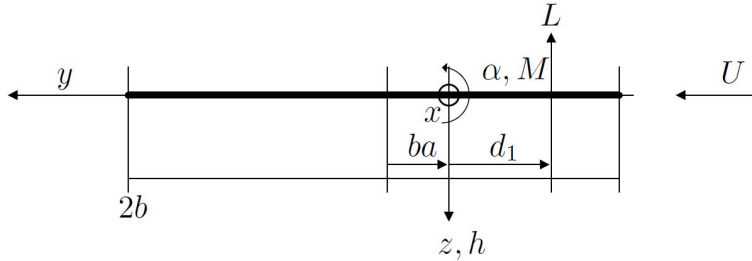


Figure 6.3: Schematic of the Theodorsen unsteady aerodynamic forces on a flat plate

Here:

L : the unsteady lift force

M : the unsteady aerodynamic force

b : semi-chord

U : wind velocity

α : the pitching motion

h : the plunging motion

a : a fraction of semi-chord that defines the location of elastic axis from the semi-chord

d_1 : the distance between the aerodynamic center and the elastic axis

The pitching and plunging motions can be represented using a harmonic solution as:

$$h = h_0 e^{i\omega t} \quad \alpha = \alpha_0 e^{i\omega t} \quad (6.10)$$

Where h_0 and α_0 are complex constants. Thus, the solution for the lift and moment (as derived by Theodorsen (1935)) is:

$$L = 2\pi\rho U^2 b \left[\frac{C(k)}{U} \dot{h} + C(k)\alpha + [1 + C(k)(1 - 2a)] \frac{b}{2U} \dot{\alpha} + \frac{b}{2U^2} \ddot{h} - \frac{b^2 a}{2U^2} \ddot{\alpha} \right] \quad (6.11)$$

$$M = 2\pi\rho U^2 b \left[d_1 \left[\frac{C(k)}{U} \dot{h} + C(k)\alpha + [1 + C(k)(1 - 2a)] \frac{b}{2U} \dot{\alpha} \right] + \frac{b^2}{2U} \dot{\alpha} \left(a - \frac{1}{2} \right) + \frac{ab^2}{2U^2} \ddot{h} + \frac{b^3}{2U^2} \ddot{\alpha} \left(\frac{1}{8} - a^2 \right) \right] \quad (6.12)$$

Here, $C(k)$ is the Theodorsen function and $k = \frac{\omega b}{U}$ is the reduced frequency. Thus, the Theodorsen function can be represented as a complex function of the reduced frequency, which is given by:

$$C(k) = \frac{H_1^{(2)}(k)}{H_1^{(2)}(k) + iH_0^{(2)}(k)} \quad (6.13)$$

In the above formulation, H denotes the Hankel function. Also, the real and imaginary parts of C are depicted in figure 6.4 as a function of reduced frequency.

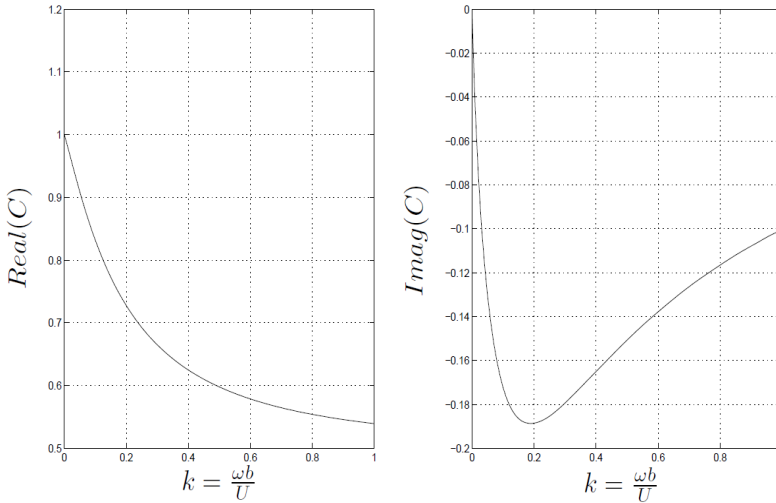


Figure 6.4: The Theodorsen function

However, the Theodorsen unsteady forces are developed for the fixed wings of aircrafts, and it need to be modified for the rotating blade of a wind turbine. Therefore, to make use of the Theodorsen function for a wind turbine several modifications are needed. These are explained in the following subsections.

6.5.1 Modification of the wind velocities

The wind velocities presented in the Theodorsen lift and moment terms are the free-stream wind velocity. However, for a wind turbine the rotor disk causes a flow blockage resulting in a change of the free-stream velocity. In addition, the rotation of the blade in its plane causes an extra velocity that each cross section of the blade experiences.

In this work, the steady BEM model is used to obtain the velocities that each cross section of the blade experiences. Since the radial induction factors are much smaller than the axial induction factors, they are neglected. The influence of the pitch controller is also taken into account for the above rated region.

These modified wind velocities are used for the calculation of instabilities at different operational points of the wind turbine from the cut-in to cut-out wind speed.

6.5.2 Modification of the airfoil data

The lift expression of the Theodorsen solution presented in equation 6.11 is developed for a flat plate. Therefore, it uses a value of 2π for the lift slope, $\frac{\partial C_l}{\partial \alpha}$.

In this work, the 2π value is replaced by the real value of $\frac{\partial C_l}{\partial \alpha}$ from the airfoil data of each section of the blade. This value, $\frac{\partial C_l}{\partial \alpha}$, is obtained by fitting a linear curve to the airfoil data between the zero-lift angle and the separation angle. Thus, the resultant lift expression can be explained by:

$$L = \frac{\partial C_l}{\partial \alpha} \rho U^2 b \left[\frac{C(k)}{U} \dot{h} + C(k)\alpha + [1 + C(k)(1 - 2a)] \frac{b}{2U} \dot{\alpha} + \frac{b}{2U^2} \ddot{h} - \frac{b^2 a}{2U^2} \ddot{\alpha} \right] \quad (6.14)$$

The expression of the moment given by equation 6.12 is also modified by replacing 2π , with the real slope of the airfoil, $\frac{\partial C_m}{\partial \alpha}$, thus:

$$M = \frac{\partial C_m}{\partial \alpha} \rho U^2 b \left[d_1 \left[\frac{C(k)}{U} \dot{h} + C(k)\alpha + [1 + C(k)(1 - 2a)] \frac{b}{2U} \dot{\alpha} \right] + \frac{b^2}{2U} \dot{\alpha} \left(a - \frac{1}{2} \right) + \frac{ab^2}{2U^2} \ddot{h} + \frac{b^3}{2U^2} \ddot{\alpha} \left(\frac{1}{8} - a^2 \right) \right] \quad (6.15)$$

6.5.3 The inclusion of the drag force

In the lift and moment expressions of the previous subsection the flow is assumed to be incompressible, irrotational and inviscid. Using these assumptions, the separation on the airfoil does not happen and the flow regime remains laminar. Thus a linear relation between the drag coefficient, C_d , and the angle of attack, α , can be assumed.

The slope of this line, $\frac{\partial C_d}{\partial \alpha}$, is obtained by fitting a linear curve to the airfoil data before the separation angle of attack. Hence, the drag coefficient is computed using the following equation:

$$C_d = \frac{\partial C_d}{\partial \alpha} \cdot \alpha \quad (6.16)$$

The unsteady angle of attack, α , can be obtained from equation 6.14, and by substituting that into equation 6.16 the drag coefficient can be found:

$$C_d = \frac{\partial C_d}{\partial \alpha} \cdot \left[\frac{L}{\frac{\partial C_l}{\partial \alpha} C(k) \rho U^2 b} - \frac{\dot{h}}{U} - \frac{b}{2U^2 C(k)} \ddot{h} - [1 + C(k)(1 - 2a)] \frac{b}{2UC(k)} \dot{\alpha} + \right.$$

$$\frac{b^2 a}{2U^2 C(k)} \ddot{\alpha}] \quad (6.17)$$

Simplifying equation 6.17, the drag force on the airfoil is obtained using the following equation:

$$D = \rho U^2 b \frac{\partial C_d}{\partial \alpha} \left[-\frac{C(k)}{U} \dot{h} - C(k) \alpha + [1 + C(k)(1 - 2a)] \frac{b}{2U} \dot{\alpha} - \frac{b}{2U^2} \ddot{h} + \frac{b^2 a}{2U^2} \ddot{\alpha} \right] \quad (6.18)$$

6.5.4 Discretization of the 3D blade to 2D sections

The blade of the wind turbine is discretized in several stations along its longitudinal axis, with each section having a fixed chord. As figure 6.5 shows, this enables the representation of a 3D blade as a summation of several 2D stations.

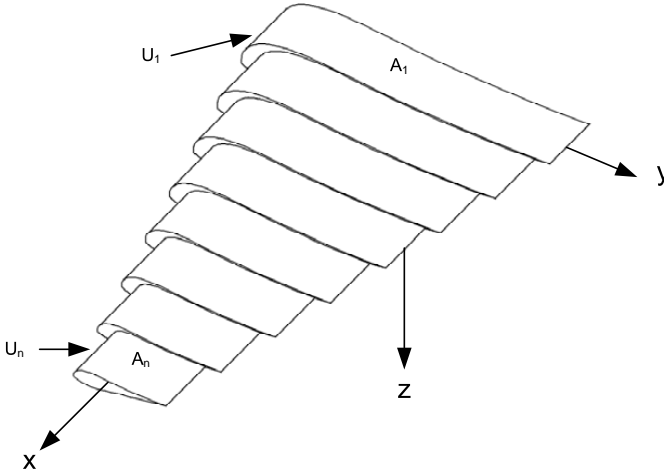


Figure 6.5: Discretization of a 3D blade to several 2D stations

Using this definition, lift, drag and moment can be calculated using the 2D unsteady aerodynamic model of Theodorsen. Thus, the lift, drag and moment on each 2D section of the blade are obtained using the following expressions:

$$L_i = \left(\frac{\partial C_l}{\partial \alpha} \right)_i \rho U_i^2 b_i \left[\frac{C(k)}{U_i} \dot{h}_i + C(k) \alpha_i + [1 + C(k)(1 - 2a_i)] \frac{b_i}{2U_i} \dot{\alpha}_i + \frac{b_i}{2U_i^2} \ddot{h}_i - \frac{b_i^2 a_i}{2U_i^2} \ddot{\alpha}_i \right] \cdot A_i \quad (6.19)$$

Where A_i is the area of each cross section.

$$M_i = \left(\frac{\partial C_m}{\partial \alpha}\right)_i \rho U_i^2 b_i \left[d_i \left[\frac{C(k)}{U_i} \dot{h}_i + C(k) \alpha_i + [1 + C(k)(1 - 2a_i)] \frac{b_i}{2U_i} \dot{\alpha}_i \right] + \frac{b_i^2}{2U_i} \dot{\alpha}_i \left(a_i - \frac{1}{2} \right) + \frac{a_i b_i^2}{2U_i^2} \ddot{h}_i + \frac{b_i^3}{2U_i^2} \ddot{\alpha}_i \left(\frac{1}{8} - a_i^2 \right) \right] \quad (6.20)$$

$$D_i = \left(\frac{\partial C_d}{\partial \alpha}\right)_i \rho U_i^2 b_i \left[-\frac{C(k)}{U_i} \dot{h}_i - C(k) \alpha_i + [1 + C(k)(1 - 2a_i)] \frac{b_i}{2U_i} \dot{\alpha}_i - \frac{b_i}{2U_i^2} \ddot{h}_i + \frac{b_i^2 a_i}{2U_i^2} \ddot{\alpha}_i \right] \quad (6.21)$$

6.5.5 Derivation of the aerodynamic matrices in a FE form

As explained in section 6.4, the structural model of the wind turbine is represented by mass, damping and stiffness matrices. Similarly, lift, drag and moment loads explained in section 6.5 need to be represented in mass, damping and stiffness matrices form to construct the aeroelastic model of the wind turbine. This enables the usage of a FE notation for both the structure and aerodynamics for the subsequent complex eigenvalue analysis.

The extraction of the aerodynamic matrices is employed using the principle of virtual work, and it is explained in detail in appendix H. With this principle, the aerodynamic mass, damping and stiffness matrices can be obtained that represent the complex-valued Theodorsen function.

6.6 Coupling structural and aerodynamic FE matrices

The coupling of the extracted FE aerodynamic and structural matrices (including the rotational effect) is presented in this section. The coupled system of equations represents the dynamic behavior of the turbine. As it was shown before, the coupling between the structural model and the body forces can be presented as:

$$[\mathbf{M}_s] \frac{d^2 \mathbf{u}}{dt^2} + [\mathbf{D}_s + \mathbf{D}_r] \frac{d\mathbf{u}}{dt} + [\mathbf{K}_s - \mathbf{K}_r] \mathbf{u} = \mathbf{F}(t) \quad (6.22)$$

The external forces, $\mathbf{F}(t)$, in this equation are the aerodynamic forces $[\mathbf{F}_a]$ that are represented by:

$$[\mathbf{F}_a] = [\mathbf{M}_A][\ddot{\mathbf{u}}] + [\mathbf{D}_A][\dot{\mathbf{u}}] + [\mathbf{K}_A][\mathbf{u}] \quad (6.23)$$

Replacing equation 6.23 on the right hand side of equation 6.22 results in:

$$[\mathbf{M}_s] \frac{d^2 \mathbf{u}}{dt^2} + [\mathbf{D}_s + \mathbf{D}_r] \frac{d\mathbf{u}}{dt} + [\mathbf{K}_s - \mathbf{K}_r] \mathbf{u} = [\mathbf{M}_A] [\ddot{\mathbf{u}}] + [\mathbf{D}_A] [\dot{\mathbf{u}}] + [\mathbf{K}_A] [\mathbf{u}] \quad (6.24)$$

Rearranging this equation by factorizing its displacement, velocity and acceleration terms results in:

$$[\mathbf{M}_s - \mathbf{M}_A] \frac{d^2 \mathbf{u}}{dt^2} + [\mathbf{D}_s + \mathbf{D}_r - \mathbf{D}_A] \frac{d\mathbf{u}}{dt} + [\mathbf{K}_s - \mathbf{K}_r - \mathbf{K}_A] \mathbf{u} = \mathbf{0} \quad (6.25)$$

Equation 6.25 represents the aeroelastic coupled matrices and can be written in its final form as:

$$[\mathbf{M}_t] \frac{d^2 \mathbf{u}}{dt^2} + [\mathbf{D}_t] \frac{d\mathbf{u}}{dt} + [\mathbf{K}_t] \mathbf{u} = \mathbf{0} \quad (6.26)$$

Where:

$[\mathbf{M}_t]$: the complex mass matrix of the complete model equal to $[\mathbf{M}_s - \mathbf{M}_A]$.

$[\mathbf{D}_t]$: the complex damping matrix of the complete model equal to $[\mathbf{D}_s + \mathbf{D}_r - \mathbf{D}_A]$.

$[\mathbf{K}_t]$: the complex stiffness matrix of the complete model equal to $[\mathbf{K}_s - \mathbf{K}_r - \mathbf{K}_A]$.

6.7 Eigenvalue analysis of the coupled aeroelastic model

The eigenvalues of the coupled aeroelastic matrices of equation 6.26 are solved using the Arnoldi algorithm with spectral transformation, Saad (1980). This algorithm treats equation 6.26 as an eigenvalue problem to find the eigenvalues and eigenvectors.

Assuming a simple harmonic motion as $\mathbf{u} = C \cdot \mathbf{X}e^{\lambda t}$, and replacing that in equation 6.26 results in:

$$([\mathbf{A}] - \lambda[\mathbf{B}])\mathbf{X} = \mathbf{0} \quad (6.27)$$

Here, λ represents the eigenvalues with the corresponding eigenvectors as \mathbf{X} . A and B matrices are also given by the following equations:

$$[\mathbf{A}] = \begin{bmatrix} \mathbf{I} & \mathbf{0} \\ \mathbf{0} & \mathbf{K}_t \end{bmatrix} \quad (6.28)$$

$$[\mathbf{B}] = \begin{bmatrix} \mathbf{0} & \mathbf{I} \\ -\mathbf{M}_t & -\mathbf{D}_t \end{bmatrix} \quad (6.29)$$

Based on the sign of the real (Γ), and the imaginary (Θ) parts of the eigenvalues that are found by the algorithm, different scenarios can happen. Figure 6.6 shows these different scenarios. As can be seen from the figure, two different instabilities can be identified, static and dynamic. These two cases are explained in more detail in the following subsections.

6.7.1 Static instability

The first unstable static operational points are computed iteratively by the algorithm in the following steps:

1. A given set of wind velocities from the cut-in to cut-out are selected.
2. At every given wind velocity the corresponding steady rotational speed and the relative wind velocities at every section are calculated.
3. The coupled aeroelastic model of the system is constructed for these initial values.
4. A set of values for the reduced frequency, k , to perturb the aeroelastic model are selected. These values are:

$$k = [0.001, 0.1429, 0.2857, 0.4286, 0.5714, 0.7143, 0.8571, 1.0000].$$

5. For the given wind and rotor speed, and a given reduced frequency the algorithm finds the eigenvalues of the problem.
6. From the obtained eigenvalues, those that have a zero imaginary part are filtered and selected.
7. From the selected eigenvalues of step 6, those that have a positive real part are filtered and selected.
8. If in step 7, no unstable point is found the process goes to step 4 and picks the next reduced frequency.
9. If in step 8, an unstable point is found it will be saved and the process goes to step 1 and picks the next wind velocity.
10. The process stops after checking the last wind velocity.

6.7.2 Dynamic instability

The first unstable dynamic operational points are computed iteratively by the algorithm in the following steps:

1. A given set of wind velocities from the cut-in to cut-out are selected.
2. At every given wind velocity the corresponding steady rotational speed and the relative wind velocities at every section are calculated.
3. The coupled aeroelastic model of the system is constructed for these initial values.
4. A set of values for the reduced frequency, k , to perturb the aeroelastic model are

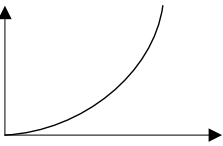
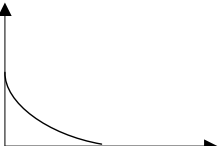

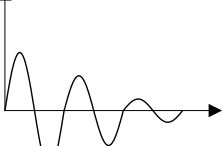
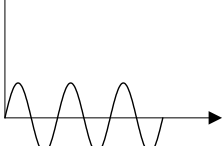
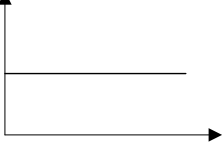
Eigenvalue = $\pm \Gamma \pm \Theta$				
Γ	Θ	Type of motion	Stability characteristic	Shape of motion
> 0	$= 0$	Continuous divergence	Unstable	
< 0	$= 0$	Continuous convergence	Stable	
> 0	$\neq 0$	Divergent oscillation	Unstable	
< 0	$\neq 0$	Convergent oscillation	Stable	
$= 0$	$\neq 0$	Simple harmonic	Stability boundary	
$= 0$	$= 0$	Time independent	Stability boundary	

Figure 6.6: Types of motion and stability characteristics for various types of eigenvalues

selected. These values are:

$$k = [0.001, 0.1429, 0.2857, 0.4286, 0.5714, 0.7143, 0.8571, 1.0000].$$

5. For the given wind and rotor speed, and a given reduced frequency the algorithm finds the eigenvalues of the problem.
6. From the obtained eigenvalues, those that have a positive imaginary part are filtered and selected.
7. From the selected eigenvalues of step 6, those that have a positive real part are filtered and selected.
8. If in step 7, no unstable point is found the process goes to step 4 and picks the next reduced frequency.
9. If in step 8, an unstable point is found it will be saved and the process goes to step 1 and picks the next wind velocity.
10. The process stops after checking the last wind velocity.

6.8 Implementation of the method

The implementation of the method is carried out in three main steps: preprocessing, processing and postprocessing. These steps are illustrated in figure 6.7. For the preprocessing part, following input data needs to be defined by the user.

1. Blade length, chord and twist distribution at each radial position along the blade
2. Material properties of the blade at every section
3. Blade pitch angle, rotational speed and cut-in to cut-out wind speeds
4. Airfoil data at every station along the blade
5. Tower height, tower diameter at the base and top, and tower thickness at the base and top
6. Mass of the nacelle and its x-y-z location
7. Geometry and density of the hub

The preprocessing part is entirely parametric and given all the input data, it creates the geometry of the wind turbine. This task is carried out by a shell program that uses Patran Command Language (PCL) to generate this geometry.

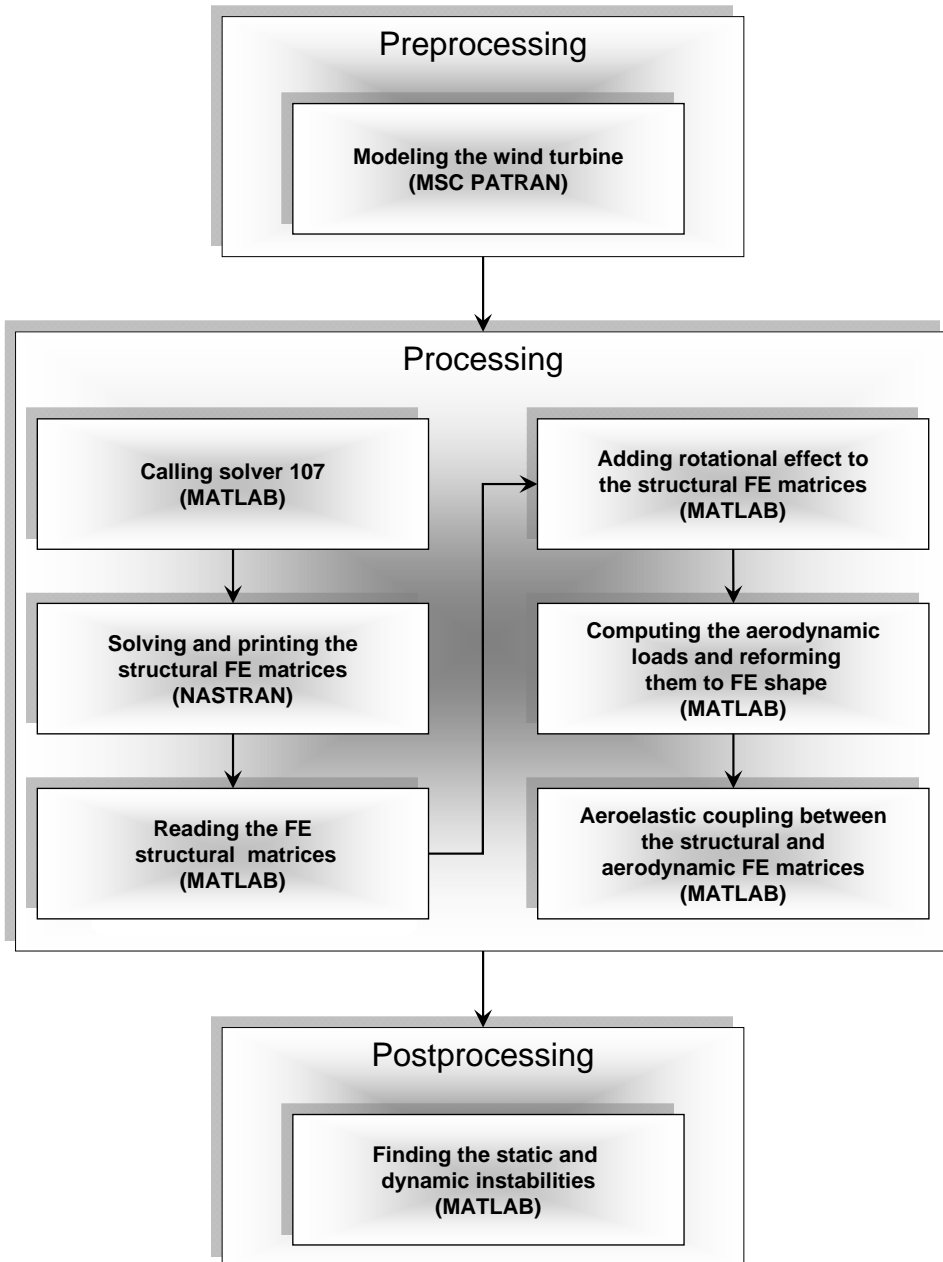


Figure 6.7: Steps of implementation the method in PATRAN/NASTRAN/MATLAB

In the processing part by executing NASTRAN solver 107, the geometry and the material property of the turbine is used to construct the FE model of the wind turbine. In this phase all the boundary conditions are applied at all the relevant junctions (the joint between the tower, nacelle, hub and blades is defined as rigid). Here, the nacelle is modeled as a nodal mass at its center of gravity that is given by the user. Then, the structural mass, damping and stiffness matrices are calculated and printed out as an output file. A MATLAB code reads these matrices and it automatically modifies the stiffness matrices to account the rotational effect.

In the next step, BEM theory is used to calculate the resultant wind velocity that each section of the blade experiences. Using this wind velocity the aerodynamic forces are calculated. As explained before, these forces are reformed in shape to have them as mass, damping and stiffness matrix form. Finally, as the last step in the processing part, the structural and aerodynamic matrices are coupled to construct the aeroelastic model of the wind turbine.

The postprocessing part starts with reading the aeroelastic model of the turbine and converting that to an eigenvalue problem. This eigenvalue problem is solved using the Arnoldi algorithm to find the eigenvectors and eigenvalues of the system. In the processing and postprocessing steps, a combination of MATLAB and DMAP (Direct Matrix Abstraction Programming) languages is used to do the programming.

Verification and aeroelastic stability analysis of the 20 MW wind turbine

7.1 Introduction

In the previous chapter the theory behind the development of the aeroelastic stability method was explained, and it was shown how the method is implemented. The result was a computer code to find the unstable operational points of a wind turbine.

This chapter shows the verification of the method by finding the stability margin of the 5 MW NREL wind turbine and compares that with existing studies on the aeroelastic stability analysis in the literature. It should be noted that the optimized 5 MW wind turbine can not be used for verification purpose, since there is no available stability data on this machine and therefore the 5 MW NREL wind turbine is used instead.

After doing the verification of the developed code, the aeroelastic stability analysis of the 20 MW wind turbine is carried out, since it is a more flexible design comparing to the 5 and 10 MW wind turbines. If the 20 MW wind turbine shows instability problems then also the smaller designs (5 and 10 MW) are checked against stability criterion. Otherwise it can be assumed that they are safe designs from an aeroelastic stability point of view.

7.2 The finite element model of the wind turbine

The finite element model of the wind turbine consists of four different submodels. These are: the tower, the nacelle, the hub and the blades. The developed parametric model is used to generate the geometry (and mesh) of the turbine.

Both the blade and tower are modeled using the Quad4 elements. For the tower, the boundary condition is imposed by fixing all the nodes at the tower base. This means that all the DOFs of the bottom nodes are zero. For the connection between the blades, hub,

nacelle and tower top, the DOF of all the common nodes is set to equal. This results in a rigid connection between these components.

For the purpose of simplicity, the nacelle is modeled with an equivalent center of gravity contributed from all components. Similarly, the hub is modeled as a disk with its center of gravity located in the geometrical center of the hub. Figure 7.1 illustrates the modeling approach of the nacelle and hub of the 20 MW wind turbine.

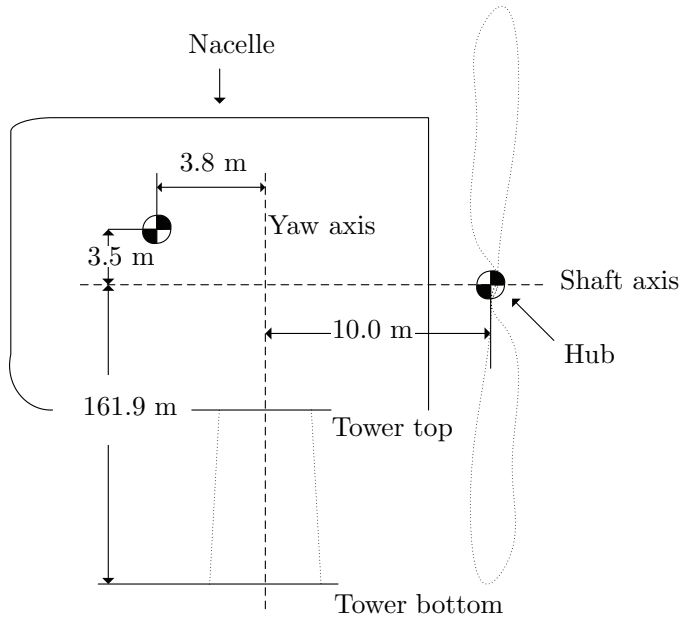


Figure 7.1: Nacelle and hub center of mass for the 20 MW wind turbine

7.3 Verification of the stability analysis method

The 5 MW NREL wind turbine is the model to verify the developed aeroelastic stability method due to the availability of a similar study in the literature on this machine, which makes the comparison and verification possible, Meng et al. (2008). Before using the method to find the instabilities, a few verification cases are useful to gain confidence in this computational tool. This is done by three different case studies as follow:

- **2D analytical stability analysis:** To have a feeling about the magnitude of instabilities and get some physical insight of the problem, a 2D analytical flutter analysis of a section of the 5 MW blade is first carried out. This can give an estimation of the instability boundary as well as the expected overall behavior of the blade at different operational points.
- **Undeformed state eigenvalue analysis of the structural model:** The eigenvalues of the structural FE model (including the rotational effect) are computed without

any aerodynamic loads (undeformed state). Then, the results are compared with an eigenvalue analysis of a rotating blade that is carried out using the FAST aeroelastic code to make sure that the structural formulation of the problem is correct and has an acceptable accuracy.

- **Full aeroelastic stability analysis:** The developed structural model is coupled with two different aerodynamic models. The first model is the original Theodorsen function with lift and moment terms and the second model is a more advanced formulation of the first model that includes the drag term as well. The results of this step can demonstrate up to a great extent the accuracy of the proposed method. Therefore, a comparison is made with a similar study to say the final words about its accuracy.

These three different case studies are explained in detail in the following subsections.

7.3.1 2D analytical stability analysis

Today, the majority of the aeroelastic stability analysis methods are complex and involve the detailed treatment of the stability problem. Although these analyses will probably yield accurate results, they are cumbersome to implement and the physical understanding of the stability problem is easily lost.

To overcome this short coming (specially in the first stages of the design), it is a common practice to use a 2D analytical stability analysis, (see for instance [Chaviaropoulos et al. \(2003\)](#)). In this way more physical insight to the problem can be achieved and the designer can have a feeling about the order of magnitude of the unstable operational points to expect.

For the same purpose, the goal of developing this analytical model here is to find the instabilities and compare the order of their magnitudes with the full aeroelastic model. This model is 2D and it uses the blade structural properties at the 75% radial position. The model has two DOFs, h for the plunge motion (corresponding to bending in flapwise direction), and α for the twist. For the aerodynamic loads, the Theodorsen unsteady aerodynamic model is used. Figure 7.2 shows this typical section.

For this configuration, the equations of motion can be obtained by applying Newton's second law as:

$$m\ddot{h} + S_\alpha\ddot{\alpha} + L(t) + K_h h = 0 \quad (7.1)$$

Where:

S_α : the static moment related to EA and defined as $m x_\alpha b$

m : mass per unit length

K_h : flapwise stiffness

Similarly, for the moments around elastic axis we have:

$$S_\alpha\ddot{h} + I_\alpha\ddot{\alpha} + K_\alpha\alpha - M(t) = 0 \quad (7.2)$$

Here, I_α is the mass moment of inertia around EA and K_α is the torsional stiffness. Also, $L(t)$ and $M(t)$ are the Theodorsen unsteady aerodynamic lift and moment, as presented before in chapter 6 by equation 6.14 and 6.15, respectively.

Table 7.1: 5 MW sectional properties at 75% blade span

Sectional property	Value (Unit)
Chord	2.7 (m)
Mass	138.9 (kg/m)
Mass moment of inertia	27.7 (kg · m ²)
Flapwise stiffness	2.7E3 (N · m ²)
Torsional stiffness	3.5E5 (N · m/rad)
Radial position	47.7 (m)

To find a solution for equation 7.3, it is assumed that the 2 DOF response of the section, $\mathbf{X} = [h \ \alpha]^t$, is of the form $X = \hat{x}e^{pt}$ (simple harmonic motion) with p defined as $p = (\sigma + i\omega)$. The real component of p corresponds to the growth rate of the motion and its imaginary part corresponds to the frequency of oscillation.

Replacing this harmonic solution in equation 7.3 leads to the characteristic equation that in this case can only be solved numerically. For non-trivial X the determinant of the coefficient matrix must be zero at instabilities. Using the values presented in table 7.1, the instabilities are found numerically and presented in figure 7.3 for the 5 MW blade section.

The unstable rotational speeds are highly dependent on the reduced frequency value. Although, this means that the model is sensitive to the input parameters, it can give reliable estimates of the magnitude of instability as well as the overall behavior of the blade at different operational points.

As expected, instabilities occur in all operational conditions from the cut-in to cut-out

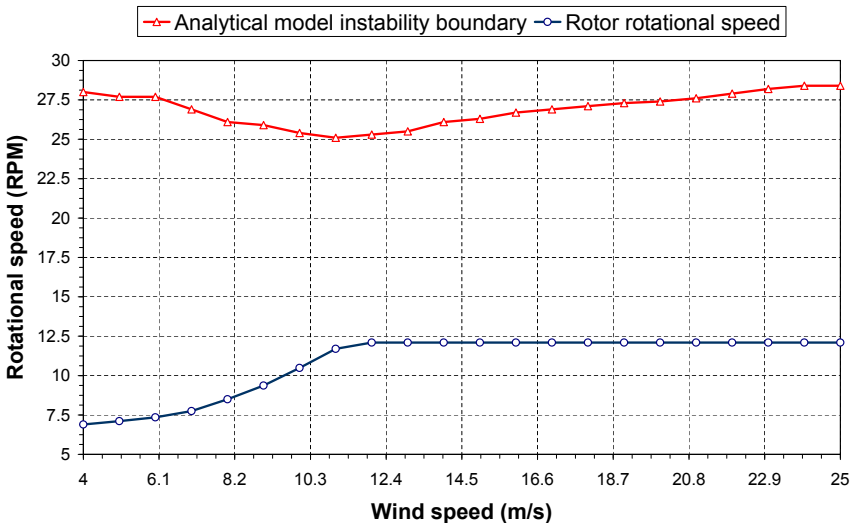


Figure 7.3: Instabilities predicted by the 2D analytical model

at low reduced frequency values. The above analysis, apart from qualitatively allowing the designer to investigate the effect of changing the value of parameters, also enables him to quantify instabilities and hence the definition of a suitable comparison case for verification purposes.

7.3.2 Undeformed state eigenvalue analysis of the structural model

In this subsection a verification study is carried out to check the modeling of the structure and investigate the influence of centrifugal forces in a rotating blade. It is also meant to verify the correct implementation of the method as a computer code. Therefore, only the structural model of the rotor is considered and the eigenfrequencies are compared with a modal analysis study in FAST aeroelastic code.

In the first verification case the rotor speed is set at zero *RPM*, without any aerodynamic loads. Thus, the modal analysis computes the eigenfrequency of this rotor without any centrifugal force and the results are compared with FAST on the same basis. In the second verification case, this approach is repeated with a spinning rotor that rotates at its rated value (again no aerodynamic loads). The results of these two cases are shown in table 7.2 and 7.3, respectively.

Table 7.2: Comparison of the 5 MW FE natural frequencies with FAST at zero RPM

Frequency	FAST (Hz)	FE (Hz)	Deviation (%)
First blade flapwise	0.6946	0.6880	- 0.95
Second blade flapwise	2.0175	2.0521	+ 1.71
First blade edgewise pitch	1.0886	1.1181	+ 2.70

Table 7.3: Comparison of the 5 MW FE natural frequencies with FAST at 12.1 RPM

Frequency	FAST (Hz)	FE (Hz)	Deviation (%)
First blade flapwise	0.7470	0.7389	- 1.08
Second blade flapwise	2.0767	2.1292	+ 2.52
First blade edgewise pitch	1.1158	1.1448	+ 2.59

As table 7.2 and 7.3 show, the absolute difference in predicting the first three eigenfrequencies when compared to FAST aeroelastic code is less than 2.7%. Small differences are due to different ways of modeling the mass and stiffness distribution along the blade. In FAST, both properties are defined as inputs at some discreet stations along the blade, whereas in the FE model of this work, the thicknesses and external geometry of the blade are defined as inputs and mass and stiffness distributions are calculated from the element properties of the continuous blade by the FE code.

7.3.3 Full aeroelastic stability analysis

As a further investigation, the aeroelastic stability computational tool is compared with another stability study on the 5 MW NREL wind turbine carried out by Meng et al. (2008).

Comparison with the result of this work is used to demonstrated the accuracy of the method.

Meng presented a method for aeroelastic modeling of a wind turbine based on time domain multibody dynamic approach that includes the rotor, nacelle and tower. However, time domain simulation of instabilities gives no information about the blade modal interactions or system frequencies. Therefore, he applied system identification on the time domain model to find the frequency that the flap and torsion mode merge together and cause instability.

At his study only the instabilities at 10 *m/s* wind speed are considered and the rotational speed of the rotor gradually speeds up from 12 to 19 *RPM*. The distinguished feature of flutter is the increasing amplitude of both torsion and flap motions to a point where in practical terms failure of the blade occurs. Thus, he found that under this assumption, the flapwise and torsional mode of the 5 MW blade merge together at 19 *RPM*.

Figure 7.4 shows the computed instabilities for the 5 MW NREL wind turbine. For the purpose of comparison, this figure also presents the 2D analytical solution and the instability analysis prediction of Meng et al. (2008).

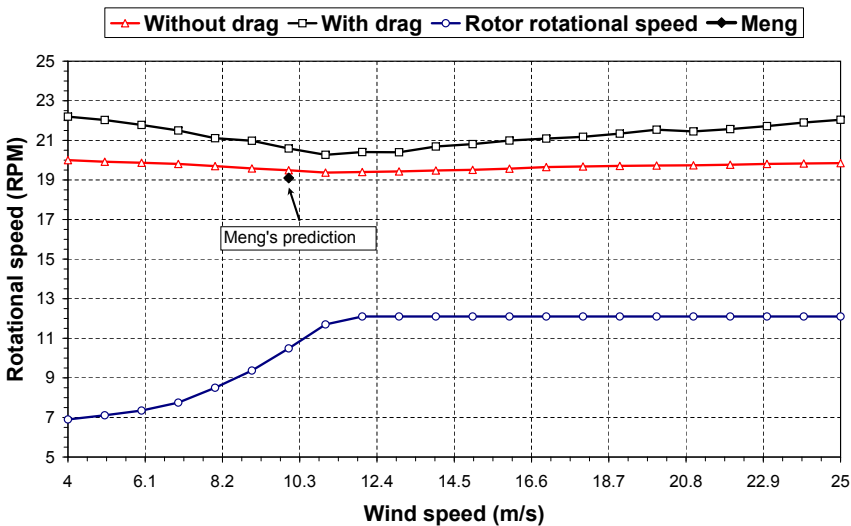


Figure 7.4: Dynamic instabilities for the 5 MW NREL wind turbine

The figure shows two type of solutions. They both use the Theodorsen unsteady aerodynamic model but one with and the other without the drag term. As it can be seen from the figure, the aerodynamic model with the drag term predicts higher rotational speed at which the instabilities occur. This is due to the dissipation of energy from the system by the drag term that means an increase of the system's capacity to carry more energy from the flow at higher rotational speeds, which at the end has an stabilizing effect.

Another fact in this figure is the overestimation of the rotor speed at which the instabilities occur by the analytical model. Although, the accuracy of this method is ques-

tionable, it predicts the physical variation of the system well.

Furthermore, at 10 m/s the instability predicted by the aerodynamic model without the drag term shows a slightly higher value than Meng's study. This difference is about 2%. Similarly, the aerodynamic model with both the lift and drag term predicts a higher value of about 7.8%. However, the difference among these three different methods is acceptable for a design study in the preliminary stage.

The safety margin of the 5 MW turbine against instabilities is another important design consideration to address. As the graph shows at the rated wind speed this margin is the minimum for the aerodynamic model without drag. Thus, using this model a safety margin of 60.1% can be concluded, which means that this is a safe design.

Considering all the facts, a good agreement between the predicted instabilities based on the work of Meng et al. (2008) and the developed method in this thesis exists.

7.4 Stability analysis of the 20 MW wind turbine

The previous section presented the verification of the method. Although instabilities are not expected for the 20 MW wind turbine, an analysis is required to guarantee the stability of this design. Therefore, this section presents the aeroelastic stability analysis for the optimized 20 MW wind turbine presented in chapter 5.

The unstable operational points can be divided into static and dynamic, and therefore also studied here in the same manner (for a definition of the static and dynamic operational points refer to section 6.7 of chapter 6). For both types of instabilities the two aerodynamic models mentioned before are used.

- **Static stability analysis**

The static unstable operational points (divergence) of the 20 MW wind turbine are plotted in figure 7.5. The plot shows two types of solutions. These two use the Theodorsen unsteady aerodynamic model but one with and the other without the drag term. As it can be seen the aerodynamic model with the drag term predicts higher unstable speeds.

Instabilities predicted without the drag term show a lower value at each operational point. The predicted rotational speeds are higher than the rated rotor speed of the 20 MW wind turbine, with a minimum of 46.0% as safety margin at the rated wind speed and therefore static instabilities are not expected here.

- **Dynamic stability analysis**

Figure 7.6 shows the dynamic unstable operational points of the 20 MW wind turbine. Similar to the static case, the plot presents two type of solutions. These are the Theodorsen aerodynamic model with and without the drag term.

Since the aerodynamic model without the drag term predicts a more conservative stability margin, it is used to obtain the safety margin. As figure 7.6 shows, at the rated wind speed this margin is minimum and has a value of 20.4%, while this value for the static case was higher with a value of 46.0%.

Based on the linear scaling laws presented in chapter 2, both the eigenfrequencies and the rated rotor speed when upscaling linearly from 5 to 20 MW decrease by 50% (or R^{-1} with $R = 2$). This means that the safety margins against instabilities

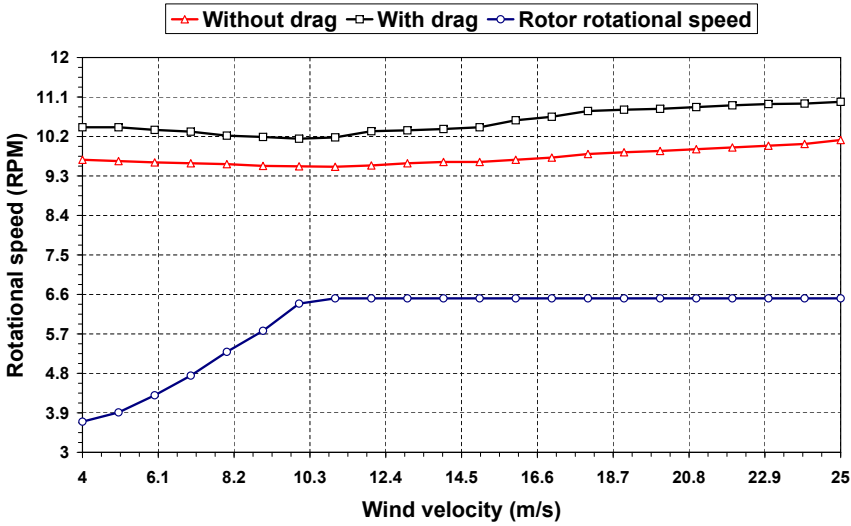


Figure 7.5: Static instabilities (divergence) for the 20 MW wind turbine

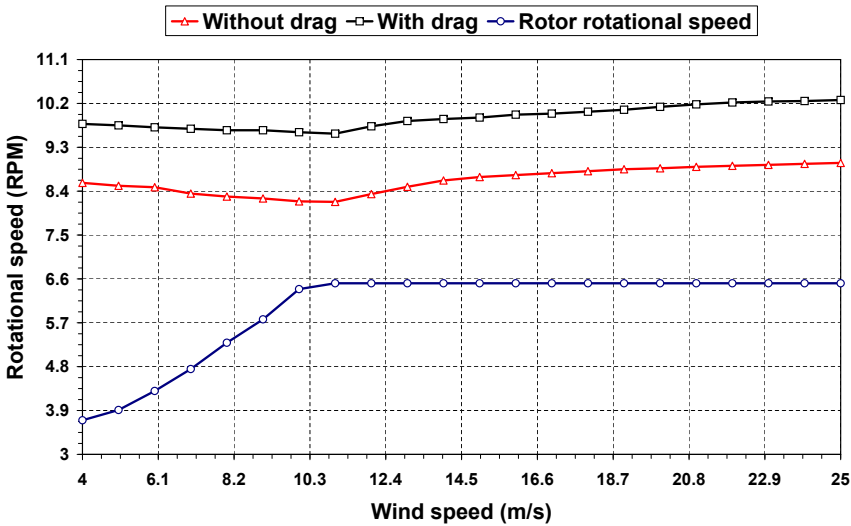


Figure 7.6: Dynamic instabilities (flutter) for the 20 MW wind turbine

remains unchanged.

When looking at the dynamic safety margins of the 5 and 20 MW wind turbines, one can see that this value decreases from 60.0% to 20.4%. This means that during the upscaling process the design experiences more reduction in its flexibility (or stiffness) than what linear scaling laws state.

Considering all the facts, the predicted rotational speeds for both the static and

dynamic instabilities are higher than the designed rated rotor speed of the 20 MW wind turbine and therefore no aeroelastic instabilities are expected for this machine.

7.5 Concluding remarks

The analysis developed here has shown to be useful for predicting instabilities of wind turbines and it can be concluded that the developed aeroelastic stability method can be used as a preliminary tool to find the unstable operational points of a given wind turbine configuration with a reasonable accuracy.

Two observations has been made based on the results of the analysis as follow:

1. By comparing the static and dynamic instability boundary of the 5 and 20 MW wind turbines, it can be concluded that the static instabilities do not occur before the dynamics one.
2. Although, the 20 MW wind turbine does not show any instability, the instability criterion should be seen as a potential design drivers for larger scale wind turbines and thus the safety margin should be included as a design constraint in the design optimization problem formulation.

It also should be noted that the analysis is potentially weak in the following aspects:

1. It does not provide any data about the mode shapes at the instability point.
2. The huge amount of DOFs of the system makes it difficult to say which modes at the instability point are vibrating.
3. The dependency of the aerodynamic model to the reduced frequency makes the method cumbersome to find, by trial and error, the instabilities.
4. The method does not provide any information about the damping value at the instability point.

Scaling trends for future offshore wind turbines

8.1 Introduction

The development of the 5, 10 and 20 MW optimized wind turbines was carried out in the previous chapters. Based on these wind turbines, this chapter constructs scaling trends to study the influence of size on future offshore wind turbine designs and discusses the technical and economical barriers associated with them. The identified barriers can help to formulate the required research and technological changes affecting the development of very large wind turbines.

Loading-diameter, mass-diameter and cost-diameter as the most important trends to monitor and examine the scaling behavior are developed and discussed. However, two other useful trends are addressed as well. Whenever suitable, a comparison is made with the linear scaling laws and existing data trends presented before in chapter 2 to explain the scaling phenomenon and the underlying reason for any similarity or discrepancy.

8.2 Development of scaling trends

To evaluate whether large wind turbines are feasible to manufacture and may eventually be more cost effective, it is needed to analyze how size influences the design. This can be done by studying the loading, mass, cost and some other useful trends. For the loading trends, the trend exponent shows how the dynamic behavior of the wind turbine components (such as blade, tower and low speed shaft) changes with size. For the mass and cost trends, the trend exponent shows how upscaling impacts every individual mass and cost element as the size increases. Additionally, by comparing the share of every mass and cost elements to the total share, it can be seen how upscaling influences the cost or mass share at different scales.

All the trends are formulated as a function of rotor diameter. Rotor diameter is the

driver for loads on the wind turbine and it can properly reflect the dependency of the trends to size. Additionally, the rotor diameter is driving many of the technological innovations and can be used as a key indicator to identify the required technological developments. These trends are constructed using a power curve fit to the data points with rotor diameter as the independent parameter, i.e: aR^b with a as the curve coefficient, R as the rotor diameter and b as the curve exponent. The reason to use a power curve is the ease of comparison with the square-cube law as formulated by linear scaling law.

As explained before, no other scaling study should be justified without an underlying physical understanding. This understanding can be achieved by constructing scaling trends using a power curve and making a comparison on the same basis with linear scaling law (as well as existing data trends that are often presented in this form for the same reason).

These scaling trends are presented in detail in the following subsections. For this purpose the optimized 5, 10 and 20 MW wind turbines technical characteristics are used as the data points.

8.2.1 Loading-diameter trends

This subsection presents the loading-diameter trends of the blade, low speed shaft and tower as the main load carrying components of a wind turbine, based on the developed 5, 10 and 20 MW machines of the previous chapters. These trends are compared with the linear scaling laws and existing data trends of chapter 2 to examine and analyze the scaling behavior of larger wind turbines. In all the figures, the existing data trends are extrapolated to enable a visual comparison with the optimized data trends at larger scales.

1. Blade

For the blades of the wind turbine the highest loads are expected at the blade root where the connection is made with the hub. The linear scaling law predicts the moments of the blade to scale with R^3 for the flapwise, and R^4 for the edgewise component.

The flapwise moment is mainly aerodynamic driven and according to the existing data trend the corresponding bending moment at the root increases with $R^{2.86}$, (figure 2.1 of chapter 2). For the edgewise moment both the gravity and aerodynamic loads play a role and existing data trend shows that it scales with $R^{3.25}$ (figure 2.2 of chapter 2).

Figure 8.1 and 8.2 show the extreme blade flapwise and edgewise loading trends for the optimized wind turbines. For the purpose of comparing the existing data trends with the optimized wind turbine scaling trends, figure 2.1 and 2.2 are reploted and extrapolated beyond 90 m.

As can be seen the bending moment scales with $R^{2.62}$ and $R^{3.41}$ for the flapwise and edgewise components respectively. This means that the edgewise moment which is mainly gravity driven increases with size more than the flapwise moment that is aerodynamic driven. This is in line with linear scaling law that predicts the gravity driven loads to scale more rapidly than the aerodynamic driven loads as presented before in chapter 2. Table 8.1 summarizes the blade loads scaling behavior.

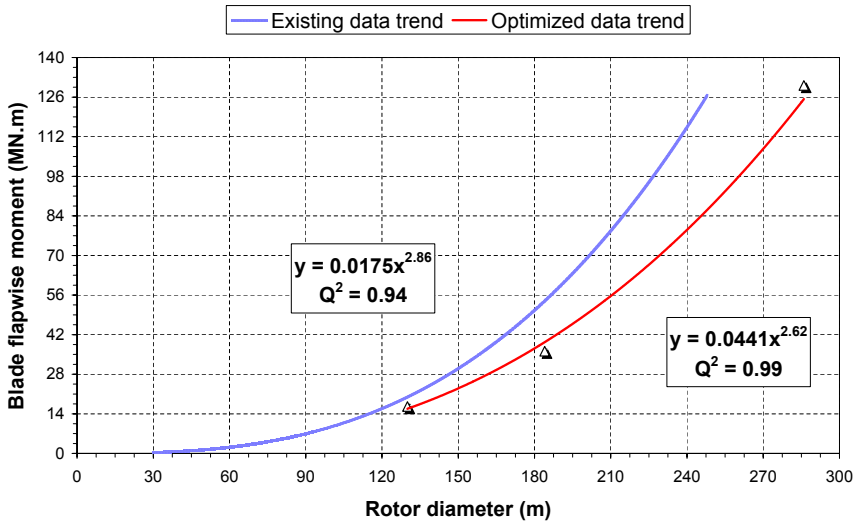


Figure 8.1: Curve fit to the extreme flapwise bending moment at blade root for the wind turbines from 5 to 20 MW and comparison with the extrapolated existing data trends

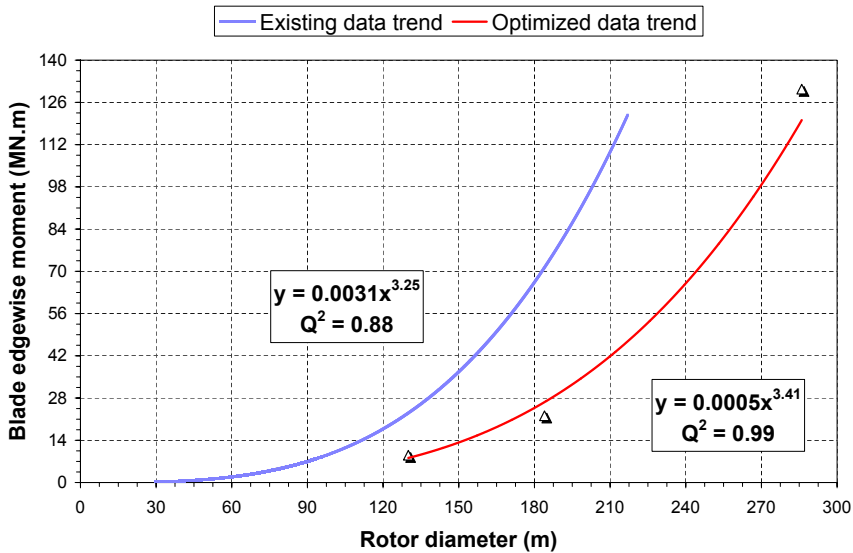


Figure 8.2: Curve fit to the extreme edgewise bending moment at blade root for the wind turbines from 5 to 20 MW and comparison with the extrapolated existing data trends

2. Low speed shaft

Shafts are mechanical components to transfer mainly torsional moments with a circular cross section that is optimal for this application. However, the low speed shaft of a wind turbine experiences bending and torsional moments at the same

Table 8.1: Comparison of the scaling trends for the blade’s loads

Loads component	Linear scaling law	Existing data	Optimized wind turbines
Flapwise	R^3	$R^{2.86}$	$R^{2.62}$
Edgewise	R^4	$R^{3.25}$	$R^{3.41}$

time. Bending on the low speed shaft is mainly gravity driven, caused by the rotor mass, and it is obtained by multiplying the rotor mass with the unsupported length of the shaft.

In this research, the length of the shaft is linearly scaled with size, but the mass of the rotor is an optimal mass obtained through optimization. According to the linear scaling law the bending moment due to the rotor weight scales with R^4 .

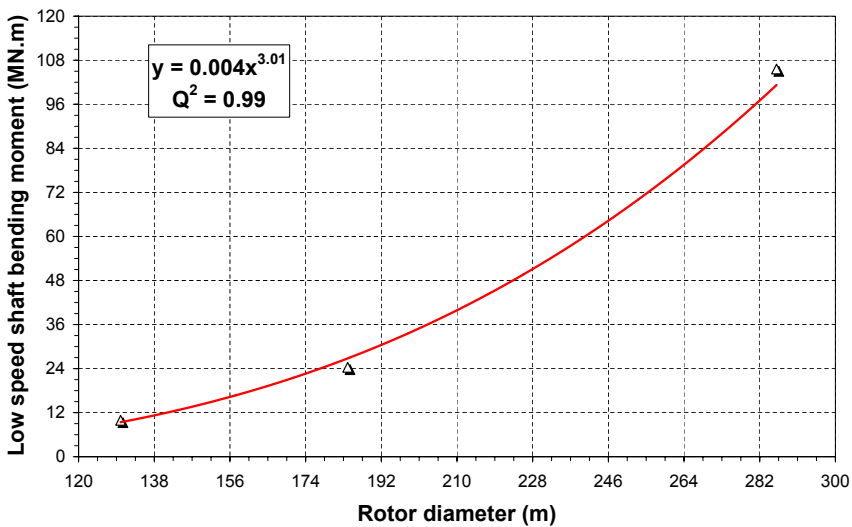


Figure 8.3: Curve fit to the extreme low speed shaft bending moment for the wind turbines from 5 to 20 MW

Figure 8.3 shows the bending moment trend for the optimized wind turbines as a function of rotor diameter. As can be seen the bending moment scales with $R^{3.01}$ for the optimized wind turbines. Unfortunately, there is no study available to show how the low speed shaft loads scale with size in practice. Therefore, this result can only be compared with the linear scaling law, which predicts a size escalation of R^4 .

For the shaft torsional moment, linear scaling law predicts the moment to scale with R^3 . Figure 8.4 shows how the shaft torsional moment scales with size for the optimized wind turbines. Here, the torsional moment scales with $R^{3.03}$, and a good match can be seen here with linear scaling law.

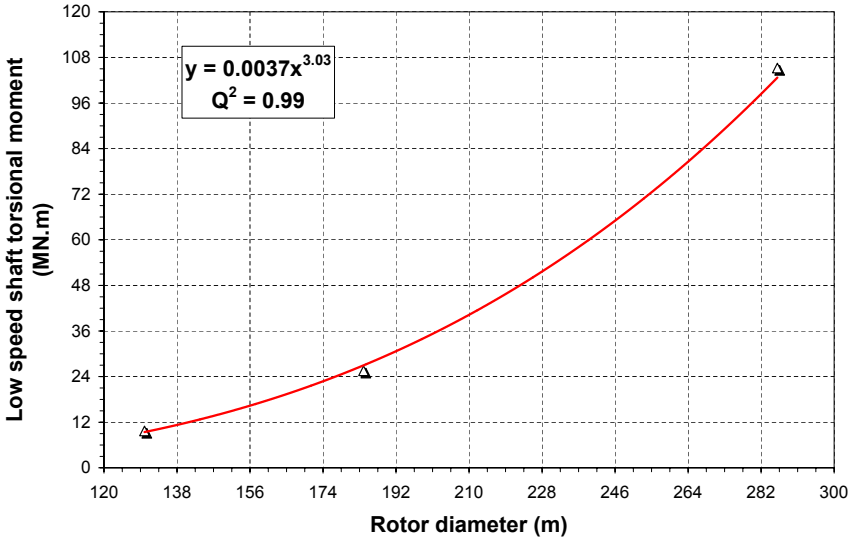


Figure 8.4: Curve fit to the extreme low speed shaft torsional moment for the wind turbines from 5 to 20 MW

3. Tower

In this research, all the loading-diameter trends are developed at the tower base where the moments are at their maximum. Figure 8.5 shows the tower fore-aft bending moment based on the optimized wind turbines data, which scales with $R^{2.92}$.

When compared with linear scaling law that predicts an increase in the moments by R^3 , a good match can be seen. However, by looking to the existing data trend with an escalation relation of $R^{2.33}$, the bending moment of the optimized wind turbines shows considerably larger increase as the turbines upscale.

However the scatter in the existing data is something to consider in this comparison. The quality of the curve fit to a data set can be measured with the Q-squared value, which in this case is 0.71. The Q-squared value is a statistical coefficient that shows the observer how effective the rotor diameter is at forecasting the fore-aft bending moment for a wide range of rotor diameters, with a value of one to show an excellent correlation and a value of zero for no correlation.

Thus, the accuracy of this correlation is questionable with such a low value Q-squared, and comparison of the optimized fore-aft moment with such a high data scatter may not be that appropriate.

It is also known from chapter 2 that the extreme tower fore-aft bending moment is mainly aerodynamic driven, and the "square" part of the linear scaling law works very well for the prediction of aerodynamic loads and performance as discussed before. Therefore, the good match between the linear scaling law and the data fit to the bending moment of the optimized wind turbines is more expected than the mismatch with the existing data trend considering such a poor Q-squared value.

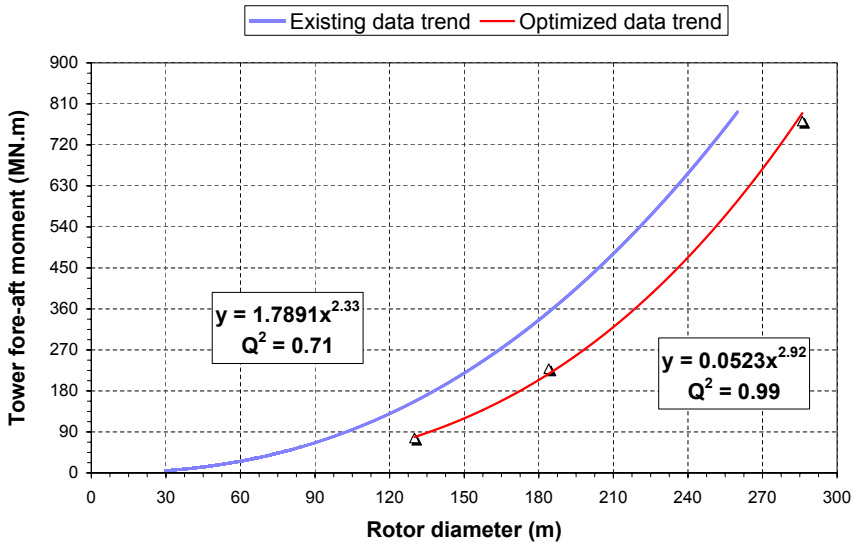


Figure 8.5: Curve fit to the extreme tower fore-aft bending moment at the base for the wind turbines from 5 to 20 MW and comparison with the extrapolated existing data trends

For the side-to-side moments, figure 8.6 shows that the bending moment of the optimized wind turbines scales with $R^{4.19}$. This is far above what linear scaling law and existing data trend predict.

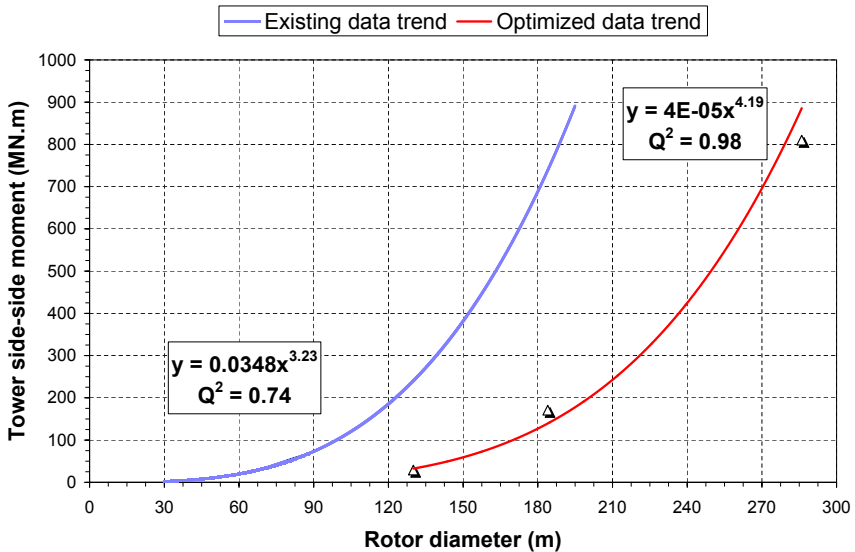


Figure 8.6: Curve fit to the extreme tower side-to-side bending moment at the base for the wind turbines from 5 to 20 MW and comparison with the extrapolated existing data trends

To explain that, first the loads that cause the side-to-side bending moment need to be identified. There are two main loading mechanisms that cause the side-to-side bending moment. First the asymmetric aerodynamic loads in the plane of rotation and second the mass imbalance at the tower top. While the former one scales with R^3 , the later scales with R^4 based on linear scaling law.

However, these scaling relations are only valid from a stationary point of view. Therefore, when doing a time domain simulation, the flexibility of the tower causes a dynamic amplification factor of the loads and this is well recognizable in the side-to-side motion.

Figure 8.7 shows the tower top fore-aft and side-to-side displacement trends. Based on this figure the tower top displacement in the fore-aft direction decreases with size, and for the side-to-side motion it shows an increase.

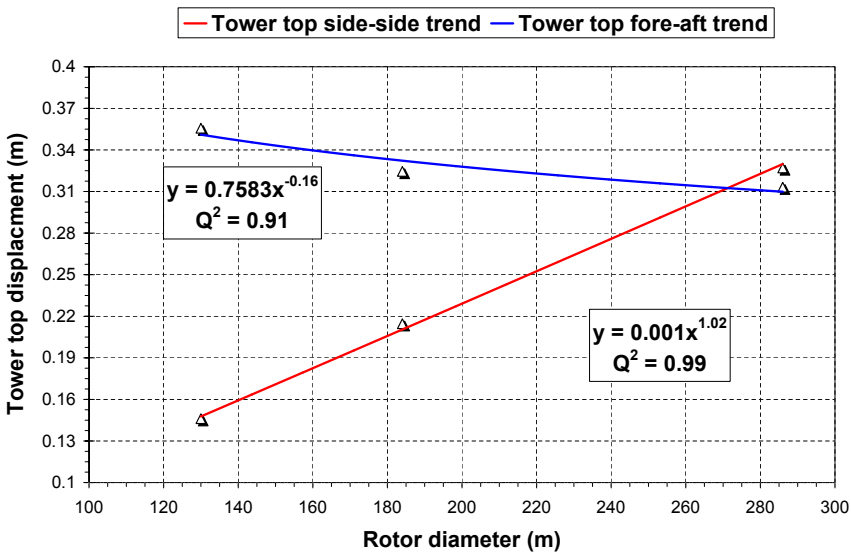


Figure 8.7: Tower top fore-aft and side-to-side deformation trend for the wind turbines from 5 to 20 MW

The trend exponent for the side-to-side moment increases more rapidly than the fore-aft, and can become a design challenge as the side-to-side moment will have almost the same magnitude as the fore-aft but being badly damped. This is an area to further investigate and to come up with new solutions to prevent such a phenomenon.

Another important load component at the tower base is the torsional moment. This is depicted in figure 8.8. Curve fit to the torsional moment of the optimized wind turbines shows a $R^{3.04}$ relation. While this is clearly a good match with the linear scaling law with an R^3 relation, it does not match with the existing data trend that has an exponent of 4.05.

As mentioned by Jamieson (2007), the reason for such a relatively high trend ex-

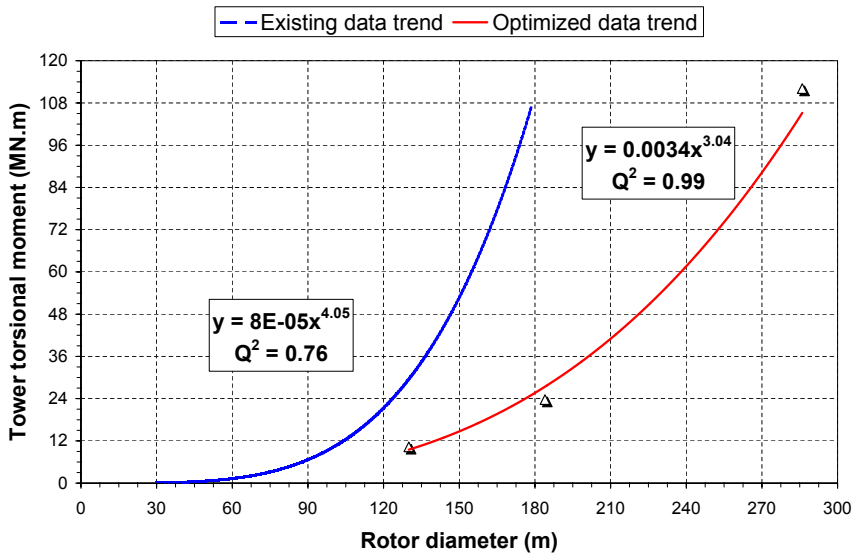


Figure 8.8: Curve fit to the extreme tower torsional moment at the base for the wind turbines from 5 to 20 MW and comparison with the extrapolated existing data trends

ponent is the imbalance of the yaw torque, which might be the effect of turbulence in creating differential loading across the rotor plane and as the size increases may become more severe. However, such a phenomenon is not visible for the larger wind turbines based on the results of this research.

Introduction of a yaw error in the simulation is another mechanism that can result in a higher torsional moment, and as the size increases it can become more severe. As requested by the IEC 61400-3 standard, wind turbines need to be simulated with the addition of $\pm 8^\circ$ yaw error for the certification purpose. Therefore, the optimised wind turbines are simulated again with the addition of $\pm 8^\circ$ yaw error. For this non-aligned case, the result is presented in figure 8.9. When comparing the curve exponent of 3.10 for the non-aligned case with the aligned case with an exponent of 3.04, it is clear that the introduction of a yaw error can also not contribute too much in the torsional moment increase at the tower base and be the reason for a high trend exponent in the existing data as the turbines upscale.

All in all, the reason to have such a high trend exponent in the existing data is not clear. However, similar to the tower base fore-aft and side-to-side moments, the Q-squared value of the torsional moment shows a poor correlation with rotor diameter with a value of 0.76, therefore, the quality of the presented curve is also questionable.

8.2.2 Mass-diameter trends

In the previous subsection, the loading-diameter trends of the optimized wind turbines were presented and analyzed. This subsection develops the mass-diameter trends and

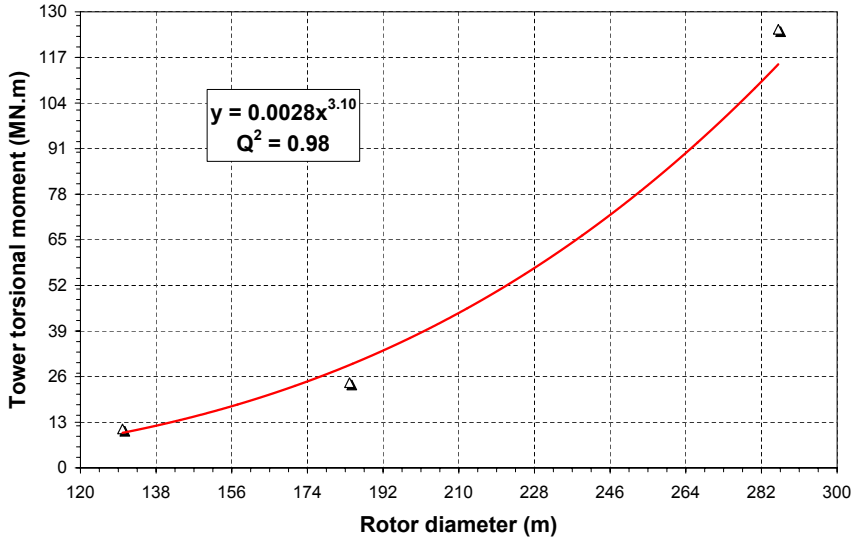


Figure 8.9: Curve fit to the extreme tower torsional moment at the base for the wind turbines from 5 to 20 MW with a yaw error

similar to the previous subsection compares that with the linear scaling law and existing data trend.

1. Blade

The mass of the optimized wind turbine blades is depicted in figure 8.10. As presented by the graph, the mass increase shows a trend exponent of 2.64. Although, this is lower than the linear scaling law exponent of 3, it is higher than the existing data with a trend exponent of 2.09.

This shows that upscaling of the existing wind turbines using the same materials, concept, topology and knowledge to larger scales influences the mass trend exponent in a negative way. Therefore, several modifications and improvements are needed to keep the trend exponent of the upscaled wind turbines in the same order (or even lower) as the existing wind turbines to mitigate this negative influence.

2. Tower top mass

As mentioned before, the tower top mass refers to all the components atop the tower including the rotor. Table 8.2 lists these components with their associated mass for the 5, 10 and 20 MW optimized wind turbines. In this table, except the mass of the blade and tower that are optimized for the given size, all the other masses are obtained using the mass models presented in appendix A. Depending on the component, these mass models are a function of the blade mass, length or turbine power output to reflect the size dependency.

According to linear scaling law, the tower top mass increases with R^3 . Figure 8.11 shows the tower top mass trend of the optimized wind turbines and existing data. For the optimized wind turbines the tower top mass increases with an exponent of

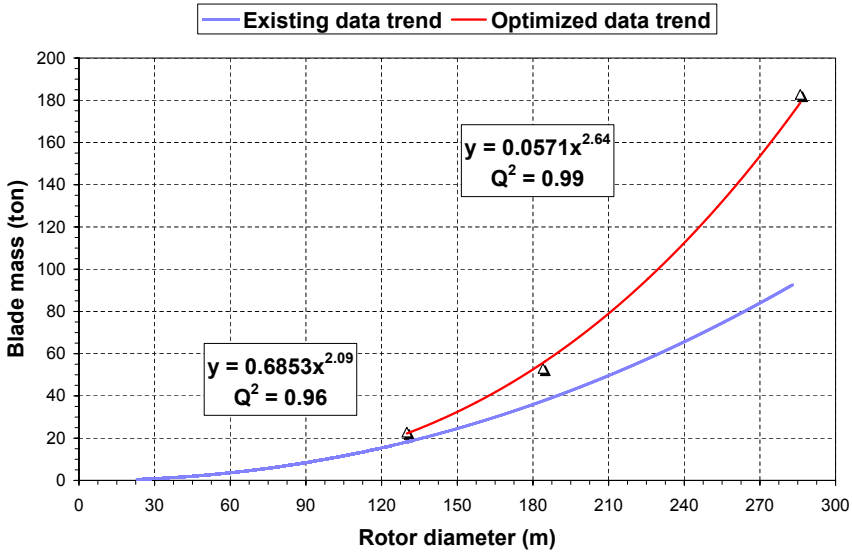


Figure 8.10: Curve fit to the single blade mass trend for the optimized wind turbines from 5 to 20 MW and comparison with the extrapolated existing data trends

2.41 and this value using the existing data is 2.39.

The reason for such a good match can be further analyzed by looking to the mass breakdown of the tower top components of the 5, 10 and 20 MW wind turbines. As figure 8.12 shows at 5 MW 23.7% of the tower top mass is directly optimized and

Table 8.2: Mass of all the components atop the optimized wind turbines

Component	5 MW (kg)	10 MW (kg)	20 MW (kg)
3 Blades	68553	159045	548250
Hub	27480	56257	180028
Pitch system	12997	28559	95476
Pitch bearing	9369	21088	71492
Nose cone	1884	2888	4775
Low speed shaft	18087	49515	176730
Main bearing	3014	10274	48251
Gearbox	36061	84161	17377
High speed shaft and brake	990	1981	3962
Generator	16646	31546	59783
Bed plate	64552	127550	301560
Platform and railing	8069	15944	37695
Hydraulic and cooling	398	796	1593
Nacelle cover	6129	11873	23361
Yaw system	14587	46330	199510
Tower top mass	Σ =288819	Σ =647808	Σ =1926269

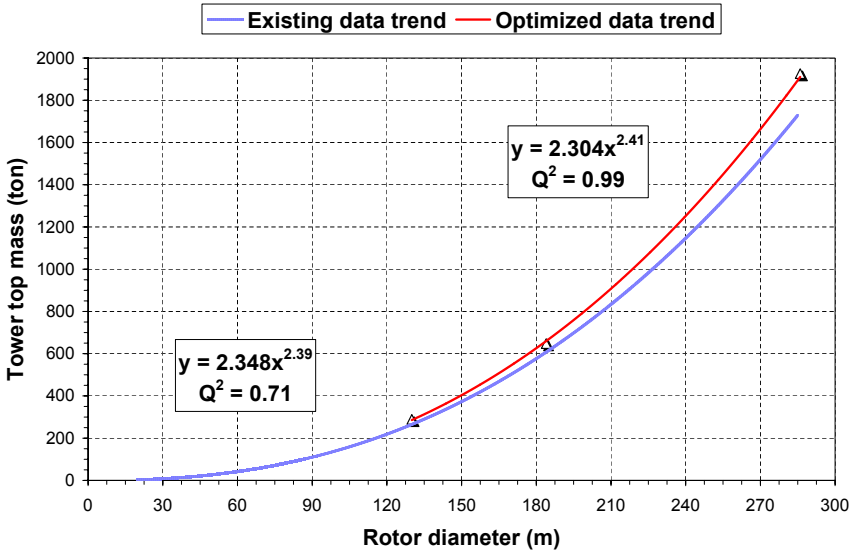


Figure 8.11: Curve fit to the tower top mass of the optimized wind turbines from 5 to 20 MW and comparison with the extrapolated existing data trends

the remaining 76.3% is obtained through the mass models. Similar share between the optimized and modeled mass can be seen for the 10 and 20 MW wind turbines. Due to the calibration of these mass models by industry data, they have the same predictive value as the existing data trend. Since the modeled mass has the main contribution to the tower top mass, it governs the trend behavior and this results in close match with the existing data trend.

3. Tower

The mass-diameter trend for the optimized towers is shown in figure 8.13. The data trend represents an exponent of 3.22 that is higher than both the linear scaling law and existing data trend. However, one should consider the low Q-squared value in the existing data trend, which should be used for the comparison carefully.

Additionally, in the optimization formulation of this research, the tower diameter and thickness are optimized only at the tower base and top, resulting in a linear variation of the diameter and thickness along the tower. This could be improved by adding more sections along the tower to be optimized and probably helping to get a lower tower mass as the tower scales and improving the trend exponent.

Having all the mass scaling trends in place, one can also look at the mass trend exponents and the mass breakdown of different components and the way they scale with size.

- Mass trend exponents

The mass breakdown is presented in figure 8.14 for the optimized 5, 10 and 20 MW wind turbines. Based on this figure, the mass trend exponent is presented in table 8.3. As the table shows the mass of the main bearing has the highest trend

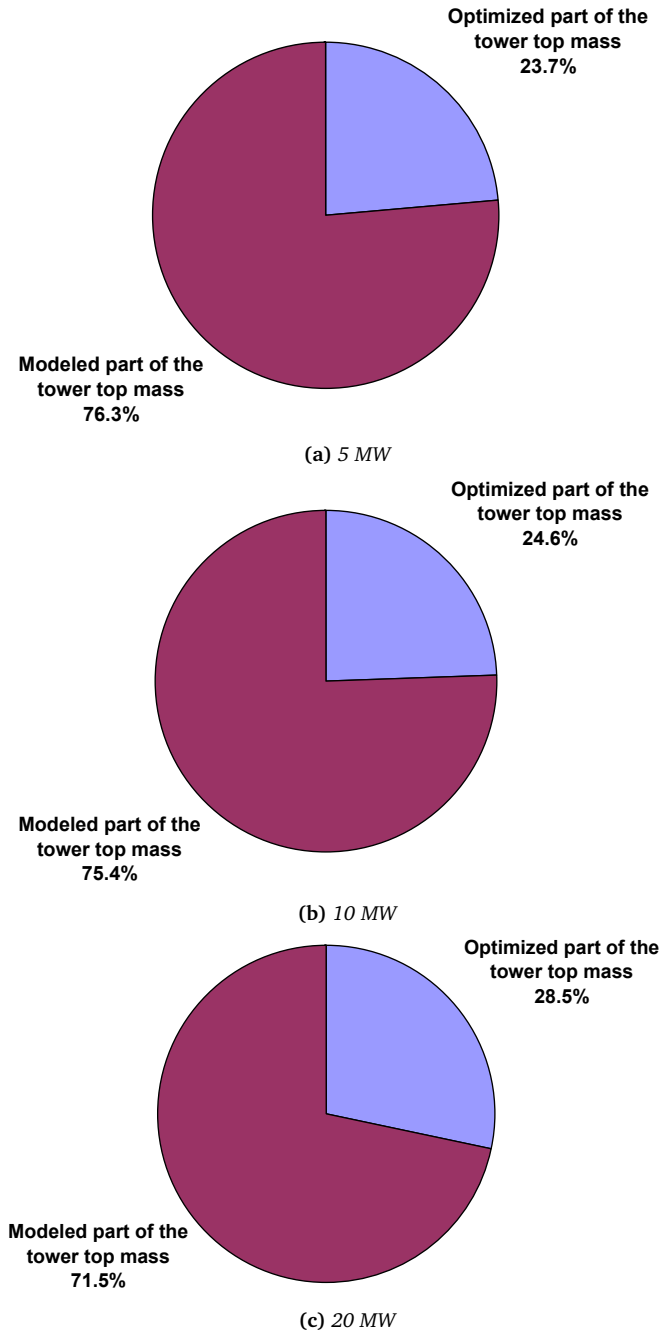


Figure 8.12: Mass breakdown of the tower top components of the optimized 5, 10 and 20 MW wind turbines to show the share between the modeled and optimized part

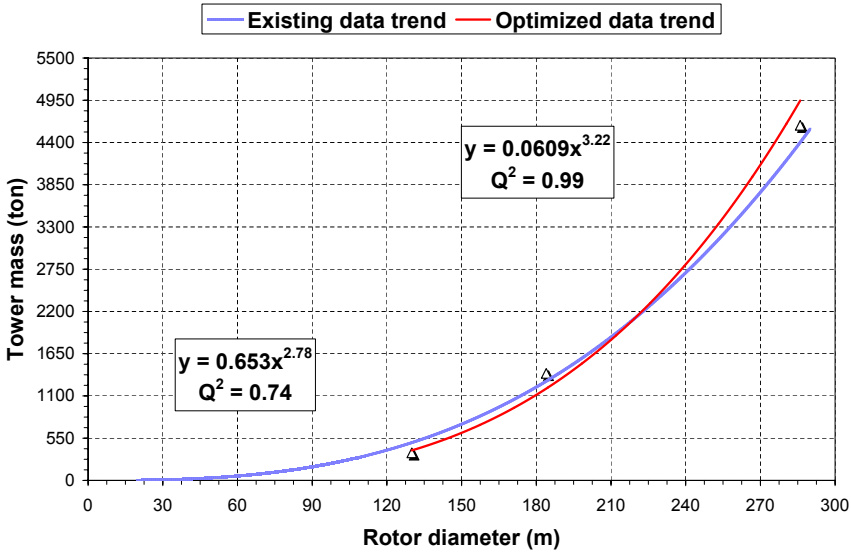


Figure 8.13: Curve fit to the tower mass of the optimized wind turbines from 5 to 20 MW and comparison with the extrapolated existing data trends

exponent followed by the yaw system, tower, low speed shaft and blade. From a design point of view, the mass of these components has a direct link with the mass of the blade. The higher the mass of the blade, the higher the mass of other components to support it.

In this case a higher trend exponent of the main bearing, yaw system, tower and low speed shaft may not imply that these components need to undergo a technological improvement. It is mainly the mass increase of the blade that is causing the mass increase of the other components. This necessitates considering alternative light weight materials for the blade when aiming at larger scales. This issue is better addressed by looking to the mass breakdown of different components at different scales as follows next.

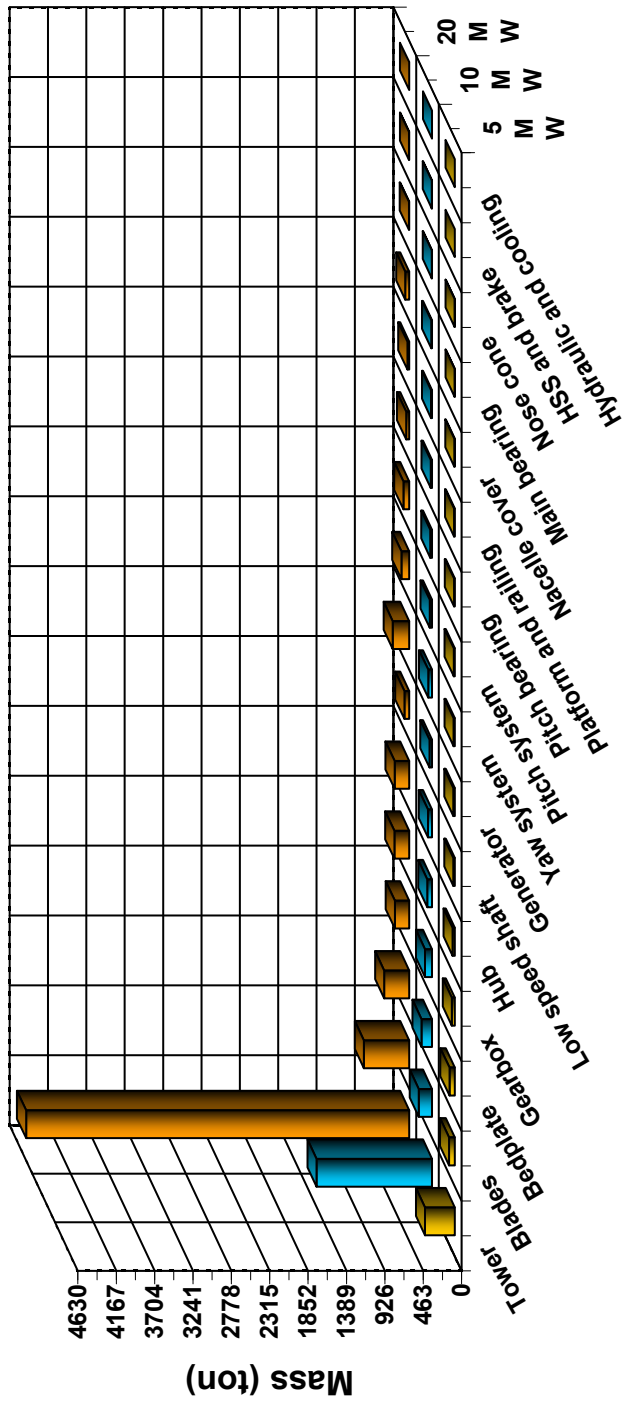


Figure 8.14: Mass breakdown of the wind turbine components of the optimized 5, 10 and 20 MW wind turbines

Table 8.3: Mass trend exponent of all the components of a wind turbine as it scales from 5 to 20 MW in the power output

Component	Trend exponent	Component	Trend exponent
Main bearing	3.52	Gearbox	1.98
Yaw system	3.32	Bedplate	1.95
Tower	3.22	Platform and railing	1.95
Low speed shaft	2.89	HSS and brake	1.75
Blade	2.65	Hydraulic and cooling	1.75
Pitch bearing	2.59	Nacelle cover	1.69
Pitch system	2.54	Generator	1.61
Hub	2.39	Nose cone	1.18

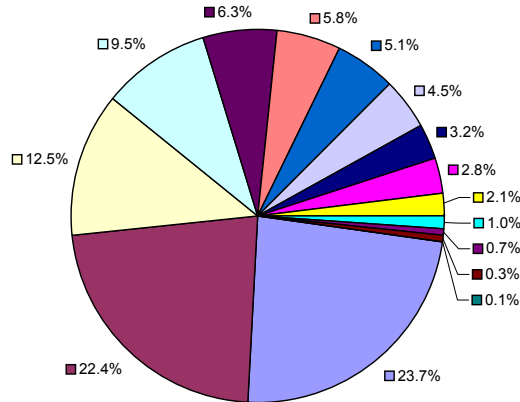
- Mass breakdown at different scales

The mass breakdown shows how upscaling influences the design at different scales. The results are presented in two separate form for the 5, 10 and 20 MW wind turbines. First, only the mass breakdown of the tower top components is presented (excluding tower) and second, the mass breakdown of all the wind turbine components (including tower) is presented.

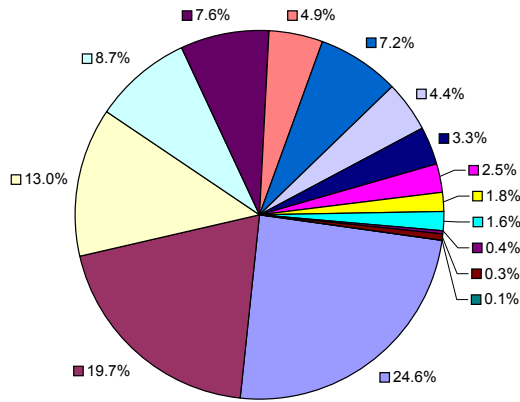
For the 5, 10 and 20 MW wind turbines, the mass breakdown of the tower top components is presented in figure 8.15. This graph has two important aspects to discuss. First, upscaling influences equally the tower top components and keeps the mass share the same with blade as the heaviest component followed by bedplate, gearbox and hub.

Second, the mass percentage of the blade increases from 23.7% at 5 MW to 28.5% at 20 MW showing that the blades of the large scale wind turbines will become progressively heavier. Referring to the results of this research, one can see that the blade-tower clearance and edgewise loads are the dominant design drivers at larger scales and keeping them satisfied most probably causes this increase.

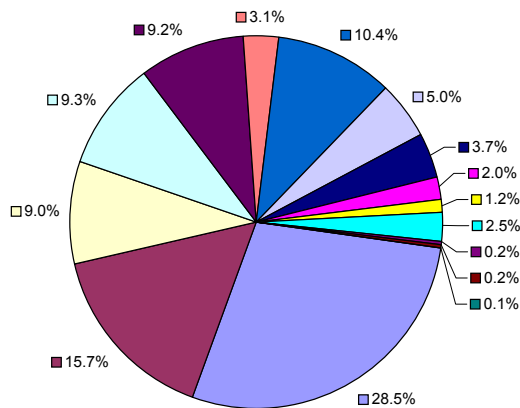
Similarly, the mass breakdown of the 5, 10 and 20 MW wind turbine components is presented in figure 8.16. As the figure shows, the tower mass increases from 55.4% at 5 MW to 70.6% at 20 MW. Taking into account that the tower function is to supply the tower top mass at the required height and withstand the loads, then it can be argued that the mass increase of the tower top components and higher loads are the two direct reasons for such an increase in the tower mass share.



(a) 5 MW



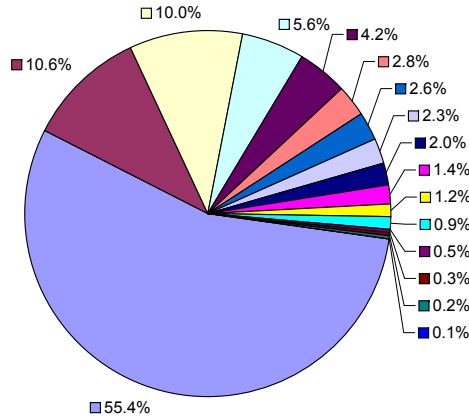
(b) 10 MW



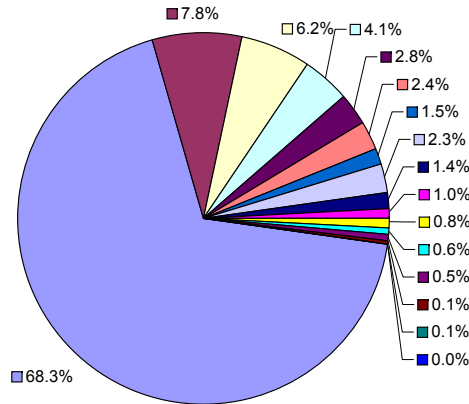
(c) 20 MW

Blades	Bedplate	Gearbox	Hub
Low speed shaft	Generator	Yaw system	Pitch system
Pitch bearing	Platform and railing	Nacelle cover	Main bearing
Nose cone	HSS and brake	Hydraulic and cooling	

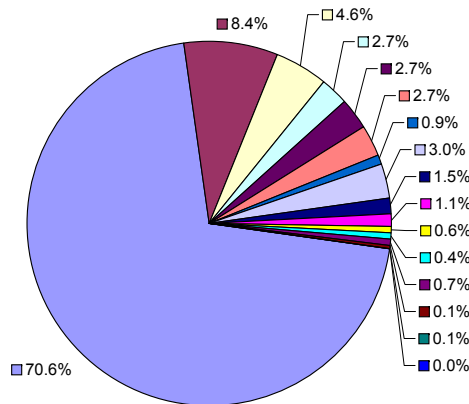
Figure 8.15: Mass breakdown of the tower top components of the optimized 5, 10 and 20 MW wind turbines



(a) 5 MW



(b) 10 MW



(c) 20 MW

Tower	Blades	Bedplate	Gearbox
Hub	Low speed shaft	Generator	Yaw system
Pitch system	Pitch bearing	Platform and railing	Nacelle cover
Main bearing	Nose cone	HSS and brake	Hydraulic and cooling

Figure 8.16: Mass breakdown of all the components of the optimized 5, 10 and 20 MW wind turbines

8.2.3 Cost-diameter trends

When making any technical improvement to the design of a wind turbine, it is necessary to evaluate the impact of the design change on the system cost as well. The impact assessment should not only be limited to the wind turbine itself, but also should consider the overall impact on the cost elements when considered as an offshore wind farm such as installation, and operation and maintenance.

As a wind turbine scales, the impact of the scale on all these cost elements and the design constraints is not clear. While an increase in the blade length results in higher annual energy production, it also increases the required space between the wind turbines to reduce the farm turbulence effect and this in consequence increases the farm interconnection cabling cost.

If one positive effect does not balance out all the other negative ones, then the proposed improvement may have a negative overall impact. This necessitates having a merit index that can measure the overall value of the design change. The LCOE is such a merit index, and its formulation was explained in chapter 3.

Using LCOE as the objective function and taking all the wind farm cost elements into account such as installation, offshore cabling, scour protection and decommissioning, this subsection presents the cost-diameter trends to investigate the economy of larger scales wind turbines and the impact of size on them.

Figure 8.17 shows the cost of all the components of the optimized wind turbines together with its associated costs as a 50 MW wind farm with an array spacing of 7 by 7 rotor diameters. Except the cost of the blade and tower that are optimized for the given size, all the other costs are obtained using the cost models presented in appendix A.

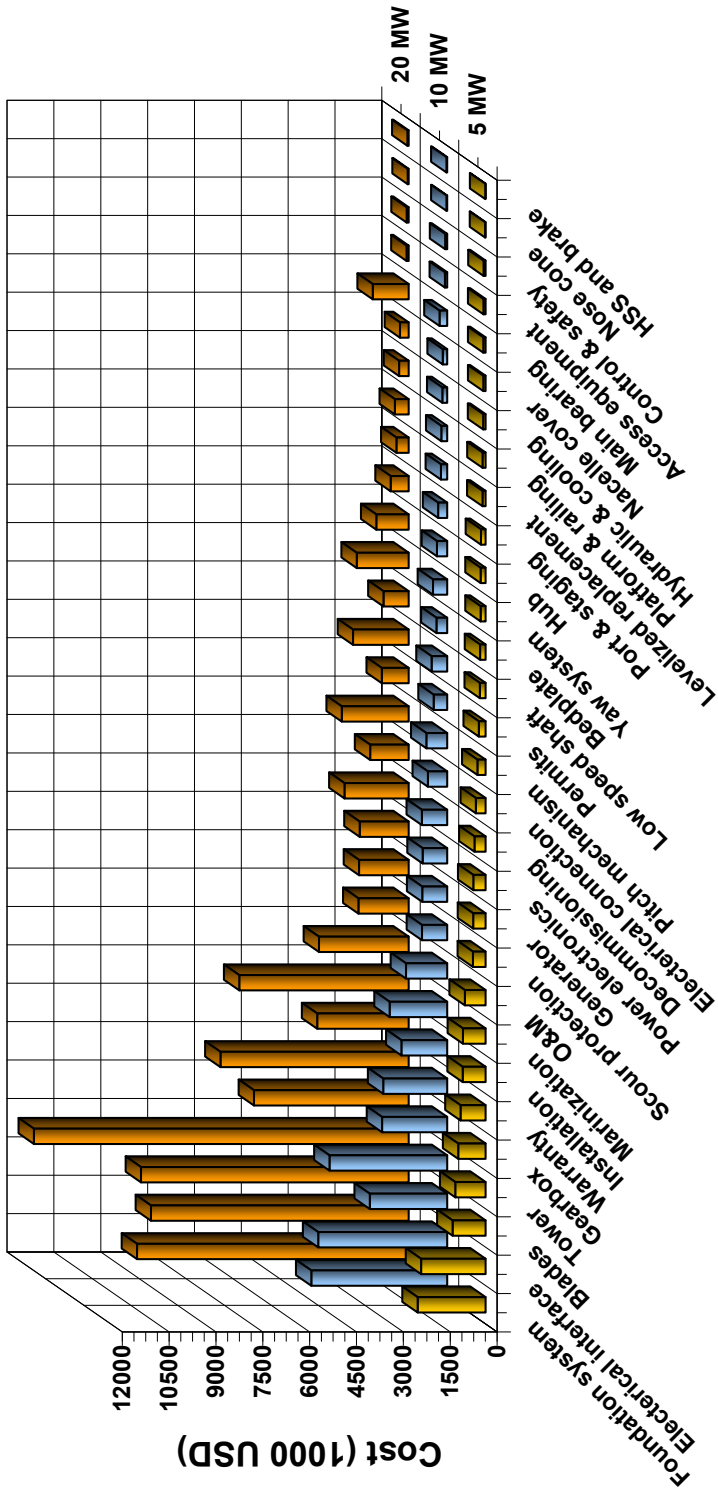


Figure 8.17: Cost elements of the optimized wind turbines from 5 to 20 MW

Table 8.4: Cost trend exponent of all the components of a wind turbine as it upscales from 5 to 20 MW in the power output, the ranking is according to the trend exponent

Cost element	Trend exponent	Cost element	Trend exponent
Tower	3.22	Electrical interface	1.75
Yaw system	2.97	Installation	1.75
Low speed shaft	2.89	Scour protection	1.75
Blade	2.66	Generator	1.75
Pitch mechanism	2.66	Power electronics	1.75
Warranty	2.55	Electrical connection	1.75
Marinization	2.55	Permits	1.75
Main bearing	2.44	Port and staging	1.75
Hub	2.39	Levelized replacement	1.75
Decommissioning	2.22	Hydraulic and cooling	1.75
Gearbox	2.19	HSS and brake	1.75
Bedplate	1.95	Nacelle cover	1.69
Platform and railing	1.95	Nose cone	1.18
O & M	1.85	Access equipment	Fixed
Foundation system	1.75	Control and safety	Fixed

To get more out of this figure, a power trend is fitted to every individual cost element, and the trend exponents are presented in table 8.4. As the table shows, from cost perspective the tower of larger scale wind turbines has the highest trend exponent followed by yaw system, low speed shaft and blade.

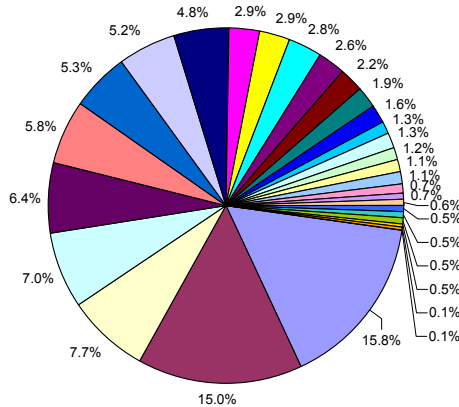
However, this does not mean that the tower will be the most expensive component, and it only shows that the tower cost will be highly influenced by the scaling when compared to other cost elements.

In this table, there are some cost elements that have the same exponent. This is not a coincidence, since these cost elements are all a function of the rated power output and therefore have the same exponent. Personnel access equipment, and control and safety devices are not scale dependent and therefore have a fixed cost at all different scales.

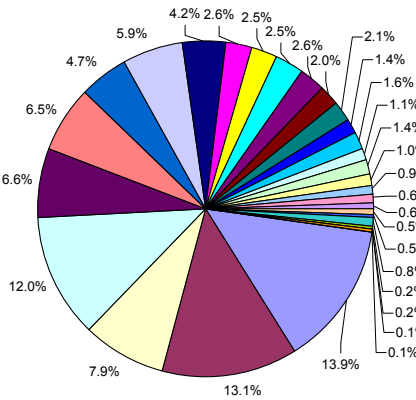
Figure 8.18 shows the cost breakdown of all different elements for the optimized 5, 10 and 20 MW wind turbines. As the figure shows, the cost share of the blades and tower increases with size. For the blades, this value is 7.7% at 5 MW and 10.7% at 20 MW meaning that the blades of large scale wind turbine increase in the cost share. For the tower, the cost share increases from 7.0% at 5 MW to 15.6% at 20 MW.

As these results show, the blade and tower cost increase is in favor of a conceptual change in the design to compensate this negative impact. As discussed before, load and mass reduction is vital for large scale wind turbines. Therefore, a 2 bladed downwind concept has the potential to overcome the problem.

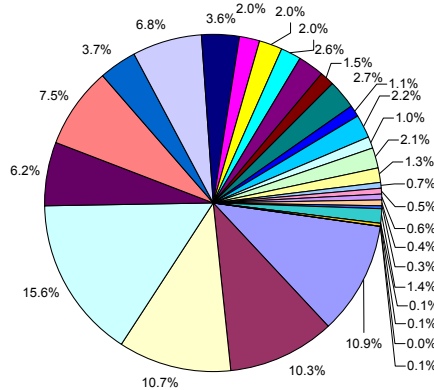
Also figure 8.19 shows how the TCC and BOS change with size. As the figure presents, at the 5 MW level the TCC and BOS are almost the same, however as the size increases the TCC is increasing more rapidly than the BOS (almost twice at the 20 MW). Therefore more emphasis should be put on the TCC when aiming at cost reduction for large scale offshore wind.



(a) 5 MW



(b) 10 MW



(c) 20 MW

Foundation system	Electrical interface	Blades	Tower
Gearbox	Warranty	Installation	Marinization
O&M	Scour protection	Generator	Power electronics
Decommissioning	Electrical connection	Pitch mechanism	Permits
Low speed shaft	Bedplate	Yaw system	Hub
Port & staging	Levelized replacement	Platform & railing	Hydraulic & cooling
Nacelle cover	Main bearing	Access equipment	Control & safety
Nose cone	HSS and brake		

Figure 8.18: Cost breakdown of the optimized 5, 10 and 20 MW wind turbines

When upscaling a wind turbine the AEP increases, however at the same time the ICC goes up. As mentioned before, if the positive effect of one change (increase in AEP) does not balance out the negative impact of the other (increase in ICC) then the proposed change has a negative overall impact by increasing the LCOE.

The ICC and AEP trends are depicted in figure 8.20 to show this tradeoff phenomenon. As the figure shows, the AEP has a trend exponent of 1.29, which does not beat the ICC trend exponent of 1.57 as the size increases. This negatively influences the LCOE as depicted in figure 8.21 and increases that with a trend exponent of 0.22 at larger scales.

The increase of LCOE over size has also another hidden message. Table 8.5 shows the increase of LCOE in percentages to decode this message. As the size is getting doubled from 5 to 10 MW the LCOE increases by 8.6%, and when it is from 10 to 20 MW it increases by 9.76%. Both scaling steps have the same scaling ratio, but the later shows a higher increase in the LCOE. This means that the negative impact of upscaling is larger when the scaling step is more beyond the existing knowledge and technology.

Table 8.5: LCOE percentage increase of a wind turbine as it upscales from 5 to 20 MW in the power output

Size increase	Percentage (%)
5 to 10 MW	8.60
10 to 20 MW	9.76
5 to 20 MW	19.20

This necessitates to do upscaling with small sequential steps to mitigate the negative economical impact of scale and benefit from technological developments in every step. Therefore to make upscaling economically attractive, size should increase with a slower rate, as also presented by Stiesdal at the conference "The science of making torque from

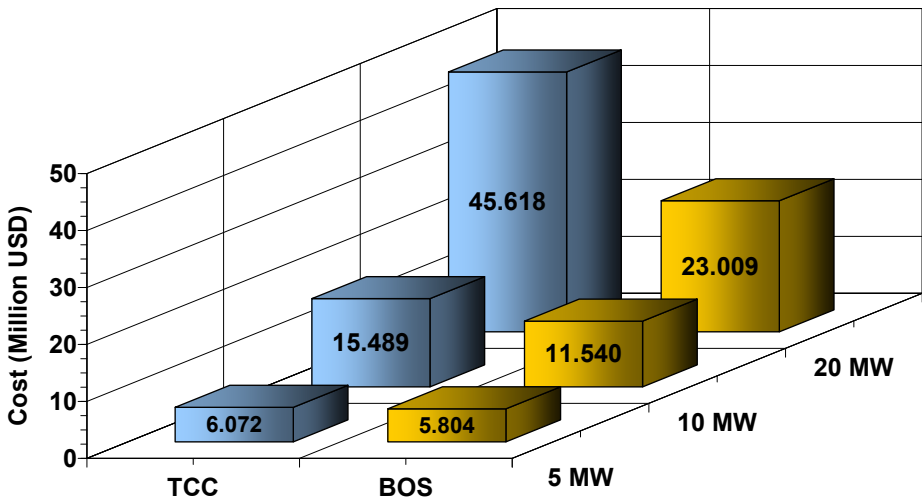


Figure 8.19: TCC and BOS of the optimized wind turbines from 5 to 20 MW

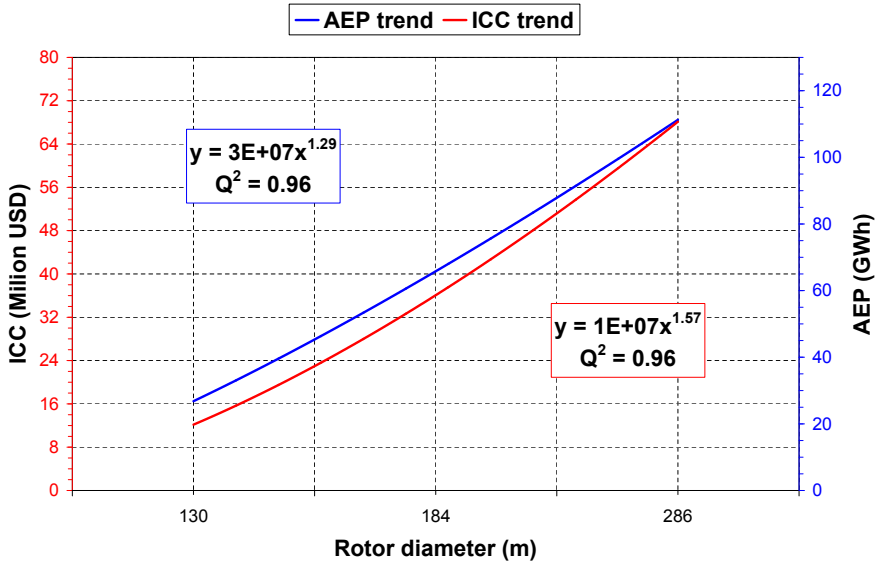


Figure 8.20: ICC and AEP trends of the optimized wind turbines from 5 to 20 MW

wind' in 2007. He showed that the growth rate of the wind turbines has reached a near to flat level during the last decade when compared with 1980's and 1990's that is mainly because of economical considerations rather than the technological limitations, and this may not mean that there is a size limit or even an optimum is achieved.

Upscaling can continue if the negative impacts of every step can be mitigated by the

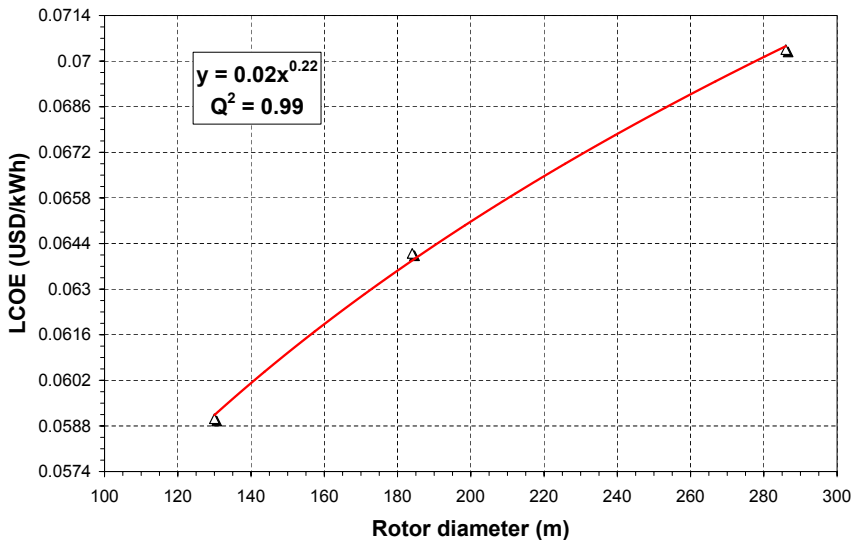


Figure 8.21: Curve fit to the LCOE of the optimized wind turbines from 5 to 20 MW

use of new technologies in the design. If not so, then the already achieved size might be considered as an optimum and economically attractive size. However, the new materials and technologies of the future may also have the potential to improve the economy of smaller scales (even better than larger scales) and down scaling the wind turbines may become more economically attractive than upscaling.

8.2.4 Other useful trends

This subsection presents two other useful trends to explain the global behavior of a wind turbine as it scales and gives the necessary background information when dealing with size increase.

1. Blade tip-speed

The tip-speed is a key parameter in wind turbine design. It influences at the same time the driving torque of the drive train, the slenderness of the blade and the aerodynamic and mechanical noise emission from the rotor and nacelle.

In that respect a higher tip-speed reduces the driving torque of the drive train for the same power output, which can be considered as a positive impact from loads perspective. A higher tip-speed also causes the blades to become more slender, a condition that has its limit due to the large deflections that a slender blade experiences and the extra material needed to avoid this increase. Similarly, it causes a higher noise emission and as a rule of thumb, the noise emission of a wind turbine increases with the fifth power of the relative wind speed.

For onshore wind turbines, the most important restriction to design for higher tip-speeds is the aerodynamic noise emission. Therefore, most of the onshore wind turbines have a maximum of $80 \left(\frac{m}{s}\right)$ as the tip-speed, a restriction that is set to not cause annoyance to the close neighborhoods and inhabitants. However, for the offshore wind turbines such a restriction does not exist and as a consequence higher tip-speeds are expected.

In this research, the tip-speed is considered as a design constraint with an allowable upper bound of $120 \left(\frac{m}{s}\right)$. Table 8.6 shows the designed tip-speed of the optimized wind turbines. These values are the result of a tradeoff study to meet all the design constraints and minimize the LCOE. As the table shows, no evidence in the data can be found to show that an increased or decreased tip-speed is beneficial as the size increases.

Therefore, no consistent pattern related to size can be formulated for the tip-speed and this is a global tradeoff study among many design variables, design constraints and LCOE that determines its value without further interpretation or judgment related to size. As the result, the 10 MW wind turbine has an optimized tip-speed that is lower than the 5 and 20 MW wind turbines.

2. Rated power to tower head mass ratio

The rated power to tower head mass is a measure of scaling benefits and it allows to distinguish light-weight and heavy designs when the same environmental condition is used. Figure 8.22 shows the ratio for the optimized wind turbines. To see how negatively upscaling influences the design, table 8.7 shows the relative reduction

Table 8.6: Blade tip-speed of the optimized 5 to 20 MW wind turbines

Power output (MW)	Tip-speed ($\frac{m}{s}$)
5	88
10	82
20	98

of the ratio in percentage at every scaling step. When the size increase from 5 to 10 the ratio decreases by 10.8%, and 32.7% from 10 to 20 MW.

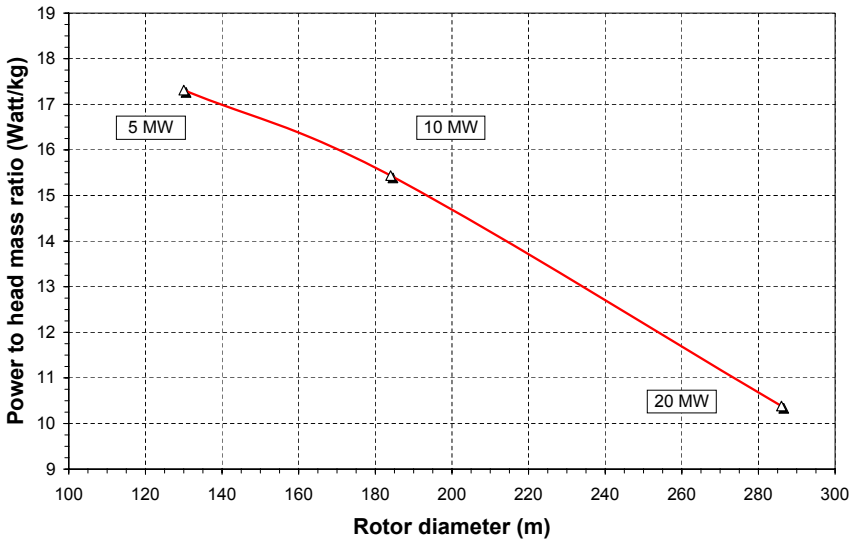


Figure 8.22: Curve fit to the power output to tower head mass ratio the of the optimized wind turbines from 5 to 20 MW

This supports the previous argument that upscaling needs to be done in small steps with the inclusion of new technological developments to mitigate the negative overall impact in every step. Upscaling using existing materials and design methods will result in massive wind turbines, which necessities the use of several design improvements to maintain the same power to tower mass ratio or even improve it. Therefore, saving weight seems to be the only option for more cost effective large wind turbines.

Table 8.7: Comparison of power output ratio for every scaling step

Scaling step	Ratio reduction (%)
5 to 10	10.8
10 to 20	32.7
5 to 20	40.0

Conclusion and recommendation for future work

9.1 Introduction

The goal of this PhD research was to investigate the influence of upscaling on future off-shore wind turbines by assessing their technical feasibility and economy. To achieve this goal all the involved disciplines and their dynamic interactions, important components and design constraints, cost elements, scaling trends and several other considerations and details had to be considered and addressed.

To show the outcomes of this research, first a discussion on the methodology is made relevant to upscaling and design. Also the application of the methodology in each context is described. Then a general conclusion is presented to show the main findings of the research. A detailed conclusion based on the answers to the research questions presented in chapter 1 follows afterwards. Next, the contribution to the state of the art is presented and finally the recommendation for future work is discussed.

9.2 Discussion on the methodology

A discussion on the methodology is presented to give an overview of its advantages, disadvantages and application. Due to the wide scope of the methodology a distinction is made between upscaling and design.

9.2.1 Upscaling context

The classical upscaling methods do not have the competence to deal with the detailed research questions of this work as discussed in chapter 2. This is mainly because of the limitation to provide size specific integral optimized wind turbines that are needed to investigate the technical feasibility, economical characteristic and to construct reliable

scaling trends. The methodology of this research enables the upscaling study of optimized wind turbines based on the same set of design assumptions and design concept for all scales.

The same set of the design assumptions minimizes the scattering of the data points. The same design concept guarantees the least inconsistency among different data points that are used to develop scaling trends. In this way the scaling trends become more confident and accurate for the concept under study. This in turn makes the end results more reliable for investigating the influence of size on the design.

Additionally, the integrated methodology of this research enables the upscaling study of any other concept as long as representative mass and cost models can be made available for. In this way one can make a trade off among different concepts to find the suitability of each at different scales. As an example, it is possible to study a two-bladed downwind machine at 5, 10 and 20 MW scales and compare its technical and economical characteristics with the results of the 3-bladed upwind concept as presented in the previous chapters. This can show how another concept could possibly mitigate the negative influence of upscaling on the present offshore wind turbine design. In a similar way a direct drive machine can be studied and compared.

With the introduction of new technological developments and design improvements there is a chance that a smaller scale machine does benefit more from it than a larger machine. This means that from an economical point of view a smaller machine can become more attractive, and it motivates downscaling the existing wind turbines. The methodology of this research allows not only the upscaling but also the downscaling of machines to be studied.

As an example, the LCOE of the upscaled wind turbines of this research shows an increase immediately after the 5 MW. This might mean that downscaling the 5 MW wind turbine may offer a better economy using the integrated methodology as a design improvement. Although not the focus of this research and therefore not considered, the methodology taken here has the potential to study this phenomenon as well.

Despite several advantages and different applications of the present methodology, it has some drawbacks as well:

- The increased complexity

The complexity of the developed methodology to deal with the upscaling problem makes it less attractive for quick size assessment studies. Formulation of the upscaling study as a MDO problem, requires many challenging steps to be taken before any results can become available. Therefore, an upscaling study based on the methodology of this research can be a cumbersome and demanding task.

- Dealing with novel concepts

The dependency of the methodology on the mass and cost models makes it less effective for dealing with novel concepts and technologies. This is due to the fact that often such cost and mass models are not available or representative enough for new technologies and concepts at the time of development. This is among the reasons why the upscaling of the well established existing concept (3-bladed, upwind, pitch regulated wind turbine) is studied in this research.

9.2.2 Design context

Typically, the design of a wind turbine takes place with isolated disciplines. In the isolated methodology, the structural and aerodynamic design are carried out first. Here, the role of the control engineer in the wind turbine design is mainly focused on designing the controller for a given configuration defined by structural and aerodynamic design in advance. However, the shift towards larger and flexible structures equipped with active control devices operating in the entire working regime of the wind turbine is demanding for innovations in design methodology.

The integrated aeroservoelastic design of this research is such an innovation. This methodology changes the existing design problems from how to increase the power output or decrease the loads to how can aerodynamic, structure and active control be optimally combined to make a wind turbine that has the lowest LCOE, while satisfying all the design constraints (thereby loosely called 'system-level design').

This has been achieved by defining the LCOE as a common objective function among all disciplines to be optimized, rather than optimizing the structure for minimum weight, aerodynamics for maximum energy output or control for load alleviation and power regulation. By optimizing the LCOE, the integrated design guarantees the optimality of the wind turbine as an aeroservoelastic system.

Additionally, instead of using the traditional methodology to design every component of the wind turbine separately, the integrated methodology enables the concurrent design of the components. In this research, blade and tower are designed at the same time and this results in a reduced design time and lower LCOE. This also helps the designer to better understand the overall impact (technical and economic) of every individual component on the design as a whole by doing a sensitivity analysis of the design constraints and objective function with respect to the design variables.

In this way, a global definition of the objective function, design variables and design constraints among all the disciplines and the concurrent design of the blades and tower helps the optimizer to move towards better design solutions. As shown in chapter 4, the use of the integrated methodology to design the 5 MW NREL wind turbine contributed to 4.2% reduction in the LCOE. Therefore, the integrated design methodology is vital for the development of future wind turbines that have to be more optimized than they are today in order to be cost competitive.

Despite several advantages of the methodology, there are some drawbacks and issues that require special attention:

- The enlarged design space

To make an aeroservoelastic design optimization happen, in addition to defining the design variables, design constraints and objective function a huge amount of additional interdisciplinary design parameters are also needed.

Although it is possible to introduce almost any design parameter as a design variable, it may become computationally very extensive. This can become worse when the concurrent design of several components has to be considered. Therefore, several design parameters need to be engineered and defined by the designer.

Taking this fact into account wind turbine design still remains a cumbersome task and the integrated methodology complicates further this task by enlarging the design space. However, the integrated methodology has the capability of doing

a sensitivity analysis of any design parameter (or design variable) to the objective function and design constraints to show the overall impact of it on the design. Based on this impact, the designer can judge which design variables or design parameters to eliminate to have a reasonable design space.

- Computational expense

Because of assessing the aeroservoelastic behavior of the wind turbine and the concurrent design of components the simulation and optimization time is expensive. Therefore, to do an aeroservoelastic design optimization in a reasonable time many advances such as parallel programmed computational codes are needed.

9.3 Conclusions

In this section an overall conclusion is presented first. Then detailed conclusions are drawn up based on the formulated research questions that were presented in chapter 1.

9.3.1 Overall conclusions

The developed methodology of this research incorporating an integrated approach for the simultaneous design of all disciplines and concurrent optimization of components turned out to be very effective. Each building block of this integrated methodology helps to address one important aspect; objective function to characterize the economy and optimizing the design, design constraints to identify the technical feasibility and finally the design variables to realize size specific optimized wind turbines to draw scaling trends. Therefore, it can be concluded that the approach of this research meets the essential requirements for a thorough analysis of upscaling of current wind turbines; a capability that does not exist in the classical upscaling methods and is beyond their reach.

The results show the technical feasibility of current wind turbines when upscaled from 5 to 20 MW. Larger wind turbines suffer mainly from the penalty of weight growth and mass reduction becomes the main design concern to handle. From cost perspective, upscaling of a three-bladed, upwind, geared and pitch regulated concept without the inclusion of several advancements in its design is detrimental beyond the 5 MW range.

The future large offshore wind turbines (similar in concept to the concept of this research) can only be realized without cost increase provided some key innovations are developed and integrated in the design. These innovations will come with extra initial costs and they will pose new challenges. This necessitates to evaluate the overall impact (technical and economical) of these innovations. For this purpose the use of the integrated design methodology (such as this research) is considered essential for the future offshore wind turbines.

9.3.2 Conclusions based on research questions

How do the technical characteristics of the larger scales change with size and can these technical characteristics appear as a barrier?

To assess the technical feasibility of wind turbines up to 20 MW, MDO was used to do the preliminary design. For this assessment, all the important design constraints of a wind turbines were considered. These included fatigue, stresses, natural frequencies, blade-tower clearance and aeroelastic instability.

For both 10 and 20 MW wind turbines, blade-tower clearance and fatigue of the tower act as active design constraints that are marginally satisfied. From a stress point of view, both machines can sustain the extreme stresses. Also the natural frequencies do not appear to pose any design challenge in the context of 1P and 3P frequencies, as well as the wave spectrum peak frequency. From an aeroelastic stability perspective, the safety margin against static and dynamic instability shows a considerable reduction for the 20 MW wind turbine. However, the remaining safety margin is still enough to allow the turbine to operate safely.

Additionally, based on the designed 5, 10 and 20 MW wind turbines, scaling trends were constructed to show the behavior of wind turbines as they scale in size. These trends were used to study the influence of size on important aspects of the wind turbines, and they were all formulated as a function of rotor diameter to properly reflect the size dependency. Loading-diameter and mass-diameter trends were extracted to investigate the scaling phenomenon. Blade and tower, as the most dynamic load carrying components, were investigated with more attention.

For the blade, the loading-diameter trend shows that the edgewise moment increases more rapidly than the flapwise moment. This is an indication that the gravity loads play a more important role at larger scales than the aerodynamic loads. Also for the tower, the side-to-side bending moment shows a higher growth rate at larger scales than the fore-aft moment. This might pose some complications in the design of future offshore wind turbines with a misaligned wind-wave loading which primarily can magnify the side-to-side moment.

Referring to the mass-diameter trends, the design shows to be negatively influenced by the penalty of weight growth that is caused by the mass of the tower top components. From a design point of view, the mass of the rotor appears to be the main reason for such an increase, since it caused the mass of other supporting components to increase in a progressive way as well. The mass trend exponents reveal that main bearing, yaw system and tower have the highest trend exponent. For the tower top components, the mass share of the blades also showed an increase at larger scales.

All in all, the results of this research show the technical feasibility of larger offshore wind turbines up to 20 MW range with no major technical barrier when referring to the design constraints and scaling trends, although some minor issues yet need to be solved as presented in the answer to the last research question.

How does the economy of the future offshore wind turbines change with size?

To evaluate the influence of size on the economy of larger future offshore wind turbines, LCOE was used as the merit index. Using this key index and taking all the wind farm cost elements into account, the cost-diameter trends were used to investigate the economy of larger scale wind turbines and study the impact of size on them.

At the component level, the tower of larger scale wind turbines has the highest trend exponent (and cost share at 20 MW) followed by yaw system, low speed shaft and the blades, meaning that the tower cost is influenced more by upscaling when compared to

other cost elements. This is in agreement with the conclusion on the mass increase of the tower top components, taking into account that the tower supports this mass and therefore gets negatively influenced by size.

The TCC and BOS have almost the same value at 5 MW, but as the size increased to 20 MW, the TCC increases more rapidly than the BOS (almost twice at the 20 MW), meaning an increased cost share of the TCC for the future offshore wind turbines.

Finally, the tradeoff between the ICC and AEP trends results in an increase of the LCOE immediately after the 5 MW. In this case, the extra energy that was captured by larger wind turbines could not balance out the associated ICC positively and this has resulted in an increase of LCOE. Overall, the results show that the economy of future offshore wind turbines is negatively influenced by upscaling with scaling trend exponents that were against any size increment of the current wind turbines beyond 5 MW.

What are the considerations and required changes for future offshore wind turbines?

Based on the results of this research, following considerations for the future large scale offshore wind turbine developments can be highlighted:

1. Mass increase of the blade

Referring to the design optimization results and making a root cause analysis of the blade mass increase for the upscaled wind turbines, prevention to hit the tower and resistance against the blade edgewise load are observed as the two main reasons (the first two design drivers for the larger blades).

Extra material to provide sufficient stiffness in longer blades causes the mass of the rotor to increase (also a progressive course toward mass increase of other components in the nacelle and tower). Future design solutions should solve the conflict between high stiffness (to have the desired blade-tower clearance) at low mass for the blade.

2. Mass and cost increase of the tower

The tower design is negatively influenced by upscaling. The two main reasons causing such an increase of mass and thereby cost of the tower are higher loads and mass increase of the tower top. Load alleviation and mass reduction are needed to overcome this problem.

3. Thickness of the blade root

The optimized design variables of the 20 MW blade (see table 5.2 in chapter 5) show that the blade root has a thickness of 20 cm. Although, it is technically feasible to construct the blade with such a thickness using the existing materials and manufacturing techniques, it becomes a complex engineering task to carry out.

4. Size of the blade and tower

A limiting size can be found for the blade and tower when looking at the existing land transportation possibilities. Assuming maximum limits of 6 m for diameter and 80 m for length, then the land transportation limit can be set at around 9 MW

for the blade. Using the same limit for the tower diameter, land transportation becomes impractical for towers corresponding to wind turbines of 5 MW power output.

5. Nacelle installation difficulties

As a result of upscaling, the weight, height and the volume of the future offshore wind turbine increase. The increase in the scale of the turbines requires special installation vessels in terms of carrying and lifting capacities specially relevant for the tower top components. The 20 MW wind turbine had a hub height of 162 m and a nacelle weight of more than 1000 tons.

Taking the mass of the nacelle and its installation height together into account, it becomes apparent how big the challenge is to overcome. At this moment, there is no lifting device in the world to lift and install such a huge mass atop the tower at this height. This can become more severe when one considers the installation of these machines in an offshore environment considering factors such as water depth variation, seabed condition, wind speed, waves and currents as the disturbing elements causing crane instability.

9.4 Contribution to the state of the art

This PhD research contributes to the state of the art knowledge and presents originality in three different aspects as discussed below:

1. The integrated aeroservoelastic design optimization method

Experience with integrated design optimization of the structure, aerodynamics and control subject to constraints on fatigue, stresses, deflections and frequencies with the LCOE as the objective function and simultaneous design of blade and tower as well as considerations on aeroelastic instability has not been published in wind energy to the knowledge of the author (system-level design). This research is the first work that explores and employs such a capability.

To design future cost effective wind turbines the integrated methodology is useful. Presented results proof the effectiveness of it and they show that through systematic integrated system optimization studies, the LCOE can be decreased significantly.

In addition, a new aeroelastic stability analysis tool is developed to address aeroelastic stability in the context of a linear eigenvalue analysis using an unsteady aerodynamic model coupled with a nonlinear FE structural formulation. Although some aspects of the modeling are not precise, the major physical aspects of the problem and reasonably accurate results can be obtained that are well suited for preliminary design purposes.

The application of the tool in predicting the aeroelastic instability margin of the 5 and 20 MW wind turbines provides new insight in the phenomenon of instability with clear relation with size. The results show how sensitive the aeroelastic stability safety margin will be and highlight the importance of considering that in the design

process of future wind turbines.

2. Development of the optimized 10 and 20 MW wind turbines

In addition to showing a clear way forward for the future offshore wind energy design methodology development, its application to design very large wind turbines and identify their technical and economical characteristics is another major contribution of this research. Using the integrated MDO methodology, the design characteristics of very large scale offshore wind turbines up to 20 MW range are explored and identified.

These results can be used as a reference to address and compare any technological development for larger scales and quantify its added value by using the developed wind turbines of this research as a baseline design. Hence, the developed wind turbines of this research can be used in a similar way as the 5 MW NREL wind turbine is used today by many researchers worldwide, since they have the same level of design details, content, and format.

3. Development of scaling trends for the ever larger offshore wind turbines

Developing the major technical and economical trends for larger offshore wind turbines that are based on existing conventional wind turbine designs is a unique contribution to the state of the art knowledge. The scaling trends enable a critical assessment of size influence on the design of a wind turbine to determine the engineering feasibility, cost implications, and overall fundamental barriers, as concerns technology, design tools and concept. Detailed analysis covering all the aspects of design clearly enables to make a fair judgment about the future research and technological development needs.

How the design of a wind turbine is influenced by upscaling is an interesting research question in the wind energy community that is covered in this research. Indeed, the scaling trends of this research demonstrates the technical feasibility of large scale offshore wind turbines though an economical barrier applies before a technical barrier.

9.5 Recommendations for future work

Due to the multidisciplinary aspects covered in this research, several directions for improvement and continuation of the research have been identified. The summary of the most important issues are classified and described below:

9.5.1 Upscaling context

- The blade edgewise load grows rapidly with size and gets more pronounced at large scales. This is mainly a gravity induced loading due to the mass increase. Therefore mass increase of the blade was identified as a problem and the design of the blade clearly dictates the mass reduction as a design solution. Carbon fiber composite is already employed by some wind turbine blade manufacturers and seems to be the best lightweight option.

- The tower clearance at large scales acts as a design driver. Tilting the rotor and preconing the blades can be of direct help (preconing also enhances the blade properties against instability). However, they both have a negative influence on power production. Therefore, this negative impact has to be evaluated at larger scales using a trade-off study to see its overall impact on the design.
- Tower side-to-side moment at the base grows more rapidly with size and becomes the design driver at larger scales. This issue with the combination of a wind-wave misalignment can result in load levels that can pose many challenges to the designers. A means of load alleviation technique has to be considered for the large scale towers. Although, it was argued that this is mainly a mass driven problem, this has to be investigated carefully with the application of lightweight materials to determine whether tower side-to-side load does not remain the design driver.
- A two-bladed, downwind offshore wind turbine with lightweight materials in its blade construction has the potential to meet all the requirements at very large scale. It generally has a higher tip speed and therefore higher noise levels, but this does not seem to be an issue offshore. The aerodynamic efficiency of a two-bladed machine may be 1-3 % lower but the reduced weight and loads, ease of installation and transportation may positively influence the energy cost calculation.

Compared to a three bladed rotor, a two-blade rotor has lower weight. This directly reduces the overall system weight that is needed to support the rotor. Therefore, such a configuration might be the ideal choice at larger scales (taking the mass problem of large scales into account) and clearly a nice future work in the upscaling context to mitigate the overall negative impact of size on the design.

9.5.2 Design context

- To overcome the negative impact of an expensive computational time introduced by multidisciplinary design, reduced order models of the wind turbines are needed. Model reduction is an efficient means to enable cheap simulation when the computational time tends to become a challenge. The experience of making reduced order models of wind turbines is very limited and it requires a long run future research before taking the advantages of it in the multidisciplinary design.
- The results of this research show the benefit of the integrated aeroservoelastic design (system-level design) over the isolated methodology. Michael Faraday said 'we should begin with the whole, then construct the parts'. Following this idea the future offshore wind turbines have to be designed at the system-level.

In this way the wind turbine design becomes the task of meeting the design requirements of the multiple components concurrently that build up the system, given only the requirements of the system to be achieved. This will be the future enabler of cheap wind turbine design but too complex to be reached soon.

- As the size increases the aeroelastic stability margin decreases. Recently, a 100 m blade corresponding to a 13.2 MW wind turbine was designed by Sandia, [Griffith and Ashwill \(2011\)](#), and by doing a stability check it was found that the blade had almost no safety margin against instability.

The results of this research show that the optimized 20 MW blade has a safety margin of about 20% against instability versus the 60% at 5 MW. This means that future wind turbine design standards have to address this issue more explicitly and make clear rules and guidelines to address the aeroelastic instability phenomenon in the design.

A.1 Introduction

The cost and mass models (except the mass model of the blade and tower that are calculated by the DOP) used in this research are based on the WindPACT project, [Fingersh et al. \(2006\)](#), developed at NREL. The foundation of the developed models come from the work originally done by University of Sutherland, [Harrison and Jenkins \(1993\)](#), under a work performed for the US Department of Energy (DOE) under its Wind Partnerships for Advanced Component Technology (WindPACT) projects.

WindPACT project provides an analytical model to project the cost for wind-generated electricity based on different scales of both onshore and offshore wind turbines. However, it should not be confused with turbine pricing, which is a function of volatile market factors beyond the goal of the original work.

In the WindPACT models, cost and mass scaling functions have been developed for major components and subsystems. Most of these cost and mass estimates are a function of wind turbine global parameters. These are the wind turbine rating, rotor diameter and hub height. However, there are also some few elements that have either another local key turbine descriptor, or they have a fixed value for all different scales and concepts.

The accuracy of the models are cross checked and improved based on the available information from the industry. The cost model includes the impact on cost from changes in economic indicators such as the Gross Domestic Product (GDP) and Producer Price Index (PPI) that was briefly explained in chapter 3. The product of the WindPACT project is a set of cost and mass scaling functions that enable work to integrate the economy of wind turbines with a MDO in consistent way, which has never been done before in the field.

A.2 Mass and cost modeling description

Increasing the size of a wind turbine is a big challenge for designers over many years. It is often very difficult to find what the total impact of increasing rotor diameter and the rating of a turbine will be on all other system parameters. Any changes to the design of a wind turbine, even if very small, influences the system cost and performance and therefore essential to the designer to evaluate the impact of these changes.

Therefore, these changes require sophisticated tools and methods to evaluate them properly. The levelized COE is used for many years in the field of wind energy to evaluate the total system impact of any changes in the design. This levelized COE is explained in equation 3.5, and a demonstration of that is presented in table 3.9. Using this definition, a true assessment of the impact of technical changes on levelized COE for larger scales is evaluated in this work.

The mass and cost estimates of all the wind turbine elements is based on a mature design of a 50 MW wind farm installation, matching with the highest design, manufacturing, installation and transportation standards of industry. For cost models, the outputs of all formulas is in 2009 US dollars, and they contain an escalation using the PPIs or GDP, as earlier described in chapter 3. The PPI related formulas are sorted by North American Industry Classification System (NAICS) codes that provide a grouping system of products and can be found at <http://www.bls.gov/ppi/>.

A.2.1 Blades

Blade mass

The blade mass is calculated as the result of optimizing its weight to satisfy the design constraints and minimize the levelized cost of energy in every iteration. The explanation to find the mass is given in appendix B and not repeated here.

Blade cost

The price of the blade is based on the work of Griffin (2001) as follow:

$$\text{Blade price} = (13.084 \times \text{blade mass} - 4452.2) \times (1 + \text{PPI})_{\text{Blade}} \quad (\text{A.1})$$

As explained before, the mass of the blade is calculated using equation 3.47 as the result of running the DOP. Also the PPI category to develop commodity inflation factor is expressed as the percentages of each commodity assumed to make up the final product, and can be explained with the following NAICS codes of the blade as:

- Fiberglass fabric (NAICS Code 3272123) with a product make up factor of 60%, and an inflation rate of 30.8% from 2002 to 2009
- Vinyl type adhesives (NAICS Code 32552044) with a product make up factor of 23%, and an inflation rate of 15.3% from 2002 to 2009
- Other externally threaded metal fasteners (NAICS Code 332722489), including studs with a product make up factor of 8%, and an inflation rate of 13.8% from 2002 to 2009
- Urethane and other foam products (NAICS Code 326150P) with a product make up factor of 9%, and an inflation rate of 24.2% from 2002 to 2009

Using this definition, a PPI of 25.2% is obtained for the blade.

A.2.2 Hub

Hub mass

The mass of the hub is based on the work of [Malcolm and Hansen \(2002\)](#), however, in this work the mass of the hub is calculated based on static analysis using peak root moments. Therefore, it underestimates the mass since it does not take into account the dynamics of the system. To correct that a correction factor of 1.92 is used that brings the mass closer to the given mass of many existing wind turbines, including the NREL 5 MW machine. The mass formula is as follow:

$$\text{Hub mass} = 1.92 \times (0.954 \times \text{blade mass} + 5680.3) \quad (\text{A.2})$$

Hub cost

The hub cost model is a function of the mass of the hub. It is assumed that the hub is made of ductile iron castings which every kilogram of its mass will cost 4.25 USD, including material, manufacturing and labor costs. Thus, its cost can be calculated by:

$$\text{Hub cost} = (4.25 \times \text{hub mass}) \times (1 + \text{PPI})_{\text{Hub}} \quad (\text{A.3})$$

The PPI has a NAICS code of 3315113, PCU3315113315113 for ductile iron castings and from year 2002 to 2009 it has an inflation rate of 35.6%.

A.2.3 Blade pitch system and its bearing

The blade pitch mechanism consists of the pitch system and bearings to support its mass.

Pitch mechanism mass

The mass of the pitch system's bearings is a function of the mass of the blade as:

$$\text{Pitch bearings mass} = 0.1295 \times \text{mass of all blades} + 491.31 \quad (\text{A.4})$$

The mass of the pitch system itself is also a function of the mass of bearings. The pitch system consists of actuators and drives and their mass is estimated as 32.8% of the bearing mass + 555 kg as it is shown below:

$$\text{Pitch system mass} = 1.328 \times \text{pitch bearings mass} + 555 \quad (\text{A.5})$$

Pitch mechanism cost

The pitch mechanism cost is a function of rotor diameter is obtained using the following equation:

$$\text{Pitch mechanism cost} = (0.4801 \times \text{rotor diameter}^{2.6578}) \times (1 + \text{PPI})_{\text{Pitch}} \quad (\text{A.6})$$

The PPI of the pitch mechanism consists of the following NAICS codes:

- Bearings (NAICS Code 332991P, PCU332991332991P) with a product make up factor of 50%, and an inflation rate of 35.6% from 2002 to 2009

- Drive motors (NAICS Code 3353123, PCU3353123353123) with a product make up factor of 20%, and an inflation rate of 32.9% from 2002 to 2009
- Speed reducer, i.e., gearing (NAICS Code 3336123, PCU333612333612) with a product make up factor of 20%, and an inflation rate of 28.0% from 2002 to 2009
- Controller and drive (NAICS Code 334513, PCU334513334513) for industrial process control with a product make up factor of 10%, and an inflation rate of 18.9% from 2002 to 2009

Adding all the inflation rates including the weight of each NAICS code in the final product make up results in a PPI of 31.87% for the pitch mechanism.

A.2.4 Nose cone of the hub

For the nose cone (or spinner) of the hub, the WindPact has derived a new mass and cost function based on the work of [Poore and Lettenmaier \(2003\)](#) and its alternative design study [Bywaters et al. \(2005\)](#), also augmented with data from the Advanced Research Turbine at the National Wind Technology Center.

Nose cone mass

The mass of the nose cone is a function of rotor diameter as:

$$\text{Nose cone mass} = 18.5 \times \text{rotor diameter} - 520.5 \quad (\text{A.7})$$

Nose cone cost

The Nose cone cost model is a function of the mass of the nose cone. It is assumed that the nose cone is made of the same material as the hub is made. However, some extra layers of coating is applied on the nose cone, which makes its price per kilogram more expensive. Thus every kilogram of its mass will cost 5.57 USD, including material, manufacturing and labor costs. The cost can be calculated by:

$$\text{Nose cone cost} = (5.57 \times \text{nose cone mass}) \times (1 + \text{PPI})_{\text{Hub}} \quad (\text{A.8})$$

As it can be seen from equation [A.8](#), the same NAICS code as the hub has is used for the nose cone with an inflation rate of 35.6% for the years of 2002 to 2009.

A.2.5 Low speed shaft

Since the mass and cost models of the low-speed shaft are concept dependent, the data presented here can not be used for direct drive, single-stage drive, or multi-generator drives, therefore, these data are only valid for a conventional three stage gearbox with a doubly fed induction generator (DFIG).

Low speed shaft mass

The mass of the low speed shaft is a function of rotor diameter as follow:

$$\text{Low speed shaft mass} = 0.0142 \times \text{rotor diameter}^{2.888} \quad (\text{A.9})$$

Low speed shaft cost

The low speed shaft cost is also a function of rotor diameter as shown below:

$$\text{Low speed shaft mass} = (0.01 \times \text{rotor diameter}^{2.887}) \times (1 + \text{PPI})_{\text{LSS}} \quad (\text{A.10})$$

The low speed shaft is made of cast carbon steel castings with an NAICS Code of 3315131 that has a subgroup code of PCU3315133315131. For this NAICS code an inflation rate of 44.1% is reported during the years of 2002 to 2009.

A.2.6 Main bearing and its housing

The main bearing is used to carry all components of the rotor load except the rotational degree of freedom, and transfer them to the tower. It consist of a main bearing and its housing.

Main bearing and housing mass

The bearing mass is a function of rotor diameter, and it is calculated by:

$$\text{Main bearing mass} = 0.0092 \times (0.0133 \times \text{rotor diameter} - 0.033) \times \text{rotor diameter}^{2.5} \quad (\text{A.11})$$

The mass of the housing is also assumed to be the same as the mass of the main bearing, therefore it shares the same formula.

Main bearing and housing cost

The main bearing cost is a function of its mass as follow:

$$\text{Main bearing cost} = 2 \times \text{bearing mass} \times 17.6 \times (1 + \text{PPI})_{\text{Bearing}} \quad (\text{A.12})$$

The main bearings has an NAICS Code of 332991P, PCU332991332991P. For this NAICS code an inflation rate of 35.6% is reported during the years of 2002 to 2009.

A.2.7 Gearbox

A proper projection of the mass and cost of the gearbox is difficult to make, since there are several different gearbox configurations and for each of which several ways to model. In the WindPACT project four standard designs are considered that can be found on [Poore and Lettenmaier \(2003\)](#) and [Bywaters et al. \(2005\)](#). These four standard models are a three-stage planetary/helical gearbox with high-speed generator, single-stage drive with medium-speed generator, a multi-path drive with multiple generators, and a direct drive with no gearbox.

In this research a planetary/helical gearbox with a high-speed doubly fed induction generator is used. This configuration is the dominant concept in use, and it matches very well with the design assumptions of the 5 MW NREL wind turbine that is used for upscaling studies of this work.

Gearbox mass

The mass of the gearbox is a function of the low-speed shaft torque and thus adjusts for differences in rotor diameter and tip speed.

$$\text{Gear box mass} = 70.94 \times \text{low speed shaft torque}^{0.759} \quad (\text{A.13})$$

Gearbox cost

The cost of the gearbox is a function of machine rating and only changes when the size of the machine changes from 5 MW to 10 MW and higher.

$$\text{Gearbox cost} = 16.45 \times \text{machine rating}^{1.249} \times (1 + \text{PPI})_{\text{Gearbox}} \quad (\text{A.14})$$

The gearbox has a NAICS Code 333612P, PCU333612333612P for industrial high-speed drive and gear. For this NAICS code an inflation rate of 28.6% is reported during the years of 2002 to 2009.

A.2.8 Mechanical brake and coupling

The mechanical brake system is made of the brake itself that is mounted on the high speed shaft and a high speed shaft coupling to remove the brake in the case of failure.

Mechanical brake and coupling mass

The mass of the mechanical brake including the coupling is a function of machine rating as follow:

$$\text{Mechanical brake \& coupling mass} = 0.19894 \times \text{machine rating} \quad (\text{A.15})$$

Mechanical brake and coupling cost

The cost model is a function of the mass of the mechanical brake, and it is assumed that every kilogram of its mass will cost 10 USD, including material, manufacturing and labor costs. Thus, its cost can be calculated by:

$$\text{Mechanical brake \& coupling cost} = 10.0 \times \text{mechanical brake mass} \times (1 + \text{PPI})_{\text{Brake}} \quad (\text{A.16})$$

The PPI has a NAICS code of 3363401, PCU3363403363401 and from year 2002 to 2009 it has an inflation rate of 12.0%.

A.2.9 Generator

WindPACT project presented several models of the generator concepts that are frequently used by industry. Among them, the doubly fed induction generator model is selected and used here.

Generator mass

The generator mass is a function of the machine rating as:

$$\text{Generator mass} = 6.478 \times \text{machine rating}^{0.9223} \quad (\text{A.17})$$

Generator cost

The generator cost is a function of the machine rating as:

$$\text{Generator cost} = 65 \times \text{machine rating} \times (1 + \text{PPI})_{\text{Generator}} \quad (\text{A.18})$$

A NAICS Code 335312P with a subcategory PCU335312335312P for motor and generator manufacturing is used to predict the inflation rate. For this NAICS code and from year 2002 to 2009 an inflation rate of 23.0% is reported.

A.2.10 Power electronic

The generator is equipped with a converter capable of carrying full power output. Mass of the power electronic is not modeled by the WindPACT project, since it is not heavy when compared to other components and can simply be ignored. Therefore only a cost model is presented that is a function of machine rating as below:

$$\text{Power electronic cost} = 79 \times \text{machine rating} \times (1 + \text{PPI})_{\text{PowElec}} \quad (\text{A.19})$$

The generator power electronic is classified in relay and industrial control manufacturing category with a NAICS code of 335314P, and a subcategory code of PCU335314335314P. For this item, an inflation rate of 21.5% is reported during the years of 2002 to 2009.

A.2.11 Bed plate

Each drive train design has a different load pattern and hence its own unique load distribution on the bed plate. As the result, bed plate mass and cost models are dependent on of the type of drive train. Mass and cost for the mainframe are calculated as a function of the rotor diameter.

Bed plate mass

For a three-Stage drive with high-Speed generator the mass model is presented below.

$$\text{Bed plate mass} = 2.233 \times \text{rotor diameter}^{1.953} \quad (\text{A.20})$$

Bed plate cost

The cost of the bed plate is a function of rotor diameter.

$$\text{Bed plate mass} = (9.489 \times \text{rotor diameter}^{1.953}) \times (1 + \text{PPI})_{\text{BedPlate}} \quad (\text{A.21})$$

The PPI has a NAICS code of 3315113, PCU3315113315113 for ductile iron castings and from year 2002 to 2009 it has an inflation rate of 35.6%.

A.2.12 Platform and railing

A platform for each component installed on the bed plate is needed. This platform transfers the loads from the component bases to the bed plate. Also a railing guide is installed on the bed plate to move the gearbox, mechanical brake and generator easily in the nacelle.

Platform and railing mass

The mass of the platform and railing is assumed to be 12.5% of the mass of the bed plate.

$$\text{Bed plate mass} = 0.125 \times \text{bed plate mass} \quad (\text{A.22})$$

Additional mass of 12.5% is added for platforms and railing for the gearbox, mechanical brake and generator and are calculated on a USD/kg basis.

Platform and railing cost

Costs for the additional platforms and railing equipment installed on the bed plate is calculated based on the mass of the platform and railing, and it is assumed that every kilogram of its mass will cost 8.7 USD, including material, manufacturing and labor costs.

$$\text{Platform \& railing} = (8.7 \times \text{platform \& railing mass}) \times (1 + \text{PPI})_{\text{Platform}} \quad (\text{A.23})$$

The NAICS code of 3315113, PCU3315113315113 is used for this item, and from year 2002 to 2009 it has an inflation rate of 35.6%.

A.2.13 Hydraulic and cooling system

The cooling system is used to keep the temperature of the gear box and mechanical brake in a certain allowable range, the hydraulic system is used to actuate the blade pitch mechanism and mechanical brake. The WindPACT project used that mass and cost models from the LWST project. The mass and cost models presented here show the summation of hydraulic and cooling system masses and costs.

Hydraulic and cooling system mass

The mass is a function of the machine rating as follow:

$$\text{Hydraulic \& cooling mass} = 0.08 \times \text{machine rating} \quad (\text{A.24})$$

Hydraulic and cooling system cost

Similar to the mass formula, the cost of the hydraulic and cooling system is a function of the machine rating as follow:

$$\text{Hydraulic \& cooling cost} = 1.2 \times \text{machine rating} \times (1 + \text{PPI})_{\text{HydCool}} \quad (\text{A.25})$$

These two system are classified as fluid power cylinder and actuators category with and NAICS Code of 339954, with a subgroup code of PCU333995333995. For this item, an inflation rate of 29.3% is reported during the years of 2002 to 2009.

A.2.14 Nacelle cover

The nacelle cover is used to enclose the nacelle from external environment. the WindPact project has derived a single function for all drivetrain configurations, since data were too scarce to develop individual formulas for different configurations.

Nacelle cover mass

The nacelle cover is a function of machine rating as follow:

$$\text{Nacelle cover mass} = 0.1 \times (11.537 \times \text{machine rating} + 3849.7) \quad (\text{A.26})$$

Nacelle cover cost

The cost of the nacelle cover is a function of nacelle mass, and it is assumed that every kilogram of its mass will cost 10.0 USD, including material, manufacturing and labor costs.

$$\text{Nacelle cover cost} = 10 \times \text{nacelle cover mass} \times (1 + \text{PPI})_{\text{NacelCovr}} \quad (\text{A.27})$$

The PPI of the nacelle cover consists of the following NAICS codes:

- Fiberglass fabric, NAICS Code 3272123, PCU3272123272123, with a product make up factor of 55%, and an inflation rate of 30.8% from 2002 to 2009
- Vinyl type adhesives, NAICS Code 32552044, with a product make up factor of 30%, and an inflation rate of 15.3% from 2002 to 2009
- Assembly labor, with a product make up factor of 15%, and general inflation index of 19.7% from the years 2002 to 2009

Using this definition, and including the product make up factor weight, a PPI of 24.4% is obtained for the nacelle cover.

A.2.15 Electrical connections

There is no mass model assumed for the electrical connection elements, since their weight can simply be ignored comparing to the weight of other elements of the wind turbine. Elements that are categorized in this item are: switchgears, transformer, cables and cabinets. The cost of these elements is a function of rated power.

$$\text{Electrical connections cost} = (40 \times \text{machine rating}) \times (1 + \text{PPI})_{\text{ElecConc}} \quad (\text{A.28})$$

The PPI of the electrical connections consists of the following NAICS codes:

- Switchgear and apparatus NAICS Code 3353133, PCU33531333353133, with a product make up factor of 25%, and an inflation rate of 24.7% from 2002 to 2009
- Power wire and cable NAICS Code 3359291, PCU3359293359291 with a product make up factor of 60%, and an inflation rate of 76.6% from 2002 to 2009
- Assembly labor, with a product make up factor of 15%, and general inflation index of 19.7% from the years 2002 to 2009

Using this definition, and including the product make up factor weight, a PPI of 55.9% is calculated for electrical connections.

A.2.16 Yaw system

The yaw system consist of the yaw drive and a bearing installed on top of the tower.

Yaw system mass The mass of the total yaw system (yaw drive and bearing) is a function of rotor diameter. Mass data are based on calculated moments. These moments were calculated using ADAMS software. However, they are presented as a function of rotor diameter:

$$\text{Yaw system mass} = 1.6 \times (0.0009 \times \text{rotor diameter})^{3.314} \quad (\text{A.29})$$

Yaw system cost Yaw bearing cost is based on quotes from Avon Bearing company, and modified based on the size of rotor. Total yaw system cost is twice the bearing cost.

$$\text{Yaw system cost} = (2 \times (0.0339 \times \text{rotor diameter})^{2.964}) \times (1 + \text{PPI})_{\text{YawSys}} \quad (\text{A.30})$$

The PPI of the yaw system consists of the following NAICS codes:

- Drive motor NAICS Code 3353123, PCU3353123353123, with a product make up factor of 50%, and an inflation rate of 32.9% from 2002 to 2009
- Ball and roller bearings NAICS Code 332991P, PCU332991332991P, with a product make up factor of 50%, and an inflation rate of 23.9% from 2002 to 2009

The weighted inflation rate based on the product make up factor given above, and each individual inflation rate is 28.4%.

A.2.17 Control system

The control system consist of safety equipments, condition monitoring equipments, wiring and sensors. The mass of these items is negligible, therefore also ignored in the WindPACT project. The total cost of these items does not have too much sensitivity to machine size and rating. Therefore, for offshore systems, a fixed price of 55000 USD, regardless of machine size or rating is used.

$$\text{Control system cost} = (55000) \times (1 + \text{PPI})_{\text{ConSys}} \quad (\text{A.31})$$

Control system has a NAICS Code of 334513, PCU334513334513 and is categorized as controller and drive with a subcategory of industrial process control. The PPI for this class of equipments has an inflation rate of 18.9% during the years 2002 to 2009.

A.2.18 Tower

The tower mass is calculated in every iteration of optimization and using the methodology explained in appendix B. The cost model of the tower uses a cost per kilogram formulation of $1.5 \frac{\text{USD}}{\text{kg}}$, including material, manufacturing and labor costs. Thus the cost model can be formulated as:

$$\text{Tower cost} = 1.5 \times \text{tower mass} \times (1 + \text{PPI})_{\text{Tower}} \quad (\text{A.32})$$

Control system has a NAICS Code of 331221, PCU331221331221 and is categorized as rolled steel shape manufacturing with a subcategory of primary products. The PPI has an inflation rate of 80.2% during the years 2002 to 2009. As it can be seen, if one would use a general inflation index of 19.7% instead of the above PPI, a big error will be introduced in the cost formula of the tower.

A.2.19 Marinization

The Marinization expenses is used for additional preparation for all components of the wind turbine, in order to increase their survivability in the extreme sea condition. These preparations include special paints and coatings, improved seals for gearboxes, generators, electrical components, and electrical connections.

The cost model is calculated as a percentage of all turbine costs, and is mainly based on the report of DUWIND (2001). However, a range of journals publications also suggest a marinization factors of between 10% and 15% of the turbine and tower cost. A number of 13.5% was selected in WindPACT and also used here. However, is also should be mentioned that this is a rough estimate and it varies with the design.

$$\text{Tower cost} = 0.135 \times \text{turbine and tower cost} \tag{A.33}$$

Turbine and tower cost, is the participation of all cost elements form equation A.1 to A.32.

A.2.20 Foundation system

The foundation system consist of the transition piece and monopile. The tower is attached to the monopile that extends from sea bed to mean sea level. There are several different concepts for the foundation, but the most often used is a driven pile (a steel pile driven into the sea bed). This allows the tower to be bolted to the top of this structure.

The associated costs to install such a driven pile is greater than the basic concrete foundation used for onshore wind turbines. The cost model presented in the WindPACT project is derived from a University of Massachusetts study done by Manwell (2002). However, this model is augmented with industry communications expressed as a function of machine rating.

$$\text{Foundation cost} = 300 \times \text{machine rating} \times (1 + \text{PPI})_{\text{SupStrc}} \tag{A.34}$$

Foundation system has a NAICS Code of BHVY, PCUBHVVY-BHVY and is categorized as heavy construction. A inflation rate of 45.6% is reported for this item during the years 2003 to 2009.

The mass model of the foundation is based on the linearly upscaled offshore version of the 5 MW NREL wind turbine.

A.2.21 Offshore transportation

There are two cost elements associated with transporting an offshore wind turbine. The first cost model covers the expenses to get the turbine components to the port staging and assembly area near the shore. The second cost model is to get the assembled turbine to the installation site. The second cost model is explained in next subsection.

The first cost model, offshore transportation, covers the expenses to bring the components to the assembly site near the shore. The costs for MW turbines show a significant increase comparing with smaller turbines. These costs can be significantly reduced by locating manufacturing facilities close to shore.

The offshore transportation cost model is based on the technical report of Smith (2001), and is a function of machine rating.

$$\text{Offshore transportaion cost} = \text{machine rating} \times \text{costfactor} \times (1 + \text{PPI})_{\text{OfshrTmstp}} \tag{A.35}$$

In the above formula, the cost factor is a function of machine rating and is given by:

$$\text{Cost factor} = 0.000015\text{machine rating}^2 + 0.0375 \times \text{machine rating} + 54.7 \tag{A.36}$$

Offshore transportation has a NAICS Code of 335312P, PCU484121484121P and is categorized as general freight trucking, long-distance, truckload. A PPI of 21.2% is reported during the years 2002 to 2009.

A.2.22 Port and staging equipment

This item covers facilities needed to bring the wind turbine components to the installation site and maintain a safe operation of wind turbine during its life time. It only covers the expenses of using special ships and barges to install piles, setting towers and turbines, laying underwater electrical lines, and providing ongoing servicing, and should not be confused with the installation expenses, explained in next subsection.

Unfortunately, long-term data on this cost element does not exist and little hard detailed industry data are available. The costs presented in WindPACT project are based on private industry communications converted to a scaling factor based on machine rating, and cross-checked with some data published in scientific journals.

$$\text{Port \& staging cost} = 20 \times \text{machine rating} \times (1 + \text{PPI})_{\text{PrstStag}} \quad (\text{A.37})$$

For port and staging cost model a NAICS Code of BHVY, PCUBHVVY-BHVY is allocated, and it is categorized as heavy construction. A PPI of 45.6% is reported during the years 2002 to 2009.

A.2.23 Offshore turbine installation

This cost model covers extra facilities required to do the installation of wind turbine such as extra tools and fixtures, cranes and hammering machines. Costs in this model are also based on private industry communications presented as the function of machine rating.

$$\text{Offshore turbine installation cost} = 100 \times \text{machine rating} \times (1 + \text{PPI})_{\text{Instltn}} \quad (\text{A.38})$$

Offshore transportation has a NAICS Code of BHVY, PCUBHVVY-BHVY and it is categorized as heavy construction. A PPI of 47.2% is reported during the years 2003 to 2009.

A.2.24 Offshore electrical interface and connection

This cost model covers expenses to bring the turbine power to shore. The cost model includes the cost of cabling between turbines and the cable to the grid interconnect at the shore and switchgears. Costs in this model are based on calculations and data formulated by [Butterfield and Laxson \(2004\)](#). This cost model should be used with care, since it is calculated specifically for a distance to shore of about 8 kilometer, a water depth of 10 meters, and an array spacing of 7 by 7.

$$\text{Offshore elcterical interface cost} = 260 \times \text{machine rating} \times (1 + \text{PPI})_{\text{ElcIntrfc}} \quad (\text{A.39})$$

The PPI of the electrical interface consists of the following NAICS codes:

- An NAICS Code of 3353119, PCU3353113353111 for power and distribution transformers with a product make up factor of 40%, and an inflation rate of 67.3% from 2002 to 2009

- An NAICS Code of 3335313P, PCU3335313335313P for switchgear and apparatus with a product make up factor of 15%, and an inflation rate of 24.7% from 2002 to 2009
- An NAICS Code of 3359291, PCU3359293359291 for power wire and cable with a product make up factor of 35%, and an inflation rate of 76.6% from 2002 to 2009
- A general inflation index for assembly and labor with a product make up factor of 10%, and an inflation rate of 19.7% from 2002 to 2009

The weighted inflation rate based on the product make up factor given above, and the participation of each individual inflation rate is 59.4%.

A.2.25 Offshore permits, engineering, and site assessment

The cost model covers developing detailed engineering plans, measuring wind conditions for an offshore site, site assessment to locate the wind farm and project management expenses. The costs in this model are based on private industry communications converted to a $\frac{USD}{kW}$ scaling factor.

$$\text{Offshore management cost} = 37 \times \text{machine rating} \times (1 + \text{GDP}) \quad (\text{A.40})$$

For this item, a general inflation index is used with a growth rate of 17.0% during the years of 2003 to 2009.

A.2.26 Personnel access equipment

Marine vessels, helicopters or small boats are needed for servicing offshore wind turbines. During the access operation, the environment will present many hazards to the personnel, and to improve the safety for these operations, special personnel access equipment is needed.

In addition, servicing requires special boat access ramps or docking equipment, lifesaving equipment located at each turbine, special tool lifts, and emergency survival equipment in case service personnel are stranded at a turbine. All these items introduce extra expenses, which are needed to make the working environment safe. The cost model presented in WindPACT project is developed from private industry communications.

$$\text{Offshore management cost} = 60000/\text{turbine} \times (1 + \text{GDP}) \quad (\text{A.41})$$

As it can be seen from equation A.41, the cost model is a fixed value regardless of turbine rating or size. For this item, a general inflation index is used with a growth rate of 17.0% during the years of 2003 to 2009.

A.2.27 Scour protection

Scour is the removal of granular bed material by hydrodynamic forces in the vicinity of offshore structures. In this case, currents swirling around the structure have a tendency to scour bottom material from the base, and increasing the risk of foundation failure.

To decrease such a risk, graded boulder and rock are placed around the base of the structure. Cost estimates in the WindPACT model are based on private industry communications converted to a scaling factor by machine rating.

$$\text{Scour protection cost} = 55 \times \text{machine rating} \times (1 + \text{PPI})_{\text{ScrPrtc}} \quad (\text{A.42})$$

For scour protection a NAICS Code of BHVY, PCUBHVY-BHVY is defined and it is categorized as heavy construction. A PPI of 47.2% is reported during the years 2003 to 2009.

A.2.28 Offshore warranty premium

Offshore wind turbines are located in remote locations and they operate in an extreme environment. Therefore, they experience a greater risk of failure than for land-based installations. As the wind turbine is getting more expensive this risk requires also a higher warranty premium. The windPACT warranty estimates are based on private industry communications and the cost model is a function of the wind turbine and tower cost.

$$\text{Offshore warranty premium cost} = 0.15 \times \text{turbine and tower cost} \quad (\text{A.43})$$

Turbine and tower cost, is the participation of all cost elements form equation A.1 to A.32.

A.2.29 Decommissioning

Offshore installations present long-term navigational hazards. However, there is unlikely that a good wind farm site will be abandoned, but to guarantee funds for removing older structures this cost element is taken into account. The decommissioning cost model is developed as a percentage of the initial capital cost, without the offshore warranty premium.

$$\text{Decommissioning cost} = 0.03 \times (\text{ICC} - \text{Offshore warranty premium cost}) \quad (\text{A.44})$$

A.2.30 Offshore levelized replacement

Offshore installations require more frequent overhaul and replacment, since they carry a higher risk of wear and tear. Levelized replacement cost (LRC) covers the long-term replacements and overhaul of major turbine components, such as blades, gearboxes, and generators. The cost model is developed based on private industry communications and converted to a scaling factor based on a fixed price of 17 USD of machine rating expressed in kW.

$$\text{LRC cost} = 17 \times (\text{machine rating in kW}) \times (1 + \text{GDP}) \quad (\text{A.45})$$

The general inflation index has a growth rate of 17.0% during the years of 2003 to 2009.

A.2.31 Operation and maintenance

Operation and maintenance expenses of offshore wind turbines are higher than those for onshore, at least during the early period of operation. Initial offshore O&M costs are expected to be almost three times that of current onshore estimates. In the WindPACT project costs are estimated on a fixed price of 0.02 USD per kWh basis.

$$\text{O\&M cost} = 0.02 \times \text{annual energy production} \times (1 + \text{GDP}) \quad (\text{A.46})$$

For the general inflation index a growth rate of 17.0% is reported during the years of 2003 to 2009.

A theoretical background of the used simulation tools

B.1 Introduction

As it was explained in chapter 3, a set of simulation tools is needed to model the physical behavior of a wind turbine. This appendix gives a theoretical background of the simulation tools that are used in this work. All these tools are open source and free to download and use for research studies from the website of the NREL.

B.2 TurbSim

TurbSim calculates a numerical simulation of a full-field flow, which contains coherent turbulence structures that reflect the proper spatiotemporal turbulent velocity field relationships. It enables the designer to simulated inflow turbulence environments that incorporate many of the important fluid dynamic features known to adversely affect turbine aeroelastic response and loading.

TurbSim supports the IEC Kaimal and von Karman Normal Turbulence Models (NTM) to generate a turbulent inflow and provides the ability to efficiently generate randomized coherent turbulent structures that are superimposed on the more random background turbulent field. The code also allows the user to use available observed turbulence information to improve the agreement in specific locations.

The presence of superimposed coherent structures can induce transient loading events on simulated turbine rotors and supporting structures. The combination of techniques; i.e., Fourier inversion plus time-domain Poisson and Lognormal modeled events, produce the highly non-Gaussian flow behavior associated with the presence of coherent structures in actual flows.

The use of the coherent events does require a bit more execution time in the AeroDyn program (where they are superimposed on the background turbulence). The exact

amount of time depends on the number of events and their lengths. The Cholesky factorization algorithm has been rewritten in TurbSim to be more efficient in terms of both CPU and memory usage.

TurbSim is intended to generate a series of inflow simulations based on a given set of initial boundary conditions that are employed with the design codes, FAST and YawDyn to produce response (load) solutions that can be analyzed using ensemble statistics.

B.3 AeroDyn

The AeroDyn code is a set of routines for aerodynamic calculations by [Laino and Hansen \(2002\)](#), to provide instantaneous aerodynamic loading in an aeroelastic simulation. AeroDyn contains two models for calculating the effect of wind turbine wakes:

- **The blade element momentum model (BEM):** It is the classical standard used by many wind turbine designers that has various corrections such as incorporating the aerodynamic effects of tip losses, hub losses, and skewed wakes.
- **The generalized dynamic-wake model:** It is a more recent model useful for modeling skewed and unsteady wake dynamics, which represents the induced velocities at the rotor plane with a series solution. It is an expanded form of the Pitt and Peters dynamic inflow [Pitt and Peters \(1983\)](#), and runs considerably faster than BEM, since it does not require iteration on the induction factors.

In addition, AeroDyn contains an important model for dynamic stall based on the semi-empirical Beddoes-Leishman model [Leishman and Beddoes \(1989\)](#). This model is particularly important for yawed wind turbines. Another aerodynamic model in AeroDyn is a tower shadow model based on potential flow around a cylinder and an expanding wake.

When comparing BEM method with other advanced methods, it offers a good prediction of loads and predicts the actual performance in post-stall conditions fairly [Duque et al. \(2000\)](#), and it runs very fast. For these reasons, modified BEM codes dominate the arena of wind turbine aerodynamic design tools, and it is used in this work.

Navier-Stokes simulations have numerical stability issues and exceptionally high expense for the unsteady cases, they suffer from inadequate turbulence models, and problems preserving the concentrated vorticity in the wake as it is convected downstream [Robinson et al. \(1999\)](#). Also CFD modeling using Euler equations yield little to no insight over vortex methods, at a higher cost, as the relevant inviscid features of the flow are already captured by Laplace's equation.

In AeroDyn, the blade is modeled as strip elements, with variable length and extend across an arbitrary disc from the blade root to tip. The blade twist, chord and airfoil characteristics are specified at the mean radius of each element. The airfoil lift, drag and moment curves are supplied separately to AeroDyn. The input wind speed is provided as a time-history rather than a constant velocity, and with a variable yaw angle. Horizontal and vertical shearing profiles are included as well. The wind field can either be described by the time-history at the hub height, or by a full grid of histories over the rotor plane area.

B.4 AirfoilPrep

Wind turbine airfoils frequently operate beyond stall condition at both negative and positive angle of attack. AirfoilPrep is a code to prepare airfoil input files over the full 360-degree data needed by AeroDyn. It uses the Viterna stall equations (see [Viterna and Janetzke \(1982\)](#)) to expand the full 360-degree data from a limited number of angle of attacks. It can also apply rotational augmentation corrections for 3-D delayed stall. It uses Du's method (see [Du and Selig \(1998\)](#)) to augment the lift, and Eggers' method to modify the drag (see [Eggers et al. \(2003\)](#)).

B.5 FAST

FAST is a medium-complexity code for nonlinear aeroservoelastic simulation of wind turbines. In addition, FAST enables:

- Generation of ADAMS models and all relevant inputs
- Extraction of linear state-space models for control design
- Interfacing with Simulink to implement advanced turbine controls in block diagram form

FAST models the wind turbine as a combination of rigid and flexible bodies and it employs a combined modal and multibody dynamics formulation. The rigid bodies are the earth, hub, nacelle, and optional tip brakes as a point mass. The flexible bodies include blades, tower, and main shaft.

These bodies are connected using 26 degrees of freedom. These include tower bending, blade bending, nacelle yaw, rotor teeter, rotor speed, and drive shaft torsional flexibility. Blades have two flapwise modes and one edgewise mode per blade, tower has two modes each in the fore-aft and side-to-side directions, and the main shaft has one torsional degree of freedom.

FAST uses Kane's method to set up equations of motion that are solved numerically. The mode shapes are described by 6th order polynomials, the first two terms of which must be zero to provide zero deflection and slope at the base of the blade. The coupled equations of motion are solved using a 4th order Runge-Kutta scheme. The implemented method makes direct use of the generalized coordinates, eliminating the need for separate constraint equations.

FAST uses the AeroDyn code to generate aerodynamic forces along the blade. The electrical characteristics of the generator response are also modeled. Two models are available for the generator: a simple induction motor with a simple torque versus speed profile, and a Thevenin equivalent circuit model.

FAST also has provisions for active control of the blade pitch angle, generator torque, tip brakes, and a high-speed shaft brake. The user can make custom control laws, or use simple switches to turn the various controls on at a certain time, which enables any test condition from start up through shutdown operations, emergency stop and grid failure.

The model complexity of this code is at the level of current detailed design and verification codes. The outputs of the code are time-histories of every degree of freedom in various reference frames (inertial, flapwise/edgewise, in-plane/out-of-plane), as well as

the displacement, velocity and accelerations acting on any component.

For flexible bodies, the bending moments, shear, and normal forces are available, together with the tip motions used in the modal analysis. Since the source code of FAST is available, it was modified many times to increase its compatibility to run in an iterative optimization process for this work.

B.6 BModes

The mode shapes of the blade and tower, and their relevant natural frequencies are needed as inputs for FAST that can be generated using the BModes code, [Bir \(2007\)](#). Modes uses the distributed inertial and stiffness properties of the blade and tower along their longitudinal axis, the rotational speed of the blade to calculate the rotational stiffening and its pitch angle as input. Polynomial expressions of the mode shapes are calculated from the solution of the associated eigenvalue vectors. In the same way, the natural frequencies are found from the solution of the eigenvalues that include stiffening effects of rotation. Since for an aeroservoelastic design optimization problem, the blade pitch and rotational speed change in every iteration, the source code of BModes is modified to account these changes automatically in every iteration.

B.7 Crunch

Crunch is a post-processing tool to perform: load-roses, rainflow cycle counting of any load history, extreme event finding for the limit load calculation, probability mass functions (histograms), azimuth averaging, channel combination, moving averages, data filtering and statistical analysis of the data. It is a user-friendly code and enables a wide variety of data processing from both field tests and time simulations.

B.8 Fatigue

Fatigue is a code to read a series of Crunch rainflow cycled files and using a Rayleigh distribution of wind speed, it calculates cumulative fatigue spectra and damage-equivalent loads. The source code used in this work is modified to work also with non-Rayleigh wind distributions.

Verification of the controller design automation

C.1 Introduction

The controller design automation and the integration of that in the design optimization loop was explained in chapter 3. However, two case studies are presented in this appendix to make sure that the controller design automation is implemented correctly, and it results in a decrease of the design constraints and objective function in practice.

Two different MDO scenarios are defined and applied on the 5 MW NREL wind turbine. In the first case the torque and pitch controller are designed for the initial design and their parameters are fixed in the entire DOP. However, at the end of the process both controllers are redesigned based on the final design variables found by the optimizer.

In the second case, both controllers are redesigned within every optimization iteration. As expected, the objective function and design constraint of case one and two are different. This shows the influence of a realistic assessment of the objective function and constraint by the optimizer, which leads to more reduction in the cost of energy and the constraint.

C.2 Applying the controller design task

To show the fundamental differences of case one and two, costs of energy as the objective function, and fatigue damage as the design constraint at the blade root are selected for this investigation. System cost consists of all the elements that a wind turbine is made of and explained in detail in appendix B and the formula to find the AEP is given by equation 3.7 of chapter 3, therefore the cost of energy can be calculated as:

$$\text{LCOE} = \frac{\text{System cost}}{\text{Annual energy production}} \quad (\text{C.1})$$

For calculating fatigue, rain flow cycle counting is applied on the time-series output of the aeroelastic solver. Based on that, the Miner rule is used to calculate the cumulative fatigue damage at the blade root, in flapwise direction.

For both cases, the level two optimization technique explained in subsection 3.12.4 of chapter 3 is used, with all the associated design variables in. This new methodology is implemented as an external master controller dynamic link library (DLL), in the format of BLADED.

For case one, the the controller is designed two times, the first design is based on the initial value of all the design variables and parameters before starting the optimization and then using it in all optimization iterations without applying any changes to it, and the second design is after the end of the optimization process, based on the final set of optimism design variables.

Therefore, case one optimization is done with two different DLL files. Contrary to case one, the controller design in case two is done in every iteration and the DLL file is automatically generated and directly used in the process.

The DOP is performed using the integrated design optimization tool developed in 3. The controller design automation is carried out in MATLAB. Therefore, an interface is developed to fully automate the DOP and guarantee the integrity of all the simulation tools.

C.3 Analysis and results

To show the influence of the selected strategy on the objective function and constraint, the final results of case one and two are compared in this section.

Using the generator torque controller, for case one a generator proportional gain of 0.02710 ($\frac{kN \cdot m}{RPM^2}$) is found. This value for case two is 0.02770 ($\frac{kN \cdot m}{RPM^2}$) that is higher than case one. This is due to the fact the optimizer has properly evaluated the objective function and constraint in every iteration that has resulted in a truly optimum values for design variables.

For the above rated pitch controller, the final aerodynamic power sensitivity to the blade pitch angle for different steady state operating points of case one and two is presented in figure C.1. As the figure shows, this sensitivity is different for case one and two, which demands a different controller design for the pitch controller.

However, the power regulation of case two is better achieved, since in every iteration the controller used the true chord and twist distribution of the blade. Consequently, this true assessment of design variables by the controller results in lower loads on the blade for case two.

For case two, the variation of the proportional and integral gains of the pitch controller to balance out the changes of the aerodynamic power is shown in figure C.2. This is done using the gain scheduling technique presented before. The calculated proportional and integral gains are obtained using equation 3.19 and 3.20 respectively.

For both scenarios, the cost of energy and flapwise fatigue at the blade root are calculated and presented in figure C.3. As the figure shows, different design strategies of implementing the controller in an MDO result in different values of the objective function and constraint.

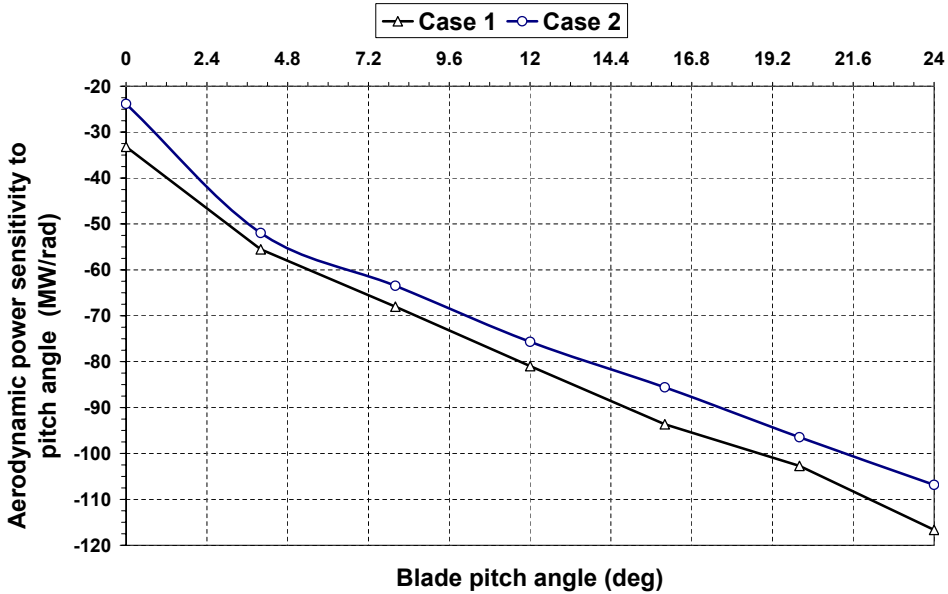


Figure C.1: Aerodynamic power sensitivity to blade pitch of the 5 MW wind turbine

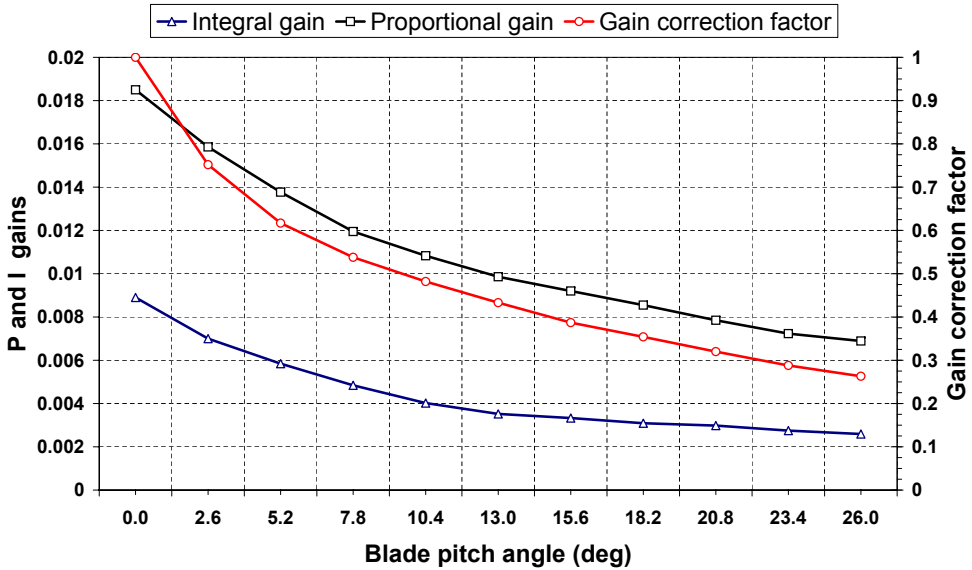


Figure C.2: PI gains and gain scheduled correction factor of case 2

As the results show, a better assessment of the objective function and the constraint helps the optimizer to move towards better design solutions for the system. This proves the importance of doing an aeroservoelastic design optimization instead of even an aer-

oelastic design optimization.

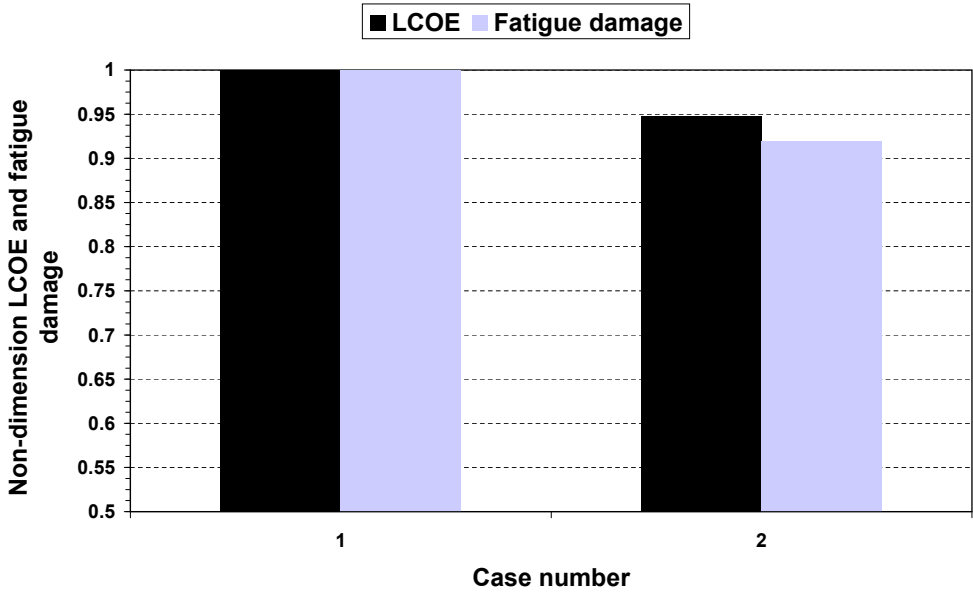


Figure C.3: Nondimension cost of energy and root fatigue damage of the 5 MW NREL wind turbine

Verification of extracting structural properties

D.1 Introduction

In chapter 3 the derivation of an analytical model to extract the blade's structural properties was explained. However, this method needs to be verified to ensure the correct implementation of formulas and check the validity of the assumptions.

This task is done in this appendix by doing a comparison with the structural properties of a 660 kW commercial blade. However, due to the confidentiality of the data used for the comparison, plots are presented in a nondimensionalized form.

D.2 Verification of the method

A 660 kW wind turbine blade, which all its structural properties are known in advance is selected for the verification of the method. Three representative structural properties of the blade, flapwise and edgewise stiffness, and mass per unit length of 20 stations along the blade are used. However, the same level of accuracy has been found in comparing other properties (strength, radius of gyration and \check{E}), but only three of them are presented here.

Figure D.1 shows the nondimensional flapwise stiffness distribution of the blade. As the figure shows, there is a good agreement between the calculated flapwise stiffness using this analytical model and the real data.

Results of the edgewise stiffness are presented in figure D.2. Comparing the accuracy of the edgewise and flapwise stiffness, the edgewise stiffness shows more discrepancy between the analytical model and the 660 kW wind turbine blade data.

This is mainly due to manufacturing modifications applied on the leading and trailing edges of the commercial blade, while in the analytical model the $X - Y$ coordinates of the airfoil are used for calculating the stiffness. This manufacturing modification has more

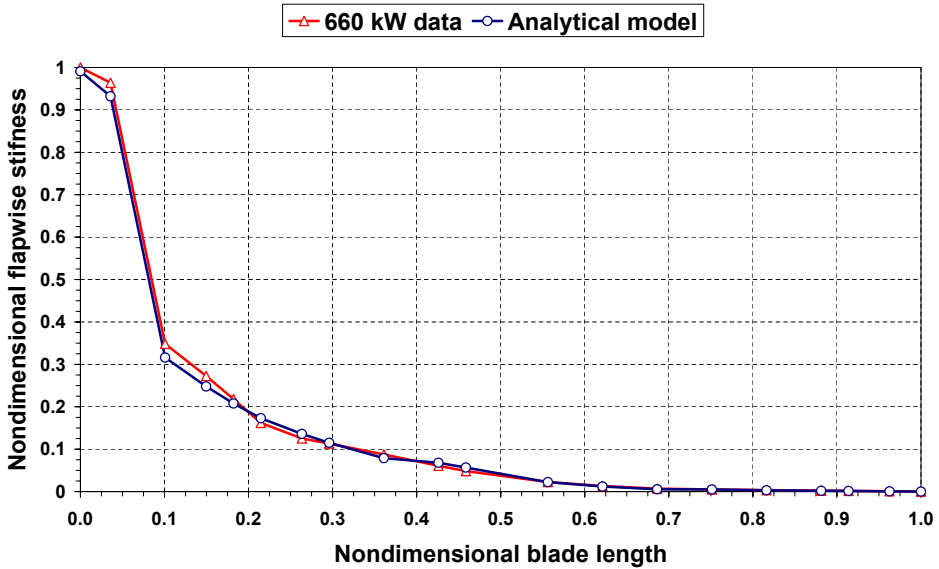


Figure D.1: Comparison of flapwise stiffness of the analytical model with the 660 kW wind turbine blade

influence on the edgewise stiffness than the flapwise stiffness, since they are more away from the bending centroid in the edgewise direction.

The comparison of the mass per unit length is presented in figure D.3. As the figure shows, the predicted values from the analytical model are very close to the values of the 660 kW wind turbine blade.

For different stations along the blade, the analytical model needs the blade geometry, the thickness of composite laminates including related material properties as inputs. The geometry should be given in terms of chord, twist, aerodynamic thickness and airfoil $X - Y$ coordinates along the blade. Since, it is a parametric code it allows any parameter such as thicknesses and the location of the shear webs to be introduced as design variable in a design optimization study. The code is very fast and runs in a fraction of a second, and requires only a little knowledge of composite materials used in wind turbine blades.

Despite the simplicity of the approach, it provides good results. However, there is no bend-twist coupling that makes the method less accurate for detailed design studies. Therefore the usage of this method should be limited to upscaling and optimization studies, as it is in this work.

Due to the analytical approach of the method, it is an excellent tool for blade's internal layout optimization as well. This can be done for example by playing with the location and the number of shear webs along the chord or adding ribs to see the influence of that on the stiffness and mass, thus the associated costs.

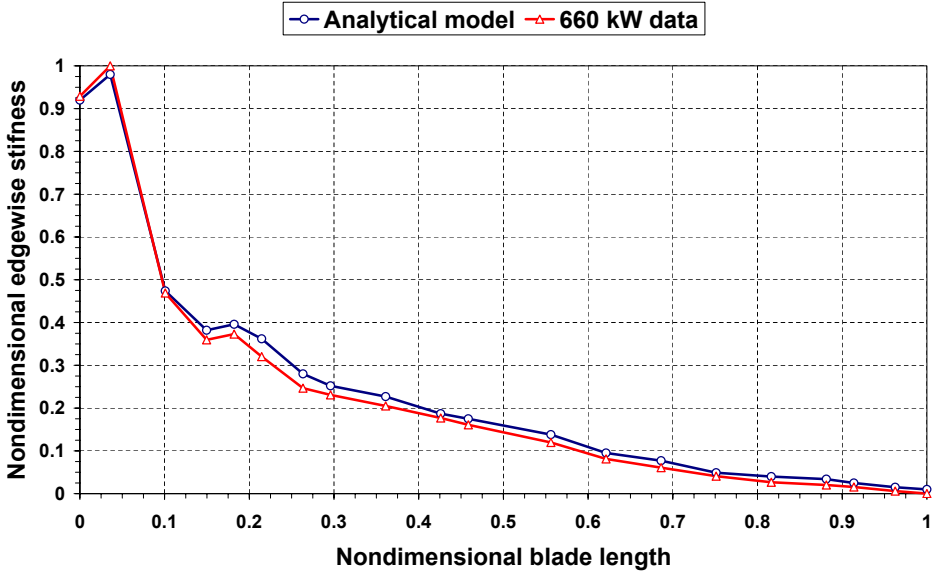


Figure D.2: Comparison of edgewise stiffness of the analytical model with the 660 kW wind turbine blade

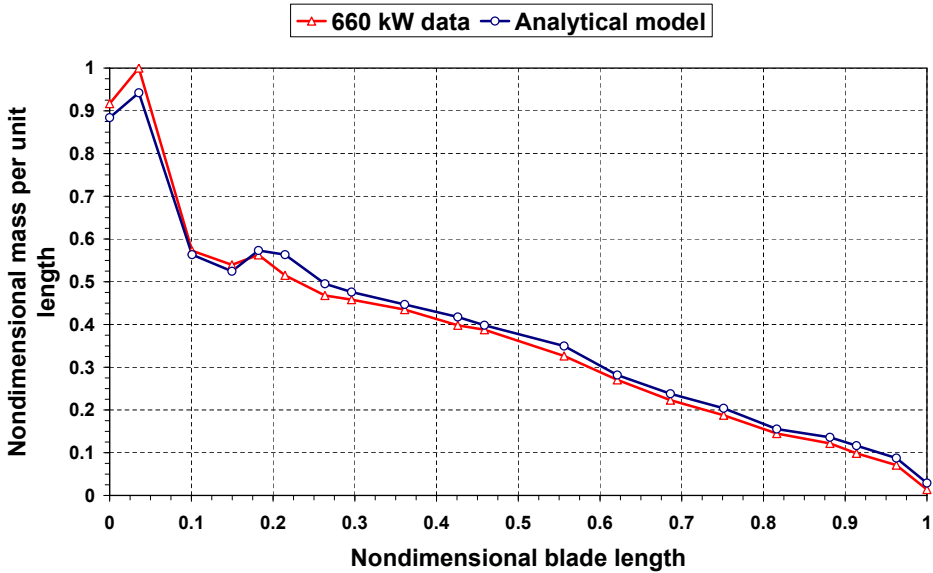


Figure D.3: Comparison of mass per unit length of the analytical model with the 660 kW wind turbine blade

Theoretical aspects of optimization algorithms

E.1 Introduction

This appendix explains the theoretical aspects of optimization algorithms used in the research. A general formulation of the optimization problem was given before in subsection 3.7 (p. 35). Therefore, the focus will be only on the two algorithms that have demonstrated strong potential for efficient solution of the DOP problems used in this research.

E.2 CONLIN

In many of the optimization problems the objective function and design constraints are non-linear and can not be explicitly given as a function of the design variables, which means that there is not an analytical expression of the problem available. In this type of problems, it is only possible to compute the values of the objective function and design constraints, and if possible also their derivatives, for a given set of design variables.

However, all optimization algorithms require several times to do a function evaluation to solve the problem and find the optimum set of design variables. To do so, it is common to build explicit approximations of the objective function and design constraints as a function of design variables and solve the approximated problem. The computational time and effort of solving the explicit approximation is negligible in practice compared to the analysis of the real problem.

Using this method, the real objective function and design constraints are replaced with a series of explicit functions that are obtained by expanding the objective function and the design constraints in the neighborhood of a given design point. By running the real analysis the values of the functions and their derivatives are calculated and generally a linearization process is performed to make the approximation functions. However, this

process is iterative and every iteration requires one analysis and one sensitivity computation.

Usually Taylor series expansion is used in combination with different choices of intermediate design variables to approximate the problem. If design variables are used directly then the problem is considered as a classical linearization problem. With a reciprocal variables the linearization leads to an inverse variables problem and with the mixed variables it leads to a linearization in terms of direct and/or inverse variables.

There are several various algorithm for approximation techniques, among them convex approximation as the widely used one. In convex approximation method the linearization process is carried out with mixed variables (either direct or reciprocal) for every function independently. The signs of the first partial derivatives determines the choice of the intermediate linearization variables . This linearization scheme leads to a convex approximation that is in the form of:

$$F(x_a^i) \simeq F(x_0^i) + \sum_i^n \frac{\partial F_0^{i+}(x_a^i - x_0^i)}{\partial x_0^i} + \sum_i^n \frac{\partial F_0^{i-}(x_0^i)^2 \left(\frac{1}{x_0^i} - \frac{1}{x_a^i}\right)}{\partial X_0^i} \quad (\text{E.1})$$

As it can be seen from this equation, a first order Taylor series expansion is used where the direct linearization is used when the first order term is positive, and the inverse linearization is used when the first order term is negative. Using this definition, the least-square problem, and linear programming problem are both special cases of the general convex optimization problem.

To illustrate the difference between a convex approximation linearization and a classical linearization approximation a graphical representation of the design space with two variables can be used. In figure E.1, the continuous curves represent the surface of a design space, with a feasible domain between these curves. Point x_0 is a given design point for which the analysis takes place. The dashed curves represent the surfaces of approximated design constraints.

Figure E.1a illustrates a classical linear approximation, and figure E.1b shows a convex linearization. As it can be seen from these two figures, the convex linearization results in an approximation of the design constraints (or objective function) that can be considered as the real problem. In the latter case, depending on a parameter called convexity factor, the feasible approximated domain can be inside, equal or outside the real feasible domain.

The convex linearization method (CONLIN) is one of these methods that is classified as a first order convex approximation method that attempts to estimate the curvature of the problem functions (see Fleury (1989) for detailed information about the algorithm). Approximation is based on first order derivatives only, and it does not use information of previous iterations.

This is an extreme useful feature for the level 1 optimization problem of this research, since the location of the chord and twist changes as a function of blade length, as well as the tower height. In this case, the external shape of the blade or tower might be different from one iteration to another and using an algorithm that uses information from a previous iteration leads to inconsistency of the approximated functions. Using this feature, iterations are independent of each other.

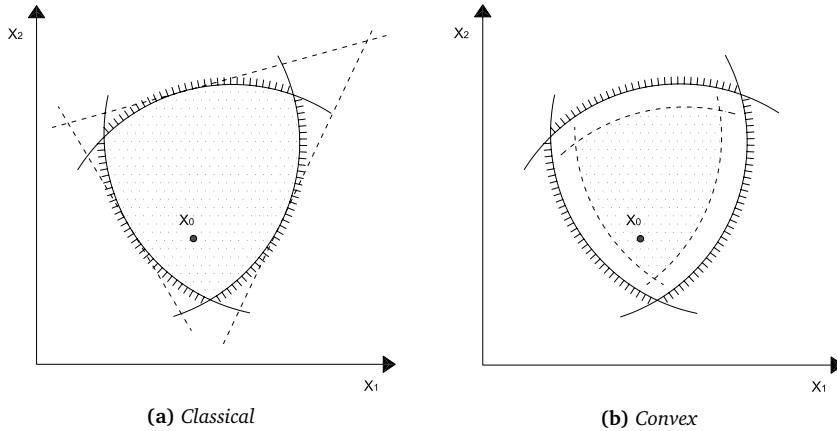


Figure E.1: 2-D representation of a classical linearization approximation versus convex linearization approximation

The settings of the algorithm used in the level 1 optimization of this work are given in the below table:

Table E.1: CONLIN algorithm settings

Property	Value
Type of design variables	continuous
Convergence precision	0.001
Global perturbation	0.01 based on range size
Move limit	100%
Scaling of design variables	enabled (by individual factor)
Scaling of functions	enabled (by individual factor)
Convexity factor	0.001
External relaxation of constraints	disabled
Internal relaxation of constraints	enabled
Discrete design variables round up	disabled

E.3 Lagrange Multiplier (LM)

Lagrange multiplier (sometimes also called augmented Lagrange multiplier or primal-dual algorithm) is one of the oldest optimization algorithms, which is still in use by many people due to its simplicity and powerfulness (for more background information see [Rao \(2009\)](#), [Weisstein \(2003\)](#), [Birgin and Martinez \(2008\)](#) and [Pierre and Lowe \(1975\)](#)). In LM, by introducing an augmented function called the Lagrangian, the original problem is transformed to a new problem that involves both the design constraints, objective function and a parameter called Lagrange multiplier as a single function. This new function is called the Lagrangian and it is a linear summation of the original objective function

and the design constraints that are multiplied by the Lagrange multipliers.

The LM was originally developed for equality constrained problems. However, during the time its reliability and efficiency was increased and it also became possible to study inequality constraints. The method presented in work is applicable for both the equality and inequality design constrained problems. As explained before, the formulation of the LM can be explained as:

$$L(x, \lambda, r_p) = F(x) + \sum_{j=1}^m (\lambda_j \cdot \psi_j + r_p \cdot \psi_j^2) + \sum_{k=1}^l (\lambda_{k+m} \cdot h_k(x) + r_p \cdot h_k^2(x)) \quad (\text{E.2})$$

where:

$$\psi_j = \max \left[g_j(x), \frac{-\lambda_j}{2r_p} \right] \quad (\text{E.3})$$

Now, equation E.2 which is the pseudo-objective of the problem needs to be minimized. This equation appears to be a simple modification to the exterior penalty function method. In this case, equation E.2 is solved sequentially by increasing r_p until the optimality criterion is reached. The algorithm starts with assuming an initial value for x , λ , r_p , ψ and r_p^{max} . Based on this assumed values the updated formulas for the Lagrangian multipliers can be found as:

$$\lambda_j^{p+1} = \lambda_j^p + 2r_p \left\{ \max \left[g_j(x), \frac{-\lambda_j^p}{2r_p} \right] \right\} \quad (\text{E.4})$$

and:

$$\lambda_{k+m}^{p+1} = \lambda_{k+m}^p + 2r_p * h_k(x) \quad (\text{E.5})$$

The main advantages of LM are as follow:

- The starting point may be either feasible or infeasible.
- The method is relatively insensitive to the value of r_p .
- Working with equality constraints is not difficult to deal with by the algorithm.

The settings that are used for this algorithm are given in table E.2.

Table E.2: *LM algorithm settings*

Property	Value
Type of design variables	continuous
Convergence precision	0.001
Convergence criteria	objective function
Global perturbation	0.01 based on range size
Move limit	100%
Scaling of design variables	enabled (by individual factor)
Scaling of functions	enabled (by individual factor)
r_p^{max}	10000
External relaxation of constraints	enabled
Internal relaxation of constraints	enabled
Discrete design variables round up	disabled

Scaling laws for initial design variable generation

F.1 Introduction

The concept of scaling laws was discussed in detail in section 2.3 (p. 12) of chapter 2. These scaling laws are implemented in this appendix as a case study. All of the scaling laws explained before are used to get the initial design variables of the 10 and 20 MW wind turbines. These laws are implemented in a MATLAB code, and this computer code can be used to extract the properties of any other scale of interest.

F.2 Derivation of scaling laws for design studies

The scaling laws not only describe the dependency of a turbine parameter to rotor diameter, but also they can be used to extract the design parameters of an unknown wind turbine with respect to the given parameters of a known wind turbine. This can be explained by the following equation:

$$\frac{P_x}{P_a} = \frac{0.5C_p^x \cdot \rho_x \cdot \pi \cdot r_x^2 \cdot V_x^3}{0.5C_p^a \cdot \rho_a \cdot \pi \cdot r_a^2 \cdot V_a^3} \quad (\text{F1})$$

Where the subscription a and x stand for the known and unknown wind turbines respectively, with the following parameters:

- P Power output of the wind turbine
- C_p Aerodynamic power coefficient
- ρ Air density
- r Rotor radius
- V Wind velocity at hub height

Assuming the same aerodynamic power sensitivity and air density for both the known and unknown wind turbines and recalling the dependency of hub height wind velocity to rotor radius from table 2.1 (p. 14) and replacing that in equation F.1, we have:

$$\frac{P_x}{P_a} = \frac{r_x^2 \cdot r_x^{3\alpha}}{r_a^2 \cdot r_a^{3\alpha}} = \frac{r_x^{2+3\alpha}}{r_a^{2+3\alpha}} \quad (\text{F.2})$$

or:

$$r_x = r_a \cdot \sqrt[2+3\alpha]{\frac{P_x}{P_a}} \quad (\text{F.3})$$

In equation F.3, the only unknown parameter is the rotor radius of the unknown wind turbine, since the designer already knows the power output of the unknown wind turbine of interest, which he is aiming to design. The ratio of the rotor radius of the unknown turbine to the known turbine is called the scaling ratio, SR . This ratio is used to calculate the other parameters of interest of the unknown wind turbine using the following formulation:

$$Q_x = Q_a \cdot (SR)^{SF} \quad (\text{F.4})$$

Here, Q is a design parameter of the wind turbine, and SF is the scaling factor of the parameter based on the given scaling relation of table 2.1 (p. 14).

F.3 Application of scaling laws

Imagine that a designer knows the design parameters of a wind turbine and he wants to upscale this turbine. The known wind turbine has a power output of 5 MW with a rotor radius of 63 meter. He is interested to design a 10 MW wind turbine, based on the 5 MW using the scaling laws. Using equation F.3, the rotor radius of the 10 MW wind turbine for a wind shear of 0.15 can be calculated as:

$$r_{10} = r_5 \times \sqrt[2+3\alpha]{\frac{P_{10}}{P_5}} = 63 \times \sqrt[2+3 \times 0.15]{\frac{10}{5}} = 83.6\text{m} \quad (\text{F.5})$$

The scaling ratio can be calculated based on the definition mentioned before as:

$$SR = \frac{r_{10}}{r_5} = \frac{83.6}{63} = 1.327 \quad (\text{F.6})$$

Assume a diameter of 3.54 meter at the root of the 5 MW wind turbine blade. The scaling factor can be found from table 2.1 (p. 14) as the power of the size dependency of the chord distribution to rotor radius. Thus in this case the scaling factor is equal to 1. Now using equation F.4 the root diameter of the 10 MW blade can be calculated as follow:

$$D_{10}^{root} = D_5^{root} \times (SR)^{SF} = 3.54 \times (1.327)^1 = 4.698\text{m} \quad (\text{F.7})$$

Using the same strategy, the designer can generate all design parameters of any size of interest, providing that he knows these parameters for any known size of a wind turbine.

This strategy is also used in this work to extract the initial design variables of the 10 and 20 MW wind turbines and hence shrink the design space. This trick helps the optimizer to search a smaller design space, which consequently reduces the computational time.

Properties of the optimized 5 MW wind turbine

G.1 Properties of the optimum 5 MW wind turbine

Most of the data presented in this appendix are summarized for conciseness and clarity. However, the design methodology used in this PhD research contains a high level of detail about the development of the optimum 5 MW wind turbines. Key data about this optimum model is presented in the following subsections.

G.1.1 Blade properties

Similar in concept to the 5 MW NREL rotor, the optimum 5 MW wind turbine has three blades of 63.5 m length. In the structural computations, 20 nonuniformly distributed blade elements are used. The properties between these elements are found by a cubic interpolation.

Table G.1 lists the resulting structural properties. The first column of the table labeled *Rad.* is the spanwise location along the blade-pitch axis relative to the rotor center (apex). The second column labeled *BldFrac* is the nondimensionalized distance along the blade-pitch axis from the root to the tip varying from 0 to 1 respectively.

The distributed blade sections mass per unit length values labeled as *BMsDen* are given in the third column. With this mass distribution and a 63.5 m blade's length, a mass of 22851 kg is calculated for the blade. However, this mass is higher than the 17740 kg mass of the NREL blade. This is due to the fact that in this work, only fiber glass composites are used, comparing to the mixture of glass and carbon fiber in the NREL blade.

The main reason for not using carbon fibers here is the uncertainties in defining representative carbon fiber structural properties (especially the S-N curve). While we know these properties very well and with a good accuracy for glass fibers that are used for many years in the wind turbine industry.

Table G.1: optimum 5 MW wind turbine structural properties

Rad. (m)	BldFrac (-)	BMsDen ($\frac{kg}{m^3}$)	BFlpStf ($N \cdot m^2$)	BEdgStf ($N \cdot m^2$)
0.0	0.000	626.4	1.21×10^{10}	1.21×10^{10}
1.2	0.019	519.0	1.05×10^{10}	1.05×10^{10}
3.3	0.052	416.3	7.57×10^9	7.83×10^9
5.4	0.084	415.1	9.20×10^9	8.38×10^9
7.4	0.117	447.0	1.60×10^{10}	1.07×10^{10}
9.5	0.149	392.3	4.81×10^9	8.89×10^9
11.5	0.182	422.1	5.53×10^9	1.05×10^{10}
13.6	0.214	428.3	5.52×10^9	1.07×10^{10}
15.7	0.247	426.5	4.48×10^9	1.04×10^{10}
18.8	0.295	435.7	4.46×10^9	1.06×10^{10}
25.0	0.393	393.3	1.82×10^9	8.60×10^9
31.1	0.491	384.0	1.11×10^9	7.33×10^9
37.3	0.588	367.5	6.26×10^8	6.32×10^9
43.6	0.686	327.0	3.24×10^8	3.97×10^9
49.7	0.783	280.6	1.92×10^8	2.46×10^9
56.0	0.881	182.9	7.67×10^7	1.00×10^9
59.0	0.930	114.0	2.94×10^7	3.94×10^8
60.6	0.954	79.9	1.38×10^7	1.87×10^8
62.1	0.978	38.3	2.20×10^6	3.03×10^7
63.5	1.000	4.2	4.26×10^3	6.00×10^4

The flapwise, *BFlpStf*, and edgewise, *BEdgStf*, section stiffnesses are presented in the 4th and 5th column respectively. These values are calculated about the principal structural axes of each cross section.

The structural damping ratio of 0.477465% critical in all modes of the isolated blade that is equal to a 3% logarithmic decrement used in the NREL and DOWEC study (see [Kooijman et al. \(2003\)](#)) is also used here without any change.

G.1.2 Aerodynamic properties

The aerodynamic properties of the optimum wind turbine are obtained by running a series of simulations from the cut-in to cut-out wind speeds. The first 60 seconds of the simulation lengths were ignored to ensure that all transient behavior were damped out. The results are obtained by running a steady wind, and the steady BEM code.

Figure [G.1](#) shows the power output curve and the blade pitch angle, which are defined as follows:

- RotSpd: the rotational speed of rotor
- RotPwr: the power of rotor
- BldPtch: the blade pitch angle

As the graph shows, in the power maximization region, the variable speed controller is active to guarantee the maximum energy capture. In the above rated region as the

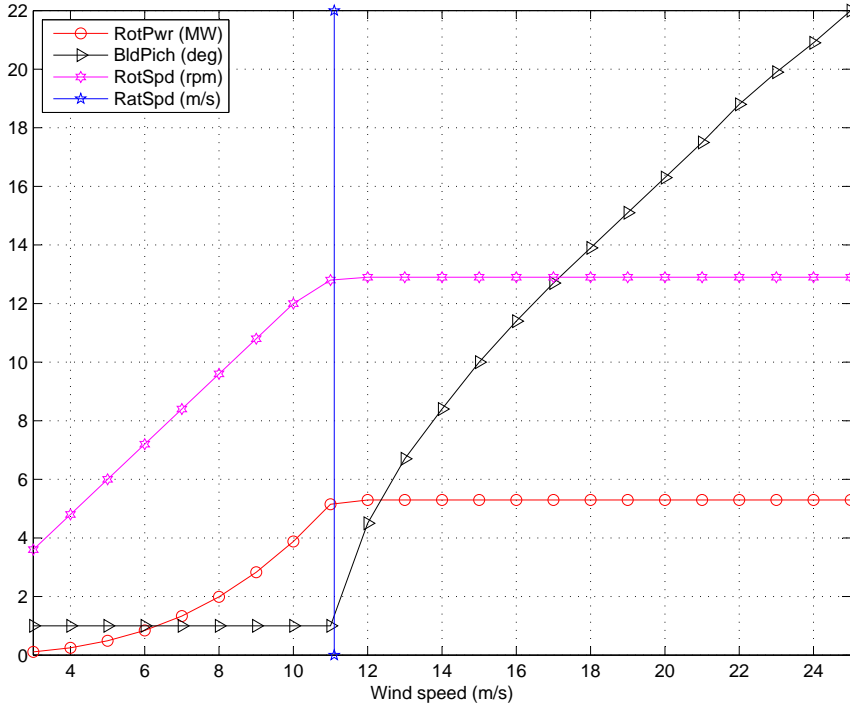


Figure G.1: Aerodynamic properties of the optimum rotor

wind speed increases, by activating the pitch mechanism the power is held constant.

Similar to the blade structural properties, the optimum blade aerodynamic properties are presented in table G.2. The first column presents the 8 different airfoil types used at different stations along the blade. The same airfoil types as the NREL are also used in this study. The two innermost airfoil types represent cylinders with drag coefficients of 0.50 (Cylinder1) and 0.35 (Cylinder2) and no lift.

For the non-cylindrical airfoils a 3D corrections is used to modify the airfoil data. In this modification, the lift and drag coefficients are corrected for rotational stall delay and the Beddoes-Leishman model is employed to estimate the dynamic-stall hysteresis parameters. For this modification, the aspect ratio of the blade is updated for every iterations during the optimization process.

The second column of this table labeled as *RNodes* shows the node locations that are directed along the blade-pitch axis from the rotor apex to the blade tip that are in total 19. All the aerodynamic loads are calculated and applied on these nodes. The third column labeled as *DRNodes* is the distance from one node to the other. The fourth column, *AeroTwst*, is the aerodynamic twist of every node, with the highest at the inboard station and a zero twist at the blade tip. Finally, the last column shows the chord of the blade at every node.

Table G.2: optimum 5 MW wind turbine aerodynamic properties

Airfoil	RNodes (m)	DRNodes (m)	AeroTwst (deg)	Chord (m)
Cylinder1	2.13	13.30	1.26	3.10
Cylinder1	3.82	13.30	2.11	3.10
Cylinder2	5.93	13.30	2.11	3.27
Cylinder2	8.04	13.30	2.11	3.82
Cylinder2	10.16	13.30	2.11	4.57
DU00W401	12.27	13.01	2.11	5.12
DU00W401	14.39	12.12	2.11	5.29
DU00W350	16.50	11.01	2.11	5.27
DU00W350	19.14	10.02	3.17	5.22
DU97W300	23.90	8.75	6.34	5.05
DU91W2250	30.24	7.28	6.33	4.73
DU93W210	36.58	6.02	6.34	4.30
DU93W210	42.92	4.84	6.33	3.81
NACA64618	49.26	3.63	6.34	3.27
NACA64618	55.61	2.32	6.34	2.68
NACA64618	60.36	1.30	3.16	2.12
NACA64618	62.74	0.80	1.5	1.10
NACA64618	64.32	0.46	1.5	1.00
NACA64618	65.81	0.14	1.3	0.80

G.1.3 Drive train properties

The NREL 5 MW baseline wind turbine has a rated rotor speed of 12.1 rpm, a rated generator speed of 1173.7 rpm and a gearbox ratio of 97:1 as the REpower 5M machine. However, during the design optimization process of this machine the rated rotor speed was found to be 12.9 rpm instead of 12.1 rpm, which is 6.4% higher.

As a result of this 6.4% increase of rated rotational speed and to keep the rated generator speed the same, the gearbox ratio was decreased to 91. The total mechanical-to-electrical conversion loss is 5.6%, which is also the same as both the NREL and DOWEC turbines at the rated power.

The generator inertia about the high-speed shaft is $534.116 \text{ kg} \cdot \text{m}^2$, which is the same inertia used by the NREL and DOWEC wind turbines. The equivalent drive shaft linear-spring constant of $8.6 \times 10^8 \frac{\text{N} \cdot \text{m}}{\text{rad}}$ and the linear-damping constant of $6.2 \times 10^6 \frac{\text{N} \cdot \text{m}}{\text{rad} \cdot \text{s}}$ are also selected to be the same as both the NREL and DOWEC wind turbines.

G.1.4 Hub and nacelle properties

From the mass models developed for hub, a mass of 27.4 (ton) is obtained. It is assumed that the hub is made from ductile iron castings and has a spherical shell. This diameter of this sphere is assumed to be 3 m, which also matches with the hub diameter of the 5 MW NREL wind turbine.

Due to the known mass and geometry of the hub, with the use of a simple algebraic

equation the thickness of the hub is found. Based on this thickness a mass moment of inertia of $121351 \text{ kg} \cdot \text{m}^2$ for the hub can be found.

The nacelle mass of the redesigned wind turbine is 168.8 ton that is 29.8% higher than the mass of the NREL machine (130 ton). The reason for this increase is the longer blade which influences also an increase on the other masses as the mass models show.

The nacelle inertia about the yaw axis was taken to be 3386244 ($\text{kg} \cdot \text{m}^2$). This value is based on the assumption that all the geometrical dimensions inside the nacelle remain the same for the optimum wind turbine, with respect to the NREL turbine. Because the mass moment of inertia is proportional to mass, and since there is a mass increase of 29.8% for the nacelle, its mass moment of inertia is also increased by 29.8%.

The nacelle-yaw actuator has a natural frequency of 3 Hz, which is the same as the NREL wind turbine. As explained in the NREL report, this is equivalent to the highest full-system natural frequency in the FAST model, and a damping ratio of 2% critical.

The gross properties of the hub and nacelle are presented in table G.3.

Table G.3: Hub and nacelle gross properties of the redesigned wind turbine

Property	Value (Unit)
Hub mass	27.4 (ton)
Hub mass moment of inertia	121351 $\text{kg} \cdot \text{m}^2$
Nacelle mass	168.8 (ton)
Nacelle mass moment of inertia	3386244 ($\text{kg} \cdot \text{m}^2$)
Elevation of yaw bearing above tower base	80.0 (m)
Vertical distance along yaw axis from yaw bearing to shaft	1.96 (m)
Distance along shaft from hub center to yaw axis	5.0 (m)
Distance along shaft from hub center to main bearing	1.9 (m)

G.1.5 Support structure properties

As explained before the support structure of the wind turbines in this work consists of the foundation system (monopile and transition piece) and tower. Additionally, the soil mechanics of the monopile is not modeled and thus it is assumed that all the DOFs of the monopile at the seabed are constrained, and tower is the only element of the support structure assembly that is optimized.

Table G.4 gives the resulting distributed tower properties of the optimum wind turbine. In this table, the first column, *Height* is the vertical locations along the tower centerline relative to the tower base. It is also assumed that the tower base is located at the mean sea level.

The second column, *TowFrac*, of the table is the fractional height along the tower centerline from the tower base to the tower top and ranges from 0 to 1 respectively. The third, fourth and fifth column also represent the diameter, thickness and stiffness of stations along the tower. Since the optimization is carried out at the tower base and top, only the results of these tow stations are given. Using an interpolation, the results at other stations can also be found.

The resulting overall tower mass is 358400 kg that is 3% higher than the mass of the NREL wind turbine (347460 kg). This increase in mass is related to a longer blade of the optimum turbine that results in higher loads on the tower.

Table G.4: *optimum 5 MW wind turbine tower properties*

Height (m)	TowFrac (-)	TowDia (m)	TowTick (cm)	TowStif ($N \cdot m^2$)
0.0	0.0	6.0	4.2	6.9×10^{11}
80.0	1.0	4.1	2.4	1.3×10^{11}

Derivation of the aerodynamic forces in a finite element form

H.1 Introduction

The deduction task is carried out in nine steps as shown in figure [H.1](#). These steps are programmed in MATLAB using its symbolic toolbox. These steps are explained in detail in the following sections.

H.2 Defining the aerodynamic coordinate system

As presented in figure [6.5](#), each section of the blade has a different chord, twist and radial position along the blade. However, to construct the aerodynamic matrices, the Degrees Of Freedom (DOF) of every section should be known with respect to a fixed reference frame.

A DOF is characterized by a direction and a position. The directions and positions of the DOF in a cross section are used to describe the energy that an external force (here aerodynamic forces) applies on a node. Therefore, a finite number of DOF are used to describe the motion of every element of a section in a local coordinate system. These local coordinates are then transformed to the reference coordinate system.

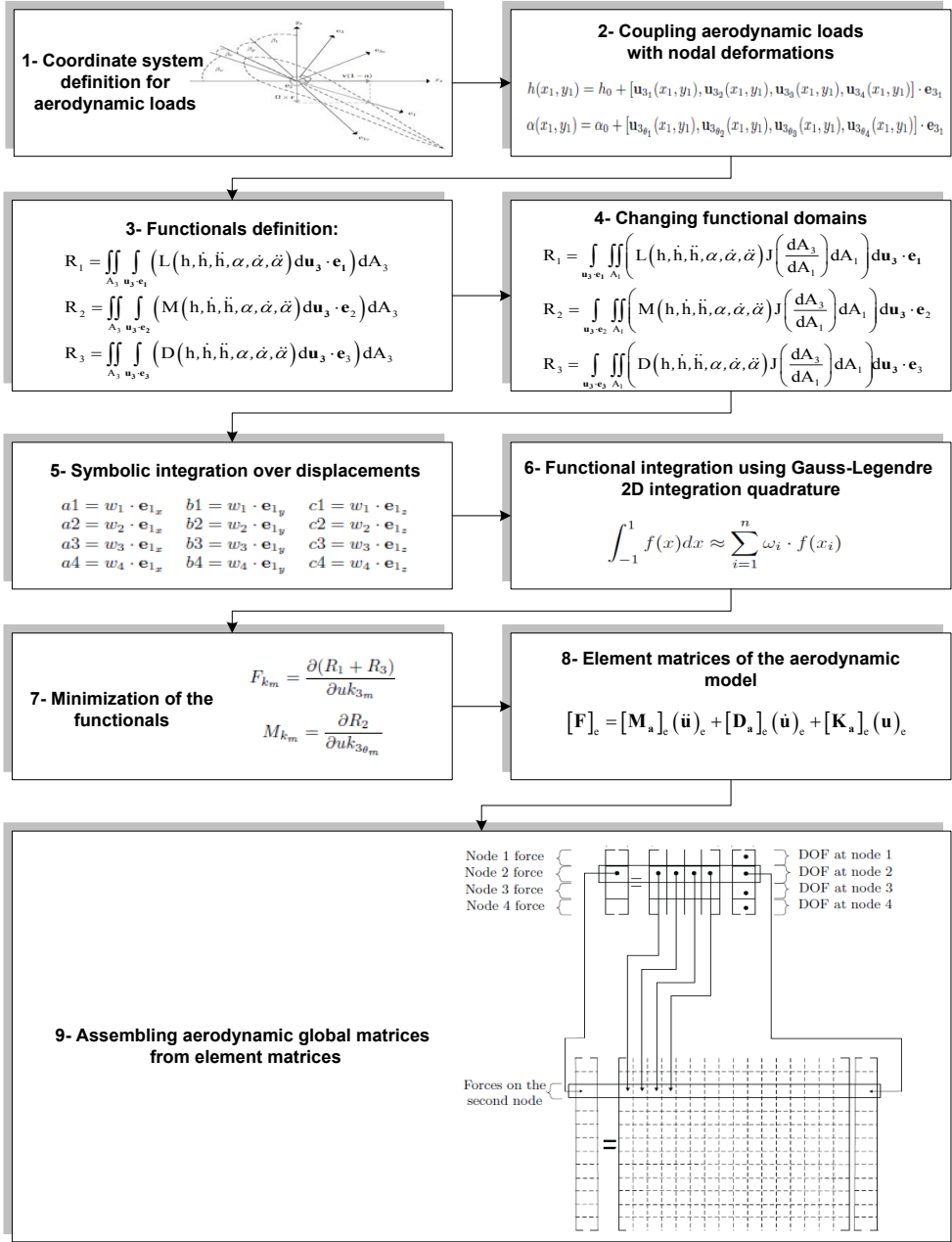


Figure H.1: Steps to derive the element matrices of the aerodynamic model

1. Direction of the DOFs:

Figure H.2 illustrates the DOFs to describe the direction of a typical section. The deformed DOFs of a section are given by the unit vectors \mathbf{e}_1 , \mathbf{e}_2 and \mathbf{e}_3 . These vectors coincide with the direction of the drag, moment and lift, respectively.

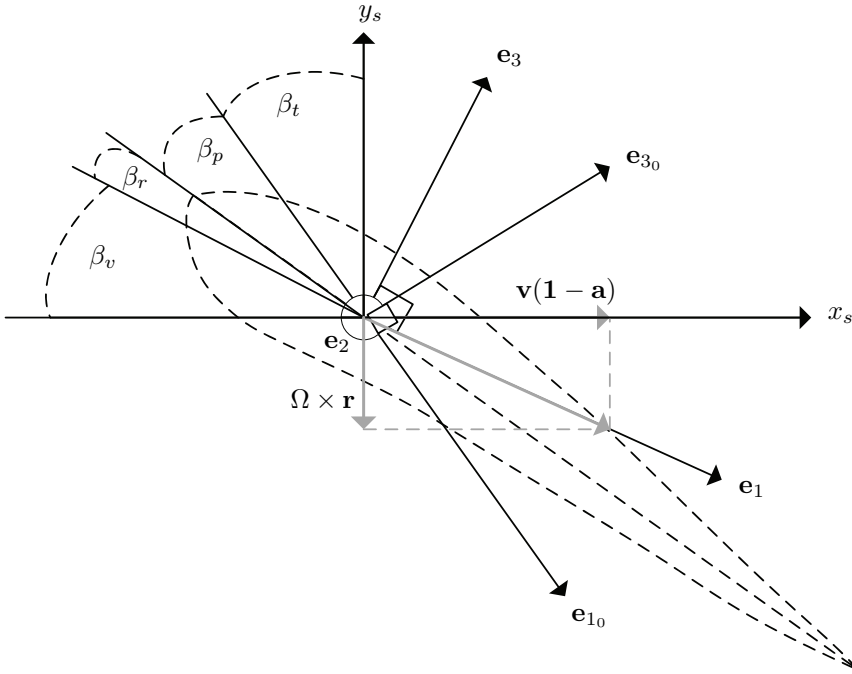


Figure H.2: Unit vectors of a given section along the blade

Here:

x_s : axis parallel to the freestream wind velocity

y_s : axis parallel to the plane of rotation

β_v : the resultant wind velocity

β_p : blade pitch

β_t : aerodynamic twist

β_r : angle of attack

\mathbf{e}_{1_0} : unit vector of the undeformed section of the blade in edgewise direction

\mathbf{e}_1 : unit vector of the deformed section of the blade

\mathbf{e}_2 and \mathbf{e}_{2_0} : unit vector of both the deformed and undeformed section of the blade in spanwise direction

\mathbf{e}_{3_0} : unit vector of the undeformed section of the blade in flapwise direction

\mathbf{e}_3 : unit vector of the deformed section of the blade

Ω : angular velocity of the rotor

v : freestream wind velocity

a : axial induction factor

r : section radius

\mathbf{e}_{1_0} , \mathbf{e}_{2_0} and \mathbf{e}_{3_0} unit vectors are defined by the user (knowing the structural twist of each section and the blade pitch). However, to calculate the work done by drag, moment and lift, \mathbf{e}_1 , \mathbf{e}_2 and \mathbf{e}_3 unit vectors are used. As figure H.2 shows, the angle of attack, β_r , can be obtained using the following equation:

$$\beta_r = \frac{\pi}{2} - \beta_t - \beta_p - \arctan\left(\frac{\Omega \times \mathbf{r}}{v(1-a)}\right) \quad (\text{H.1})$$

Unlike the \mathbf{e}_1 and \mathbf{e}_3 vectors, the direction of the vector \mathbf{e}_2 is based on the azimuthal position of the blade and it does not change with the wind or rotational speed of the blade. These vectors can be obtained using the following rotation matrix:

$$\begin{Bmatrix} e_1 \\ e_2 \\ e_3 \end{Bmatrix} = \begin{bmatrix} \cos(\beta_r + \beta_p) & 0 & \sin(\beta_r + \beta_p) \\ 0 & 1 & 0 \\ -\sin(\beta_r + \beta_p) & 0 & \cos(\beta_r + \beta_p) \end{bmatrix} \begin{Bmatrix} e_{1_0} \\ e_{2_0} \\ e_{3_0} \end{Bmatrix} \quad (\text{H.2})$$

2. Position of the DOFs:

The undeformed 3D geometry of the blade is discretized using 2D Quad (Quadrilateral Plate Element Connection) elements. By applying an external force to the nodes of these elements, their nodal positions change as well. Therefore, by tracking the changes of the position of these nodes the deformation of the blade can be modeled. These deformations together with the forces applied on every node are used to calculate the energy transformed in every cycle to the structure.

However, the position of these nodes is only known in the element coordinate system referred as coordinate system 3. To obtain the energy terms, this coordinate system is first transformed to a local 2D coordinate system referred as coordinate system 2, and then the reference coordinate system referred as 1.

These transformations are explained below.

- From element coordinate system 3 to local coordinate system 2
The position of the Quad elements on the discretized blade is given in the element coordinate system, and the position of all the elements is defined by four nodes in this coordinate system. The transformation that relates the Quad elements in coordinate system 3 to coordinate system 2 is as follow:

$$\mathbf{u}_2 = \mathbf{u}_{32} - \mathbf{u}_3 \cdot \mathbf{e}_{32} \quad (\text{H.3})$$

Where:

\mathbf{u}_2 : nodal position of element \mathbf{u} in coordinate system 2

\mathbf{u}_{32} : relative displacement of coordinate system 3 with respect to coordinate system 2

\mathbf{u}_3 : nodal position of element \mathbf{u} in coordinate system 3

\mathbf{e}_{32} : rotation matrix from coordinate system 3 to 2

Using equation H.3, the position of the nodes of an element can be transformed from one coordinate system to another. Figure H.3 shows these transformations.

- From local coordinate system 2 to reference coordinate system 1
The Quad elements are transformed from the coordinate system 2 to the reference coordinate system (coordinate system 1), using the bilinear interpolation functions between the corner values of the Quad elements. Equation H.4 shows this transformation.

$$\mathbf{u}_1(x_1, y_1) = \mathbf{u}_{12} \cdot w_1(x_1, y_1) + \mathbf{u}_{22} \cdot w_2(x_1, y_1) + \mathbf{u}_{32} \cdot w_3(x_1, y_1) + \mathbf{u}_{42} \cdot w_4(x_1, y_1) \quad (\text{H.4})$$

The expression on equation H.4 contains 4 bilinear shape functions presented in equation H.5 to H.8. These shape functions are linear independent as plotted in figure H.4.

$$w_1(x_1, y_1) = \left(y_1 - \frac{1}{2}\right) \cdot \left(x_1 - \frac{1}{2}\right) \quad (\text{H.5})$$

$$w_2(x_1, y_1) = -\left(y_1 - \frac{1}{2}\right) \cdot \left(x_1 + \frac{1}{2}\right) \quad (\text{H.6})$$

$$w_3(x_1, y_1) = \left(y_1 + \frac{1}{2}\right) \cdot \left(x_1 + \frac{1}{2}\right) \quad (\text{H.7})$$

$$w_4(x_1, y_1) = -\left(y_1 + \frac{1}{2}\right) \cdot \left(x_1 - \frac{1}{2}\right) \quad (\text{H.8})$$

- The final form of the deformation in the reference coordinate system
The displacements for the 6 DOFs of each node are obtained using the bilinear shape functions. Thus, by substituting equation H.3 into H.4 and using the shape functions as presented in equations H.5 to H.8, the final transformation from coordinate system 3 to 1 can be formulated as:

$$\mathbf{u}_1(x_1, y_1) = \mathbf{u}_{13} \cdot \left(y_1 - \frac{1}{2}\right) \cdot \left(x_1 - \frac{1}{2}\right) - \mathbf{u}_{23} \cdot \left(y_1 - \frac{1}{2}\right) \cdot \left(x_1 + \frac{1}{2}\right) + \mathbf{u}_{33} \cdot \left(y_1 + \frac{1}{2}\right) \cdot \left(x_1 + \frac{1}{2}\right) - \mathbf{u}_{43} \cdot \left(y_1 + \frac{1}{2}\right) \cdot \left(x_1 - \frac{1}{2}\right) \quad (\text{H.9})$$

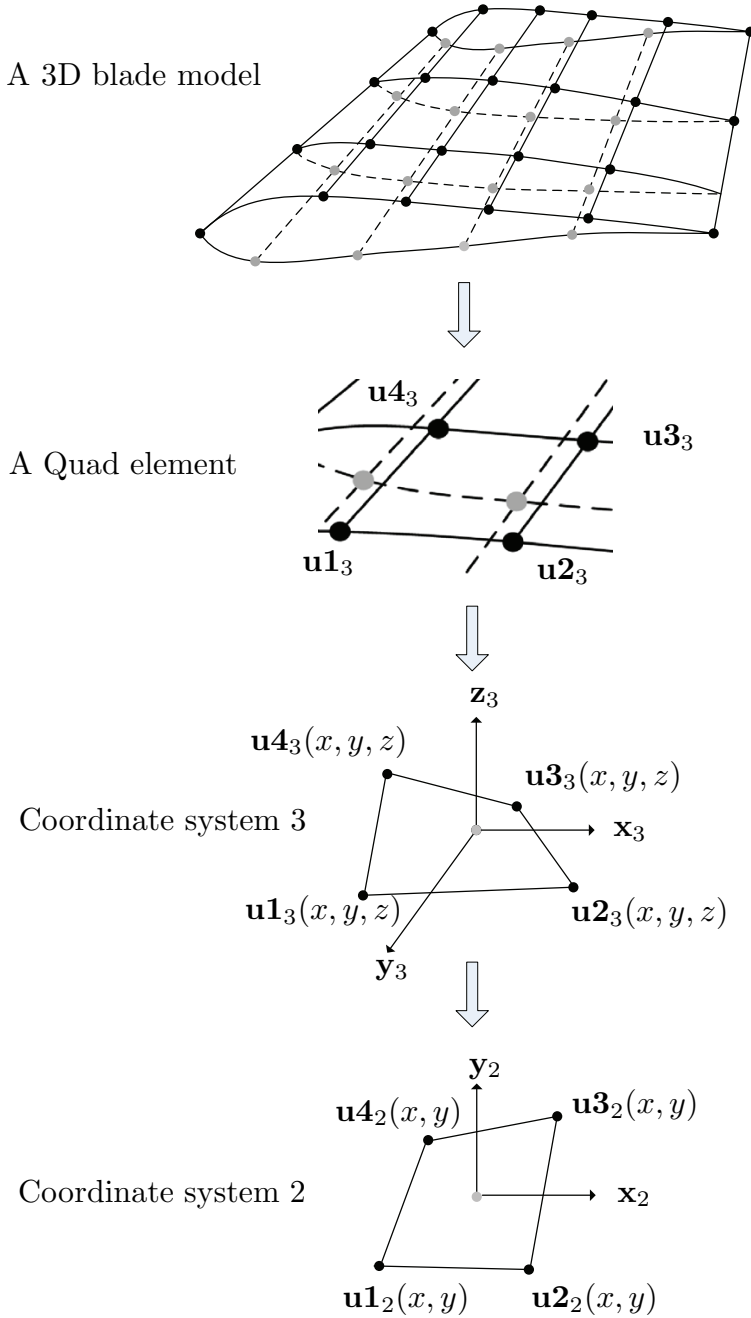


Figure H.3: From a 3D blade geometry to a 2D Quad element coordinate

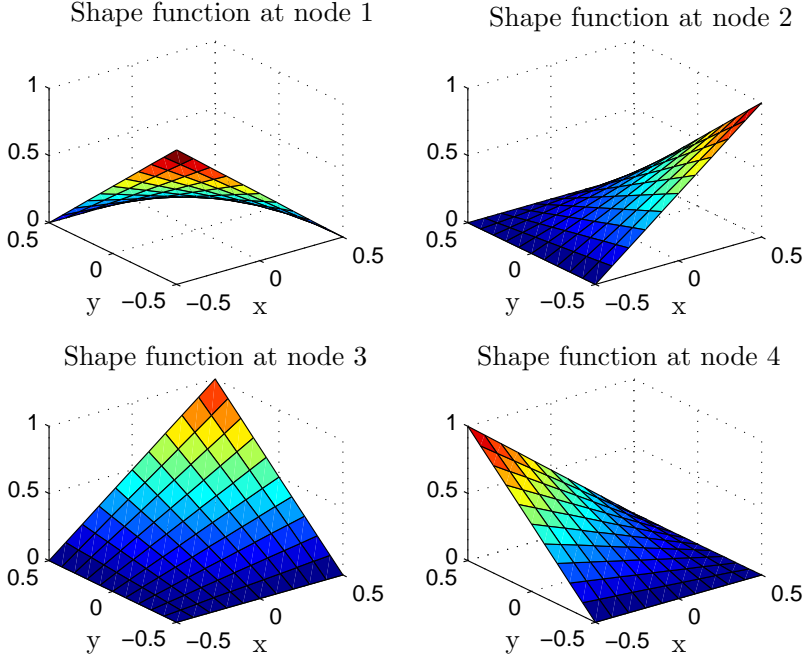


Figure H.4: Shape functions for the bilinear Quad element

H.3 Coupling aerodynamic loads with nodal deformations

The generalized aerodynamic forces are a function of $h, \dot{h}, \ddot{h}, \alpha, \dot{\alpha}$ and $\ddot{\alpha}$. However, the aerodynamic forces should be formulated as function of the node deformations to see the influence of structural deformations on loads. Thus, a new arrangement for pitching and plunging motion is needed to couple the aerodynamic forces with structural deformation. This coupling can be formulated as:

$$h(x_1, y_1) = h_0 + [\mathbf{u}_{3_1}(x_1, y_1), \mathbf{u}_{3_2}(x_1, y_1), \mathbf{u}_{3_3}(x_1, y_1), \mathbf{u}_{3_4}(x_1, y_1)] \cdot \mathbf{e}_{3_1} \tag{H.10}$$

$$\begin{aligned} \dot{h}(x_1, y_1) = & [\dot{\mathbf{u}}_{3_1}(x_1, y_1), \dot{\mathbf{u}}_{3_2}(x_1, y_1), \dot{\mathbf{u}}_{3_3}(x_1, y_1), \dot{\mathbf{u}}_{3_4}(x_1, y_1)] \cdot \mathbf{e}_{3_1} + \\ & [\mathbf{u}_{3_1}(x_1, y_1), \mathbf{u}_{3_2}(x_1, y_1), \mathbf{u}_{3_3}(x_1, y_1), \mathbf{u}_{3_4}(x_1, y_1)] \cdot \dot{\mathbf{e}}_{3_1} \end{aligned} \tag{H.11}$$

$$\begin{aligned} \ddot{h}(x_1, y_1) = & [\ddot{\mathbf{u}}_{3_1}(x_1, y_1), \ddot{\mathbf{u}}_{3_2}(x_1, y_1), \ddot{\mathbf{u}}_{3_3}(x_1, y_1), \ddot{\mathbf{u}}_{3_4}(x_1, y_1)] \cdot \mathbf{e}_{3_1} + \\ & 2 [\dot{\mathbf{u}}_{3_1}(x_1, y_1), \dot{\mathbf{u}}_{3_2}(x_1, y_1), \dot{\mathbf{u}}_{3_3}(x_1, y_1), \dot{\mathbf{u}}_{3_4}(x_1, y_1)] \cdot \dot{\mathbf{e}}_{3_1} + \\ & [\mathbf{u}_{3_1}(x_1, y_1), \mathbf{u}_{3_2}(x_1, y_1), \mathbf{u}_{3_3}(x_1, y_1), \mathbf{u}_{3_4}(x_1, y_1)] \cdot \ddot{\mathbf{e}}_{3_1} \end{aligned} \tag{H.12}$$

$$\alpha(x_1, y_1) = \alpha_0 + [\mathbf{u}_{3_{\theta_1}}(x_1, y_1), \mathbf{u}_{3_{\theta_2}}(x_1, y_1), \mathbf{u}_{3_{\theta_3}}(x_1, y_1), \mathbf{u}_{3_{\theta_4}}(x_1, y_1)] \cdot \mathbf{e}_{3_1} \quad (\text{H.13})$$

$$\dot{\alpha}(x_1, y_1) = [\dot{\mathbf{u}}_{3_{\theta_1}}(x_1, y_1), \dot{\mathbf{u}}_{3_{\theta_2}}(x_1, y_1), \dot{\mathbf{u}}_{3_{\theta_3}}(x_1, y_1), \dot{\mathbf{u}}_{3_{\theta_4}}(x_1, y_1)] \cdot \mathbf{e}_{3_1} + [\mathbf{u}_{3_{\theta_1}}(x_1, y_1), \mathbf{u}_{3_{\theta_2}}(x_1, y_1), \mathbf{u}_{3_{\theta_3}}(x_1, y_1), \mathbf{u}_{3_{\theta_4}}(x_1, y_1)] \cdot \dot{\mathbf{e}}_{3_1} \quad (\text{H.14})$$

$$\ddot{\alpha}(x_1, y_1) = [\ddot{\mathbf{u}}_{3_{\theta_1}}(x_1, y_1), \ddot{\mathbf{u}}_{3_{\theta_2}}(x_1, y_1), \ddot{\mathbf{u}}_{3_{\theta_3}}(x_1, y_1), \ddot{\mathbf{u}}_{3_{\theta_4}}(x_1, y_1)] \cdot \mathbf{e}_{3_1} + 2 [\dot{\mathbf{u}}_{3_{\theta_1}}(x_1, y_1), \dot{\mathbf{u}}_{3_{\theta_2}}(x_1, y_1), \dot{\mathbf{u}}_{3_{\theta_3}}(x_1, y_1), \dot{\mathbf{u}}_{3_{\theta_4}}(x_1, y_1)] \cdot \dot{\mathbf{e}}_{3_1} + [\mathbf{u}_{3_{\theta_1}}(x_1, y_1), \mathbf{u}_{3_{\theta_2}}(x_1, y_1), \mathbf{u}_{3_{\theta_3}}(x_1, y_1), \mathbf{u}_{3_{\theta_4}}(x_1, y_1)] \cdot \ddot{\mathbf{e}}_{3_1} \quad (\text{H.15})$$

Where:

h_0 : the initial distance from the pitch axis of the section to the center of the given element in y_s direction (please refer to figure H.2)

α_0 : the steady angle of attack (equal to β_r in figure H.2)

H.4 Defining aerodynamic loads in terms of functionals

To find an approximation for the generalized aerodynamic loads similar to equation 6.1, the concept of functional minimization is used. Here, the idea is to minimize the integral of the work done by an external force on a node. The work done by the force can be defined as:

$$W \approx \min [\langle \mathbf{F}(\mathbf{u}), \mathbf{u} \rangle] \quad (\text{H.16})$$

Where:

W : work done on the node

\mathbf{F} : external force vector

\mathbf{u} : deformation vector of the node

Integrating this work over its domain results in:

$$W \approx \min \int_V \mathbf{F}(\mathbf{u}) \cdot d\mathbf{u} \quad (\text{H.17})$$

This way of representing the generalized aerodynamic forces has two main advantages. First, discretizing the whole domain V into many subdomains, $V = \sum_{j=1}^n V_j$, by using the property of the integral. Second, using different deformation approximations for the deformation vector \mathbf{u} in each of the subdomains.

The integral part of the right hand side of the equation is called the functional and in this case represents the work done by the generalized force \mathbf{F} on the domain of integration, V . The lift, moment and drag expressions given in equations 6.19, 6.20 and

6.21 are now replaced in equation H.17 to obtain an approximated expression for the aerodynamic loads.

$$W_{lift} = \min \left(\int_V \sum_{j=1}^{n_s} \left[\frac{\partial C_l}{\partial \alpha} \rho U^2 b \left[\frac{C(k)}{U} \dot{h} + C(k)\alpha + [1 + C(k)(1 - 2a)] \frac{b}{2U} \dot{\alpha} + \frac{b}{2U^2} \ddot{h} - \frac{b^2 a}{2U^2} \ddot{\alpha} \right] \cdot A_{section} \right]_j \cdot d\mathbf{u} \right) \quad (H.18)$$

$$W_{moment} = \min \left(\int_V \sum_{j=1}^{n_s} \frac{\partial C_m}{\partial \alpha} \rho U^2 b \left[d_1 \left[\frac{C(k)}{U} \dot{h} + C(k)\alpha + [1 + C(k)(1 - 2a)] \frac{b}{2U} \dot{\alpha} \right] + \frac{b^2}{2U} \dot{\alpha} \left(a - \frac{1}{2} \right) + \frac{ab^2}{2U^2} \ddot{h} + \frac{b^3}{2U^2} \ddot{\alpha} \left(\frac{1}{8} - a^2 \right) \right] \cdot A_{section} \right]_j \cdot d\mathbf{u} \right) \quad (H.19)$$

$$W_{drag} = \min \left(\int_V \sum_{j=1}^{n_s} \left[\rho U^2 b \frac{\partial C_d}{\partial \alpha} \left[-\frac{C(k)}{U} \dot{h} - C(k)\alpha + [1 + C(k)(1 - 2a)] \frac{b}{2U} \dot{\alpha} - \frac{b}{2U^2} \ddot{h} + \frac{b^2 a}{2U^2} \ddot{\alpha} \right] \cdot A_{section} \right]_j \cdot d\mathbf{u} \right) \quad (H.20)$$

Presenting these functionals in a general form and breaking the integral domain results in:

$$R_1 = \int_{A_3} \left(\int_{\mathbf{u}_3 \cdot \mathbf{e}_1} L(h, \dot{h}, \ddot{h}, \alpha, \dot{\alpha}, \ddot{\alpha}) d\mathbf{u}_3 \cdot \mathbf{e}_1 \right) dA_3 \quad (H.21)$$

$$R_2 = \int_{A_3} \left(\int_{\mathbf{u}_3 \cdot \mathbf{e}_2} M(h, \dot{h}, \ddot{h}, \alpha, \dot{\alpha}, \ddot{\alpha}) d\mathbf{u}_3 \cdot \mathbf{e}_2 \right) dA_3 \quad (H.22)$$

$$R_3 = \int_{A_3} \left(\int_{\mathbf{u}_3 \cdot \mathbf{e}_3} D(h, \dot{h}, \ddot{h}, \alpha, \dot{\alpha}, \ddot{\alpha}) d\mathbf{u}_3 \cdot \mathbf{e}_3 \right) dA_3 \quad (H.23)$$

Where:

R1: lift functional

R2: moment functional

R3: drag functional

A₃: domain of integration that is the area of the element in coordinate system 3

H.5 Transforming the functionals domain of integration to coordinate system 1

The integration domain of the functionals given by equations H.21, H.22 and H.23 are in coordinate system 3. Therefore, a coordinate system transformation is employed to

change the domain of integration from coordinate system 3 to 1. This has been done before for the aerodynamic loads and deformations, and only needs to be repeated again for the domain of integration of the functionals to have a consistent set of equations. This results in having the functionals in the reference integration domain 1. The new functionals now read as :

$$R_1 = \int_{A_1} \int_{\mathbf{u}_3 \cdot \mathbf{e}_1} \left(L(h, \dot{h}, \ddot{h}, \alpha, \dot{\alpha}, \ddot{\alpha}) d\mathbf{u}_3 \cdot \mathbf{e}_1 \right) \cdot J \left(\frac{dA_3}{dA_1} \right) dA_1 \quad (\text{H.24})$$

$$R_2 = \int_{A_1} \int_{\mathbf{u}_3 \cdot \mathbf{e}_2} \left(M(h, \dot{h}, \ddot{h}, \alpha, \dot{\alpha}, \ddot{\alpha}) d\mathbf{u}_3 \cdot \mathbf{e}_2 \right) J \left(\frac{dA_3}{dA_1} \right) dA_1 \quad (\text{H.25})$$

$$R_3 = \int_{A_1} \int_{\mathbf{u}_3 \cdot \mathbf{e}_3} \left(D(h, \dot{h}, \ddot{h}, \alpha, \dot{\alpha}, \ddot{\alpha}) d\mathbf{u}_3 \cdot \mathbf{e}_3 \right) J \left(\frac{dA_3}{dA_1} \right) dA_1 \quad (\text{H.26})$$

Where:

A_1 : reference area of integration in the coordinate system 1

$J \left(\frac{dA_3}{dA_1} \right)$: Jacobian of the coordinate transformation 3 to 1

The jacobian of the transformation is given by the expression:

$$J \left(\frac{dA_3}{dA_1} \right) = \begin{vmatrix} \frac{\partial x_3}{\partial x_1} & \frac{\partial x_3}{\partial y_1} \\ \frac{\partial y_3}{\partial x_1} & \frac{\partial y_3}{\partial y_1} \end{vmatrix} \quad (\text{H.27})$$

H.6 Symbolic integral replacement of the deformations

The functional expressions [H.24](#), [H.25](#) and [H.26](#) are integrated over the deformations. The integration is done using the interpolation functions presented in [H.4](#). The following variables are defined to integrate these expressions:

$$\begin{aligned} a_1 &= w_1 \cdot \mathbf{e}_{1_x} & b_1 &= w_1 \cdot \mathbf{e}_{1_y} & c_1 &= w_1 \cdot \mathbf{e}_{1_z} \\ a_2 &= w_2 \cdot \mathbf{e}_{1_x} & b_2 &= w_2 \cdot \mathbf{e}_{1_y} & c_2 &= w_2 \cdot \mathbf{e}_{1_z} \\ a_3 &= w_3 \cdot \mathbf{e}_{1_x} & b_3 &= w_3 \cdot \mathbf{e}_{1_y} & c_3 &= w_3 \cdot \mathbf{e}_{1_z} \\ a_4 &= w_4 \cdot \mathbf{e}_{1_x} & b_4 &= w_4 \cdot \mathbf{e}_{1_y} & c_4 &= w_4 \cdot \mathbf{e}_{1_z} \end{aligned}$$

Thus, for the lift force it reads as:

$$R_1 = \int_{A_1} g_1 J \left(\frac{dA_3}{dA_1} \right) dA_1 \quad (\text{H.28})$$

Where:

$$\begin{aligned}
 g_1 = & \int L \cdot a_1 \cdot du1_{3_1} + \int L \cdot a_2 \cdot du2_{3_1} + \int L \cdot a_3 \cdot du3_{3_1} + \int L \cdot a_4 \cdot du4_{3_1} + \\
 & \int L \cdot b_1 \cdot du1_{3_2} + \int L \cdot b_2 \cdot du2_{3_2} + \int L \cdot b_3 \cdot du3_{3_2} + \int L \cdot b_4 \cdot du4_{3_2} + \\
 & \int L \cdot c_1 \cdot du1_{3_3} + \int L \cdot c_2 \cdot du2_{3_3} + \int L \cdot c_3 \cdot du3_{3_3} + \int L \cdot c_4 \cdot du4_{3_3} \quad (H.29)
 \end{aligned}$$

Similarly, for the moment the following expressions are used:

$$\begin{aligned}
 a_1 = w_1 \cdot \mathbf{e}_{2_x} & \quad b_1 = w_1 \cdot \mathbf{e}_{2_y} & \quad c_1 = w_1 \cdot \mathbf{e}_{2_z} \\
 a_2 = w_2 \cdot \mathbf{e}_{2_x} & \quad b_2 = w_2 \cdot \mathbf{e}_{2_y} & \quad c_2 = w_2 \cdot \mathbf{e}_{2_z} \\
 a_3 = w_3 \cdot \mathbf{e}_{2_x} & \quad b_3 = w_3 \cdot \mathbf{e}_{2_y} & \quad c_3 = w_3 \cdot \mathbf{e}_{2_z} \\
 a_4 = w_4 \cdot \mathbf{e}_{2_x} & \quad b_4 = w_4 \cdot \mathbf{e}_{2_y} & \quad c_4 = w_4 \cdot \mathbf{e}_{2_z}
 \end{aligned}$$

Thus, for the moment it reads as:

$$R_2 = \int_{A_1} g_2 J \left(\frac{dA_3}{dA_1} \right) dA_1 \quad (H.30)$$

Where:

$$\begin{aligned}
 g_2 = & \int M \cdot a_1 \cdot du1_{3_{\theta_1}} + \int M \cdot a_2 \cdot du2_{3_{\theta_1}} + \int M \cdot a_3 \cdot du3_{3_{\theta_1}} + \int M \cdot a_4 \cdot du4_{3_{\theta_1}} + \\
 & \int M \cdot b_1 \cdot du1_{3_{\theta_2}} + \int M \cdot b_2 \cdot du2_{3_{\theta_2}} + \int M \cdot b_3 \cdot du3_{3_{\theta_2}} + \int M \cdot b_4 \cdot du4_{3_{\theta_2}} + \\
 & \int M \cdot c_1 \cdot du1_{3_{\theta_3}} + \int M \cdot c_2 \cdot du2_{3_{\theta_3}} + \int M \cdot c_3 \cdot du3_{3_{\theta_3}} + \int M \cdot c_4 \cdot du4_{3_{\theta_3}} \quad (H.31)
 \end{aligned}$$

The following variables are used to define the drag functional:

$$\begin{aligned}
 a_1 = w_1 \cdot \mathbf{e}_{3_x} & \quad b_1 = w_1 \cdot \mathbf{e}_{3_y} & \quad c_1 = w_1 \cdot \mathbf{e}_{3_z} \\
 a_2 = w_2 \cdot \mathbf{e}_{3_x} & \quad b_2 = w_2 \cdot \mathbf{e}_{3_y} & \quad c_2 = w_2 \cdot \mathbf{e}_{3_z} \\
 a_3 = w_3 \cdot \mathbf{e}_{3_x} & \quad b_3 = w_3 \cdot \mathbf{e}_{3_y} & \quad c_3 = w_3 \cdot \mathbf{e}_{3_z} \\
 a_4 = w_4 \cdot \mathbf{e}_{3_x} & \quad b_4 = w_4 \cdot \mathbf{e}_{3_y} & \quad c_4 = w_4 \cdot \mathbf{e}_{3_z}
 \end{aligned}$$

Thus, for the drag it reads as:

$$R_3 = \int_{A_1} g_3 J \left(\frac{dA_3}{dA_1} \right) dA_1 \quad (H.32)$$

Where:

$$\begin{aligned}
g_3 = & \int D \cdot a_1 \cdot du_{1_{3_1}} + \int D \cdot a_2 \cdot du_{2_{3_1}} + \int D \cdot a_3 \cdot du_{3_{3_1}} + \int D \cdot a_4 \cdot du_{4_{3_1}} + \\
& \int D \cdot b_1 \cdot du_{1_{3_2}} + \int D \cdot b_2 \cdot du_{2_{3_2}} + \int D \cdot b_3 \cdot du_{3_{3_2}} + \int D \cdot b_4 \cdot du_{4_{3_2}} + \\
& \int D \cdot c_1 \cdot du_{1_{3_3}} + \int D \cdot c_2 \cdot du_{2_{3_3}} + \int D \cdot c_3 \cdot du_{3_{3_3}} + \int D \cdot c_4 \cdot du_{4_{3_3}} \quad (\text{H.33})
\end{aligned}$$

H.7 Integrating functionals using Gauss-Legendre technique

To solve equations H.28, H.30 and H.32, they are integrated numerically using the two-point Gauss-Legendre integration technique, Golub and Welsch (1967). In this method the integral of the function $f(x)$ in the domain $[-1, 1]$ is carried out using some weighting functions as follow:

$$\int_{-1}^1 f(x) dx \approx \sum_{i=1}^n \omega_i \cdot f(x_i) \quad (\text{H.34})$$

Where:

n : number of evaluation points

ω_i : weighting values

x_i : evaluation points

The error of this method can be decreased by increasing the number of evaluation points and choosing the right weighting values. There are several variants of this method that can be classified based on the number of evaluation points and weighting values.

In the Gauss-Legendre two-point variant, two points and two weighting values are used. These are presented in table H.1.

Table H.1: Gauss-Legendre two-point method

Points number	ω_i	x_i
1	1.0	$\frac{1}{\sqrt{3}}$
2	1.0	$\frac{-1}{\sqrt{3}}$

In this work, the reference integration domain is defined between $[-1/2, 1/2]$ for x_1 and y_1 axis. For this domain the evaluation points and weighting functions are presented in table H.2.

Thus, the application of the Gauss-Legendre two-point method on the function $f(x, y)$ in the defined reference domain reads as:

Table H.2: Gauss-Legendre two-point method in domain $[-1/2, 1/2]$

Points number	ω_i	x_i
1	2.0	$\frac{1}{2\sqrt{3}}$
2	2.0	$\frac{-1}{2\sqrt{3}}$

$$\int_{-\frac{1}{2}}^{\frac{1}{2}} \int_{-\frac{1}{2}}^{\frac{1}{2}} f(x, y) dx dy \approx 4 \left(f\left(\frac{-1}{2\sqrt{3}}, \frac{-1}{2\sqrt{3}}\right) + f\left(\frac{-1}{2\sqrt{3}}, \frac{1}{2\sqrt{3}}\right) + f\left(\frac{1}{2\sqrt{3}}, \frac{-1}{2\sqrt{3}}\right) + f\left(\frac{1}{2\sqrt{3}}, \frac{1}{2\sqrt{3}}\right) \right) \quad (\text{H.35})$$

Using this integration technique, the integral expression for the aerodynamic functionals, defined at the four nodes of the Quad elements can be given by:

$$R_1 = 4 \cdot \left(g_1 \left|_{\left(\frac{-1}{2\sqrt{3}}, \frac{-1}{2\sqrt{3}}\right)} + g_1 \left|_{\left(\frac{-1}{2\sqrt{3}}, \frac{1}{2\sqrt{3}}\right)} + g_1 \left|_{\left(\frac{1}{2\sqrt{3}}, \frac{-1}{2\sqrt{3}}\right)} + g_1 \left|_{\left(\frac{1}{2\sqrt{3}}, \frac{1}{2\sqrt{3}}\right)} \right. \right) \quad (\text{H.36})$$

$$R_2 = 4 \cdot \left(g_2 \left|_{\left(\frac{-1}{2\sqrt{3}}, \frac{-1}{2\sqrt{3}}\right)} + g_2 \left|_{\left(\frac{-1}{2\sqrt{3}}, \frac{1}{2\sqrt{3}}\right)} + g_2 \left|_{\left(\frac{1}{2\sqrt{3}}, \frac{-1}{2\sqrt{3}}\right)} + g_2 \left|_{\left(\frac{1}{2\sqrt{3}}, \frac{1}{2\sqrt{3}}\right)} \right. \right) \quad (\text{H.37})$$

$$R_3 = 4 \cdot \left(g_3 \left|_{\left(\frac{-1}{2\sqrt{3}}, \frac{-1}{2\sqrt{3}}\right)} + g_3 \left|_{\left(\frac{-1}{2\sqrt{3}}, \frac{1}{2\sqrt{3}}\right)} + g_3 \left|_{\left(\frac{1}{2\sqrt{3}}, \frac{-1}{2\sqrt{3}}\right)} + g_3 \left|_{\left(\frac{1}{2\sqrt{3}}, \frac{1}{2\sqrt{3}}\right)} \right. \right) \quad (\text{H.38})$$

Where g_1 , g_2 and g_3 are defined in equations H.29, H.31 and H.33, respectively.

H.8 Minimizing the functionals

To get the aerodynamic loads in a FE form, the functionals, R_1 , R_2 and R_3 are minimized. These functionals are a function of the four nodes displacements of the Quad elements. The partial derivative of these functionals with respect to the DOFs of a node gives a FE form of the loads as follow:

$$F_{k_m} = \frac{\partial(R_1 + R_3)}{\partial uk_{3_m}} \quad (\text{H.39})$$

$$M_{k_m} = \frac{\partial R_2}{\partial uk_{3_{\theta_m}}} \quad (\text{H.40})$$

Where:

$k=1,2,3,4$: node numbering

$m=1,2,3$: the 3 orthogonal axis of a Quad element

Using equations H.39 and H.40, the generalized aerodynamic loads, $[\mathbf{F}]_e$, of the element e can be approximated by the following expression:

$$[\mathbf{F}]_e = \left[\begin{array}{c} F_{1_1} F_{1_2} F_{1_3} M_{1_1} M_{1_2} M_{1_3} F_{2_1} F_{2_2} F_{2_3} M_{2_1} M_{2_2} M_{2_3} \\ F_{3_1} F_{3_2} F_{3_3} M_{3_1} M_{3_2} M_{3_3} F_{4_1} F_{4_2} F_{4_3} M_{4_1} M_{4_2} M_{4_3} \end{array} \right]_e^t \quad (\text{H.41})$$

Using this expression, the generalized aerodynamic loads are represented as a function of the generalized displacements, velocities and acceleration of the nodes.

H.9 Element matrices for the aerodynamic model

Using equation H.41, the generalized aerodynamic forces acting on a Quad element are defined. These forces are a function of the DOFs of every node and can be resorted in the form of element matrices, i.e. $[\mathbf{M}_A]_e$, $[\mathbf{D}_A]_e$ and $[\mathbf{K}_A]_e$.

This results in having the aerodynamic loads as an equivalent FE representation given by the following equation:

$$[\mathbf{F}]_e = [\mathbf{M}_A]_e [\ddot{\mathbf{u}}]_e + [\mathbf{D}_A]_e [\dot{\mathbf{u}}]_e + [\mathbf{K}_A]_e [\mathbf{u}]_e \quad (\text{H.42})$$

Where:

$[\mathbf{F}]_e$: generalized force vector acting on the nodes of the Quad elements

$[\mathbf{u}, \dot{\mathbf{u}}, \ddot{\mathbf{u}}]_e$: displacement, velocity and acceleration of the nodes of the Quad elements

$[\mathbf{M}_A]_e$: mass matrix of the generalized aerodynamic forces due to the acceleration of the nodes of the Quad elements

$[\mathbf{D}_A]_e$: damping matrix of the generalized aerodynamic forces due to the velocity of the nodes of the Quad elements

$[\mathbf{K}_A]_e$: stiffness matrix of the generalized aerodynamic forces due to the movement of the nodes of the Quad elements

The aerodynamic loads acting on the nodes of the Quad elements can be interpreted as a mechanical system with an equivalent mass $[\mathbf{M}_A]$, damping $[\mathbf{D}_A]$ and stiffness matrix $[\mathbf{K}_A]$. However, the equivalent aerodynamic mass, damping and stiffness matrices are complex and they are not always positive definite matrices.

The complex nature of these matrices introduce some phase shift between the forces and displacements on the nodes (non-orthogonality), and this phase shift introduces the possibility of having the instability.

In addition, in the FE representation of a structural system, the mass, damping and stiffness matrices are only dependent on the local properties of the element. However, the aerodynamic matrices have more dependency. For the aerodynamic element matrices of a wind turbine three type of dependencies can be foreseen:

- Positional: The element matrices are dependent on the radial position of the blade. This also introduces a different velocity that each section of the blade experiences.
- Angle of attack: The aerodynamic element matrices are dependent on the angle of attack of the blade section in which they lie. All the elements that are in the same blade section have the same angle of attack.

- Reduced frequency: Although the rotation speed is the same for every section of the blade, the reduced frequency changes for different blade sections.

H.10 Assembling the global aerodynamic matrices

To couple the aerodynamic element matrices with the structural elements, the aerodynamic matrices of the Quad elements should now be assembled into a global aerodynamic matrix. This global aerodynamic matrix represents the aerodynamic forces over the nodes of the blade in the global coordinate system. The assembling procedure is illustrated in figure [H.5](#).

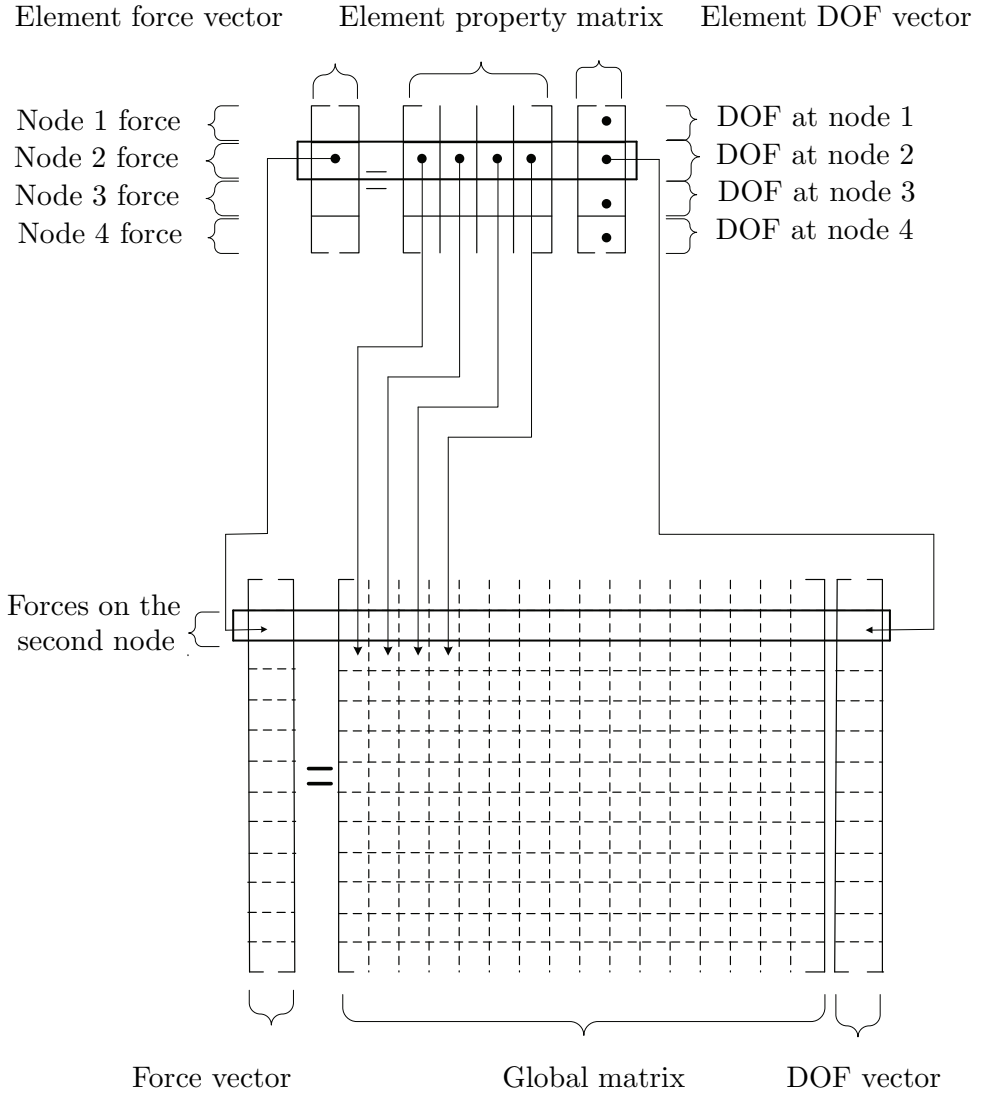


Figure H.5: Global matrix assembling diagram

Bibliography

- Agar, T. (1989). Aerodynamic flutter analysis of suspension bridges by a modal technique. *Engineering Structures*, 11(2):75–82. [6.2](#)
- Ashuri, T., Bussel, G., and Mieras, S. (2012). Development and validation of a computational model for design analysis of a novel marine turbine. *Wind Energy*. [3.6](#)
- Ashuri, T. and Zaaijer, M. (2007). Review of design concepts, methods and considerations of offshore wind turbines. *European Offshore Wind Conference and Exhibition, Berlin, Germany*. [3.5](#)
- Ashuri, T., Zaaijer, M., van Bussel, G., and van Kuik, G. (2010a). An analytical model to extract wind turbine blade structural properties for optimization and up-scaling studies. *The science of making torque from wind conference, Crete, Greece*. [3.10](#)
- Ashuri, T., Zaaijer, M., van Bussel, G., and van Kuik, G. (2010b). Controller design automation for aeroservoelastic design optimization of wind turbines. *The science of making torque from wind conference, Crete, Greece*. [3.9](#)
- Ashuri, T. and Zaayer, M. (2008). Size effect on wind turbine blade’s design drivers. *European Wind Energy Conference and exhibition, EWEC*. [2.3](#)
- Bauchau, O. and Craig, J. (2009). *Structural Analysis: With Applications to Aerospace Structures*. Springer Verlag. [3.10.1](#)
- Bayazit, N. (2004). Investigating design: A review of forty years of design research. *Design Issues, MIT Press*, 20(1):16–29. [3.2.1](#)
- Beer, F., Johnston, E., and DeWolf, J. (2006). *Mechanics of Materials*. The McGraw-Hill Companies Publishing. [3.10.1](#), [3.10.1](#)
- Benini, E. and Toffolo, A. (2002). Optimal design of horizontal-axis wind turbines using blade-element theory and evolutionary computation. *Journal of Solar Energy Engineering*, 124:357. [3.10](#), [3.12.1](#)
- Bianchi, F., Battista, H. D., and Mantz, R. (2006). Wind Turbine Control Systems: Principles, Modelling and Gain-scheduling Design (Advances in Industrial Control). *La-*

voisier Ed. [3.9.5](#)

- Bir, G. (2007). BModes user's guide. Technical report, National Renewable Energy Laboratory, Golden, Colorado. [B.6](#)
- Birgin, E. and Martinez, J. (2008). Improving ultimate convergence of an augmented lagrangian method. *Optimization Methods and Software*, 23(2):177–195. [3.12.4](#), [E.3](#)
- Björck, A., Dahlberg, J., Östman, A., and Ganander, H. (1997). Computations of aerodynamic damping for blade vibrations in stall. *European Wind Energy Conference*, pages 503–507. [6.2](#)
- Bossanyi, E., Burton, T., Sharpe, D., and Jenkins, N. (2001). Wind energy handbook. West Sussex, England: John Wiley & Sons Ltd. [3.11.3](#)
- Brand, A. (2008). Offshore Wind Atlas of the Dutch part of the North Sea. Technical report, ECN-M-09-050, Energy research Centre of the Netherlands, Petten. [3.7.4](#)
- Bulder, B., Hendriks, H., Langen, P., Lindenburg, C., Snel, H., Bauer, P., Polinder, H., Rooij, R., Subroto, H., and Zaayer, M. (2007). The icorass feasibility study. *ECN Wind Energy*. [1.1](#)
- Butterfield, S. and Laxson, W. M. A. (2004). Feasibility of Floating Platform Systems for Wind Turbines. *Global Windpower 2004 Conference Proceedings (CD-ROM)*, Chicago, Illinois. [A.2.24](#)
- Bywaters, G., John, V., Lynch, J., Mattila, P., Norton, G., Stowell, J., Salata, M., Labath, O., Chertok, A., and Hablanian, D. (2005). Northern Power Systems WindPACT drive train alternative design study report. Technical report, National Renewable Energy Laboratory, NREL/SR-500-35524, Golden, CO. [A.2.4](#), [A.2.7](#)
- Capponi, P. and Ashuri, T. (2010). A non-linear upscaling approach for wind turbine blades based on stresses. *European Wind Energy Conference, Brussels, Belgium*. [2.3](#)
- Chaviaropoulos, P. (1999). Flap/lead-lag aeroelastic stability of wind turbine blade sections. *Wind Energy*, 2(2):99–112. [6.2](#)
- Chaviaropoulos, P. (2007). Similarity rules for wind turbine upscaling. Internal report, UPWIND. [2.3](#), [2.1](#), [2.2](#), [2.3](#), [2.4](#), [2.5](#)
- Chaviaropoulos, P., Sørensen, N., Hansen, M., Nikolaou, I., Aggelis, K., Johansen, J., Gaunaa, M., et al. (2003). Viscous and aeroelastic effects on wind turbine blades. the viscel project. part ii: aeroelastic stability investigations. *Wind Energy*, 6(4):387–403. [6.2](#), [7.3.1](#)
- Dessi, D. and Mastroddi, F. (2008). A nonlinear analysis of stability and gust response of aeroelastic systems. *Journal of Fluids and Structures*, 24(3):436–445. [6.2](#)
- Dowell, E. (1970). Panel flutter—a review of the aeroelastic stability of plates and shells. *AIAA Journal*, 8:385–399. [6.2](#)
- Du, Z. and Selig, M. (1998). A 3-D stall-delay model for horizontal axis wind turbine performance prediction. *AIAA-98-0021*. [B.4](#)
- Duque, E., Johnson, W., van Dam, C., Cortes, R., and Yee, K. (2000). Numerical predictions of wind turbine power and aerodynamic loads for the NREL phase ii combined

- experiment rotor. *AIAA Paper*, 38:2000. [B.3](#)
- DUWIND (2001). Offshore Wind Energy: Ready to Power a Sustainable Europe, Concerted Action on Offshore Wind Energy in Europe. Technical report, Delft University of Technology, NNE5-1999-562, The Netherlands. [A.2.19](#)
- Eggers, A., Chaney, K., Digumarthi, R., and Incorporated, R. (2003). An assessment of approximate modeling of aerodynamic loads on the UAE rotor. *41st Aerospace Sciences Meeting and Exhibit, Reno, NV*, pages 6–9. [B.4](#)
- Fingersh, L., Hand, M., and Laxson, A. (2006). Wind turbine design cost and scaling model. Technical report, National Renewable Energy Laboratory, NREL/TP-500-40566, Golden, Colorado. [1.1](#), [2.2.2](#), [3.7.4](#), [3.11.2](#), [A.1](#)
- Fleury, C. (1989). Conlin: an efficient dual optimizer based on convex approximation concepts. *Structural and Multidisciplinary Optimization*, 1(2):81–89. [3.12.4](#), [E.2](#)
- Friedmann, P. (1976). Aeroelastic modeling of large wind turbines. *Journal of the American Helicopter Society*, 21:17. [6.2](#)
- Fuglsang, P., Bak, C., Schepers, J., Bulder, B., Cockerill, T., Claiden, P., Olesen, A., and van Rossen, R. (2002). Site-specific design optimization of wind turbines. *Wind Energy*, 5(4):261–279. [3.9](#)
- Fuglsang, P. and Madsen, H. (1999). Optimization method for wind turbine rotors. *Journal of Wind Engineering and Industrial Aerodynamics*, 80(1-2):191–206. [3.10](#), [3.12.1](#)
- Goland, M. (1957). An appraisal of aeroelasticity in design, with special reference to dynamic aeroelastic stability. In *Sixth Anglo-American Aeronautical Conference, London*. [6.2](#)
- Golub, G. and Welsch, J. (1967). Calculation of Gauss quadrature rules. *Stanford University, Department of Computer Science, USA*. [H.7](#)
- Griffin, D. (2001). WindPACT Turbine Design Scaling Studies Technical Area 1œComposite Blades for 80-to 120-Meter Rotor. Technical report, National Renewable Energy Laboratory, NREL/SR-500-29492, Golden, CO. [A.2.1](#)
- Griffith, D. and Ashwill, T. (2011). The sandia 100-meter all-glass baseline wind turbine blade: Snl100-00. *The Sandia national laboratories, USA, Report No. SAND2011-3779*. [9.5.2](#)
- Guo, D., Chu, F., and Zheng, Z. (2001). The influence of rotation on vibration of a thick cylindrical shell. *Journal of sound and vibration*, 242(3):487–505. [6.4.2](#)
- Haftka, R. and Gürdal, Z. (1992). *Elements of structural optimization*, volume 11. Springer. [3.4.4](#)
- Hansen, M. (2004). Aeroelastic stability analysis of wind turbines using an eigenvalue approach. *Wind Energy*, 7(2):133–143. [6.2](#)
- Hansen, M. (2007). Aeroelastic instability problems for wind turbines. *Wind Energy*, 10(6):551–577. [6.2](#)
- Hansen, M., Hansen, A., Larsen, T., Øye, S., Sørensen, P., and Fuglsang, P. (2005). Control

- design for a pitch-regulated, variable speed wind turbine. Technical report, Risø-R-1500(EN). 3.9
- Hansen, M., Thomsen, K., Fuglsang, P., and Knudsen, T. (2006). Two methods for estimating aeroelastic damping of operational wind turbine modes from experiments. *Wind Energy*, 9(1-2):179–191. 6.2
- Harrison, R. and Jenkins, G. (1993). Cost modeling of horizontal axis wind turbines. Technical Report ETSU W/34/00170/REP, University of Sunderland, School of Environment. 2.2.2, A.1
- Hendriks, H. and Zaijjer, M. (2004). Dowec: Executive summary of the public research activities. Technical report, ECN, Petten, NL. 1.1
- Holierhoek, J. (2008). Aeroelasticity of large wind turbines. *PhD dissertation, Delft University of Technology*. 6.2
- Hong, C. and Chopra, I. (1985). Aeroelastic stability analysis of a composite rotor blade. *Journal of the American Helicopter Society*, 30:57. 6.2
- Honneff, H. (1932). Windkraftwerke. *Elektrotechnik und Maschinenbau*. 2.2.1
- Hütter, U. (1942). Beitrag zur schaffung von gestaltungsgrundlagen für windkraftwerke. *Dissertation at TH Wien*. 2.2.1
- Jamieson, P. (2007). Loading and cost trends using certification calculation. Internal report, UPWIND. 2.4, 2.1, 2.2, 2.3, 2.4, 2.5, 2.9, 3
- Jamieson, P. (2011). *Innovation in Wind Turbine Design*. Wiley. 2.3, 2.4
- Janetzke, D. and Kaza, K. (1983). Whirl flutter analysis of a horizontal-axis wind turbine with a two-bladed teetering rotor. *Solar Energy*, 31(2):173–182. 6.2
- Jia, Z. (1998). A refined iterative algorithm based on the block arnoldi process for large unsymmetric eigenproblems*. *Linear algebra and its applications*, 270(1-3):171–189. 6.3
- Johnson, K., Fingersh, L., Balas, M., and Pao, L. (2004). Methods for increasing region 2 power capture on a variable speed HAWT. *Collection of the 2004 ASME Wind Energy Symposium Technical Papers Presented at the 42nd AIAA Aerospace Sciences Meeting and Exhibit, Reno, Nevada*, pages 103–113. 3.9.5
- Jonkman, J. and Buhl, M. (2004). FAST user's guide. Technical report, National Renewable Energy Laboratory, NREL/EL-500–29798, Golden, Colorado. 3.9.5
- Jonkman, J., Butterfield, S., Musial, W., and Scott, G. (2009). Definition of a 5-MW reference wind turbine for offshore system development. Technical report, National Renewable Energy Laboratory, NREL/TP-500-38060, Golden, CO. 1.1, 1.3, 4.3.1
- Kallesoe, B. (2011). Effect of steady deflections on the aeroelastic stability of a turbine blade. *Wind Energy*, 14(2):209–224. 6.2
- Kaza, K. and Hammond, C. (1976). An investigation of flap-lag stability of wind-turbine rotors in the presence of velocity gradients and helicopter rotors in forward flight. *17th Structures, Structural Dynamics and Materials Conference*. 6.2
- Kühn, M. et al. (1998). Opti-owecs project final report volume 0: Executive summary.

- Institute for Wind Energy, Delft University of Technology, Delft, The Netherlands.* 1.1
- Kirchgässner, B. (1983). Arlis: A program system for aeroelastic analysis of rotating linear systems. *Proceedings of European Wind Energy Conference*, pages 253–258. 6.2
- Kleinhenz, F. (1942). Projekt eines grosswindkraftwerkes. *Der Bauingenieur*, Vol 23/24. 2.2.1
- Kooijman, H., Lindenburg, C., Winkelaar, D., and van der Hooft, E. (2003). DOWEC 6 MW pre design, Aero-elastic modelling of the DOWEC 6 MW pre-design in PHATAS. Technical report, ECN-CX-01-135, Energy Research Center of the Netherlands, Petten. G.1.1
- Laino, D. and Hansen, A. (2002). User's Guide to the Wind Turbine Dynamics Aerodynamics Computer Software AeroDyn. Technical report, Windward Engineering LLC, Prepared for the National Renewable Energy Laboratory under Subcontract No. TCX-9-29209-01, Salt Lake City, UT. B.3
- Leishman, J. and Beddoes, T. (1989). A semi-empirical model for dynamic stall. *Journal of the American Helicopter Society*, 34:3. B.3
- Lindenburg, C. and Snel, H. (2003). Aeroelastic stability analysis tools for large wind turbine rotor blades. *Proceedings of the 2003 European Wind Energy Conference and Exhibition*. 6.2
- Lobitz, D. (2005). Parameter sensitivities affecting the flutter speed of a mw-sized blade. *Journal of solar energy engineering*, 127:538. 6.2
- Malcolm, D. and Hansen, A. (2002). WindPACT turbine rotor design study. Technical report, National Renewable Energy Laboratory, NREL/SR-500-32495, Golden, CO. 4.4, A.2.2
- Malcolm, D. and Laird, D. (2007). Extraction of equivalent beam properties from blade models. *Wind Energy*, 10(2):135–157. 3.10
- Manwell, J. (2002). An overview of the technology and economics of offshore wind farms. Technical report, Renewable Energy Research Laboratory, University of Massachusetts. A.2.20
- Martin, G. and Roux, J., editors (2011). *Wind Turbines: Types, Economics and Development*. Nova Publisher. 2.6
- Martins, J. and Lambe, A. (2011). Multidisciplinary design optimization: Survey of architectures. *AIAA Journal*. 3.6
- Meng, F., Pavel, M., and van Tooren, M. (2008). Aeroelastic stability analysis of large scale horizontal axis wind turbines using reduced order system identification based on flexible nonlinear multi-body dynamics. *46th AIAA Aerospace Sciences Meeting and Exhibit, Reno, Nevada, USA*, pages 7–10. 6.2, 7.3, 7.3.3, 7.3.3
- Milton, N. (2007). Knowledge acquisition in practice: a step-by-step guide. *Springer Verlag*. 3.4.3
- Molly, J. (1989). Maximum economic size of wind energy converters. *European Wind Energy Conference*. 2.3

- Musial, W. and Butterfield, C. (1997). Using partial safety factors in wind turbine design and testing. *Wind Power* 97. 3.7.3
- Nijssen, R., Zaaijer, M., Bierbooms, W., van Kuik, G., and van Delft, D. (2001). The application of scaling rules in up-scaling and marinisation of a wind turbine. *Offshore Wind Energy Special Topic Conference*. 2.3
- Oberkampff, W., Helton, J., Joslyn, C., Wojtkiewicz, S., and Ferson, S. (2004). Challenge problems: uncertainty in system response given uncertain parameters. *Reliability Engineering & System Safety*, 85(1-3):11–19. 3.3.3
- Online-Reader, E. (2007). Power: Pushing offshore wind energy regions, <http://www.offshore-power.net/>, retrieved on 25 march 2012. 1.1
- Online-Reader, E. (2010). Autograph, <http://www.jacobswind.net/>, retrieved on 21 june 2010. 2.2.1
- Online-Reader, E. (2012). Upwind: Eu's sixth framework programme (fp6), <http://www.upwind.eu>, retrieved on 2 may 2012. 1.1
- Ormiston, R. (1973). Rotor dynamic considerations for large wind power generator systems. *Wind Energy Conversion Systems Workshop, National Science Foundation*, pages 80–88. 6.2
- Ormiston, R. (1975). Dynamic response of wind turbine rotor systems. *American Helicopter Society, Annual National Forum*, 1. 6.2
- Pahl, G., Beitz, W., and Wallace, K. (1996). *Engineering design: a systematic approach*. Springer Verlag. 3.2.1
- Patil, M., Hodges, D., and Cesnik, C. (2001). Nonlinear aeroelasticity and flight dynamics of high-altitude long-endurance aircraft. *Journal of Aircraft*, 38(1):88–94. 6.2
- Petersen, B., Pollack, M., Connell, B., Greeley, D., Davis, D., Slavik, C., and Goldman, B. (2010). Evaluate the Effect Of Turbine Period of Vibration Requirements on Structural Design Parameters: Technical Report of Findings. *Applied Physical Sciences: Report Number M10PC00066-8*. 4.4
- Petersen, J., Madsen, H., Björck, A., Enevoldsen, P., Øye, S., Ganander, H., and Winkelaar, D. (1998). Prediction of dynamic loads and induced vibrations in stall. *Risø internal reports*. 6.2
- Pierre, D. and Lowe, M. (1975). *Mathematical programming via augmented lagrangians: An introduction with computer programs*. Addison-Wesley Reading, Mass. E.3
- Pitt, D. and Peters, D. (1983). Rotor dynamic inflow derivatives and time constants from various inflow models. 9th European Rotorcraft Forum. *Stresa, Italy*, pages 13–15. B.3
- Politis, E., Chaviaropoulos, P., Riziotis, V., Voutsinas, S., and Romero-Sanz, I. (2009). Stability analysis of parked wind turbine blades. *European Wind Energy Conference*, pages 59–63. 6.2
- Poore, R. and Lettenmaier, T. (2003). Alternative design study report: WindPACT advanced wind turbine drive train designs study. Technical report, National Renewable Energy Laboratory, NREL/SR-500-33196, Golden, CO. A.2.4, A.2.7

- Putnam, P. (1947). Power from the wind. *Van Nostrand Reinold Company*. 2.2.1
- Rao, S. (2009). *Engineering optimization: theory and practice*. Wiley. E.3
- Robinson, M., Hand, M., Simms, D., and Schreck, S. (1999). Horizontal axis wind turbine aerodynamics: three-dimensional, unsteady, and separated flow influences. *Presented at the 3rd ASME/JSME Joint Fluids Engineering Conference, San Francisco, CA (US)*. B.3
- Roth, E., Verhoef, L., and Dingenouts, M. (2005). Concerted action for offshore wind energy deployment (cod). *European Commission Directorate-General for Energy DGXVII*. 1.1
- Roy, R., Azene, Y., Farrugia, D., Onisa, C., and Mehnen, J. (2009). Evolutionary multi-objective design optimisation with real life uncertainty and constraints. *CIRP Annals-Manufacturing Technology*, 58(1):169–172. 3.3.3
- Saad, Y. (1980). Variations on Arnoldi's method for computing eigenelements of large unsymmetric matrices. *Linear algebra and its applications*, 34:269–295. 6.7
- Sarkar, S. and Bijl, H. (2008). Nonlinear aeroelastic behavior of an oscillating airfoil during stall-induced vibration. *Journal of Fluids and Structures*, 24(6):757–777. 6.2
- Savransky, S. (2000). *Engineering of creativity*. CRC Press. 3.2.1
- Schreiber, G., Akkermans, H., Anjewierden, A., de Hoog, R., Shadbolt, N., de Velde, W. V., and Wielinga, B. (2000). Knowledge engineering and management: the CommonKADS methodology. *the MIT Press*. 3.4.3
- Sektorov, V. (1933). The present state of planning and erection of large experimental wind power stations. *NASA*. Translation from Russian. 2.2.1
- Semyon, D. (2000). *Engineering of creativity: Introduction to TRIZ Methodology of Inventive Problem Solving*. CRC Press. 3.2.2
- Smith, K. (2001). WindPACT Turbine Design Scaling Studies Technical Area 2: Turbine, Rotor, and Blade Logistics. Technical report, National Renewable Energy Laboratory, NREL/SR-500-29439, Golden, CO. A.2.21
- Spera, D. (1994). *Wind Turbine Technology: Fundamental Concepts of Wind Turbine Engineering*. New York. 2.2
- Stiesdal, H. (1994). Extreme wind loads on stall regulated wind turbines. *Proceedings of the 16th British Wind Energy, Association Conference, London*, pages 101–106. 6.2
- Stokes, M. (2001). Managing engineering knowledge: MOKA: methodology for knowledge based engineering applications. *Professional Engineering Publishing*. 3.4.3
- Su, W. and Cesnik, C. (2010). Nonlinear aeroelasticity of a very flexible blended-wing-body aircraft. *Journal of Aircraft*, 47(5):1539–1553. 6.2
- Theodorsen, T. (1935). General theory of aerodynamic instability and the mechanism of flutter. Technical report, NACA report. 6.2, 6.5
- van Engelen, T. (2007). Control design based on aero-hydro-servo-elastic linear models from TURBU (ECN). *Proceeding of the European Wind Energy Conference, Milan, Italy*. 3.9.5

- VanGundy, A. (1992). *Techniques of structured problem solving*. Van Nostardam Reinhold Company, New York. [3.2.1](#)
- Viterna, L. and Janetzke, D. (1982). Theoretical and experimental power from large horizontal-axis wind turbines. *NASA STI/Recon Technical Report N*, 82:33830. [B.4](#)
- Warne, D. and Calnan, P. (1977). Generation of electricity from the wind. *Proceedings of the Institution of Electrical Engineers*, 124(11R):963–985. [2.2](#)
- Weisstein, E. (2003). *CRC concise encyclopedia of mathematics*. CRC Press International. [E.3](#)
- Xudong, W., Shen, W., Zhu, W., Sørensen, J., and Jin, C. (2009). Shape optimization of wind turbine blades. *Wind Energy*, 12(8):781–803. [3.9](#)

Curriculum vitae

Turaj Ashuri was born on 1975 in Kermanshah, Iran (Persian). He obtained his high-school diploma in 1992 with distinction. He proceeded to obtain his bachelor of science degree in mechanical engineering with a specialization in heat and fluid mechanics at Tehran Azad University. The title of his bachelor graduation thesis is; 'Modeling, Design Analysis and Optimization of a Hydropneumatic Suspension System'. He defended his thesis with the grade 19/20 and obtained his bachelor of science degree in 1999.

Turaj worked in Iranian railway industry for five years, in the same time also functioning as a certified design and inspection engineer in Heating, Ventilating and Air-Conditioning of buildings (HVAC CEng). In 2002 he successfully passed the national university exam for higher education in Iran and ranked among the top 1% of the candidates. Based on this ranking he was admitted with a full scholarship at the prestigious technical university of the middle-east, Sharif University of Technology.

He continued his graduate education in the aerospace engineering faculty of Sharif with aerostructures as the major and aeroelasticity as the minor track. The title of his master graduation thesis is; 'A Computational Model for Wind Turbine Composite Blade Design and Optimization: A Finite Element Approach'. He defended his thesis with the grade 20/20 and obtained his master of science degree in 2005.

After completing his MSc degree, he worked for two years in TUGA Company as a gas turbine auxiliary and accessory professional engineer. He joined the department of aerodynamics and wind energy of Delft University of Technology in 2007 as a PhD researcher to do research in a very exciting and interesting field, wind energy. In his research, he explores the horizon of larger scale offshore wind turbines using multidisciplinary design optimization.

He is currently employed by Siemens wind power. He will join the multidisciplinary design optimization laboratory (MDOLAB) of university of Michigan as a postdoctoral research fellow next year. In his new position in MDOLAB, he further develops the research that he carried out in his PhD.

Turaj is happily married and has two sons; Ryan (4 years old) and Dorian (1 year old).